Phase evolution and reactivity of Pr_2NiO_{4+d} and $Ce_{0.9}Gd_{0.1}O_{2-d}$ solid oxide cell electrodes

A thesis submitted to fulfil the requirements of the Doctor of Philosophy degree at the Department of Materials, Imperial College London and Diploma of Imperial College London

Chen-Yu Tsai

Supervised by Prof. Stephen J. Skinner

Dr. Ainara Aguadero

Department of Materials

Imperial College London

2020

Declaration

I hereby declare that the thesis is my own work. Any presented information which is not my original research has been appropriately acknowledged and referenced.

Chen-Yu Tsai (2020)

Copyright Declaration

The copyright of this thesis rests with the author. Unless otherwise indicated, its contents are licensed under a Creative Commons Attribution-Non Commercial-No Derivatives 4.0 International Licence (CC BY-NC-ND).

Under this licence, you may copy and redistribute the material in any medium or format on the condition that; you credit the author, do not use it for commercial purposes and do not distribute modified versions of the work.

When reusing or sharing this work, ensure you make the licence terms clear to others by naming the licence and linking to the licence text.

Please seek permission from the copyright holder for uses of this work that are not included in this licence or permitted under UK Copyright Law.

Acknowledgements

I would like to thank my family for their selfless support during my PhD study at Imperial College London. I would also like to thank Prof. Stephen J. Skinner and Dr. Ainara Aguadero for their supervision of my research. Indeed, I would like to acknowledge the help from Dr. Catriona M. McGilvery for STEM EDS mapping, Dr. Cati Ware for TEM lamella preparation and Mr. Richard Sweeney for *in-situ* XRD. In addition, the author is grateful for the access to the synchrotron and neutron facilities at Diamond Light Source Ltd (proposal no. EE19574) and at ISIS, Science and Technology Facilities Council (STFC) (proposal RB1890250). Finally, the author would like to acknowledge the partial funding from the Department of Materials, Imperial College London through the EPSRC Centre for Doctoral Training in the Advanced Characterisation of Materials (EP/L015277/1).

Abstract

$Pr_2NiO_{4+\delta}$ has been reported to possess a better solid oxide cell air electrode performance than the conventional $La_{0.6}Sr_{0.4}Fe_{0.8}Co_{0.2}O_{3-\delta}$ air electrode. However, $Pr_2NiO_{4+\delta}$ is not stable and can decompose and even react with the $Ce_{0.9}Gd_{0.1}O_{2-\delta}$ interface layer, located between $Pr_2NiO_{4+\delta}$ and the zirconia based electrolyte, but the detailed mechanism is unclear. This research has identified the phase evolution of $Pr_2NiO_{4+\delta}$ and $Ce_{0.9}Gd_{0.1}O_{2-\delta}$ under solid oxide air electrode sintering and operating temperatures in air. For example, praseodymium was observed to diffuse from $Pr_2NiO_{4+\delta}$ to $Ce_{0.9}Gd_{0.1}O_{2-\delta}$ to form $Ce_{1-x-y}Gd_xPr_yO_{2-\delta}$ at 1100°C, leaving NiO as a secondary phase. The praseodymium content of $Ce_{1-x-y}Gd_xPr_yO_{2-\delta}$ depended on the distance of the initial $Ce_{0.9}Gd_{0.1}O_{2-\delta}$ from the interface between $Pr_2NiO_{4+\delta}$ and $Ce_{0.9}Gd_{0.1}O_{2-\delta}$. The closer it was, the more praseodymium was incorporated. On the other hand, the unreacted $Pr_2NiO_{4+\delta}$ decomposed to $Pr_4Ni_3O_{10-\delta}$ and Pr_6O_{11} at 800°C in air.

As the aim of the research was to develop an air electrode material which has a reasonable and stable performance operating in the intermediate temperature range of 500-800°C, the resulting products from the previous reactions were chosen, especially $Pr_4Ni_3O_{10-\delta}$ and $Ce_{0.75}Gd_{0.10}Pr_{0.15}O_{2-\delta}$, to form a composite air electrode. The synthesis kinetics, the crystal structure, the oxygen content and the electrical conductivity were first investigated for the $Pr_4Ni_3O_{10-\delta}$ phase. A 50:50 wt.% $Pr_4Ni_3O_{10-\delta}$ and $Ce_{0.75}Gd_{0.10}Pr_{0.15}O_{2-\delta}$ composite was demonstrated to provide the best air electrode performance in comparison with all other compositions. Its area specific resistance was even lower than 0.15 Ωcm^2 at temperatures greater than 711°C in air. Indeed, the 50:50 wt.% of $Pr_4Ni_3O_{10-\delta}$-$Ce_{0.75}Gd_{0.10}Pr_{0.15}O_{2-\delta}$ composite electrode showed a stable electrode performance in a long term (7 days) test without any apparent degradation. Therefore, $Pr_4Ni_3O_{10-\delta}$-$Ce_{0.75}Gd_{0.10}Pr_{0.15}O_{2-\delta}$ composites are promising air electrode materials which seem to inherit the electrocatalytic activity of $Pr_2NiO_{4+\delta}$ but are thermodynamically more stable.

Table of Contents

Declaration ii

Copyright Declaration ii

Acknowledgements iii

Abstract iv

Table of Contents v

List of Figures x

List of Tables xxi

List of Abbreviations xxiii

Chapter 1 Introduction 1

1.1 Advantages of solid oxide cells (SOCs) 1

1.2 SOFC/ SOEC operation 3

1.2.1 Working principle 3

1.2.2 Thermodynamics 5

1.3 General requirements for SOC components 11

1.3.1 SOC air electrode requirements 11

1.3.2 SOC electrolyte requirements 15

1.3.3 SOC fuel electrode requirements 15

1.3.4 SOC interconnect requirements 16

1.4 Conductivity in ceramics 16

1.4.1 Electronic conductivity 16

1.4.2 Oxygen ionic conductivity 19

1.4.3 Mixed ionic and electronic conductivity 20

1.5 Summary 21

References 21

Chapter 2 Materials for solid oxide cells (SOCs) 24

2.1 Introduction....24
2.2 Oxide ion conducting electrolytes....24
2.2.1 Substituted zirconia....24
2.2.2 Substituted ceria....26
2.2.3 Substituted lanthanum gallate....27
2.3 Hydrogen electrode....28
2.4 Air electrode....29
2.4.1 Lanthanum strontium manganites....29
2.4.2 Mixed ionic and electronic conducting (MIEC) perovskite oxides....29
2.4.3 Double perovskites....30
2.4.4 Ruddlesden-Popper phases....31
2.5 Ruddlesden-Popper phases as air electrode materials....32
2.5.1 Thermal expansion coefficients (TEC)....32
2.5.2 Electrical conductivity....33
2.5.3 Oxygen diffusion and surface exchange coefficients....34
2.5.4 Electrode performance....36
2.5.5 Thermal stability and chemical reactivity at high temperature....38
2.6 $Pr_2NiO_{4+\delta}$ decomposition and possible approaches to stabilise it....40
2.6.1 Substituting Sr and Ca at the Pr site....40
2.6.2 Substituting La and Nd at the Pr site....41
2.6.3 Substituting Cu or Fe at the Ni site....42
2.6.4 Praseodymium deficiency....42
2.6.5 Other approaches....43
2.7 The derived products from the chemical reactions related to $Pr_2NiO_{4+\delta}$....44
2.7.1 $Pr_4Ni_3O_{10+/-\delta}$ and $PrNiO_{3-\delta}$....45
2.7.2 $Ce_{1-x-y}Gd_xPr_yO_{2-\delta}$ (CGPO)....47

2.7.3 PrO_x and NiO 49
2.8 Effective medium percolation theory 51
2.9 Summary 54
References 54
Chapter 3 Experimental methods 61
3.1 Introduction 61
3.2 Materials synthesis 61
3.2.1 Solid state reaction 61
3.2.2 Sol-gel synthesis 62
3.3 Test cell fabrication 64
3.3.1 Ball milling of the synthesised powder 64
3.3.2 Electrolyte fabrication 64
3.3.3 Electrode ink fabrication 65
3.3.4 Ink deposition 65
3.4 Materials characterisation 66
3.4.1 X-ray/synchrotron source X-ray/neutron diffraction 66
3.4.2 Scanning electron microscopy (SEM) 74
3.4.3 Energy dispersive spectroscopy (EDS) 77
3.4.4 Electrical conductivity measurement using the van der Pauw approach 79
3.4.5 AC impedance spectroscopy 80
3.4.6 Inductively coupled plasma atomic emission spectroscopy (ICP-AES) 86
3.4.7 Archimedes density testing 87
3.4.8 Electrode adherence testing 88
3.4.9 Iodometric titrations 89
3.5 Summary 90
References 90

Chapter 4 Chemical compatibility between $Pr_2NiO_{4+\delta}$ and $Ce_{0.9}Gd_{0.1}O_{2-\delta}$ under solid oxide cell sintering and operating temperatures 93

4.1 Introduction 93

4.2 Detailed experimental procedures 94

4.3 Phase identification of the synthesised materials and the thermally untreated powder mixture 96

4.4 Thermal treatment of the composites at cell sintering conditions 100

4.5 Thermal treatment of the composites at cell operating temperature 113

4.6 Summary 118

References 119

Chapter 5 Synthesis kinetics and physical properties of $Pr_4Ni_3O_{10-\delta}$ 120

5.1 Introduction 120

5.2 Detailed experimental procedures 121

5.3 The synthesis kinetics of $Pr_4Ni_3O_{10+/-\delta}$ 123

5.4 Re-evaluation of the crystal structure of $Pr_4Ni_3O_{10+/-\delta}$ 130

5.5 The oxygen content of the synthesised $Pr_4Ni_3O_{10-\delta}$ 138

5.6 The electrical conductivity of $Pr_4Ni_3O_{10+/-\delta}$ and *in-situ* XRD results 139

5.7 Summary 145

References 146

Chapter 6 Evaluation of the electrochemical performance of $Pr_4Ni_3O_{10-\delta}$ and CGPO composite electrodes 148

6.1 Introduction 148

6.2 Detailed experimental procedures 149

6.3 Chemical synthesis and phase identification 151

6.4 Chemical compatibility test of electrode and electrolyte components 155

6.5 As-sintered electrodes 161

6.6 Electrochemical performance of the composite electrode with various compositions 163
6.7 Post-mortem test of the composite electrodes 174
6.8 7-day electrode performance 179
6.9 Discussions of artifacts in the experiments 188
6.10 Summary 193
References 194
Chapter 7 Conclusions and future work 196
References 198
Publications and presentations 199
Appendices 200

List of Figures

Figure 1.1: Schematic representation of how SOCs can be integrated with intermittent renewable energy sources to solve the issue of energy supply/ demand mismatch. 2

Figure 1.2: The working principle of **(a)** SOFC and **(b)** SOEC when using hydrogen and steam, respectively as a reactant. Reproduced from [5] with kind permission from John Wiley and Sons. 3

Figure 1.3: The enthalpy and Gibbs free energy of water gas shift reaction over different temperatures. Reproduced from [13] with kind permission from Elsevier. 5

Figure 1.4: The total energy, electricity and heat requirement for H_2O and CO_2 electrolysis. Reproduced from [14] with kind permission from Elsevier. 6

Figure 1.5: The thermodynamic efficiency comparison between fuel cell (both LHV and HHV) and Carnot cycle. Replotted from [8]. 8

Figure 1.6: The typical I-V curves in SOFC and SOEC modes. 10

Figure 1.7: The elemental steps of ORR on solely electronic conducting air electrode and the TPB reactive site located between air electrode, oxygen ionic conducting electrolyte and gas (pore). Reproduced from [18] with kind permission from Elsevier. 12

Figure 1.8: The DPB on a porous MIEC air electrode in SOFC. Reproduced from [18] with kind permission from Elsevier. 13

Figure 1.9: The illustration of the ORR elemental steps (left) and the OER elemental steps (right) on a MIEC air electrode. Replotted from [24]. 15

Figure 1.10: The impact of electrical bias on electron transfer. **(a)** The case of a metallic conductor, without bias. **(b)** The case of metallic conductor, with bias. **(c)** The case of insulators, with bias. The grey filling in the figures indicate if a particular band is fully or partially filled. Replotted from [30]. 17

Figure 1.11: Semiconductor electronic conductivity activated by **(a)** temperature, **(b)** donor dopants, **(c)** acceptor dopants. Replotted from [30]. 18

Figure 1.12: The hopping mechanisms of oxygen charge carriers. **(a)** Vacancy mechanism. **(b)** Interstitial mechanism. **(c)** Interstitialcy mechanism. Reproduced from [31] under a Creative Commons Attribution Non-Commercial No Derivatives licence. 20

Figure 2.1: The change of oxygen ionic conductivity of $(ZrO_2)_{1-x}(Y_2O_3)_x$ (YSZ) and $(ZrO_2)_{1-x}(Sc_2O_3)_x$ (ScSZ) by varying the amount of x at 1000°C in air. The various labels indicate the experimental data from different references mentioned in the original paper whereas the curve shows the overall trend. Reproduced from [6] with kind permission from Elsevier. 25

Figure 2.2: The oxygen ionic conductivity comparison between each conventional electrolyte material under different temperatures. The reference numbers on the plot relate to the current reference list. 28

Figure 2.3: Crystal structure of A site ordered double perovskite with chemical formula of $LnBaM_2O_{5+\delta}$, where Ln and M can be Gd, Pr, Nd and Sm and Co, Fe, Mn and Cu, respectively. Adapted from [20] with kind permission from Elsevier. 31

Figure 2.4: The two dimensional RP phase crystal structures which show the increasing number of perovskite layers on increasing n, where n=1, 2 and 3. Reproduced from [51] with kind permission from Elsevier. 32

Figure 2.5: Electrical conductivity of different air electrode materials under various temperatures. Reproduced from [20] with kind permission from Elsevier. 34

Figure 2.6: Oxygen diffusion (D*) **(a)** and surface exchange (k) **(b)** coefficients of various air electrode materials in different temperature. Reproduced from [20] with kind permission from Elsevier. 36

Figure 2.7: Electrode polarization resistance (R_p) for different air electrode materials **(a)** without and **(b)** with an interlayer at the air electrode/electrolyte interface measured under open circuit condition over different temperature ranges. Reproduced from [77] with kind permission from Elsevier. 37

Figure 2.8: Anodic polarization curves of cells when using $Pr_2NiO_{4+\delta}$ and LSCF as an air electrode without CGO interlayer. They are compared with the results of $Pr_2NiO_{4+\delta}$ with CGO interlayer. All the measurements were conducted at 800°C in air. Replotted from [77]. 38

Figure 2.9: **(a)** Nyquist plot and **(b)** Bode plot for the symmetrical cell ($Pr_2NiO_{4+\delta}$/CGO/YSZ) aged for one month at 700°C in air. Reproduced/adapted from [92] with kind permission from IOP Publishing. 45

Figure 2.10: The electrochemical performance comparisons between NiO, $Pr_2NiO_{4+\delta}$, Pr_6O_{11}, $La_2NiO_{4+\delta}$, $Sm_{0.5}Sr_{0.5}CoO_{3-\delta}$ and $La_{0.6}Sr_{0.4}CoO_{3-\delta}$ when they are infiltrated on a CGO or CSO backbones. The CGO and CSO are presented as GDC and SDC, respectively in the original paper. The references are also corresponding to the ones in the original paper. Reproduced from [118] with kind permission from Elsevier. ……50

Figure 2.11: The overall surface exchange rate comparison between $PrNiO_3$, $Pr_2NiO_{4+\delta}$, $Pr_4Ni_3O_{10+\delta}$, Pr_6O_{11} and $La_2NiO_{4+\delta}$ at various temperatures under $pO_2 = 0.21$ atm. Adapted from [119] with kind permission from Royal Society of Chemistry. ……51

Figure 2.12: The calculated results of effective electronic conductivity **(a)** and effective ionic conductivity **(b)** in a porous Ag-YSB composite using the EMPT approach. Reproduced from [121] with kind permission from Elsevier. ……53

Figure 3.1: The metal complex (gel) after removing water in metal citrate solution. Reproduced from [4] published by The Royal Society of Chemistry under a Creative Commons Attribution 3.0 Unported Licence. ……63

Figure 3.2: **(a)** The scenario when the incident X-ray angle (θ) is different from the scattered X-ray angle (α). **(b)** X-ray reflection from the consecutive atomic planes which are separated by distance, d. ……67

Figure 3.3: The source of signals and their corresponding interaction volume when the sample is exposed by the primary electron beam. ……75

Figure 3.4: An illustration of a square sample in which its resistivity is measured by the van der Pauw approach. The probes are labelled with number and are located at the four corners. ……80

Figure 3.5: A Nyquist plot with one semi-circle and one depressed semi-circle to resemble possible results from AC impedance measurement. An equivalent circuit model used to simulate the Nyquist plot is present and this is together with the parameters used for each circuit element. As the simulated ohmic resistance (R1) was 15 Ω, the whole Nyquist plot horizontally shifted to the right from the origin to the same magnitude. ……81

Figure 3.6: The corresponding Bode plots **(a)** in the form of the impedance magnitude over various frequencies and **(b)** in the form of the phase shift over various frequencies with respect to the Nyquist plot in **Figure 3.5**. ……82

Figure 3.7: An example of a Gerischer electrode response in a Nyquist plot with the corresponding equivalent circuit model and parameters provided. ……..84

Figure 3.8: The custom-built sample holder used for AC impedance test. Au meshes were also used to replace the Pt meshes. Reproduced from [2] under a Creative Commons Attribution Non-Commercial No Derivatives licence. ……..85

Figure 4.1: Rietveld refinement of the as-synthesised $Pr_2NiO_{4+\delta}$ powder based on the laboratory based XRD. The figure demonstrates that a single phase was received with acceptable goodness of fit (χ^2=2.74, R_{wp}= 7.57%, R_p= 5.96%). Reproduced from Tsai et al. [9]. ……..96

Figure 4.2: HR-SXRPD data of the untreated $Pr_2NiO_{4+\delta}$/CGO10 composite powder analysed by Le Bail refinement. The figure highlights the peak position of each phase with acceptable goodness of fit (χ^2=4.90, R_{wp}=12.1, R_p=8.86). Reproduced from Tsai et al. [9]. ……..98

Figure 4.3: **(a)** The low magnification of the backscattered image showing bimodal distribution of particle size. **(b)** The magnification image of the red square region in **Figure 4.3(a)**. Point EDS was conducted at each location with red dots being identified as $Pr_2NiO_{4+\delta}$ and blue dots were CGO10. The corresponding EDS spectrum of red dots and blue dots can be found in **Figure 4.4(a)** and **(b)**. Reproduced from Tsai et al. [9]. ……99

Figure 4.4: EDS spectrum corresponding to **(a)** red dots ($Pr_2NiO_{4+\delta}$) and **(b)** blue dots (CGO10) in **Figure 4.3(b).** The observed Ge signal in **Figure 4.4(b**) might be due to the presence of an impurity at the local regions. ……100

Figure 4.5: **(a)** Laboratory XRD data analysis results of the thermally treated (1100°C, 12 hours, air) $Pr_2NiO_{4+\delta}$ and CGO10 mixture in loose powder form using Le Bail refinement with both CGO10 and CGPO phases included in the model. The goodness of fit parameters are χ^2=1.97, R_{wp}=5.97% and R_p=4.69%. **(b)** The magnification of **Figure 4.5(a)** highlights the presence of the unreacted CGO10 and the newly formed CGPO phases at (422) reflection. ……..102

Figure 4.6: **(a)** Laboratory XRD data analysis results of the thermally treated (1100°C, 6 hours, air) $Pr_2NiO_{4+\delta}$ and CGO10 mixture in pressed pellet form using Le Bail refinement with one CGPO phase included in the model. The goodness of fit parameters are χ^2=2.14, R_{wp}=6.02% and R_p=4.72%. **(b)** The magnification of **Figure 4.6(a)** shows the extra unindexed peak at the left shoulder of the CGPO (422) reflection, highlighting the presence of more than one substituted ceria phase. Reproduced from Tsai et al. [9]. ……..103

Figure 4.7: Laboratory XRD data obtained in the 2θ region corresponding to the (422) substituted ceria reflection. The figure demonstrates that a single CGPO phase cannot model the data for the $Pr_2NiO_{4+\delta}$:CGO10 sample thermally treated at 1100°C for 12 hours under air in loose powder form. ……104

Figure 4.8: The summary of the CGO10/CGPO lattice parameters after thermal treatment at 1100°C between 0 and 12 hours under air in **(a)** loose powder form and **(b)** pressed pellet form. The data were obtained from the laboratory based X-ray diffractometer. The error bar in each point represents three estimated standard deviations. ……..105

Figure 4.9: A selected region of the HR-SXRPD data which illustrates the relative change of the quantity of CGO10, $Pr_2NiO_{4+\delta}$ and the newly formed CGPO after different thermal treatment conditions in various sample forms. The CGPO phases with (222) reflection locate at 2θ between 30.57° and 30.70°. Reproduced from Tsai et al. [9]. ……..107

Figure 4.10: The presence of two NiO phases in the HR-SXRPD data for the $Pr_2NiO_{4+\delta}$:CGO10 sample (ground dense pellet) which was thermally treated at 1100°C for 12 hours in air. …..108

Figure 4.11: The high-angle annular dark-field (HAADF) image of the CGO10 commercial powder mounted on a TEM copper grid. The STEM EDS mapping data at the selected regions were quantified and the results are presented in **Table 4.2**. ……109

Figure 4.12: The STEM EDS mapping results from a TEM lamella which originates from a $Pr_2NiO_{4+\delta}$:CGO10 pressed pellet sample being heated at 1100°C for 12 hours in air. **(a)** HAADF image. The blue curve indicates the interface between the $Pr_2NiO_{4+\delta}$ and the substituted ceria phases. **(b)** Ni elemental map. **(c)** Ce elemental map. **(d)** Pr elemental map. Reproduced from Tsai et al. [9]. ……110

Figure 4.13: STEM EDS mapping for a TEM lamella prepared from the $Pr_2NiO_{4+\delta}$:CGO10 pressed pellet sample heat treated at 1100°C for 12 hours in air. The selected areas are the unreacted CGO10 regions without the Pr signals **(a)** HAADF image. **(b)** Pr elemental map. ……..112

Figure 4.14: STEM EDS mapping for a TEM lamella prepared from the $Pr_2NiO_{4+\delta}$:CGO10 pressed pellet sample heat treated at 1100°C for 2 hours in air. **(a)** HAADF image. **(b)** Ni elemental map. ……...113

Figure 4.15: Laboratory XRD data analysis results of the $Pr_2NiO_{4+\delta}$:CGO10 pressed pellet sample, which was previously sintered at 1100°C for 12 hours in air and was further heated at 800°C for 24 hours in air, using Le Bail refinement. The figure highlights a significant decompositon of $Pr_2NiO_{4+\delta}$ to $Pr_4Ni_3O_{10+/-\delta}$ and Pr_6O_{11}. The goodness of fit parameters were χ^2=1.41, R_{wp}=4.78% and R_p=3.73%. Reproduced from Tsai et al. [9]. ……..114

Figure 4.16: Laboratory XRD data analysis results of the $Pr_2NiO_{4+\delta}$:CGO10 pressed pellet sample, which was sintered at 1100°C for 12 hours in air, using Le Bail refinement. The goodness of fit parameters were χ^2=2.21, R_{wp}=6.22% and R_p=4.83%. Reproduced from Tsai et al. [9] ……..116

Figure 4.17: **(a)** Comparisons between the CGPO peak position before (red) and after (blue) further heating at 800°C for 24 hours in air. **(b)** The change of NiO content before (red) and after (blue) the as-mentioned heat treatment. All the data were measured using a laboratory based X-ray diffractometer. Reproduced from Tsai et al. [9]. ……116

Figure 5.1: The XRD data shows the change of phases after the decomposition stage (600°C, 12 hours, air) and after further calcination stage at various conditions in air. Reproduced from Tsai et al. [18]. ……125

Figure 5.2: (a) The XRD data shows the change of phases at various total calcination time at 1000°C in oxygen. **(b)** The snapshot of the XRD data which illustrates an insignificant change of PrO_2 content when increasing the total calcination time from 48 hours to 60 hours at 1000°C in oxygen. Reproduced from Tsai et al. [18]. ……..127

Figure 5.3: The XRD data shows the change of phases at various total calcination time at 1050°C in oxygen. $Pr_4Ni_3O_{10+/-\delta}$ miller indices were labelled and the figure highlights that no secondary phase was observed after calcining for more than 84 hours. Reproduced from Tsai et al. [18]. ……..128

Figure 5.4: The gradual decrease of $Pr_2NiO_{4+\delta}$ secondary phase when increasing the total calcination time from 60 hours to 96 hours at 1050°C in oxygen. The background fit of each diffractogram was indicated by the straight lines. Reproduced from Tsai et al. [18]……..129

Figure 5.5: (a) Laboratory XRD data analysis results of the as-synthesised $Pr_4Ni_3O_{10+/-\delta}$ powder using Rietveld refinement. The goodness of fit parameters are χ^2=6.54, R_{wp}= 9.81% and R_p= 7.23%. **(b)** The selected region in **Figure 5.5(a)** which highlights the asymmetric peak broadening issue at ~46° and the peak shape mismatch at ~47.5°. These issues can be easily observed from the Y_{obs}-Y_{calc} curve. Reproduced from Tsai et al. [18]. ……131

Figure 5.6: (a) The comparison between the simulated *Fmmm*, *Bmab* and *C*2/*m* patterns and Rietveld refinement results of $Pr_4Ni_3O_{10-\delta}$ based on $P2_1/a$ space group. **(b)** The confirmation of the monoclinic distortion due to the evidence of peak splitting and the presence of extra peaks not indexed by either *Bmab* and *Fmmm*. Reproduced from Tsai et al. [18]. 132

Figure 5.7: Neutron diffraction data analysis results of the as-synthesised $Pr_4Ni_3O_{10-\delta}$ powder using Rietveld refinement. The goodness of fit parameters are R_{wp}= 6.77%, R_p= 6.12%. Reproduced from Tsai et al. [18]. 134

Figure 5.8: (a) Neutron diffraction data analysis results of the as-synthesised $Pr_4Ni_3O_{10-\delta}$ using Rietveld refinement with two $P2_1/a$ monoclinic phases introduced in the model. The goodness of fit parameters are R_{wp}= 5.68% and R_p= 5.21%. (b) Evidence of the improved fitting of the peak at d ~ 1.97 Å. 135

Figure 5.9: The illustration of the refined monoclinic crystal structure with space group of $P2_1/a$ based on the parameters used in **Table 5.1**. The figure was plotted using CrystalMaker software package. Reproduced from Tsai et al. [18]. 137

Figure 5.10: The change of the phase after post-annealing the sintered $Pr_4Ni_3O_{10+/-\delta}$ pellet for various amount of time at 1050°C under oxygen flow. Reproduced from Tsai et al. [18]. 140

Figure 5.11: The backscattered electron image highlights the presence of secondary phase, which was later identified as NiO using EDS (**Table 5.2**), on the post-annealing (1050°C, 108 hours, oxygen) sintered $Pr_4N_3O_{10+/-\delta}$ pellet. Reproduced from Tsai et al. [18]. 140

Figure 5.12: Comparison of $Pr_4Ni_3O_{10+/-\delta}$ electrical conductivity from this study with data reported from other literature sources, and with the estimated values when the solid is pore-free using **Equation 5.2**. All the measurement were conducted in air at different temperatures. The size of the measurement errors are smaller than the labels. Adapted from Tsai et al. [18]. 142

Figure 5.13: **(a) (b)** The change of the $Pr_4Ni_3O_{10-\delta}$ lattice parameters from 35°C to 1000°C in air. The *in-situ* XRD data were analysed using Le Bail refinement. The error bar in each point represents three estimated standard deviations. **(c)** The figure highlights the small distortion of the crystal structure at ~300°C in air. Each diffractogram was placed on top of each other along the heating direction from 50°C to 1000°C in air with temperature step size of 50°C. Reproduced from Tsai et al. [18]. 144

Figure 5.14: The *in-situ* XRD data analysis of the as-synthesised $Pr_4Ni_3O_{10-\delta}$ powder at **(a)** 35°C and **(b)** 1000°C in air using Le Bail refinement. The goodness of fit parameters are χ^2=11.9, R_{wp}= 3.96%, R_p= 2.39% and χ^2=16.3, R_{wp}= 4.44%, R_p= 2.73%, respectively. The evidence of peak shape mismatch is shown in the insets and they are the reasons for the relatively poor fit of the calculated model. Reproduced from Tsai et al. [18]. ……145

Figure 6.1: **(a)** Evolution of the $Ce_{0.75}Gd_{0.1}Pr_{0.15}O_{2-\delta}$ peak shape on heating. The figure highlights a sharpening of the peaks after further heating to 700°C and 900°C in air. **(b)** Le Bail refinement of the synthesised $Ce_{0.75}Gd_{0.1}Pr_{0.15}O_{2-\delta}$ experiencing further thermal treatment. χ^2=2.56, R_{wp}= 7.14%, R_p= 5.52%. ……..152

Figure 6.2: The change of lattice parameters for $Ce_{0.9-x}Gd_{0.1}Pr_xO_{2-\delta}$ with various x which equals to 0, 0.15, 0.30 and 0.45. The error bar in each point represents three estimated standard deviations. ……..153

Figure 6.3: **(a)** The XRD data of the as-received 10Sc1CeSZ powder. **(b)** Le Bail refinement of the thermally treated 10Sc1CeSZ powder at 1500°C for 5 hours in air. χ^2=3.20, R_{wp}= 6.71%, R_p= 4.95%. ……155

Figure 6.4: The XRD results of the chemical compatibility test between 10Sc1CeSZ and $Pr_4Ni_3O_{10-\delta}$ at various conditions in air. ……156

Figure 6.5: The XRD results of the chemical compatibility test between 10Sc1CeSZ and CGPO at various conditions in air. ……..158

Figure 6.6: **(a)** The XRD results of the chemical compatibility test between $Pr_4Ni_3O_{10-\delta}$ and CGPO at various conditions in air. **(b)** The variation of NiO content before and after each different type of thermal treatment. ……160

Figure 6.7: The XRD results of the as-sintered electrodes with various $Pr_4Ni_3O_{10-\delta}$ and CGPO compositions. ……161

Figure 6.8: The electrode microstructure of the as-sintered $Pr_4Ni_3O_{10-\delta}$:CGPO electrodes. **(a)** 100:0 wt.%. **(b)** 75:25 wt.%. **(c)** 50:50 wt.%. **(d)** 25:75 wt.%. **(e)** 0:100 wt.%. ……..163

Figure 6.9: Secondary electron images show the particle size of (a) $Pr_4Ni_3O_{10-\delta}$ and (b) CGPO after ball-milling. ……..163

Figure 6.10: Kramer-Kronig test for the AC impedance data of a 50:50 wt.% composite electrode measured at 686°C in air. ……..164

Figure 6.11: Fitting the AC impedance data (measured at ~686°C in air) of each composite electrode (including pure $Pr_4Ni_3O_{10-\delta}$ and pure CGPO electrodes) with the corresponding proposed equivalent circuit model. L, R_{ohmic}, $R_{surf.\ layer}$ /$CPE_{surf.\ layer}$, $R_{int.}$/$CPE_{int.}$, $R_{elec.}$/$CPE_{elec.}$ and $GE_{elec.}$ are inductor, ohmic resistance, resistance/constant phase element of surface layer, resistance/constant phase element of interface, resistance/constant phase element of electrode and Gerischer element corresponding to an electrode response, respectively. ….166

Figure 6.12: The ASR versus temperature plot for each of the composite electrodes. The figure highlights the decrease in ASR on increasing the CGPO composition, with the lowest values reported for the 50:50 wt.% compositions. ……171

Figure 6.13: The change in **(a)** effective electronic conductivity, **(b)** effective ionic conductivity and **(c)** ambipolar conductivity at various relative volume fractions of $Pr_4Ni_3O_{10-\delta}$ in the $Pr_4Ni_3O_{10-\delta}$:CGPO composite electrode system. The calculation is based on the input data from **Table 6.2** and the effective medium percolation theory mentioned in **Section 2.8**. ……174

Figure 6.14: The post-mortem XRD results of each composite electrode (including pure $Pr_4Ni_3O_{10-\delta}$ and pure CGPO electrodes) after the electrode performance test under OCV. ….175

Figure 6.15: Analysis of the electrode microstructure of **(a) (b)** $Pr_4Ni_3O_{10-\delta}$, **(c) (d)** 75:25 wt.%, **(e) (f)** 50:50 wt.%, **(g) (h)** 25:75 wt.% and **(i) (j)** CGPO after the electrode performance tests under OCV. The figures highlight the excellent adhesion and robust structure. The white dashed lines in **Figure 6.15(a)**, **(c)**, **(e)**, **(g)** and **(i)** illustrate the composite air electrode/electrolyte interface. ……..177

Figure 6.16: The EDS line scan results of CGPO (0:100) symmetrical cell cross-section after the electrode performance test under OCV. **(a)** The interface of CGPO electrode and electrolyte was examined by EDS line scan. The corresponding signals (counts) to location plots for **(b)** praseodymium, **(c)** cerium, **(d)** gadolinium, **(e)** scandium, and **(f)** zirconium are illustrated with annotation linking to **Figure 6.16(a)**. ……179

Figure 6.17: The 7-day performance of the 50:50 wt.% composite electrode with platinum as the current collector. **(a)** The change of the electrode ASR over time. **(b)** The change of the ohmic ASR over time. ……..180

Figure 6.18: The XRD results of the sample (50:50 wt.%) using platinum as the current collector after the 7-day performance test. The chosen 2θ range best describes the presence of the secondary phases compared to the other 2θ regions where peak overlapping is significant. ……..181

Figure 6.19: The cross-section electrode microstructure of the sample (50:50 wt.%) using platinum as the current collector after the 7-day performance test. ……..181

Figure 6.20: **(a)** The DRT results of the newly prepared sample using gold as the current collector (measured at ~680°C in air) and the 7-day performance test samples using either gold or platinum as the current collector (measured at ~685°C in air). **(b)** The change of the DRT results at various temperatures for the newly prepared sample using gold as the current collector. ……..183

Figure 6.21: The 7-day performance of the 50:50 wt.% composite electrode with gold as the current collector. **(a)** The change of the electrode ASR over time. **(b)** The change of the ohmic ASR over time. ……184

Figure 6.22: The top-down microstructure of the gold current collector **(a)** and the platinum current collector **(b)** for the samples after 7-day performance test. **(c)** The backscattered image of the 7-day performance test sample using gold as the current collector. The brighter part at the bottom is gold whereas the darker one at the top is the composite electrode. This was confirmed by the point mode EDS at the location of blue dot and red dot, respectively (**Figure 6.23**). ……185

Figure 6.23: EDS spectrum correspond to **(a)** the blue dot (Au current collector) and **(b)** the red dot (the $Pr_4Ni_3O_{10-\delta}$:CGPO composite air electrode) in **Figure 6.22(c).** The observed Tc signal in **Figure 6.23(b**) might be due to the presence of an impurity at the local regions. …..186

Figure 6.24: The XRD results of the sample (50:50 wt.%) using gold as the current collector after the 7-day performance test. The gold current collector was manually removed by SiC paper before examining the sample using XRD. The chosen 2θ range best describes the presence of the secondary phases compared to the other 2θ regions where peak overlapping is significant. ……..187

Figure 6.25: The cross-section electrode microstructure of the sample (50:50 wt.%) using gold as the current collector after the 7-day performance test. ……..188

Figure 6.26: (left): The new AC impedance fitting of previous 50:50 wt.% electrode performance data (the one using platinum as the current collector) at 686°C in air using finite length Gerischer element in the equivalent circuit model. ……190

Figure A1: The magnification of **Figure 4.15** to illustrate the presence of each phase after further heating the pre-sintered (1100°C, 12 hours, air) $Pr_2NiO_{4+\delta}$:CGO10 pressed pellet sample at 800°C for 24 hours in air. ……200

List of Tables

Table 4.1: The corresponding refined lattice parameters from **Figure 4.2** for $Pr_2NiO_{4+\delta}$ and CGO10. Reproduced from Tsai et al. [9]. 98

Table 4.2: Composition of the commercial CGO10 powder, corresponding to the areas in **Figure 4.11**. 109

Table 4.3: The chemical composition of each CGPO site correspond with the regions identified in **Figure 4.12(a)**, where 1 represents the closest region to the $Pr_2NiO_{4+\delta}$/substituted ceria interface and 7 is the furthest. Reproduced from Tsai et al. [9]. 111

Table 4.4: Composition of the unreacted CGO10 regions, corresponding to the areas in **Figure 4.13**. 112

Table 4.5: The refined lattice parameters corresponding to the data in **Figure 4.15**. Reproduced from Tsai et al. [9]. 117

Table 5.1: Refined lattice and atomic parameters for the $Pr_4Ni_3O_{10-\delta}$ phase corresponding to the data presented in **Figure 5.7**. The parentheses labelled adjacent to each atom are the corresponding Wyckoff site. Reproduced from Tsai et al. [18]. 136

Table 5.2: The EDS results of each site of interest in **Figure 5.11**. Reproduced from Tsai et al. [18]. 141

Table 6.1: The AC impedance fitting summary of each composite electrode (including pure $Pr_4Ni_3O_{10-\delta}$ and pure CGPO electrodes). 167

Table 6.2: Electronic conductivity and oxygen ionic conductivity of $Pr_4Ni_3O_{10-\delta}$ and $Ce_{0.75}Gd_{0.1}Pr_{0.15}O_{2-\delta}$ at 700°C under pO_2 of 0.21 bar. The values are based on the data reported in **Section 5.6**, [3] and [23]. 173

Table 6.3: The summary results of the $Pr_4Ni_3O_{10-\delta}$ decomposition investigation. Both as-sintered $Pr_4Ni_3O_{10-\delta}$:CGPO (50:50 wt.%) composite electrode and as-sintered $Pr_4Ni_3O_{10-\delta}$ electrode were prepared and treated at various conditions to identify the factor resulting to the $Pr_4Ni_3O_{10-\delta}$ decomposition. Each column represents a new sample treated at different conditions/procedures before final phase identification by XRD. The columns in blue (sample 1, 3, and 6) are treated as a reference. 189

Table 6.4 (right): The change of L/λ_0 at various temperatures. Refit the previous 50:50 wt.% electrode performance data (the one using platinum as the current collector) using finite length Gerischer element in the equivalent circuit model. ……190

Table A1: The resulting interatomic distances in (Å) between Pr/Ni and O and Ni-O-Ni bond angles (°) from the $Pr_4Ni_3O_{10-\delta}$ Rietveld refinement results shown in **Figure 5.7** and **Table 5.1**. Reproduced from Tsai et al. [18]. ……201

List of Abbreviations

ALS model- Alder-Lane-Steele model

ASR- area specific resistance

BSCF- $Ba_{1-x}Sr_xCo_{1-y}Fe_yO_{3-\delta}$

C- capacitance

CGO- gadolinium substituted ceria

CGO10- $Ce_{0.9}Gd_{0.1}O_{2-\delta}$

CGPO- $Ce_{1-x-y}Gd_xPr_yO_{2-\delta}$/ $Ce_{0.75}Gd_{0.1}Pr_{0.15}O_{2-\delta}$

CPE- constant phase element

CPO10- $Ce_{0.9}Pr_{0.1}O_{2-\delta}$

CPO20- $Ce_{0.8}Pr_{0.2}O_{2-\delta}$

cps- count per seconds

CSO- samarium substituted ceria

D*- oxygen self-diffusion coefficient

DPB- double phase boundary

DRT- distribution of relaxation time

EDS- energy dispersive spectroscopy

EMPT- effective medium percolation theory

FEG- field emission electron gun

FIB-SEM- focused ion beam scanning electron microscope

FRA- frequency response analyser

FWHM- full width at half maximum

G- Gerischer element

GBCO- $GdBaCo_2O_{5+\delta}$

HAADF- high-angle annular dark-field

HHV- high heating value

HR-SXRPD- high resolution synchrotron X-ray powder diffraction

HRPD- high resolution powder neutron diffraction

ICP-AES- inductively coupled plasma atomic emission spectroscopy

ICSD- Inorganic crystal structure database

IEDP- isotopic exchange depth profile

I-V curve- current-voltage curve

k- oxygen surface exchange coefficient

K-K test- Kramer-Kronig data validity test

L_c- characteristic thickness

LHV- low heating value

LSC- $La_{1-x}Sr_xCoO_{3-\delta}$

LSCF- $La_{0.6}Sr_{0.4}Fe_{0.8}Co_{0.2}O_{3-\delta}$

LSF- $La_{1-x}Sr_xFeO_{3-\delta}$

LSFN- $La_{0.6}Sr_{0.4}Fe_{0.8}Ni_{0.2}O_{3-\delta}$

LSGM- $La_{0.8}Sr_{0.2}Ga_{0.8}Mg_{0.2}O_{3-\delta}$

LSM- lanthanum strontium manganites

MIEC- mixed ionic and electronic conductors

OCV- open circuit voltage

OER- oxygen evolution reaction

ORR- oxygen reduction reaction

PBCO- $PrBaCo_2O_{5.5+\delta}$

PIE- pulse isotopic exchange

$(PL)_{2.0}NCG$- $(Pr_{0.9}La_{0.1})_{2.0}Ni_{0.74}Cu_{0.21}Ga_{0.05}O_{4+\delta}$

$(PL)_{1.9}NCG$- $(Pr_{0.9}La_{0.1})_{1.9}Ni_{0.74}Cu_{0.21}Ga_{0.05}O_{4+\delta}$

ppm- part per million

R- resistance

R_p- profile residual/ polarization resistance

RP- Ruddlesden-Popper phase

R_{wp}- weighted profile residual

SEM- scanning electron microscopy

SIMS- secondary ion mass spectroscopy

SOCs- solid oxide cells

SOEC- solid oxide electrolysis cells

SOFC- solid oxide fuel cells

STEM- scanning transmission electron microscopy

TEC- thermal expansion coefficient

TEM- transmission electron microscopy

TGA- thermogravimetric analysis

TPB- triple phase boundary

vol.%- volume percentage

WGS- water gas shift reaction

XRD- X-ray diffraction

wt.%- weight percentage

Y_{calc}- calculated intensity

YDC- $Ce_{0.72}Y_{0.18}O_{2-\delta}$

Y_{obs}- experimentally observed intensity

YSB- yttria-stabilised bismuth oxide

YSZ- yttrium stabilised zirconia

10Sc1CeSZ- 10 mol.% Sc_2O_3- 1 mol. %CeO_2- 89 mol.% ZrO_2

Chapter 1 Introduction

1.1 Advantages of solid oxide cells (SOCs)

In the past few years, there are increasing concerns about global warming and CO_2 emission globally [1]. There is also a potential stress that the fossil fuel reserves might not meet the increasing energy demand in the near future [2]. One of the approaches to solve the problem is to change the current energy mix supply towards sustainable and renewable sources such as solar, wind, geothermal, etc. or nuclear energy [3]. The idea of increasing renewable energy usage is more popular than nuclear energy due to the potential radiation pollution from nuclear waste and from the power plants themselves [4]. On the other hand, the applications of renewable energy are limited due to their intermittent nature which causes the mismatch between energy supply and demand [1]. Therefore, an energy storage mechanism must be introduced to widen the applications of renewable energy [1, 5]. Solid oxide cells are one of the promising candidate technologies. The concept of the integration between solid oxide cells and renewable energy is illustrated in **Figure 1.1**. In the case when electricity supply is greater than electricity demand, solid oxide cells can work in the electrolysis mode, so called solid oxide electrolysis cells (SOEC), to convert excess electricity to chemicals/fuels for temporary storage purposes [1, 5]. When electricity is demanded, the solid oxide cells can operate in the fuel cell mode, solid oxide fuel cells (SOFC), to convert previously produced chemicals/fuels to electricity [1, 5]. It is important to note that unlike batteries, solid oxide cells are an energy convertor which does not have any energy capacity [6, 7]. The reaction can be continuous so long as the chemicals or/and electricity are supplied to the system [6, 7]. This provides the potential for solid oxide cells to balance energy supply and demand in large scale (e.g. greater than GWh level) and in a cost competitive manner [6, 7].

In addition, solid oxide cells possess the advantages of high efficiency, fuel flexibility and scalability. The fuel cell mode efficiency is much higher than conventional power generation via the route of heat driven engines because chemical energy in the fuel is directly converted to electricity and heat [8]. Hence, the Carnot cycle is avoided [8]. In the electrolysis mode, on the other hand, high temperature operation (e.g. >600^{o}C) in solid oxide cells allows the use of much less electricity to generate a fuel with the rest

of the energy being compensated by heat [6]. This increases the thermodynamic efficiency when comparing to the other low temperature electrolyser technologies such as alkaline electrolysers and proton exchange membrane electrolysers which usually operate below 100^{o}C [6, 8, 9].

In terms of fuel flexibility, besides pure hydrogen and water, carbon based chemicals can be used as an input to solid oxide cells [9, 10]. This is unlike alkaline fuel cells/electrolysers and proton exchange membrane fuel cells/electrolysers which can only operate in the condition of hydrogen/steam and are vulnerable to CO_2/CO poisoning [9, 10]. For the solid oxide fuel cells, the high operating temperature allows internal fuel reforming to occur in the system [11]. Hence, methane and methanol can be used as a fuel [11]. On the other hand, solid oxide electrolysis cells can operate under CO_2 electrolysis and even H_2O and CO_2 co-electrolysis modes to generate carbon based fuels rather than just conducting H_2O electrolysis to produce hydrogen [9, 12]. Moreover, the current design of solid oxide cells is easy to scale in power (from kW and beyond) as solid oxide cells are usually connected in series [4, 9, 12]. Depending on the final power requirement, certain numbers of cells can be included in a stack or connection between stacks can be achieved.

Overall, the advantages of solid oxide cells increase their applications to solve the complex energy problem. Considering that most of the current fuel distribution systems are designed to deliver carbon based chemicals, it is believed that solid oxide cells will play an important role in assisting with the transition towards a hydrogen economy in the future [1].

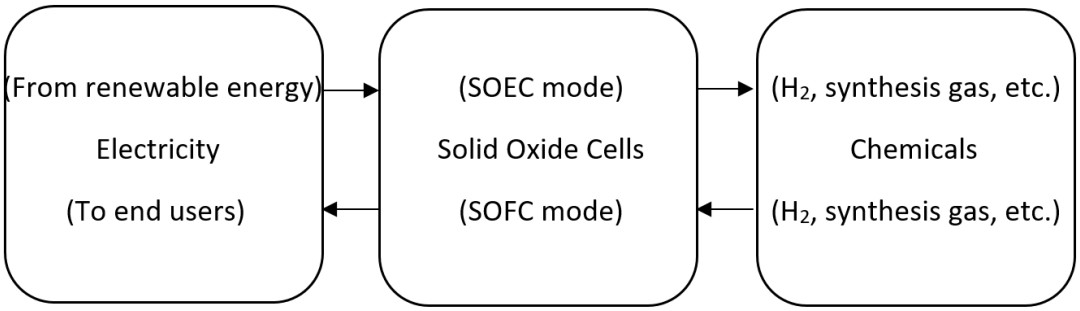


Figure 1.1: Schematic representation of how SOCs can be integrated with intermittent renewable energy sources to solve the issue of energy supply/demand mismatch.

1.2 SOFC/ SOEC operation

1.2.1 Working principle

Solid oxide cells are mainly comprised of three components and they are fuel (hydrogen) electrode, electrolyte and air (oxygen) electrode. **Figure 1.2** illustrates the input and output of each gas species at each electrode and the direction of electrons and oxygen ion movement in the external circuit and the electrolyte, respectively for both SOFC and SOEC modes [5]. As indicated by the half and the overall reactions in **Equations 1.1**, **1.3** and **1.4** and **Figure 1.2(a)**, gaseous fuel, such as hydrogen, is oxidised at the fuel electrode side by the oxygen ions produced from the air electrode via an oxygen reduction reaction (ORR) and transported through the dense, gas tight electrolyte. The hydrogen oxidation will liberate electrons which are then transported via the external circuit to the air electrode side for the ORR. Overall, the oxygen from the air electrode side is consumed and the hydrogen at the fuel electrode side is electrochemically converted to steam with the heat and electricity being generated at the same time. SOEC, on the other hand, is the reverse operation of SOFC (**Figure 1.2(b)** and **Equations 1.6**, **1.8** and **1.9**) which consumes electricity and heat. Instead of consuming fuel and oxygen from the air, it converts steam into hydrogen by reduction at the fuel electrode side. The oxygen ions are transported through the electrolyte and are oxidised at the air electrode side to generate oxygen. The electrons released by oxygen evolution reaction (OER) at the air electrode side are transported via the external circuit to the fuel electrode side for steam reduction.

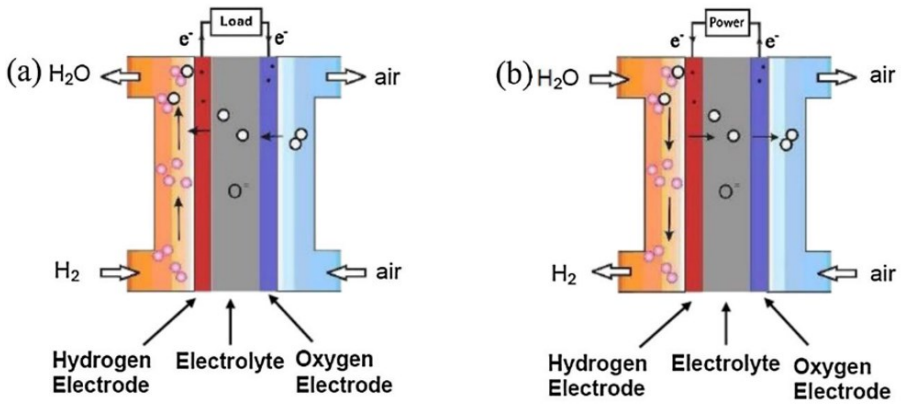


Figure 1.2: The working principle of **(a)** SOFC and **(b)** SOEC when using hydrogen and steam, respectively as a reactant. Reproduced from [5] with kind permission from John Wiley and Sons.

Fuel (hydrogen) electrode half reaction in SOFC mode:

$$H_{2(g)} + O^{2-} \rightarrow H_2O_{(g)} + 2e^- \quad \textbf{Equation 1.1}$$

$$CO_{(g)} + O^{2-} \rightarrow CO_{2(g)} + 2e^- \quad \textbf{Equation 1.2}$$

Air (oxygen) electrode half reaction in SOFC mode:

$$\frac{1}{2}O_{2(g)} + 2e^- \rightarrow O^{2-} \quad \textbf{Equation 1.3}$$

Overall reaction in SOFC mode:

$$H_{2(g)} + \frac{1}{2}O_{2(g)} \rightarrow H_2O_{(g)}\ \Delta H = -242\frac{kJ}{mol}\ at\ 298K \quad \textbf{Equation 1.4}$$

$$CO_{(g)} + \frac{1}{2}O_{2(g)} \rightarrow CO_{2(g)}\ \Delta H = -283\frac{kJ}{mol}\ at\ 298K \quad \textbf{Equation 1.5}$$

Fuel (hydrogen) electrode half reaction in SOEC mode:

$$H_2O_{(g)} + 2e^- \rightarrow H_{2(g)} + O^{2-} \quad \textbf{Equation 1.6}$$

$$CO_{2(g)} + 2e^- \rightarrow CO_{(g)} + O^{2-} \quad \textbf{Equation 1.7}$$

Air (oxygen) electrode half reaction in SOEC mode:

$$O^{2-} \rightarrow \frac{1}{2}O_{2(g)} + 2e^- \quad \textbf{Equation 1.8}$$

Overall reaction in SOEC mode:

$$H_2O_{(g)} \rightarrow H_{2(g)} + \frac{1}{2}O_{2(g)}\ \Delta H = 242\frac{kJ}{mol}\ at\ 298K \quad \textbf{Equation 1.9}$$

$$CO_{2(g)} \rightarrow CO_{(g)} + \frac{1}{2}O_{2(g)}\ \Delta H = 283\frac{kJ}{mol}\ at\ 298K \quad \textbf{Equation 1.10}$$

Water gas shift reaction:

$$CO_{(g)} + H_2O_{(g)} \rightarrow CO_{2(g)} + H_{2(g)}\ \Delta H = -41\frac{kJ}{mol}\ at\ 298K \quad \textbf{Equation 1.11}$$

Moreover, if CO or CO_2 is used as a fuel or reacting gas, fed into the fuel electrode side, in SOFC or SOEC mode, respectively, then it will be converted to CO_2 or CO as indicated by the half equations (**Equations 1.2** and **1.7**) and the overall equations (**Equations 1.5** and **1.10**). In SOEC mode, the solely electrochemical conversion of CO_2 to CO is called CO_2 electrolysis whereas co-electrolysis occurs when steam is also present in the feed

gas. It is important to note that the mixture of H_2/H_2O and CO_2/CO will lead to the water gas shift reaction (WGS), **Equation 1.11** [1, 12, 13]. Unlike **Equations 1.1-1.10**, which are electrochemical reactions, WGS is a chemical reaction and its reaction equilibrium constant is operating temperature dependent [1, 12, 13]. **Figure 1.3** indicates that WGS is mildly exothermic (ΔH curve) and forward WGS is favourable at temperatures below 816^{o}C (ΔG curve) [12, 13]. WGS or reverse WGS will have a significant impact on the inlet and outlet gas composition of the solid oxide cells and hence the voltage of the cells [1].

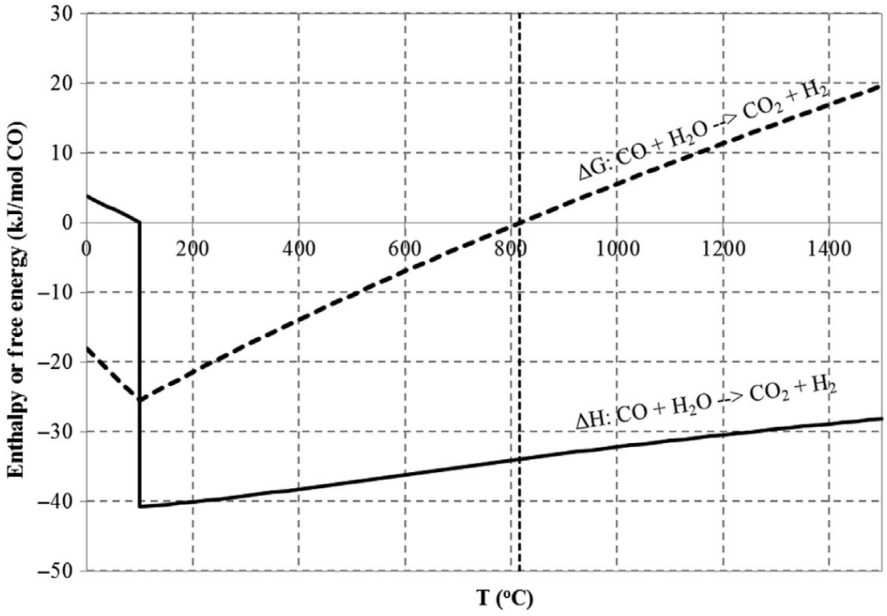


Figure 1.3: The enthalpy and Gibbs free energy of water gas shift reaction over different temperatures. Reproduced from [13] with kind permission from Elsevier.

1.2.2 Thermodynamics

Thermodynamics helps with understanding the energy conversion in SOC systems. Under the reversible condition, the transformation of energy can be summarised by **Equation 1.12**, where ΔH, ΔG and ΔS represent the enthalpy, Gibbs free energy and entropy of the electrochemical reaction. It is important to note that the enthalpy here is the total energy supply/demand in SOFC/SOEC mode, respectively whereas the Gibbs free energy and TΔS indicate the electricity generated/consumed and the heat released/consumed [8, 14]. **Equations 1.13**, **1.14** and **1.15** suggest that ΔH, ΔS and ΔG are temperature dependent and their values are illustrated in **Figure 1.4** [14]. In **Equations 1.13** and **1.14**, ΔH^0 and ΔS^0 are enthalpy and entropy under standard

conditions (298K and 1 bar) [14]. ΔCp, on the other hand, is the change of the specific heat and it is also a temperature dependent variable [14].

$$\Delta H = \Delta G + T\Delta S$$ **Equation 1.12**

$$\Delta H = \Delta H^{\circ} + \int_{298}^{T} \Delta C_p \, dT$$ **Equation 1.13**

$$\Delta S = \Delta S^{\circ} + \int_{298}^{T} \frac{\Delta C_p}{T} dT$$ **Equation 1.14**

$$\Delta G = \Delta H - T\Delta S$$ **Equation 1.15**

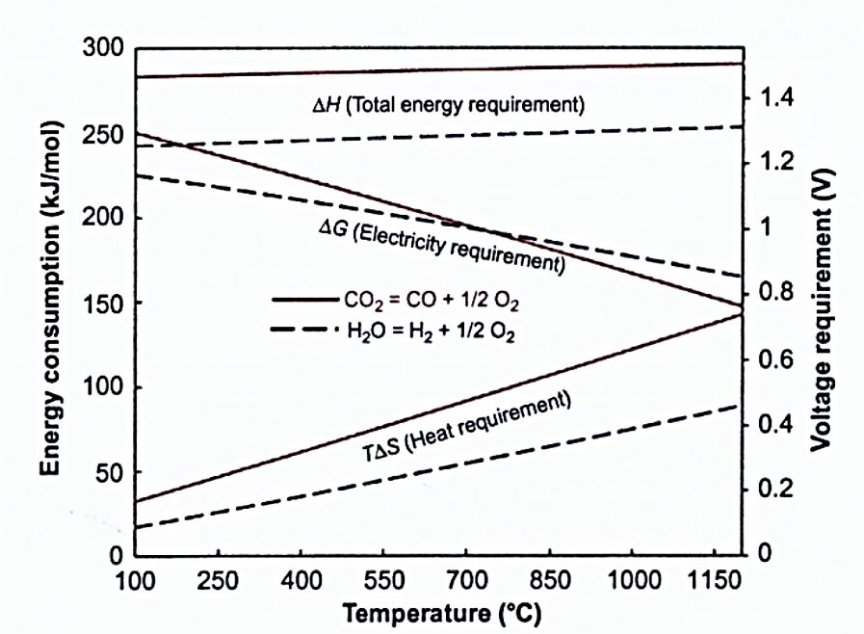


Figure 1.4: The total energy, electricity and heat requirement for H_2O and CO_2 electrolysis. Reproduced from [14] with kind permission from Elsevier.

Each energy in the unit of $kJmol^{-1}$ can be converted to voltage and this is achieved by **Equation 1.16** where n and F are the number of electrons transferred in the electrochemical reaction and Faraday's constant, respectively [14]. E is the so called open circuit voltage (OCV) or Nernst potential and it indicates the maximum voltage in SOFC mode or the minimum voltage to generate chemical fuel in SOEC mode [8, 14]. **Figure 1.4** shows the change of ΔH, ΔG and TΔS over temperature under steam and CO_2 electrolysis modes. Although increasing SOEC operating temperature increases the total energy demand slightly, there is a significant decrease in electricity

requirement and is compensated by the increase of heat demand [6, 14]. This explains the reason that high temperature SOEC tends to have higher thermodynamic efficiency than low temperature electrolysers as the efficiency (η_{SOEC}) is defined as **Equation 1.17** [8]. From an economic point of view, the chemical fuel produced from a high temperature SOEC has relatively low operating cost since the unit price of waste heat is much lower than electricity [14]. With respect to the CO_2 electrolysis, it requires higher total energy than steam electrolysis (**Figure 1.4**) [14].

$$\Delta G = -nFE \qquad \textbf{Equation 1.16}$$

$$\eta_{SOEC} = \frac{\Delta \mathrm{H}}{\Delta \mathrm{G}} \qquad \textbf{Equation 1.17}$$

Moreover, as the reversible process is considered here, **Figure 1.4** can be used to theoretically predict the amount of heat and electricity generated in SOFC mode when consuming each unit of chemical energy. **Equation 1.18** and **Figure 1.4** suggest that the thermodynamic efficiency of fuel cell decreases with increasing temperature [8, 14]. However, when comparing to the thermodynamic efficiency of the Carnot cycle (**Equation 1.19**, where T_{high} and T_{low} are the temperature of hot and cold reservoirs, respectively), the thermodynamic efficiency of a hydrogen fuel cell in low heating value (LHV) is higher at temperature below 860^{o}C than the efficiency from the Carnot cycle with T_{low} varied from 0^{o}C to 100^{o}C (**Figure 1.5**) [8]. On the other hand, if the definition of fuel cell efficiency is based on the higher heating value (HHV) then the hydrogen fuel cell efficiency is greater than the Carnot efficiency at temperatures lower than 600^{o}C (**Figure 1.5**) [8]. The variation between LHV and HHV efficiency is because a different definition of ΔH is used in the calculation (**Equation 1.18**). For HHV efficiency calculation, ΔH considers the heat of water condensation and vice versa [8]. The ΔH values in **Figure 1.4** are based on the definition of LHV.

$$\eta_{SOFC} = \frac{\Delta \mathrm{G}}{\Delta \mathrm{H}} \qquad \textbf{Equation 1.18}$$

$$\eta_{Carnot} = \frac{T_{high} - T_{low}}{T_{high}} \qquad \textbf{Equation 1.19}$$

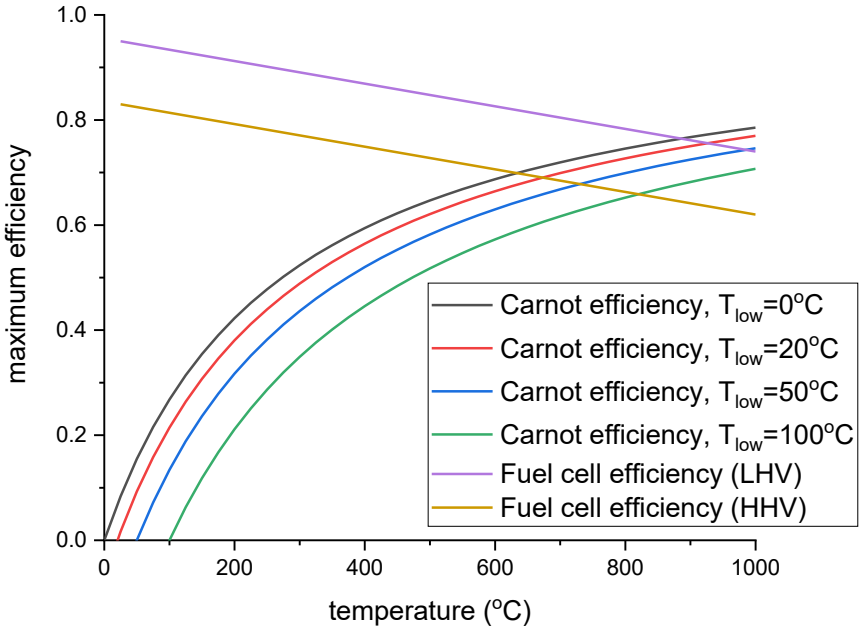


Figure 1.5: The thermodynamic efficiency comparison between fuel cell (both LHV and HHV) and Carnot cycle. Replotted from [8].

It is worth mentioning that the above calculation only considers the condition when the equilibrium constant of the electrochemical reaction is equal to one [15]. However, in practice, partial pressure of the reactants and products can vary. In this case, the Nernst equation (**Equations 1.20** and **1.21**) can be used to calculate the OCV under the specific nonstandard conditions [1]. E^0 is the OCV calculated from the ΔG value in **Figure 1.4** using **Equation 1.16**. R, T and P_x are the real gas constant, temperature in Kelvin and partial pressure of each gas species.

$$E = E^{\circ} + RTln(\frac{P_{H_2}P_{O_2}^{0.5}}{P_{H_2O}}) \qquad \textbf{Equation 1.20}$$

$$E = E^{\circ} + RTln(\frac{P_{CO}P_{O_2}^{0.5}}{P_{CO_2}}) \qquad \textbf{Equation 1.21}$$

In practice, the real solid oxide cells process is irreversible [8]. Therefore, extra energy is required to drive the electrochemical reaction. This extra energy requirement is indirectly reflected on the real cell voltage (V_{cell}) as described by **Equation 1.22**, where V_a, V_{ohm} and V_c are activation, ohmic and concentration overvoltages. γ is -1 and +1 in SOFC and SOEC modes, respectively [8, 15]. In general, activation overvoltage considers the extra energy barrier for charge transfer reactions between molecules

and materials occurring at both the fuel electrode and air electrode sides whereas concentration overvoltage considers the limitation of gas transport in the electrodes [14, 15]. Ohmic overvoltage is mainly contributed by the ohmic losses from the electrolyte and the contact resistance between cells [16]. It is worth mentioning that both activation and concentration overvoltages depend heavily on the electrode microstructure [16]. Material selections of electrolyte and electrode have a significant impact on ohmic overvoltage and activation overvoltage, respectively [16].

$$V_{cell} = E + \gamma(V_a + V_{ohm} + V_c) \qquad \textbf{Equation 1.22}$$

The domination of each overvoltage at different current densities in SOFC and SOEC modes is illustrated in **Figure 1.6**, the current-voltage (I-V) curve [8, 16]. Since the direction of current is reverse in SOEC mode in comparison to SOFC mode, the current density in SOEC mode is negative [8]. With the increase of current density magnitude, the real cell voltage decreases/increases from the open circuit voltage in SOFC/SOEC mode [8, 15]. At low magnitude of current density, activation loss dominates although this is usually not observed in high temperature solid oxide cells but the low temperature ones [8, 16]. This is because the relatively high operating temperature helps with easily overcoming the activation barrier of the charge transfer processes in the electrodes [16]. In the mild magnitude of current density, ohmic losses dominate and this is usually the region where cell operates [8, 16]. At even high magnitude of current density, mass transport loss starts to occur which finally results in current limitation in the case of fuel starvation [8, 16].

In terms of the heat transport in the system, SOFC mode is always exothermic whereas it varies in SOEC mode [6, 8]. Thermal neutral voltage in **Figure 1.6** is calculated using **Equation 1.16**, but replacing ΔG by ΔH, the total energy requirement for electrolysis [6, 8]. When a cell is operated below thermal neutral voltage in SOEC mode, the system is consuming heat overall and requires an external heat supply to maintain the operating temperature [6, 8]. At thermal neutral voltage, part of the electricity is lost as joule heat because of the ohmic losses and the heat and the rest of the electricity are supplied to the cell for electrolysis [6, 8]. No net heat release/consumption is happening at this point. At higher applied current density, which corresponds to the

region beyond thermal neutral voltage, the system is releasing heat and hence external cooling might be required to maintain the operating temperature [6, 8].

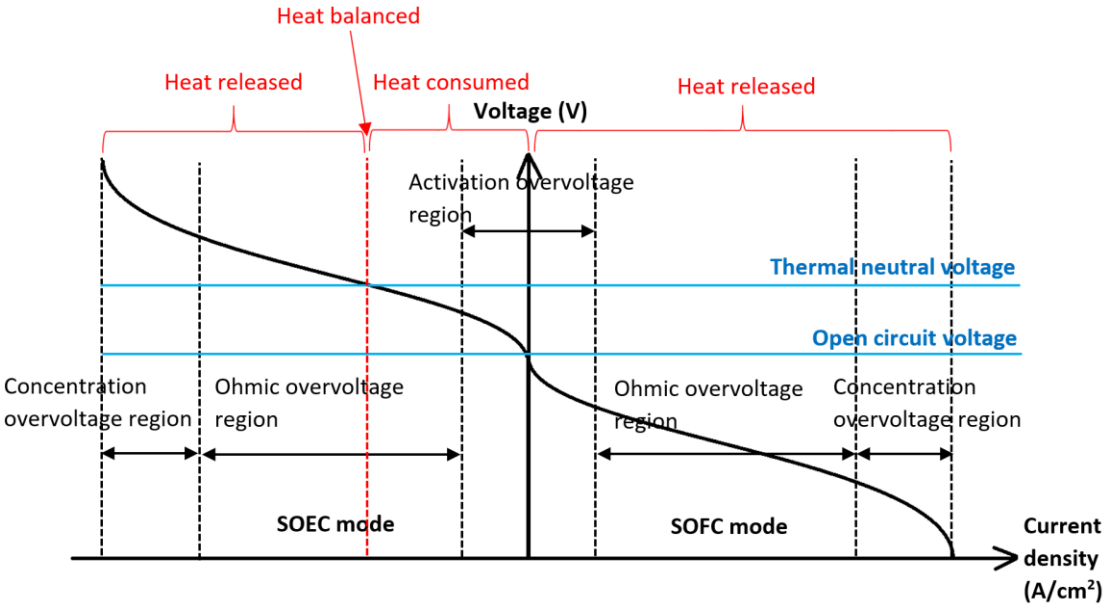


Figure 1.6: The typical I-V curves in SOFC and SOEC modes.

Area specific resistance (ASR), the slope of the I-V curve in **Figure 1.6**, is an indicator that reflects the performance of a cell [17]. Since ASR, with the unit of Ωcm^2, is normalised by the cell area, this value can be compared from cell to cell regardless of its geometry [17]. In SOFCs, the common target of total ASR is 0.45 Ωcm^2, given that the aim of power density is 0.5 Wcm^{-2} and the common cell operating voltage is around 0.7 V [17]. As there are three main components in the cell and they are fuel electrode, electrolyte and air electrode, the normalised resistance contributed by each component should not exceed 0.15 Ωcm^2 at a specific temperature [17]. This value, also called the polarisation resistance of the electrode, is used as a benchmark to judge the air electrode performance in the following research. On the other hand, there is no apparent cell performance target in SOEC mode. In general, the higher the current density at a specific operating voltage, the better the cell performance is as more chemical fuel, such as hydrogen, is generated according to Faraday's Law.

1.3 General requirements for SOC components

1.3.1 SOC air electrode requirements

To be a candidate for the air electrode material, the following criteria need to be met.

- High thermal stability under sintering and operating conditions (e.g. no issue of cation segregation and decomposition) [18-20].
- High compatibility in terms of chemical and mechanical (e.g. thermal expansion coefficient (TEC)) aspects with the adjacent cell components (e.g. electrolyte and interconnectors), especially under sintering and operating conditions [18-20]. The normal TEC values for the conventional electrolyte (e.g. yttrium stabilised zirconia (YSZ), gadolinium substituted ceria (CGO), samarium substituted ceria (CSO), $La_{0.8}Sr_{0.2}Ga_{0.8}Mg_{0.2}O_{3-\delta}$ (LSGM)) ranges from 10.8 to 13.5 x 10^{-6} K^{-1} when being measured between 300-1000°C in air [21].
- High electronic conductivity to facilitate electron transport [19]. The value should be greater than 100 Scm^{-1} under operating conditions (e.g. at 700°C) in air [18, 20].
- High ionic conductivity to promote oxygen ion transport from the electrolyte [19, 20]. The value should be similar to that of the electrolyte (e.g. 0.01 Scm^{-1} at 700°C) [18, 22].
- High electrocatalytic activity to lower the activation barrier in the air electrode and enhance the rate of oxygen reduction reaction (ORR) or oxygen evolution reaction (OER) [18-20].
- Adequate porosity to facilitate oxygen gas diffusion through the air electrode and a stable microstructure under operating conditions in the long term [18-20].
- High tolerance to impurities such as chromium from interconnectors [23].

In SOFC, the oxygen reduction reaction (ORR) mechanism in an air electrode (porous cathode) is summarized in **Figure 1.7** [18]. Assuming the cathode material used here is a purely electronic conductor, the only ORR active sites are the location where electrons (cathode), oxygen ions (electrolyte) and oxygen molecules (pores/gases) meet. This location is also known as the triple phase boundary (TPB) [18]. As shown in

Figure 1.7 [18], oxygen molecules first diffuse to the air electrode (1). They are then adsorbed on the electrode surface and are dissociated into oxygen atoms before being surface-diffused to the TPB site (2). Charge transfer occurs at the TPB to convert oxygen atoms to oxygen ions and oxygen ions are then incorporated into the oxygen defects such as oxygen vacancies in the electrolyte crystal lattice, ready to be transferred to the fuel electrode side (anode) (3). From **Figure 1.7**, it is apparent that the air electrode performance is heavily relied on the TPB length and it can be enhanced by optimizing the electrode microstructure and/or introducing oxygen ion conducting material (e.g. electrolyte) in the air electrode to form a composite electrode with percolated pathways for electron and oxygen ion conducting phases and the accessible of gas to the active sites [18].

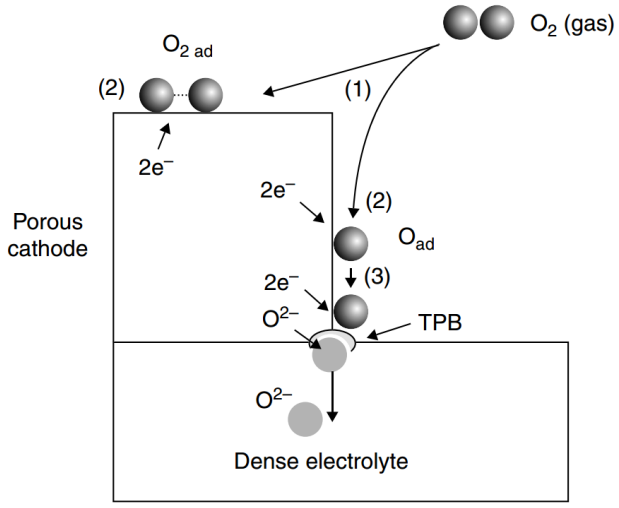


Figure 1.7: The elemental steps of ORR on solely electronic conducting air electrode and the TPB reactive site located between air electrode, oxygen ionic conducting electrolyte and gas (pore). Reproduced from [18] with kind permission from Elsevier.

One of the major disadvantages of traditional solid oxide cells which operate at temperatures greater than 800 ^{o}C is that it will facilitate chemical reaction between each cell component and accelerate cell degradation [18]. It also limits the flexibility of materials selection in a cell/stack (e.g. cannot use cheap metallic interconnectors but have to use the more expensive ceramic material) and hence this increases the overall fabrication cost [18]. Therefore, from the economic and applications points of view, there is a significant advantage in lowering the solid oxide cells operating

temperature to around 500°C-800°C (intermediate temperature range), keeping the advantages mentioned in **Section 1.1** [18, 24, 25]. However, the decrease of temperature causes the increase of electrolyte ohmic resistance and high polarization resistance from both electrodes [18]. This is especially the case for the air electrode as lower operating temperatures significantly decreases the reaction kinetics of both the ORR and OER [18, 24]. These issues might be solved by engineering approaches such as fabricating thin electrolytes to reduce ohmic losses and/or using microstructure optimized composite air electrodes to enhance the active region for the electrochemical reaction [18]. Otherwise, new materials have to be developed to achieve an acceptable performance at lower operating temperatures [18].

Mixed ionic and electronic conductors (MIEC) are a promising air electrode candidate for intermediate temperature solid oxide cells. Due to their ability to conduct both electrons and oxygen ions simultaneously, they enlarge the active sites from just the TPB regions (**Figure 1.7**) to the whole air electrode surface, termed the double phase boundary (DPB) (**Figure 1.8**) [18]. This creates a new oxygen atom/ion transport pathway, from the previous surface pathway (**Figure 1.7**) to the bulk pathway (**Figure 1.8**), where oxygen ions can also diffuse through the bulk material towards the air electrode/electrolyte interface [18, 24]. Therefore, it drastically decreases the air electrode polarization resistance in the intermediate temperature range [18, 24].

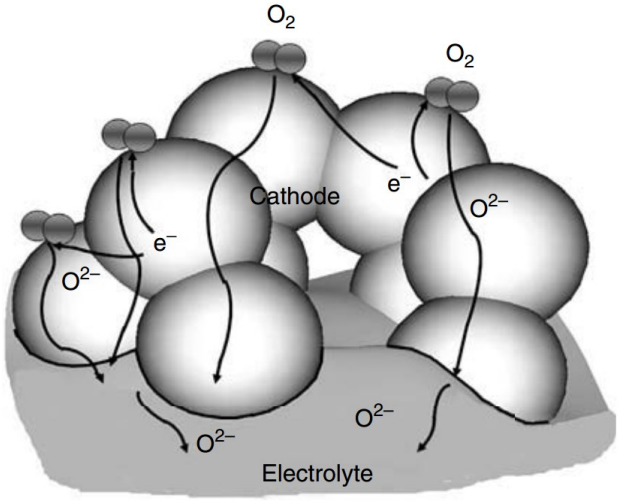


Figure 1.8: The DPB on a porous MIEC air electrode in SOFC. Reproduced from [18] with kind permission from Elsevier.

For the MIEC with high oxygen ionic transport, the electrocatalytic activity of an electrode material can be summarized by surface exchange coefficient (k) and oxygen self-diffusion coefficient (D^*) [18, 24, 26]. Surface exchange coefficient takes into account the ORR elemental steps of oxygen adsorption, dissociation, charge transfer and incorporation into the electrode bulk whereas oxygen self-diffusion coefficient is directly related to the oxygen ion transport/oxygen ionic conductivity in the material [24]. Considering microstructure parameters of an air electrode such as tortuosity (τ), porosity (ε) and surface area (α), air electrode polarization resistance (R_p) can be estimated using the Alder-Lane-Steele (ALS) model (**Equation 1.23**, where R, T, F and C_o are the gas constant, temperature, Faraday constant and surface concentration of oxygen, respectively) [18, 21 ,26]. The current data suggests that low air electrode polarization resistance tends to occur when using a material with the product of D* and k that is greater than $10^{-14}cm^3s^{-2}$ [18]. In addition, the ALS model can calculate the extension of reaction zone beyond the TPB, the so-called penetration depth, δ, when using a MIEC as an air electrode and this is shown in **Equation 1.24** [26]. Usually, the thickness of the active region away from the air electrode/electrolyte interface is only a few microns [26].

$$R_p = \frac{RT}{2F^2}\sqrt{\frac{\tau}{(1-\varepsilon)\alpha C_O^2 D^* k}} \qquad \textbf{Equation 1.23}$$

$$\delta \approx \sqrt{\frac{(1-\varepsilon)}{\tau\alpha}\frac{D^*}{k}} \qquad \textbf{Equation 1.24}$$

With respect to the oxygen evolution reaction (OER) in a SOEC air electrode, it is believed that the sequence of the oxygen elemental steps is the reverse of the ORR in SOFC mode (**Figure 1.9**) [24].

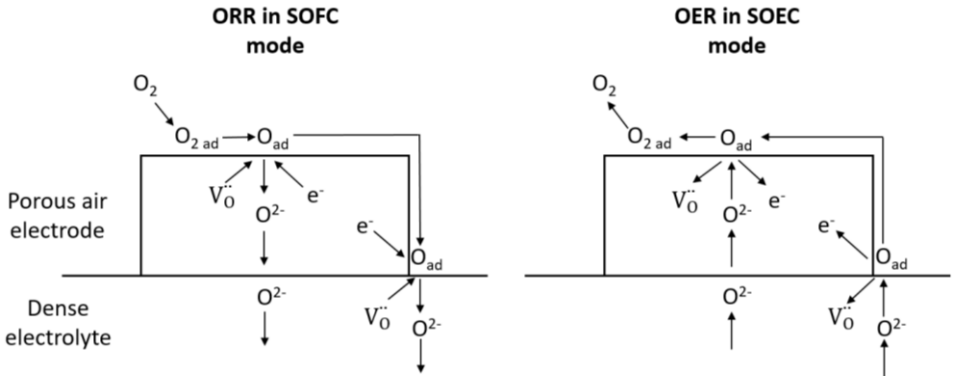


Figure 1.9: The illustration of the ORR elemental steps (left) and the OER elemental steps (right) on a MIEC air electrode. Replotted from [24].

1.3.2 SOC electrolyte requirements

With respect to the electrolyte, apart from being thermally and mechanically compatible with the adjacent electrodes under cell sintering and operating conditions, other requirements are listed as below [22]:

- It must possess high oxygen ion conductivity and be insulating to electronic conductivity. Otherwise, electricity leakage will occur.
- It must be dense to avoid gas crossover from each side of the electrodes.
- It is preferable to be thin to decrease the ohmic resistance.
- The material must be stable under the reducing and oxidising atmospheres present at each of the electrodes.
- It should also possess acceptable mechanical properties if it is used in the electrolyte supported cell geometry.

1.3.3 SOC fuel electrode requirements

Similar to the requirements for air electrode, the criteria of SOC fuel electrodes are as follows:

- The fuel electrode must be stable under normal operation conditions. For example, high tolerance to airborne impurity poisoning, metal oxidation, particle agglomeration and coke formation [2].
- During the transient operation of solid oxide cells, the fuel electrode should withstand both redox and thermal cycling [27].

- The fuel electrode must be thermally and mechanically compatible with the adjacent materials, especially the electrolyte and the interconnectors, under sintering and operating conditions [2, 27]. This is indicated by no undesired chemical reaction and similar thermal expansion coefficient between each cell component [2, 27].
- The fuel electrode materials should possess minimum electronic conductivity of 1 Scm^{-1} and the electronic conductivity is ideally greater than 10 Scm^{-1} in order to facilitate electron transport [27].
- Some oxygen ionic conductivity is also preferable to extend the active sites from the TPB to DPB [27].
- High electrocatalytic activity towards fuel oxidation or electrochemical reduction of H_2O and CO_2 is also required [2, 27].
- Finally, the fuel electrode must be porous for facile gas transport [2, 27].

1.3.4 SOC interconnect requirements

Interconnectors are only used when individual single cells are connected in series to form a stack. Hence, they must possess high electrical conductivity [28]. Since the interconnectors also act as a gas separator to avoid gas crossover occurring between the fuel side and air side, they experience dual atmosphere operating conditions [28]. It is important for the interconnectors to be thermally stable under these conditions [28]. In addition, interconnectors should have similar thermal expansion coefficient to the adjacent electrodes, high thermal conductivity and mechanical strength [28].

1.4 Conductivity in ceramics

1.4.1 Electronic conductivity

In general, materials can be classified as either metallic conductors, semiconductors or insulators, depending on their electronic band structure [29]. The metallic conductors have partially filled bands, the conduction bands, whereas both semiconductors and insulators have filled valence bands and several empty bands at higher energy levels [29]. When no electrical bias is applied to a system of a metallic conductor, the total number of electrons in each energy state is equal and there is no current flow (**Figure 1.10(a)**) [30, 31]. However, with the introduction of electrical bias, the energy of two states change and one is higher than the other. This allows electrons

to transfer leading to a flow of current (**Figure 1.10(b)**) [30, 31]. In the case of an insulator, despite the application of electrical bias, the fully filled valence bands do not allow the transfer of electrons from one state to the other (**Figure 1.10(c)**) [30, 31].

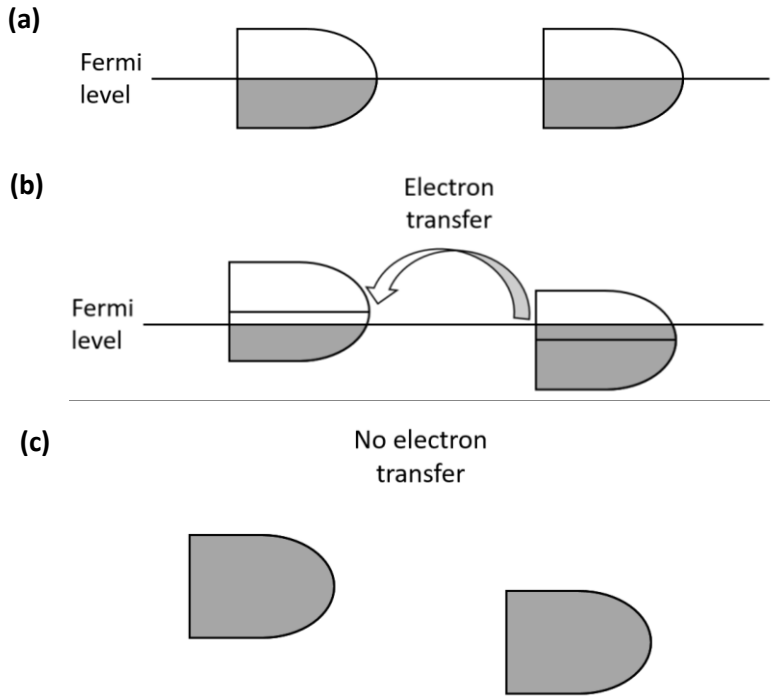


Figure 1.10: The impact of electrical bias on electron transfer. **(a)** The case of a metallic conductor, without bias. **(b)** The case of metallic conductor, with bias. **(c)** The case of insulators, with bias. The grey filling in the figures indicate if a particular band is fully or partially filled. Replotted from [30].

The energy difference between the highest filled and the lowest empty bands is known as the band gap and insulators have a much larger band gap than semiconductors [29, 31]. Due to the relatively small band gap in semiconductors, it is likely that the electrons (e^-) from a valence band could be thermally excited to the adjacent conduction band, leaving holes ($h^\cdot$) in the valence band [30, 31]. These intrinsic defects (e^- and $h^\cdot$) create the electronic conductivity of a semiconductor (**Figure 1.11(a)**) [30, 31].

The other approach to conduct electrons in a semiconductor is to introduce foreign cations, which can be either donor or acceptor type [30, 31]. The donor type dopants add filled energy levels just below the conduction band, called the donor levels,

resulting in the electrons (e^-) entering the adjacent conduction band to conduct electricity (**Figure 1.11(b)**) [30, 31]. This is known as a n-type conductor [30, 31]. The acceptor type dopants, on the other hand, causes a p-type conductor by introducing empty energy levels, just above the valence band, to allow electrons from the valence band to fill. This creates holes ($h^\cdot$) in the valence band which are ready to move (**Figure 1.11(c)**) [30, 31].

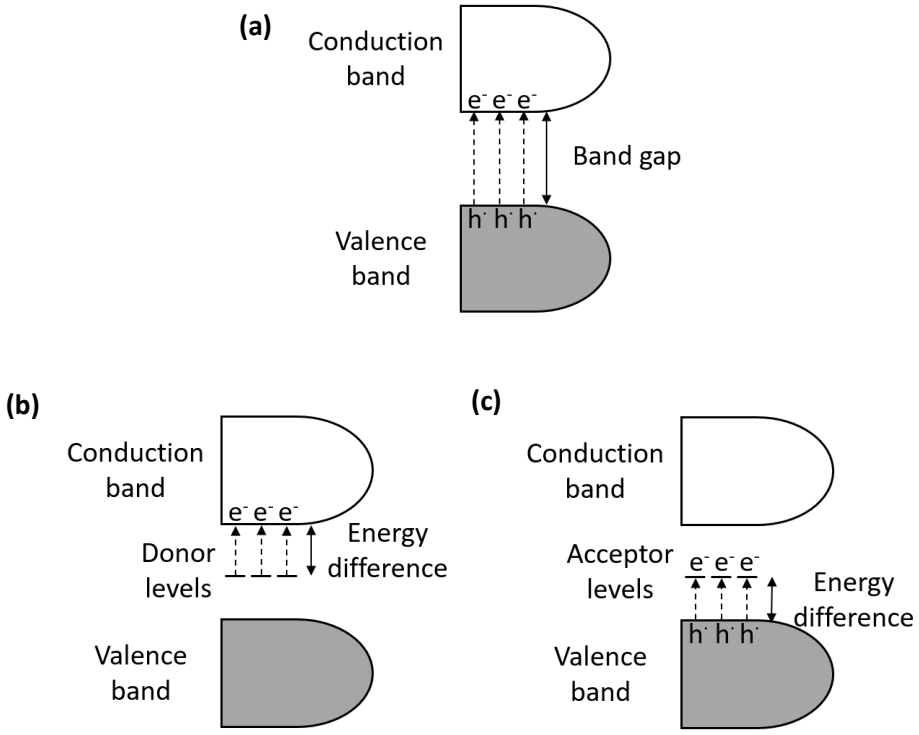


Figure 1.11: Semiconductor electronic conductivity activated by **(a)** temperature, **(b)** donor dopants, **(c)** acceptor dopants. Replotted from [30].

In addition, the oxidation or reduction of a transition metal oxide will change the valence of the transition metal [31, 32]. Although this is charge compensated by the creation/elimination of oxygen vacancies/interstitials, the new cation valence will develop new donor levels or acceptor levels in the existing band structure causing n-type or p-type conductivity [31, 32].

$$\sigma = ne\mu \qquad \textbf{Equation 1.25}$$

The electronic conductivity can be derived by **Equation 1.25**, where n, e and μ are number of charge carriers, charge and mobility of charge carriers, respectively [29].

Metallic conductors tend to have a greater abundance of charge carriers than semiconductors and hence have a higher electronic conductivity at room/low temperature [29, 31]. The electronic conductivity of metallic conductors usually decreases with increasing temperature and this is mainly due to the decrease of the charge carrier mobility caused by detrimental electron-phonon collisions [29, 31]. On the other hand, the electronic conductivity of semiconductors usually increases with temperature because of the increase of charge carrier concentration which overwhelms the effect of decreasing charge carrier mobility [29, 31].

1.4.2 Oxygen ionic conductivity

Similar to the as-mentioned electronic conductivity (**Equation 1.25**), oxygen ionic conductivity also depends on charge carrier concentration and mobility [24, 29]. Since both n and μ can be described by the Arrhenius equation, their product leads to **Equation 1.26**, where σ^0 and E_a are the pre-exponential factor and activation energy [24, 29]. It is important to note that E_a consists of the activation energy of charge carrier formation, the activation energy of charge carrier migration and the activation energy of defects association [29, 33].

$$\sigma = \frac{\sigma^o}{T}\exp(\frac{-E_a}{RT}) \qquad \textbf{Equation 1.26}$$

Depending on materials, there are two different types of oxygen charge carrier and they are oxygen vacancies and oxygen interstitials [18, 24, 29]. Oxygen vacancies are usually formed by introducing acceptor substitutes (e.g. Y_2O_3) in a system (e.g. ZrO_2) (**Equation 1.27**) whereas oxygen interstitials can be formed by charge compensating a transition metal cation valence change in a system (**Equation 1.28**) [18, 22].

$$ZrO_2 \xrightarrow{Y_2O_3} Y'_{Zr} + 2O_O^x + V_O^{\cdot\cdot} \qquad \textbf{Equation 1.27}$$

$$\frac{1}{2}O_2 \rightarrow O_i'' + 2h^{\cdot} \qquad \textbf{Equation 1.28}$$

Moreover, charge carrier migration is different for various types of charge carrier species. For example, an oxygen vacancy is moved by having the adjacent oxygen atoms hop into the existing vacant site and creating a new vacant site (**Figure 1.12(a)**) [24, 29, 31]. This is known as the vacancy mechanism [24, 29, 31]. On the other hand, an oxygen interstitial can migrate by either the interstitial mechanism (**Figure 1.12(b)**)

or interstitialcy mechanism (**Figure 1.12(c)**) [24, 29, 31]. In the interstitial mechanism, an oxygen interstitial hops into the adjacent vacant interstitial site whereas in the interstitialcy mechanism, an oxygen interstitial knocks off the adjacent oxygen atom and causes it to occupy the nearby vacant interstitial site [24, 29, 31].

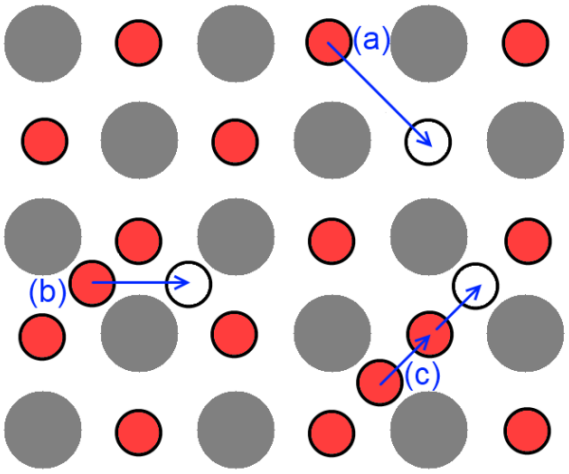


Figure 1.12: The hopping mechanisms of oxygen charge carriers. **(a)** Vacancy mechanism. **(b)** Interstitial mechanism. **(c)** Interstitialcy mechanism. Reproduced from [31] under a Creative Commons Attribution Non-Commercial No Derivatives licence.

In general, assuming the charge carrier concentration is almost constant for some acceptor substituted materials, the oxygen ionic conductivity will increase with temperature as the energy barrier of charge carrier migration, caused by the size of the cation around the migrating species, is overcome [29, 31]. However, when there is a change of oxygen charge carrier concentration over temperature, it will have a positive or negative impact on the overall oxygen ionic conductivity [18, 29].

1.4.3 Mixed ionic and electronic conductivity

For materials such as MIECs which have more than one charge carrier type and are able to conduct both oxygen ions and electrons, understanding the contribution of each type of conductivity towards the total electrical conductivity can be important. This is described by the transport number (t_x) (**Equation 1.29**, where x, σ_{total} and σ_x are charge carrier of interest, total conductivity and conductivity of the specific charge carrier) [31]. For the conventional MIEC air electrode materials, the electronic

conductivity (σ_e) is at least 10^3 higher than their oxygen ionic conductivity (σ_i) [18]. Electrolyte materials, on the other hand, should have a transport number of oxygen ions close to unity to avoid electronic leakage in a cell [22].

$$t_x = \frac{\sigma_x}{\sigma_{total}} \qquad \textbf{Equation 1.29}$$

1.5 Summary

This chapter summarises the advantages of solid oxide cells and their potential to widen the applications of renewable energy. An introduction to solid oxide cells working principle, their thermodynamics, the criteria for each cell component and electronic/oxygen ionic conduction mechanism in electroceramics were also conducted. The slow air electrode reaction kinetics under intermediate temperature operating conditions (500-800^{o}C) was identified as one of the main challenges for this technology. Developing a new material has the potential to solve this problem and this is discussed in the next chapter.

References

[1] Y. Wang, T. Liu, L. Lei, F. Chen, *Fuel Processing Technology,* 161, 248-258, 2017.

[2] X. Zhang, Y. Song, G. Wang, X. Bao, *Journal of Energy Chemistry,* 26, 839-853, 2017.

[3] X. Zhang, J. E. O'Brien, R. C. O'Brien, J. J. Hartvigsen, G. Tao, G. K. Housley, *International Journal of Hydrogen Energy ,* 38, 20-28, 2013.

[4] A. Ursua, L. M. Gandia, P. Sanchis, *Proceedings of the IEEE,* 100, 410-426, 2012.

[5] S. P. Jiang, *Asia-Pacific Journal of Chemical Engineering,* 11, 386-391, 2016.

[6] M. A. Laguna-Bercero, *Journal of Power Sources,* 203, 4-16, 2012.

[7] X. Xing, J. Lin, Y. Song, Y. Zhou, S. Mu, Q. Hu , *CSEE Journal of Power and Energy Systems,* 4, 168-178, 2018.

[8] J. O. Jensen, *Thermodynamics and efficiency of electrochemical cells,* Joint European Summer School, Athen, Greece: DTU Energy Technical University of Denmark, 2018. Available: https://www.dropbox.com/sh/1oidb8074a5s37r/AAB3_e1ZZ-_yD2514-1cGeRha/Plenary?dl=0&preview=P03+Thermodynamics+and+efficiency+2019.pdf&subfolder_nav_tracking=1.

[9] A. Buttler, H. Spliethof, *Renewable and Sustainable Energy Reviews,* 82, 2440-2454, 2018.

[10] K. Kordesch, G. Simader, “Fuel Cells and Their Applications”, Weinheim, Germany, VCH Verlagsgesellschaft mbH, 1996.

[11] S. Sui, G. H. Xiu, “Fuels and fuel processing in SOFC applications,” in *High-Temperature Solid Oxid Fuel Cells for the 21st Century- Fundamentals, Design, and Applications*, Editors: K. Kendall, M. Kendall, London, UK; San Diego, USA; Waltham, USA; Oxford, UK, Academic Press, 461-495, 2016.

[12] Y. Zheng, J. Wang, B. Yu, W. Zhang, J. Chen, J. Qiao, J. Zhang, *Chemical Society Reviews,* 46, 1427-1463, 2017.

[13] R. Elder, D. Cumming, M. B. Mogensen, “High Temperature Electrolysis,” in *Carbon Dioxide Utilisation: Closing the Carbon Cycle*, Editors: P. Styring, E. A. Quadrelli, K. Armstrong, Amsterdam, The Netherlands; Oxford, UK; Waltham, USA, Elsevier, 183-209, 2015.

[14] S. Gunduz, D. J. Deka, U. S. Ozkan, “Advances in High-Temperature Electrocatalytic Reduction of CO_2 and H_2O,” in *Advances in catalysis, volume 62*, Editor: C. Song, New York, USA; London, UK, Academic Press, 113-165, 2018.

[15] A. Pandiyan, A. Uthayakumar, R. Subrayan, S. W. Cha, S. B. K. Moorthy, *Nanomaterials and Energy,* 8, 2-22, 2019.

[16] E. Ivres-Tiffee, A. V. Virkar, “Electrode Polarisations,” in *High Temperature Solid Oxide Fuel Cells: Fundamentals, Design and Applications*, Editors: S. C. Singhal, K. Kendall, Oxford, UK, Elsevier Advanced Technology, 229-260, 2003.

[17] N. P. Brandon, S. Skinner, B. Steele, *Annual Review of Materials Research,* 33, 183-213, 2003.

[18] J. C. Grenier, J. M. Bassat, F. Mauvy, “Novel cathodes for solid oxide fuel cells,” in *Functional materials for sustainable energy applications*, Editors: J. A. Kilner, S. J. Skinner, S. J. C. Irvine, P. P. Edwards, Cambridge, UK, Woodhead Publishing Limited, 402-444, 2012.

[19] P. Mocoteguy, A. Brisse, *International Journal of Hydrogen Energy,* 38, 15887-15902, 2013.

[20] N. Mahato, A. Banerjee, A. Gupta, S. Omar, K. Balani, *Progress in Materials Science,* 72, 141-337, 2015.

[21] H. Zhao, Q. Li, L. Sun, *Science China Chemistry,* 54, 898-910, 2011.

[22] N. Preux, A. Rolle, R. N. Vannier, “Electrolytes and ion conductors for solid oxide fuel cells (SOFCs),” in *Functional materials for sustainable energy applications*, Editors: J. A. Kilner, S. J. Skinner, S. J. C. Irvine, P. P. Edwards, Cambridge, UK, Woodhead Publishing Limited, 370-401, 2012.

[23] K. Chen, S. P. Jiang, *Journal of The Electrochemical Society,* 163, F3070-F3083, 2016.

[24] S. Liu, B. Yu, W. Zhang, J. Zhu, Y. Zhai, J. Chen, *Progress in Chemistry,* 26, 1570-1585, 2014.

[25] C. Berger, E. Bucher, A. Egger, N. Schrödl, J. Lammer, C. Gspan, R. Merkle, W. Grogger, J. Maier, W. Sitte, *Solid State Ionics ,* 348, 115282, 2020.

[26] S. B. Adler, J. A. Lane, B. C. H. Steele, *Journal of Electrochemical Society,* 143, 3554-3564, 1996.

[27] S. W. Tao, P. I. Cowin, R. Lan, "Novel anode materials for solid oxide fuel cells," in *Functional materials for sustainable energy applications*, Editors: J. A. Kilner, S. J. Skinner, S. J. C. Irvine, P. P. Edwards, Cambridge, UK, Woodhead Publishing Limited, 445-477, 2012.

[28] X. Wu, W. Zhang, B. Yu, X. Guo, J. Xu, *Rare Metal Materials and Engineering,* 44, 1555-1560, 2015.

[29] A. R. West, "Basic Solid State Chemistry", Second Edition, Chichester, UK, John Wiley & Sons, Ltd, 1999.

[30] J. E. Huheey, E. A. Keiter, R. L. Keiter, O. K. Medhi, "Inorganic Chemistry: principles of structure and reactivity", Fourth Edition, Uttar Pradesh, India, Pearson India Education Services Pvt. Ltd, 2006.

[31] R. Woolley, "PhD thesis: Ruddlesden-Popper Phases as Solid Oxide Fuel Cell Cathodes: Electrochemical Performance and In Situ Characterisation," Imperial College London, London, 2014.

[32] S. P. Mitoff, *The Journal of Chemical Physics,* 35, 882-889, 1961.

[33] J. T. S. Irvine, J. W. L. Dobson, T. Politova, S. G. Martin, A. Shenouda, *Faraday Discussions,* 134, 41-49, 2007.

Chapter 2 Materials for solid oxide cells (SOCs)

2.1 Introduction

This chapter attempts to review materials used for the electrolyte, fuel electrode and air electrode in solid oxide cells. Chemical and physical properties of each material will be discussed but more emphasis will be given to the air electrode materials, especially Ruddlesden-Popper (RP) phases. The later part of this chapter will focus on how to stabilise a first order praseodymium nickelate RP phase under intermediate temperature (500-800°C) operating condition in air. Indeed, discussion will be made regarding whether the decomposed/reacted products of the praseodymium nickelate and a gadolinium substituted ceria, usually used as a barrier layer between an air electrode and an electrolyte, are good candidates to develop a novel composite air electrode for solid oxide cells.

2.2 Oxide ion conducting electrolytes

2.2.1 Substituted zirconia

The unsubstituted zirconia (ZrO_2) has negligible oxygen ion conductivity and has a monoclinic crystal structure at room temperature [1]. With increasing temperature, the monoclinic phase will transition to a tetragonal phase and then a cubic phase at 1170°C and 2370°C, respectively [1, 2]. By introducing acceptor substitutes into the ZrO_2 system such as an alkaline earth metal oxide or a rare earth metal oxide, the monoclinic ZrO_2 structure can be stabilised to a cubic phase at room temperature [1]. Therefore, there will be no abrupt volume change when heating the material from room temperature to sintering temperature and a dense body can be achieved [1]. Being able to densify is important for an electrolyte material used for solid oxide cells as it prevents gas mixing from a fuel electrode and an air electrode (**Section 1.3.2**) [3]. In addition, the trivalent or the divalent substitutes will generate oxygen vacancies simultaneously in the system to maintain the charge neutrality [1, 3]. At elevated temperatures when the activation energy of charge carrier (oxygen vacancies) migration is overcome (**Section 1.4.2**), these mobile oxygen vacancies allow the substituted zirconia to conduct oxygen ions [1, 4].

Yttrium stabilised zirconia (YSZ) with formula of $(ZrO_2)_{1-x}(Y_2O_3)_x$ is one of the well-studied oxygen ion conductors [1-3]. Y^{+3} is introduced to the ZrO_2 lattice and forms oxygen vacancies [1, 3]. Research shows that 8 mol.% (x=0.08) of Y_2O_3 provides the highest electrical (oxygen ionic) conductivity [1, 3, 5, 6]. When the substitution level is above this threshold, the electrical conductivity will start decreasing (**Figure 2.1**) [1, 5, 6]. This is due to the defect association between the increasing amount of oxygen vacancies and the acceptor substitutes [1, 5, 6]. The electrostatic interaction between the positively charged oxygen vacancies and the negatively charged acceptor substitute will be dominant after the threshold and limits the mobility of oxygen vacancies and hence the decrease of the oxygen ionic conductivity [1, 5, 6].

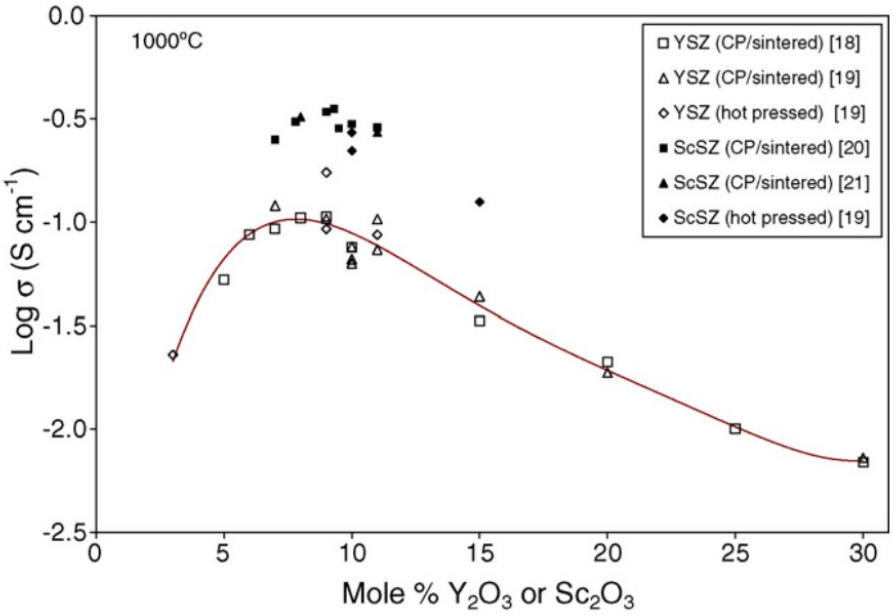


Figure 2.1: The change of oxygen ionic conductivity of $(ZrO_2)_{1-x}(Y_2O_3)_x$ (YSZ) and $(ZrO_2)_{1-x}(Sc_2O_3)_x$ (ScSZ) by varying the amount of x at 1000°C in air. The various labels indicate the experimental data from different references mentioned in the original paper whereas the curve shows the overall trend. Reproduced from [6] with kind permission from Elsevier.

The main disadvantage of YSZ is its low oxygen ionic conductivity when operating in the intermediate temperature range of 500-800°C [1, 3]. Therefore, YSZ usually requires operation at a higher temperature such as between 800° and 1000°C [1, 3]. For example, the oxygen ionic conductivity of YSZ (with 8 mol.% of Y_2O_3 substitution) at 600°C is only 0.005 Scm^{-1} whereas it increases to 0.039 Scm^{-1} at 800°C (**Figure 2.2**)

[3]. As intermediate temperature operating condition is aiming here, YSZ can only be used when the thickness of the sintered electrolyte is decreased, or other electrolytes with higher oxygen ionic conductivity should be considered (**Section 1.3.1**) [1, 3].

Replacing yttrium by scandium allows further enhancement of oxygen ionic conductivity in zirconia based electrolytes (**Figure 2.1**), and it was reported to be the highest in the substituted ZrO_2 system [1, 3, 6, 7]. The main reason for the promising performance of scandium substituted zirconia is because of the similar ionic radius between Sc^{+3} and Zr^{+4} compared to Y^{+3} and Zr^{+4} [1, 7]. For the cubic fluorite structure, Sc^{+3}, Y^{+3} and Zr^{+4} have 8 coordination number and their corresponding ionic radii are 0.870 Å, 1.019 Å and 0.840 Å [8]. By substituting trivalent scandium in zirconia, the created oxygen vacancies have a lower migration enthalpy and a higher association enthalpy with the substituted cations, leading to the higher oxygen ionic conductivity [1]. However, it is important to note that the price of Sc_2O_3 is much higher than Y_2O_3 and scandium stabilised zirconia has an issue of performance aging which is usually not observed in YSZ [1, 3, 7, 9, 10]. This performance degradation is mainly due to the phase transition from the favorable cubic phase to the less conductive tetragonal phase or rhombohedral phase depending on the amount of scandium substitute in the system [5, 9, 10]. Co-substituting scandium with small amount of other substitutes having larger ionic radius such as cerium helps to solve the problem as cerium will form an eight-fold coordination with oxygen in the cubic fluorite structure [7, 10, 11]. This prevents the system from forming a less symmetric structure and leaves the oxygen vacancies to interact with zirconium ions [7, 10, 11]. The optimized chemical composition in terms of material performance and its stability was reported to be 10 mol.% Sc_2O_3- 1 mol.% CeO_2- 89 mol.% ZrO_2 (10Sc1CeSZ) [10, 11] and its oxygen ionic conductivity is compared with other electrolyte materials in **Figure 2.2**.

2.2.2 Substituted ceria

Samarium and gadolinium trivalent cation are usually used as a substitute in the fluorite structure ceria as their ionic radiuses in 8 coordination number (e.g. 1.079 Å and 1.053 Å, respectively) are similar to the one of Ce^{+4} (0.970 Å) [1, 8]. The oxygen vacancies are also generated simultaneously to maintain the charge neutrality of the material. The resulting oxygen ionic conductivity of ceria based electrolytes is between

several times to several orders of magnitude greater than YSZ at temperatures below 800°C and the difference is larger at the lower temperatures (**Figure 2.2**) [1, 3]. For example, the electrical conductivity of gadolinium substituted ceria ($Ce_{0.9}Gd_{0.1}O_{1.95}$) is about 0.033 Scm^{-1} at 700°C and this is compared with $(ZrO_2)_{0.92}(Y_2O_3)_{0.08}$ of 0.013 Scm^{-1} at the same temperature (**Figure 2.2**) [3]. Despite the promising ionic conductivity in the intermediate temperature range, Ce^{+4} can be easily reduced to Ce^{+3} depending on the operating temperature, the local oxygen partial pressure and the applied bias [1, 3, 12]. The reduction of cerium will not only decrease the oxygen ionic conductivity transport number and causes electricity leakage of the electrolyte, but the lattice will also expand leading to potential mechanical damage of solid oxide cells [1, 3]. Several solutions were proposed to mitigate the issue including co-substituting and introducing a dense barrier layer between the fuel electrode and the electrolyte [1, 3, 9].

2.2.3 Substituted lanthanum gallate

A lanthanum gallate based electrolyte was first discovered by Ishihara et al. and Feng and Goodenough in 1994 [1, 13, 14]. The concept is to introduce acceptor substitutes such as Sr^{+2} and Mg^{+2} in the La and Ga site of $LaGaO_3$ perovskite to enhance the oxygen vacancy concentration [1, 3, 13, 14]. The oxygen ionic conductivity of $La_{0.9}Sr_{0.1}Ga_{0.8}Mg_{0.2}O_{2.8}$ (LSGM) is as high as 0.030 Scm^{-1} at 700°C, similar to the conductivity of $Ce_{0.9}Gd_{0.1}O_{1.95}$ (**Figure 2.2**) [1, 3]. LSGM also possesses a wide oxygen ionic conduction range between 10^{-22} and 1 atm oxygen partial pressures [1, 15].

Nevertheless, LSGM has several drawbacks. Firstly, it is relatively difficult to synthesise the chemical with proper chemical composition as there are four different cations in the system [1]. Any mixing inhomogeneity of the precursors will result in the formation of less conductive phases [1]. Moreover, similar to the substituted ceria, LSGM has been shown to possess a small electronic conductivity at reducing atmosphere as Ga^{+3} can be reduced to Ga^{+2} [9]. Lastly, LSGM has a chemical compatibility issue with nickel at the fuel electrode side and secondary phase such as $LaNiO_3$ can form at the interface [3, 9].

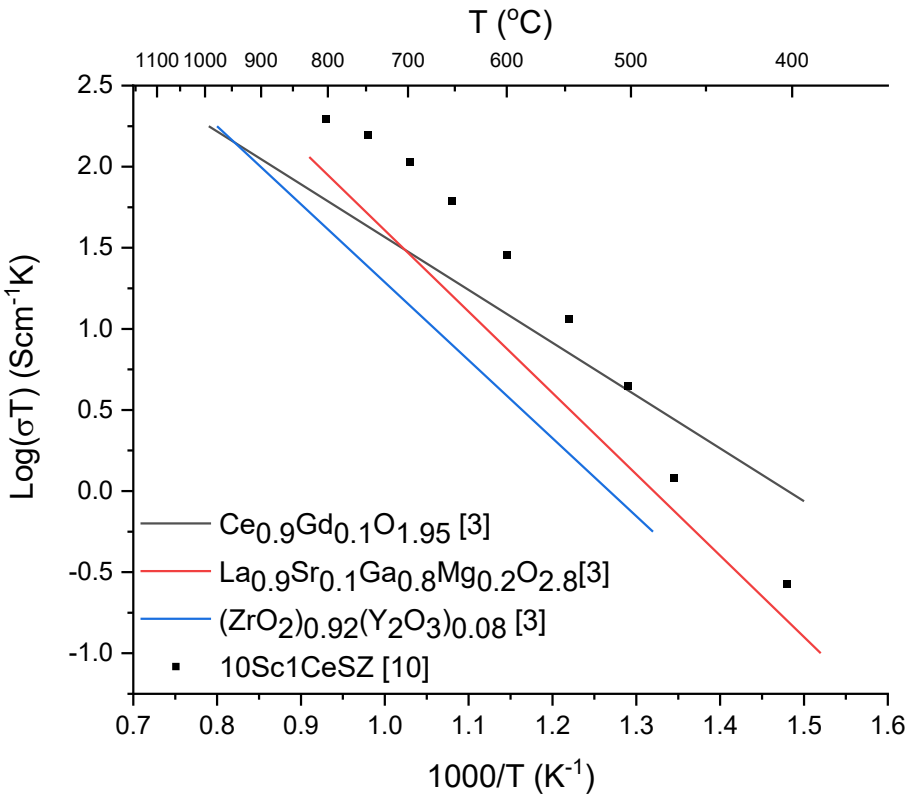


Figure 2.2: The oxygen ionic conductivity comparison between each conventional electrolyte material under different temperatures. The reference numbers on the plot relate to the current reference list.

2.3 Hydrogen electrode

Ni cermets such as the Ni-YSZ composite electrode are a typical hydrogen electrode material used in solid oxide cells [9, 16, 17]. Nickel is used in the composite because of its excellent electrocatalytic activity towards fuel oxidation/reduction and high electronic conductivity [16, 17, 18]. YSZ, on the other hand, is responsible for conducting oxygen ions and mitigating the thermal expansion coefficient difference between nickel and conventional electrolyte materials such as YSZ [16, 18]. In general, Ni-YSZ composite electrode satisfies most of the requirements listed in **Section 1.3.3** but have suffered from several drawbacks such as impurity poisoning, carbon formation, nickel coarsening and oxidation [16-19]. Therefore, alternative materials have been developed and are mainly in the form of perovskites including lanthanum strontium chromium manganites, lanthanum substituted strontium titanates, lanthanum strontium vanadates, substituted lanthanum ferrites and $Sr_2Fe_{1.5}Mo_{0.5}O_{6-\delta}$ double perovskite oxides [9, 16-19]. Since fuel electrode is not the main focus of this

research, useful references can be found above for more information about fuel electrode materials.

2.4 Air electrode

2.4.1 Lanthanum strontium manganites

Lanthanum strontium manganites ($La_{1-x}Sr_xMnO_3$, LSM) are a traditional air electrode material used for high temperature solid oxide fuel cells [20]. The substituting of strontium at the lanthanum site which is up to 20-30%, increases the valence of manganese to +4 [20, 21]. This leads to the enhancement of p-type electronic conductivity of the materials [20, 21]. LSM is almost a pure electronic conductor and has a very low oxygen diffusion coefficient [20-22]. For example, depending on the strontium substitution concentration in LSM, the electrical conductivity is reported to range from 40 to 485 Scm^{-1} at 1000°C whereas the oxygen ionic conductivity is around 10^{-7}-10^{-6} Scm^{-1} at the same temperature [23]. An acceptable air electrode performance is usually achieved at temperatures greater than 900°C but the active surface area can be extended by introducing oxygen ionic conductors such as YSZ and CGO (gadolinium substituted ceria) [20, 24-27]. This allows decreasing the operating temperatures to lower than 800°C [20, 28].

2.4.2 Mixed ionic and electronic conducting (MIEC) perovskite oxides

As mentioned in **Section 1.3.1**, MIECs have the advantage of enlarging the electrochemically active area from a TPB to DPB and this is achieved by replacing manganese in LSM with other transition metals such as Fe, Co, Ni and Cu [9, 20]. Alkaline earth metals such as strontium and barium are also used to substitute/replace lanthanum [9, 20]. The change of the transition metal at the B site to Co, for example, allows the strontium substitute to create both oxygen vacancies and the mixed valence of cobalt (+3/+4) [20, 29, 30]. Hence, materials such as $La_{1-x}Sr_xCoO_{3-\delta}$ (LSC) possess MIEC properties [20, 29, 30]. In terms of electrochemical activity, it strongly depends on the transition metal used at the B site and research shows that the order from high to low is cobaltites, manganites, ferrites and chromites [20, 31, 32].

Despite the promising electrochemical performance of LSC at intermediate temperature operating conditions, these electrodes present several drawbacks such

as the high TEC values (~23x10^{-6} K^{-1}) compared to the ones of conventional electrolytes (~12x10^{-6} K^{-1}) and the chemical reactivity with YSZ [20, 28]. The relatively high TEC value is common for cobalt based perovskite oxides because Co^{+3} tends to transform from the low spin to high spin state at elevated temperature [33]. Chemical compatibility between LSC and YSZ can also result in the formation of insulating secondary phases such as $La_2Zr_2O_7$ and $SrZrO_3$ at the electrolyte/electrode interface but this can be effectively solved by introducing a substituted ceria barrier layer at the interface [20, 34].

To solve the issue of TEC mismatch, partially replacing cobalt by iron is effective to reduce the TEC of the materials [20, 35]. Considering the compensation between TEC and electrochemical performance reduction, $La_{0.6}Sr_{0.4}Fe_{0.8}Co_{0.2}O_{3-\delta}$ (LSCF) is the best chemical composition [20, 35]. Apart from LSCF, other perovskites such as $Gd_{1-x}Sr_xCoO_{3-\delta}$, $Sm_{1-x}Sr_xCoO_{3-\delta}$, $La_{0.6}Sr_{0.4}Fe_{0.8}Ni_{0.2}O_{3-\delta}$ (LSFN) and $Ba_{1-x}Sr_xCo_{1-y}Fe_yO_{3-\delta}$ (BSCF) also show promising electrochemical properties [20, 36-39]. The oxygen diffusion coefficient and oxygen surface exchange coefficient of BSCF are even higher than LSCF [40, 41]. However, BSCF suffers from larger TEC and chemical reactivity with CO_2, leading to rapid performance loss over time [20, 39, 42].

2.4.3 Double perovskites

Double perovskite oxides are one of the layered perovskites with a two-dimensional character of oxygen ion carrier distribution [20, 43, 44]. Depending on the cation size difference between lanthanide ions (Ln^{+3}, Ln= Gd, Pr, Nd and Sm) and alkaline earth ions (e.g. Ba^{+2}) at the A site of $LnBaMO_{5+\delta}$ (M= Co, Fe, Mn and Cu), an ordered structure of LnO and BaO alternating layers will form with various amounts of oxygen vacancies located in the LnO layer as shown in **Figure 2.3** [20, 43, 44]. Oxygen diffusion rate was found to be higher in the LnO layer of the ordered structure compared with the disordered one [20, 43, 45]. The oxygen bonding strength is expected to be lower at this layer and hence a fast oxygen diffusion channel is developed [20, 43, 45].

In SOCs applications, the most well studied double perovskite is $GdBaCo_2O_{5+\delta}$ (GBCO) and it was demonstrated to have a high oxygen diffusion coefficient (4.8 x 10^{-10} cm^2/s) and oxygen surface exchange coefficient (2.8 x 10^{-7}cm/s) at 575°C, which is a suitable air electrode candidate for intermediate temperature operation [20, 44, 46]. Other

modifications of this material have also been conducted including co-substituting Ba and Sr and replacing Gd with Pr, Nd or Sm which all showed very promising electrochemical performance [20, 44, 47-50].

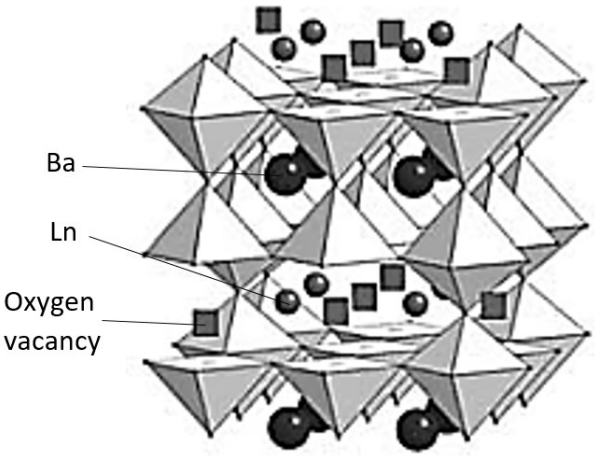


Figure 2.3: Crystal structure of A site ordered double perovskite with chemical formula of $LnBaM_2O_{5+\delta}$, where Ln and M can be Gd, Pr, Nd and Sm and Co, Fe, Mn and Cu, respectively. Adapted from [20] with kind permission from Elsevier.

2.4.4 Ruddlesden-Popper phases

Ruddlesden-Popper (RP) phases have the general chemical formula of $A_{n+1}B_nO_{3n+1}$ or $(AO)(ABO_3)_n$ where n=1, 2 and 3 which shows that their crystal structure is formed by alternating rock salt and perovskite layers as illustrated in **Figure 2.4** [51]. This intrinsic heterostructure results in the RP materials possessing promising physical/chemical properties and performance as an air electrode [9, 40]. For example, the intrinsic lattice mismatch between the two layers can be adjusted by including oxygen interstitials at the rock salt layers and this will increase the size of the rock salt layer [20, 52-55]. Simultaneously, to maintain the charge neutrality, the valence of the transition metal increases at the B site, which then decreases the size of the perovskite layers [20, 52-55]. Overall, this causes the material possessing a MIEC property as the introduction of oxygen interstitials will contribute to the oxygen ionic conductivity and the change of valence at the B site will result in p-type electronic conductivity [20, 56-59]. In addition, the stresses between these two layers also help with maintaining the material MIEC properties at significant reducing and oxidizing conditions or under high cathodic or anodic bias [20, 60-64]. For example, the expansion of the perovskite

layers under reducing conditions due to the lower content of Ni^{+3} will avoid further oxygen interstitial loss in the rock salt layers whereas under oxidizing conditions, oxygen interstitials will be included in the rock salt layers until their size match to the perovskite layers [20]. These features are very important as oxygen ion carriers, oxygen interstitials in this case, will always exist in different operating conditions as well as the mixed valence transition cation (e.g. $Ni^{+2/+3}$) [20]. This is unlike normal perovskite materials which can have oxygen saturation issues when oxygen vacancies are filled under extreme oxidizing conditions. Hence, the oxygen mobility is reduced [20]. Moreover, when comparing to n=2 and 3 RP materials, there is more research on n=1 materials in the literature. Therefore, the review below will mainly focus on n=1 RP phases and their comparison to other well-known air electrode materials, especially LSCF.

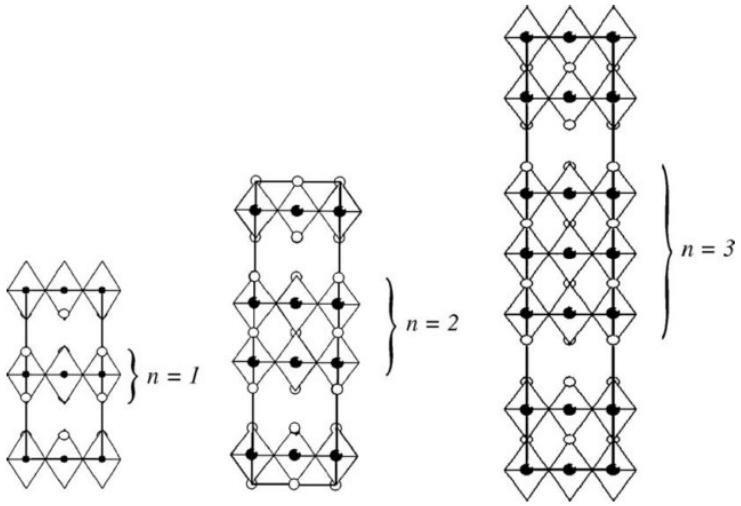


Figure 2.4: The two dimensional RP phase crystal structures which show the increasing number of perovskite layers on increasing n, where n=1, 2 and 3. Reproduced from [51] with kind permission from Elsevier.

2.5 Ruddlesden-Popper phases as air electrode materials

2.5.1 Thermal expansion coefficients (TEC)

One of the major disadvantages of perovskite materials such as (La, Sr/Ba)(Co, Fe)$O_{3-\delta}$ are their mismatch of TEC values in comparison with the conventional electrolytes [40]. The TEC values can be at least 16.3 x 10^{-6} K^{-1} for $La_{1-x}Sr_xFeO_{3-\delta}$ (LSF) and as high as 20.5 x 10^{-6} K^{-1} for $La_{1-x}Sr_xCoO_{3-\delta}$ (LSC) at 300-1000°C in air with LSCF and $Ba_{1-x}Sr_xCo_{1-y}Fe_yO_{2-\delta}$ (BSCF) values located within these two extremes [40, 65-67]. This is also in

contrast to the TEC of LSM which is 12.3 x 10^{-6} K^{-1} and was measured at the same condition [40, 66]. Although substitution of cobalt with other transition metals such as iron can reduce the TEC values, their TEC are still much higher than the target range of 10.8 to 13.5 x 10^{-6} K^{-1} [33, 40, 68]. $Ln_2NiO_{4+\delta}$ (where Ln is La, Nd and Pr) RP phase materials, however, have much smaller and more compatible TEC values in the range of 12.7-13.6 x 10^{-6} K^{-1} at 300-1000°C in air [40, 69, 70].

In addition, the chemical expansion of a material caused by the change of oxygen stoichiometry should be considered when operating under different temperatures and oxygen partial pressures [40]. Kharton et al. [69] suggested that for the case of Ln_2NiO_4 based materials, the chemical expansion will not contribute to more than 5% of the overall TEC under oxidizing conditions and this is much lower than the cobalt/ferrite based perovskites [40, 71, 72]. Such favorable observation can be explained by the anisotropic expanding nature of Ln_2NiO_4 when there is a change in oxygen stoichiometry [40, 69]. Indeed, structural transition from *Fmmm* or *Bmab* towards more symmetric *I4/mmm* usually occurs for $Ln_2NiO_{4+\delta}$ or analogous materials (with various substitute such as Co at the Ni site) when heating from room temperature, but several researches have demonstrated that there was no abrupt change of volume at the point of transition [20, 64, 73, 74]. Overall, $Ln_2NiO_{4+\delta}$ RP phase materials are mechanically compatible to the conventional electrolytes.

2.5.2 Electrical conductivity

Figure 2.5 shows the electrical conductivity of different $Ln_2NiO_{4+\delta}$ phases and their comparison to LSM, MIEC perovskites and double perovskites at various temperatures [20]. Among the different lanthanide series elements at the A site, only $Pr_2NiO_{4+\delta}$ shows an appropriate electrical conductivity which is about 100 Scm^{-1} at intermediate temperature operating range [20, 70]. Although the value is much smaller than LSCF (which is 191 Scm^{-1} at 700°C [33]), it is still acceptable compared to the required value of at least 100 Scm^{-1} as defined in **Section 1.3.1**. With respect to $La_2NiO_{4+\delta}$ and $Nd_2NiO_{4+\delta}$, their electrical conductivities are much lower than the criteria of the general SOC air electrodes [20, 70]. Substituting with an alkaline earth element at the A site helps with enhancing the electronic conductivity of a material but with the cost of reducing oxygen interstitial concentration and hence the oxygen ionic conductivity

[44, 70]. On the other hand, LSFN and both GBCO and $PrBaCo_2O_{5.5+\delta}$ (PBCO) double perovskites possess a much higher electrical conductivity, which is greater than 300 Scm^{-1} at temperatures above 500°C [20, 75].

It is important to note that all the $Ln_2NiO_{4+\delta}$ materials show a semi-conducting behavior as the maximum electronic conductivity can be observed at around 400°C to 500°C and it drops at higher temperatures [20, 70]. This can be explained by the decrease of oxygen content when the temperature increases and it results in the corresponding decrease of the amount of Ni^{+3} electronic charge carriers [20, 70].

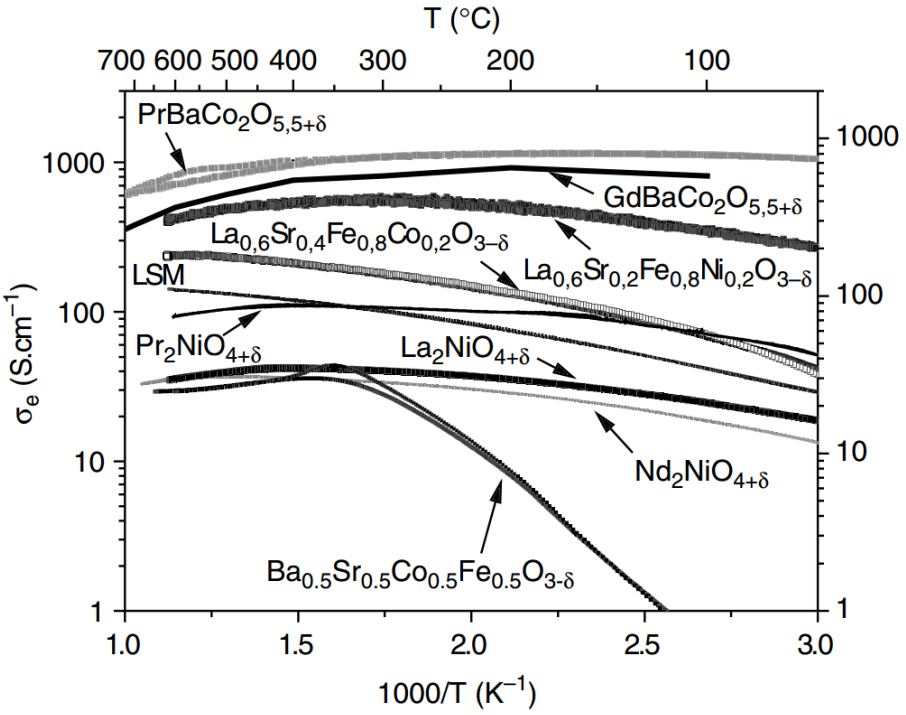
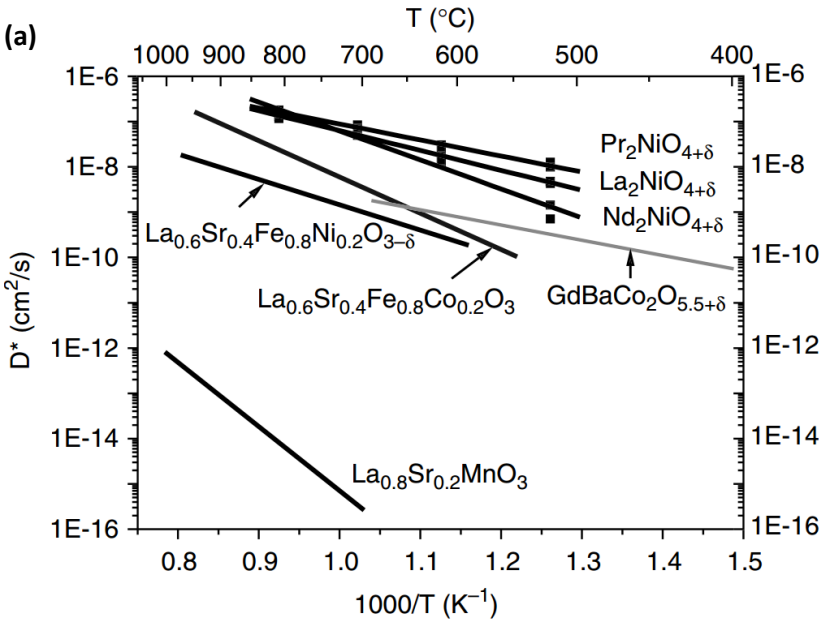


Figure 2.5: Electrical conductivity of different air electrode materials under various temperatures. Reproduced from [20] with kind permission from Elsevier.

2.5.3 Oxygen diffusion and surface exchange coefficients

As mentioned in **Section 1.3.1**, oxygen diffusion coefficient (D*) and surface exchange coefficient (k) are two important parameters when evaluating the performance of MIEC type of SOC air electrodes. In general, materials with high D* and k are favorable. With respect to $Ln_2NiO_{4+\delta}$ RP phases, **Figure 2.6(a)** and **(b)** show that most of them possess higher D* and k values than LSCF, LSFN, GBCO and LSM in the intermediate temperature operating range [20, 43, 70, 76]. However, the D* and k of BSCF were about one order of magnitude and two order of magnitude larger than $Ln_2NiO_{4+\delta}$ at

700°C, respectively (not shown in **Figure 2.6**) [40, 41]. On the other hand, LSC has slightly lower value of D* (1.5 x 10^{-8} cm^2s^{-1}) and slightly larger k value (4 x 10^{-6} cms^{-1}) compared to $Ln_2NiO_{4+\delta}$ at 700°C but they are within the same order of magnitude [40]. Among $Ln_2NiO_{4+\delta}$, $Pr_2NiO_{4+\delta}$ has the highest D* and k over $Nd_2NiO_{4+\delta}$ and $La_2NiO_{4+\delta}$ as shown in **Figure 2.6(a)** and **(b)** [20, 70]. Hence $Pr_2NiO_{4+\delta}$ is a promising RP phase for SOC air electrodes. In addition, it is important to note that the activation energies of D* and k are relatively small for $Ln_2NiO_{4+\delta}$ compared with LSCF and LSM [20, 70]. This preferable nature allows $Ln_2NiO_{4+\delta}$ to keep relatively high D* and k values at a lower temperature and this is beneficial when operating SOC at the intermediate temperature range [20].



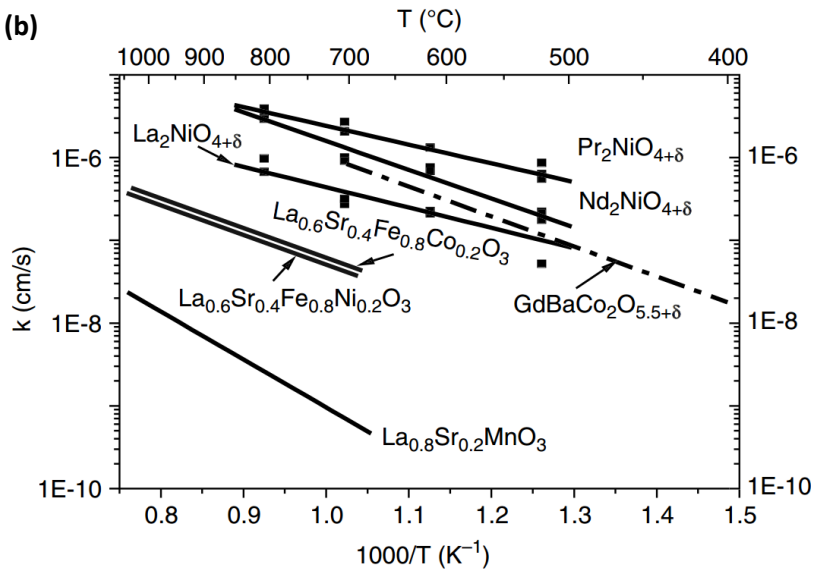


Figure 2.6: Oxygen diffusion (D*) **(a)** and surface exchange (k) **(b)** coefficients of various air electrode materials in different temperature. Reproduced from [20] with kind permission from Elsevier.

2.5.4 Electrode performance

The kinetics of the oxygen reduction/evolution reactions can be evaluated by the electrode polarization resistance (R_p) measured under open circuit condition [40]. As mentioned in **Section 1.3.1**, the R_p value of a MIEC air electrode mainly depends on two factors, which are the intrinsic physicochemical properties of the selected materials and the microstructure of the air electrode. The R_p values of $Ln_2NiO_{4+\delta}$ were compared with LSCF by Ogier et al. with the similar fabrication process of the symmetrical cell with different air electrode materials [77]. The preliminary results are shown in **Figure 2.7(a)** when using YSZ as the electrolyte and no barrier layer between the air electrode and the electrolyte [77]. $Pr_2NiO_{4+\delta}$ shows the lowest R_p value for the $Ln_2NiO_{4+\delta}$ series and its R_p value is comparable to LSCF but lower when temperature is below 675°C [77].

To prevent any possible chemical reaction with the YSZ electrolyte and to enhance the contact at the air electrode/electrolyte interface, it was proposed to introduce a ceria substituted interlayer between the electrolyte and the electrodes, and the corresponding R_p values are shown in **Figure 2.7(b)** [77-79]. When comparing with the result in **Figure 2.7(a)**, introducing the ceria substituted interlayer further decreased the R_p values in different materials [77]. The $Pr_2NiO_{4+\delta}$/CGO configuration showed the

lowest R_p value especially when comparing with the LSCF/CGO and the $Pr_2NiO_{4+\delta}$/$Ce_{0.72}Y_{0.18}O_{2-\delta}$ (YDC) configurations [77, 78]. Generally, CGO is a better interface candidate than YDC because of its higher oxygen ionic conductivity [79, 80].

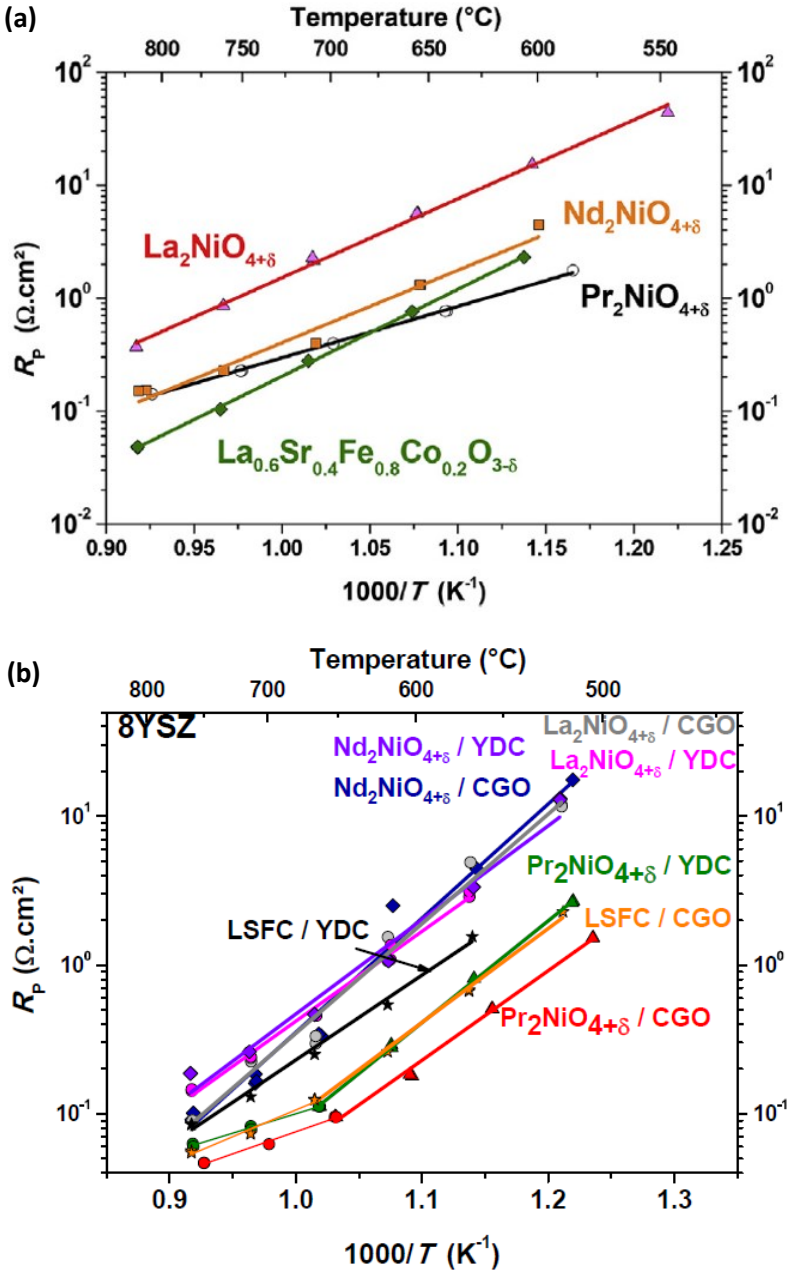


Figure 2.7: Electrode polarization resistance (R_p) for different air electrode materials **(a)** without and **(b)** with an interlayer at the air electrode/electrolyte interface measured under open circuit condition over different temperature ranges. Reproduced from [77] with kind permission from Elsevier.

Moreover, in terms of the electrode performance under anodic polarization, resemble to the air electrode operating condition in electrolysis mode, Ogier et al. [77] have demonstrated that $Pr_2NiO_{4+\delta}$ provided a much higher current density than LSCF at a given temperature and a given anodic overpotential (**Figure 2.8**). It is important to note that no CGO interlayer was initially introduced for both of the samples [77]. On the other hand, with the introduction of CGO interlayer to $Pr_2NiO_{4+\delta}$ cells, there was a further enhancement of the current density (**Figure 2.8**) [77]. The performance of $Pr_2NiO_{4+\delta}$ air electrode at high anodic overpotential changed from Tafel behavior to current limitation response for the samples without and with the CGO interlayer, respectively [77]. The presence of the current limitation response might be due to oxygen diffusion limitation within the less porous electrode active layer and hence further optimization of electrode microstructure is required [77]. Overall, $Pr_2NiO_{4+\delta}$ with CGO interlayer is a promising air electrode material especially for the applications in electrolysis mode.

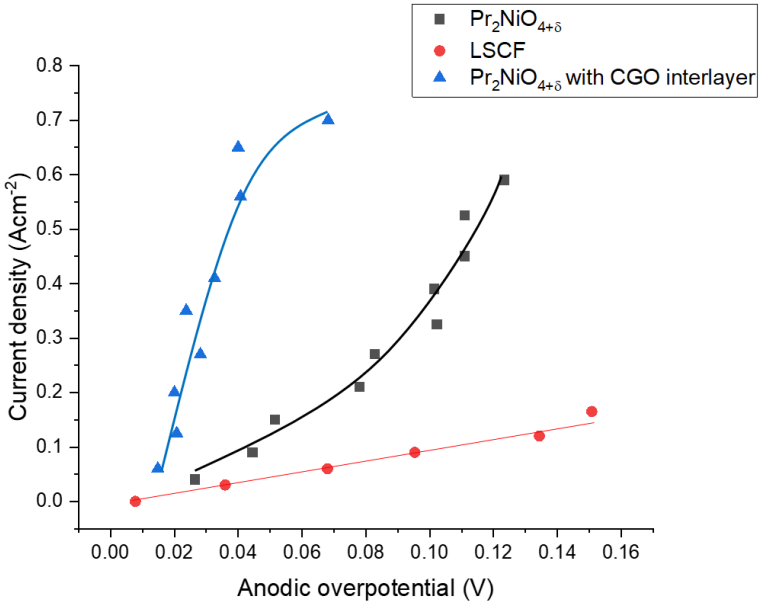


Figure 2.8: Anodic polarization curves of cells when using $Pr_2NiO_{4+\delta}$ and LSCF as an air electrode without CGO interlayer. They are compared with the results of $Pr_2NiO_{4+\delta}$ with CGO interlayer. All the measurements were conducted at 800°C in air. Replotted from [77].

2.5.5 Thermal stability and chemical reactivity at high temperature

Both thermal stability of the materials and their chemical reactivity with the conventional electrolyte (e.g. YSZ, CGO and LSGM) under sintering and operating

conditions should be evaluated as any formation of secondary phase at the bulk and/or at the air electrode/electrolyte interface usually decreases the electrode performance [40]. Montenegro-Hernandez et al. [81] examined the thermal stability of different $Ln_2NiO_{4+\delta}$ with separate heat treatments of 700°C and 900°C under air for 72 hours. No decomposition was observed for $La_2NiO_{4+\delta}$ and $Nd_2NiO_{4+\delta}$, regardless of the sample preparation methods which result in different sample particle sizes and shapes [81]. However, it is important to note that a higher order RP phase was detected for $La_2NiO_{4+\delta}$ when annealing at 900°C for two weeks in air [51]. For the case of $Pr_2NiO_{4+\delta}$, the secondary phase of Pr_6O_{11} started to form at 700°C and $Pr_2NiO_{4+\delta}$ decomposed to Pr_6O_{11} and $Pr_4Ni_3O_{10+/-\delta}$ at 900°C [81]. The latter result is in agreement with the observation from Kovalevsky et al.'s who tested at 800°C in air [82]. Further investigation of thermal stability of $Pr_2NiO_{4+\delta}$ has also been undertaken by Vibhu [83] who reported the pattern of the decomposed products at various temperature ranges from 600°C to 800°C for a month of heat treatment under air. It was found that at lower temperature such as 600°C, $PrNiO_{3-\delta}$ and Pr_6O_{11} were the major decomposition products and $Pr_4Ni_3O_{10+\delta}$ started to appear at higher annealing temperatures [83].

Despite promising features, as mentioned in the previous sections, one of the main drawbacks of $Ln_2NiO_{4+\delta}$ phases is that they tend to react with the conventional electrolytes at different temperatures. For $La_2NiO_{4+\delta}$, the secondary phases of $La_2Zr_2O_7$ and $La_3Ni_2O_7$ were detected at 900°C when mixing with YSZ [81]. When $La_2NiO_{4+\delta}$ mixed with CGO powder, depending on the powder morphology of $La_2NiO_{4+\delta}$, some $La_2NiO_{4+\delta}$ was decomposed to $La_3Ni_2O_{7-\delta}$ at 700°C for 2 hours and to $La_4Ni_3O_{10-\delta}$ and $LaNiO_{3-\delta}$ or $La_3Ni_2O_{7-\delta}$ at 900°C for 72 hours [81]. $Pr_2NiO_{4+\delta}$ showed similar reaction products to $La_2NiO_{4+\delta}$ in compatibility tests with YSZ and CGO but it also self-decomposed simultaneously to form $Pr_4Ni_3O_{10+/-\delta}$ and Pr_6O_{11} even without the presence of YSZ and CGO powder [81]. When $Pr_2NiO_{4+\delta}$ was mixed with YSZ powder and heated at 900°C for up to 72 hours, Pr_6O_{11} and $Pr_2Zr_2O_7$ were observed as well as $Pr_4Ni_3O_{10+/-\delta}$ and NiO [81]. Chemical reaction/decomposition of $Pr_2NiO_{4+\delta}$ also occurred at the same temperature when mixing with CGO and the secondary phases were $Pr_4Ni_3O_{10+/-\delta}$, Pr_6O_{11} and possibly $Ce_{1-x-y}Gd_xPr_yO_{2-\delta}$ (CGPO) [81]. Philippeau et al. [84] have found secondary phases of Pr_6O_{11} and NiO, and $PrNiO_3$ and NiO after

sintering the powder mixture at 1150°C for 1 hour and then annealing at 800°C for 5 days under air, respectively. In terms of $Nd_2NiO_{4+\delta}$, it reacted with YSZ and CGO to from $Nd_2Zr_2O_7$ and $Nd_2Ce_2O_7$ at 1000°C, respectively [81]. In addition, Philippeau et al. [84] observed the chemical reaction/electrolyte decomposition between $Ln_2NiO_{4+\delta}$ and LSGM electrolyte at 1150°C for 1 hour in air with the products of $Sr_4Ga_2O_7$, $Nd_4Ga_2O_9$ and $Pr_4Ga_2O_9$ for $La_2NiO_{4+\delta}$, $Nd_2NiO_{4+\delta}$ and $Pr_2NiO_{4+\delta}$, respectively. They suggested that the formation of the gallates was due to the high volatility of gallium at high temperature [84, 85].

2.6 $Pr_2NiO_{4+\delta}$ decomposition and possible approaches to stabilise it

The previous section shows that $Pr_2NiO_{4+\delta}$ is a promising candidate as a SOC air electrode due to its acceptable electrical conductivity, high D* and k and low R_p value in comparison to LSCF. However, the lack of thermodynamic stability at temperatures below 900°C in air and its reactivity with conventional electrolytes limits its application. The decomposition reaction of $Pr_2NiO_{4+\delta}$ under oxidative atmosphere can be summarized in **Equation 2.1**:

$$3Pr_2NiO_{4+\delta} + b\ O_2 \rightarrow Pr_4Ni_3O_{10\pm\delta'} + 2PrO_{2+\delta''} \qquad \textbf{Equation 2.1}$$

where $b = 1 - 1.5\delta \pm 0.5\delta' + \delta''$ and indicates the amount of oxygen required to oxidize the $Pr_2NiO_{4+\delta}$ so that the phase decomposition occurs [86].

In this section, several approaches used to stabilise $Pr_2NiO_{4+\delta}$ under intermediate temperature operating conditions (500-800°C in air) were reviewed. They can be mainly classified into four categories and they are substituting foreign cations (**Sections 2.6.1-2.6.3**), creating praseodymium deficiency (**Section 2.6.4**), increasing the grain size and introducing the $Pr_2NiO_{4+\delta}$ to an electrolyte backbone by infiltration. The latter two were discussed in **Section 2.6.5**.

2.6.1 Substituting Sr and Ca at the Pr site

It is proposed that substituting strontium and calcium at the praseodymium site can help with increasing the thermal stability of $Pr_2NiO_{4+\delta}$ [52, 87, 88]. This is due to the charge compensation mechanism of the introduced divalent acceptor resulting in an increase of the average nickel valence [52, 88]. Istomin et al. [52] have demonstrated that $Pr_{1.35}Sr_{0.65}Ni_{0.75}Co_{0.25}O_{4\pm\delta}$ is more stable than $Pr_{1.75}Sr_{0.25}Ni_{0.75}Co_{0.25}O_{4\pm\delta}$ as no

decomposition was observed for $Pr_{1.35}Sr_{0.65}Ni_{0.75}Co_{0.25}O_{4\pm\delta}$ after heating the samples at 900°C under oxygen flow for 24 hours. Indeed, Pikalova et al. [88] showed similar results when annealing $Pr_{2-x}Ca_xNiO_{4+\delta}$ (x=0-0.5) at 850°C for 250 hours. They found the formation of secondary phases such as $Pr_4Ni_3O_{10+/-\delta}$, Pr_6O_{11} and NiO for the post-tested samples of x=0 and 0.1 but the rest of the Ca-enriched materials were stable [88].

However, it is important to note that although substituting divalent alkaline earth cations at the praseodymium site can increase material stability and even the electrical conductivity, there is evidence that both D* and k drop with increasing of the substituting level [44, 89, 90].

2.6.2 Substituting La and Nd at the Pr site

Another approach to stabilise the $Pr_2NiO_{4+\delta}$ at the lower temperatures is to substitute either lanthanum or neodymium at the praseodymium site as it is known that $La_2NiO_{4+\delta}$ and $Nd_2NiO_{4+\delta}$ are more thermally stable than $Pr_2NiO_{4+\delta}$ [91]. Vibhu et al. tried to vary the amount of the lanthanum substitution level at the praseodymium site with the attempt to avoid decomposition of $Pr_2NiO_{4+\delta}$ [83, 92]. The proper amount of lanthanum substitution was found to be 1.5 with the chemical formula of $La_{1.5}Pr_{0.5}NiO_{4+\delta}$ as no decomposed product such as perovskite, higher order RP phase and/or praseodymium oxide were detected after one month of thermal treatment between 600°C and 800°C under air [83, 92]. However, the introduction of lanthanum to $Pr_{2-x}La_xNiO_{4+\delta}$ decreased the electrical conductivity and the D* value, reflecting a higher polarization resistance than $Pr_2NiO_{4+\delta}$ at a given operating temperature [83, 93].

With respect to neodymium substitution at the praseodymium site, Dogdibegovic et al. [94] found no phase decomposition after annealing $Nd_{1.5}Pr_{0.5}NiO_{4+\delta}$ at 750°C in air for 2500 hours. A similar tendency of the decrease of electrochemical performance was also observed for neodymium substituted $Pr_{2-x}Nd_xNiO_{4+\delta}$ compared to $Pr_2NiO_{4+\delta}$ [95]. Dogdibegovic et al. [95] showed an increase of polarization resistance for $Pr_{2-x}Nd_xNiO_{4+\delta}$ when more praseodymium was replaced by neodymium.

The most recent research shows that the decomposition of $Pr_2NiO_{4+\delta}$ starts from the oxidation of praseodymium [96]. The introduction of other lanthanide ions such as

neodymium at the praseodymium site has a capacity to suppress praseodymium from oxidation under oxidizing conditions [96].

2.6.3 Substituting Cu or Fe at the Ni site

Substituting of copper and iron at the nickel site was found to change the phase transition/decomposition temperature of $Pr_2NiO_{4+\delta}$ to the higher order $Pr_4Ni_3O_{10+\delta}$ and praseodymium oxide [97]. Copper (Cu^{+2}) and iron (Fe^{+3}) are acting as a substituting cation with lower and higher valence compared to the average valence of nickel [97]. When copper is introduced, it will decrease the average valence at the transition metal site in $Pr_2Ni_{1-x}Cu_xO_{4+\delta}$ and will lead to the reduction of the overall oxygen content (i.e. δ in **Equation 2.1**) [86, 97]. More oxygen (i.e. b in **Equation 2.1**) is then needed for the decomposition process to occur [86]. Hence, it was found that $Pr_2Ni_{1-x}Cu_xO_{4+\delta}$ has a lower phase transition temperature (800°C) compared to $Pr_2NiO_{4+\delta}$ (900°C) in air [97]. The oxygen non-stoichiometry (δ) of $Pr_2Ni_{0.8}Cu_{0.2}O_{4+\delta}$ was measured to be 0.116 at around 927°C in air and this was compared with 0.148 for $Pr_2NiO_{4+\delta}$ at the same measuring condition [97]. The decrease of oxygen content was also observed in $Nd_2NiO_{4+\delta}$ when substituting divalent copper at the nickel site [98]. On the other hand, iron substitution has an opposite impact due to the fact that it increases the oxygen content of $Pr_2Ni_{1-x}Fe_xO_{4+\delta}$ and the phase transition temperature was reported to be higher (950°C) in air [86, 97].

2.6.4 Praseodymium deficiency

Several researchers have shown that praseodymium and neodymium deficiency in n=1 RP phase would reduce the oxygen content when comparing to their primitive chemical compositions [70, 86, 99]. As suggested **Equation 2.1**, this might be beneficial in terms of improving n=1 praseodymium nickelate RP phase thermal stability at lower temperature range because more oxygen will then be required to oxidise the n=1 praseodymium nickelate [86]. This was demonstrated by Xue et al. [86] experiment when thermally heating both $(Pr_{0.9}La_{0.1})_{2.0}Ni_{0.74}Cu_{0.21}Ga_{0.05}O_{4+\delta}$ ($(PL)_{2.0}NCG$) and $(PL)_{1.9}NCG$ sintered pellets at 900°C for up to 10 hours in air. $(PL)_{1.9}NCG$ was observed to have less amount of n=3 praseodymium nickelate RP phase formed at any given amount of heating time [86].

However, Ning et al. [100] proved that the introduction of praseodymium deficiency in $Pr_{2-x}NiO_{4+\delta}$ (x=0-0.2) would not change the content of oxygen interstitial in the rock salt layer but it increased the oxygen vacancy concentration in the perovskite layer. Ning et al. [100] also observed the nearly complete decomposition of $Pr_{2-x}NiO_{4+\delta}$ (x=0-0.2) when heating from 580°C to 800°C in air. The decomposition rate constant (assuming first order reaction) of various $Pr_{2-x}NiO_{4+\delta}$ had no apparent difference at a given temperature [100]. This suggests that incorporating praseodymium deficiency have little impact on improving the thermal stability of $Pr_2NiO_{4+\delta}$. Therefore, the thermal stability improvement observed by Xue et al. [86] should be attributed to the other factor such as relatively larger grain size observed from $(PL)_{1.9}NCG$ sintered pellet compared to the one of $(PL)_{2.0}NCG$ as $(PL)_{1.9}NCG$ had a greater sinterability. The effect of grain size on $Pr_2NiO_{4+\delta}$ thermal stability is discussed next.

2.6.5 Other approaches

Apart from different types of substitution strategy to improve the thermodynamic stability of $Pr_2NiO_{4+\delta}$, it is also proposed that the issue can be resolved kinetically [86]. For example, by calcining at a higher temperature for a given amount of time, the final sample with larger grain size or in sintered ceramics form tends to be more resistant to the decomposition process (e.g. lower amount of high order RP phase was observed) than the reference sample with smaller grain size or in powder form, respectively [86, 100]. This might be due to the fact that the decomposition process starts at the grain boundary/powder surface where cation diffusion is kinetically favorable [86, 100].

Railsback et al. [101] found that $Pr_2NiO_{4+\delta}$ is more stable when being infiltrated on a LSGM scaffold. When aging the $Pr_2NiO_{4+\delta}$ powder and the infiltrated $Pr_2NiO_{4+\delta}$ separately at 650°C under air for 100 hours, $Pr_4Ni_3O_{10+/-\delta}$ and Pr_6O_{11} were detected for the first case [101]. On the other hand, the latter case showed minor changes in the phase before and after the aging process [101]. These results can be explained by the physical constraint imposed by the LSGM scaffold adjacent to the infiltrated $Pr_2NiO_{4+\delta}$. It limited the $Pr_2NiO_{4+\delta}$ phase transformation [101]. Since phase transformation usually includes volume change and/or distortion, it is much more difficult for the infiltrated $Pr_2NiO_{4+\delta}$ decomposition to proceed [101]. The other explanation for the improved stability results for the infiltrated $Pr_2NiO_{4+\delta}$ might be the possible lanthanum,

strontium and/or gallium cation diffusion from LSGM, although it was not confirmed by Railsback et al. [101].

Although the methods proposed above tend to contribute to a higher thermal stability of $Pr_2NiO_{4+\delta}$ at temperatures below 900°C under air/oxygen, they all have some disadvantages that require further consideration. For example, substitution of strontium should be avoided for possible strontium segregation observed in LSM and LSCF [34]. As mentioned before, material properties such as D* and k are also compromised when substituting strontium and calcium at the praseodymium site of $Pr_2NiO_{4+\delta}$. Partially replacing praseodymium by lanthanum and neodymium looks promising in terms of the demonstrated long term (relatively) phase stability of the materials but they suffer from higher polarization resistance. In addition, substituting copper at the nickel site can only extend the lower boundary of $Pr_2NiO_{4+\delta}$ thermodynamic stability to 800°C in air which is the upper boundary of the intermediate temperature SOC operation range. With respect to the kinetic approaches such as increasing the grain size and infiltration of $Pr_2NiO_{4+\delta}$ on LSGM, the long term stability of the material is in doubt.

2.7 The derived products from the chemical reactions related to $Pr_2NiO_{4+\delta}$

Alternatively, considering that the intermediate temperature operating conditions are between 500°C and 800°C in air, it would be interesting to investigate the properties and the electrochemical performance of the products of the $Pr_2NiO_{4+\delta}$ decomposition reaction, which are $Pr_4Ni_3O_{10+/-\delta}$, $PrNiO_{3-\delta}$ and Pr_6O_{11} [83]. Vibhu et al. [83, 92] found the full decomposition of $Pr_2NiO_{4+\delta}$ after aging the symmetrical cell with the configuration of $Pr_2NiO_{4+\delta}$/CGO/YSZ at 700°C and 600°C under air for one month. With respect to the electrode performance, the electrode resistance (the distance between the two furthest Re(Z) intercepts of each set of data in Nyquist plots, **Figure 2.9(a)**) measured in open circuit condition increased from 0.03 Ωcm^2 to 0.045 Ωcm^2 before and after aging at 700°C for one month in air [83, 92]. **Figure 2.9(b)** shows the corresponding Bode plots which illustrate the formation of an extra peak (P3) over time [83, 92]. The introduction of a Nyquist plot and a Bode plot can be found in **Section 3.4.5.1**. This additional peak (P3) not only shows the change of air electrode reaction but it also demonstrates the dissociation of $Pr_2NiO_{4+\delta}$ [83, 92]. The relatively

small electrode resistance value after the full decomposition of $Pr_2NiO_{4+\delta}$ might suggest that the decomposed products are still catalytically active to the air electrode reaction [83, 92]. Therefore, the evaluation of each decomposed product might help with identifying a more thermally stable material with a comparable electrochemical performance to $Pr_2NiO_{4+\delta}$ for the SOC air electrode.

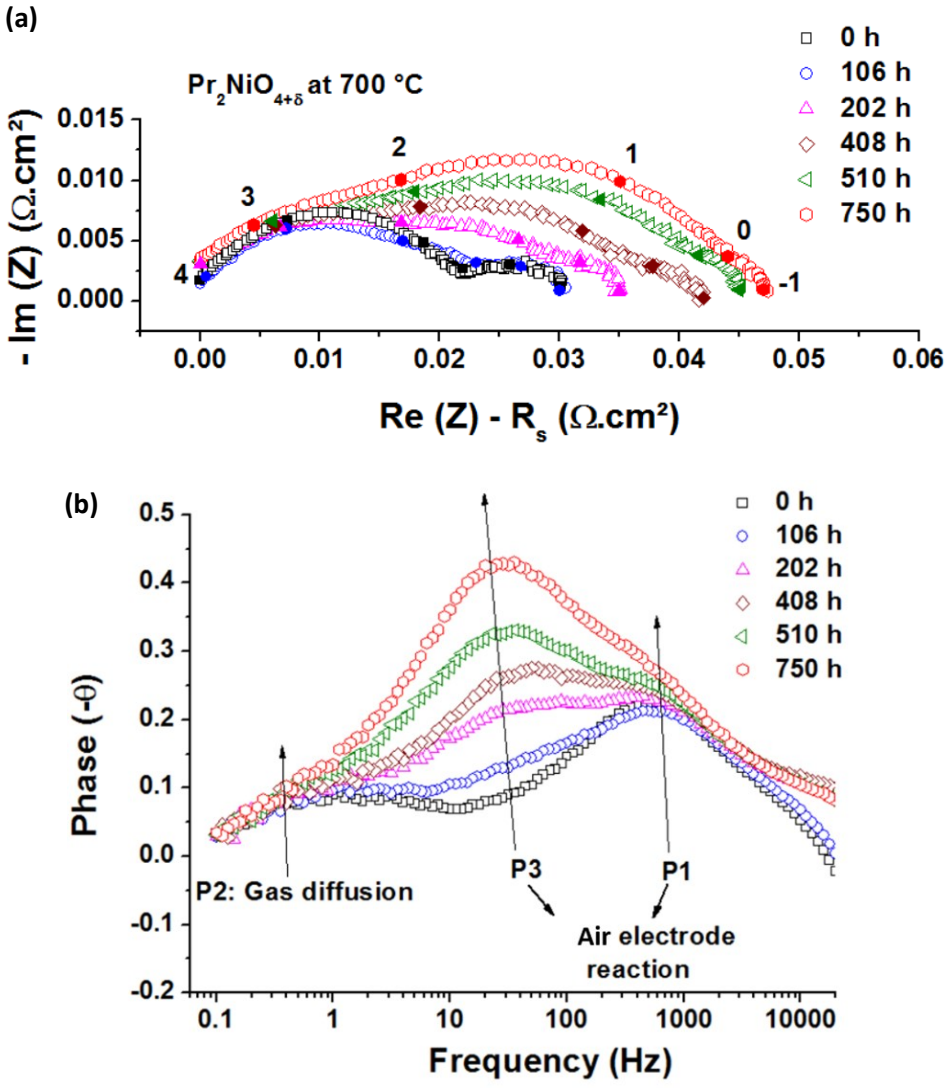


Figure 2.9: **(a)** Nyquist plot and **(b)** Bode plot for the symmetrical cell ($Pr_2NiO_{4+\delta}$/CGO/YSZ) aged for one month at 700°C in air. Adapted from [92] with kind permission from IOP Publishing.

2.7.1 $Pr_4Ni_3O_{10+/-\delta}$ and $PrNiO_{3-\delta}$

Vibhu further fabricated symmetrical cells with the same configuration as before but using different decomposed products such as $Pr_4Ni_3O_{10+\delta}$ and $PrNiO_{3-\delta}$ [83, 102, 103].

He then compared the electrode resistance measured in open circuit condition [83, 102, 103]. The results indicated that $Pr_4Ni_3O_{10+\delta}$ is a promising candidate for the air electrode as its electrode resistance value of 0.16 Ωcm^2 at 600°C in air was almost the same as the one for $Pr_2NiO_{4+\delta}$ (0.15 Ωcm^2 at the same measuring condition) [83, 102]. On the other hand, the electrode resistance value of $PrNiO_{3-\delta}$ was 0.91 Ωcm^2 at 600°C in air which is much larger [83, 103]. Hence, further research on the material properties of $Pr_4Ni_3O_{10+/-\delta}$ was undertaken.

The thermal stability of $Pr_4Ni_3O_{10+/-\delta}$ was first examined and no decomposition was observed when annealing the powder at different temperatures from 600°C to 800°C under air for one month [83, 102]. The upper temperature boundary for the phase stability was also verified using thermogravimetric analysis (TGA) and the formation of $Pr_2NiO_{4+\delta}$ and NiO was observed after heating at temperatures greater than 1050°C and 1120°C under air and oxygen, respectively [83, 102]. However, Vibhu et al. [83, 102] suggested that when considering the kinetic impact on the phase transformation which might be due to instrumental or sample effects, the confirmed temperatures for long term $Pr_4Ni_3O_{10+\delta}$ phase stability were 950°C under air and 1000°C under oxygen.

With respect to the oxygen content, Vibhu et al. [83, 102] found that $Pr_4Ni_3O_{10+\delta}$ always shows an oxygen hyper-stoichiometry at different temperatures (measured from room temperature to 800-1000°C) under air, oxygen and even argon. However, these results are inconsistent with those reported by Zhang et al. [104] and with the other higher order RP phases such as $La_4Ni_3O_{10-\delta}$ that usually shows oxygen hypo-stoichiometry [51]. Based on Vibhu et al.'s results [83, 102], the oxygen content of $Pr_4Ni_3O_{10+\delta}$, decreased with the increase of temperature and the oxygen content under oxygen condition will be slightly higher than the oxygen content in air and argon for a given temperature. The TGA results showed that the oxygen content at room temperature under argon, air and oxygen are 10.07(δ=0.07), 10.10 (δ=0.10) and 10.14 (δ=0.14), respectively [83, 102]. This is compared with the $Pr_2NiO_{4+\delta}$ oxygen content of δ=0.22 at room temperature [79].

In addition, both electrical conductivity and TEC seem to be acceptable for $Pr_4Ni_3O_{10+\delta}$ according to the general criteria for air electrode materials selection in **Section 1.3.1**.

$Pr_4Ni_3O_{10+\delta}$ exhibits a metallic behavior of electrical conductivity and the conductivity value decreases with increasing temperature [83, 102, 105]. The reported electrical conductivity at 600°C and 800°C was 90 Scm^{-1} and 85 Scm^{-1}, respectively but it is important to note that these values are likely to be underestimated as the samples were not fully densified [83, 102]. The density of the samples used in this case was only 70% [83, 102]. In terms of TEC, it was found to be 10 x 10^{-6} K^{-1} between room temperature and 1000°C in air and this was comparable to the TEC of the conventional electrolytes [83, 102]. Since there was no abrupt structure phase transition observed in the corresponding XRD data measuring at the same conditions, the TEC was constant at any given temperature in between [83, 102]. Less thermo-mechanical stress between $Pr_4Ni_3O_{10+\delta}$ air electrode and an electrolyte would therefore be expected, especially under thermal cycling [106].

The attempt to measure the D* and k values of $Pr_4Ni_3O_{10+\delta}$ was conducted in order to have a better understating of the oxygen ionic conductivity of the material [83]. However, they were about one order of magnitude lower than $Pr_2NiO_{4+\delta}$ at 600°C in pO_2=0.21 bar [83, 93]. Considering the as mentioned oxygen non-stoichiometry of $Pr_2NiO_{4+\delta}$ and $Pr_4Ni_3O_{10+\delta}$, $Pr_4Ni_3O_{10+\delta}$ had a much lower oxygen ionic conductivity than $Pr_2NiO_{4+\delta}$. However, it is reasonable to conjecture that $Pr_4Ni_3O_{10+/-\delta}$ is a better electronic conductor than $Pr_2NiO_{4+\delta}$ as $Pr_4Ni_3O_{10+/-\delta}$ possess more perovskite layers. NiO_6 octahedra in the perovskite layers were known to be responsible for the electronic conductivity [20, 51].

Therefore, a material with dominant oxygen ionic conductivity is required to compensate the shortcoming of $Pr_4Ni_3O_{10+/-\delta}$. It is important to note that the CGO interlayer was used in Vibhu et al.'s experiments [83, 92, 102]. Therefore, the impact of CGO should be considered.

2.7.2 $Ce_{1-x-y}Gd_xPr_yO_{2-\delta}$ (CGPO)

Although no CGPO formation is confirmed in the previous discussion of the chemical reactivity between $Pr_2NiO_{4+\delta}$ and CGO (**Section 2.5.5**), Laguna-Bercero et al. [107] observed its presence after mixing $Pr_2NiO_{4+\delta}$ and CGO powder and annealing the two mixtures for 2 hours in air at 1100°C and 1120°C, respectively. It was suggested that the praseodymium diffused into the substituted ceria structure as the lattice

parameter of the substituted ceria decreased after the heat treatments [107]. The other evidence for the praseodymium diffusion was the formation of NiO as a secondary phase [107]. Laguna-Bercero et al. [107] did not identify the composition of the final CGPO phase but they suggested that the formation of CGPO might contribute to the performance improvement of a SOFC cell (with the configuration of $Pr_2NiO_{4+\delta}$/$Pr_2NiO_{4+\delta}$-CGO/YSZ/Ni-YSZ) over time due to its expected high oxygen diffusivity. Indeed, a promising cell performance was received when operating the same tubular cell in SOEC mode and this gave the highest reported current densities of 800 $mAcm^{-2}$ at 1.3V, 800°C in microtubular electrolysis cells [107, 108].

In Vibhu's work [83], the chemical reaction between $Pr_2NiO_{4+\delta}$ and CGO interlayer was also observed at the interface for the electrodes operated under SOEC and SOFC modes on each side of the symmetrical cell as the new secondary phase had a brown color. The author suspected that that this is the result of the praseodymium diffusion to CGO interlayer but no direct evidence was given [83]. Such secondary phase might be formed under the electrode sintering process at high temperature (e.g. 1150°C for 1 hour) but further investigation is required to confirm this [83].

Moreover, CGPO with the composition of $Ce_{0.75}Gd_{0.05}Pr_{0.20}O_{2-\delta}$ was investigated as the SOC air electrode by Chockalingam et al. [109]. However, they concluded that the electronic conductivity, which originates from the introduction of impurity bands in the ceria band gap by praseodymium, was low and it limited the performance of the air electrode, despite the promising oxygen ionic conductivity (greater than 0.02 Scm^{-1} at 700°C in air) [109]. Based on the simulation results from Dholabhai et al. [110], it was found that for a given amount of total substituting level, double substituting of praseodymium and gadolinium will have a higher oxygen ionic conductivity than the single substituted ceria. This is due to the fact that the number of minimum energy pathways for oxygen diffusion is increased for the double substituting case [110]. They suggested that the highest oxygen ionic conductivity can be reached between 600°C and 800°C when the total substitution amount of praseodymium and gadolinium did not exceed 25 mol.% [110]. Within 25 mol.% of substituting composition, including 25% of praseodymium (Gd-rich CGPO) will provide higher oxygen ionic conductivity than having 50% (equal Gd-Pr CGPO) and 75% (Pr-rich CGPO) of praseodymium at the

different temperatures [110]. The simulated Gd-rich CGPO results qualitatively agree with the experimental results when replacing gadolinium with a small amount of praseodymium and the enhancement of the oxygen ionic conductivity was also confirmed when co-substituting different amounts of praseodymium in $Ce_{0.9-x}Gd_{0.1}Pr_xO_{3-\delta}$ with x ranging from 0-0.4 [110-113].

2.7.3 PrO_x and NiO

Praseodymium oxide (PrO_x) is a popular rare earth metal oxide catalyst used to enhance the electrochemical activity of an air electrode [44, 80, 114-117]. This is usually achieved by infiltrating PrO_x at the surface of existing air electrode materials which are limited by the surface exchange reaction such as $La_2Ni_{0.8}Cu_{0.2}O_{4+\delta}$, $LaNi_xFe_{1-x}O_{3-\delta}$ and LSM-CGO [44, 80, 114-117]. For example, Navarrete et al. [115] tried infiltrating different metal oxides, including Pr, Sm, Ce, Zr, Ba and Co oxide, on the surface of the LSM-CGO composite electrode and found that infiltrated PrO_x boosted the oxygen dissociation and adsorption processes of the composite electrode and provided the best electrochemical performance when compared to other infiltrated oxides.

In addition, the electrode performance of the infiltrated PrO_x was compared with the infiltrated $Pr_2NiO_{4+\delta}$, NiO, $La_2NiO_{4+\delta}$, $Sm_{0.5}Sr_{0.5}CoO_{3-\delta}$ and $La_{0.6}Sr_{0.4}CoO_{3-\delta}$ on the gadolinium/samarium substituted ceria backbones (CGO/ CSO) as illustrated in **Figure 2.10** [118]. It is surprising to see that CGO infiltrated with Pr_6O_{11} provided the best result at temperatures between 400°C and 600°C although the electrical conductivity of PrO_x is as low as 1.3 Scm^{-1} at 600°C [118]. The promising result for PrO_x can be attributed to the reported high oxygen surface exchange coefficient ($5.4x10^{-7} \pm 0.1x10^{-7}$ cms^{-1}) and high oxygen diffusion coefficient ($3.4x10^{-8} \pm 0.1x10^{-8}$ cm^2s^{-1}) at 600°C and pO_2 of 210 mbar [118]. It is believed that the mix of praseodymium valence (+3/+4) is beneficial to oxygen reduction/evolution reaction in the air electrode [118].

Figure 2.11 compares the overall oxygen surface exchange rates between $PrNiO_3$, $Pr_2NiO_{4+\delta}$, $Pr_4Ni_3O_{10+\delta}$, Pr_6O_{11} and $La_2NiO_{4+\delta}$ at different temperatures under $pO_2 = 0.21$ bar [119]. It is important to note that most of the data in **Figure 2.11** were collected at temperatures lower than 600°C, except for La_2NiO_4. As expected, $PrNiO_3$ and $La_2NiO_{4+\delta}$ have relatively low oxygen surface exchange rates when compared with the

other three compositions. However, it is surprising to find that the oxygen surface exchange rates are higher for $Pr_4Ni_3O_{10+\delta}$ than $Pr_2NiO_{4+\delta}$ and even Pr_6O_{11}. It is believed that the results here is more reliable compared to Vibhu's results discussed previously as pulse isotopic exchange was used to measure the overall oxygen surface exchange rate of each powder sample rather than using a sintered pellet [83, 119]. Therefore, the issue of secondary phases remaining after the sintering process in $Pr_4Ni_3O_{10+\delta}$ is less likely to occur [83].

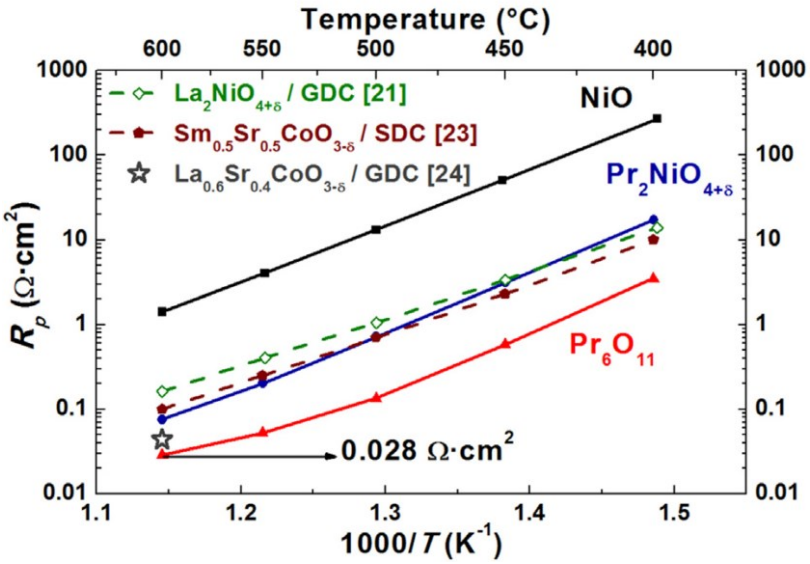


Figure 2.10: The electrochemical performance comparisons between NiO, $Pr_2NiO_{4+\delta}$, Pr_6O_{11}, $La_2NiO_{4+\delta}$, $Sm_{0.5}Sr_{0.5}CoO_{3-\delta}$ and $La_{0.6}Sr_{0.4}CoO_{3-\delta}$ when they are infiltrated on a CGO or CSO backbones. The CGO and CSO are presented as GDC and SDC, respectively in the original paper. The references are also corresponding to the ones in the original paper. Reproduced from [118] with kind permission from Elsevier.

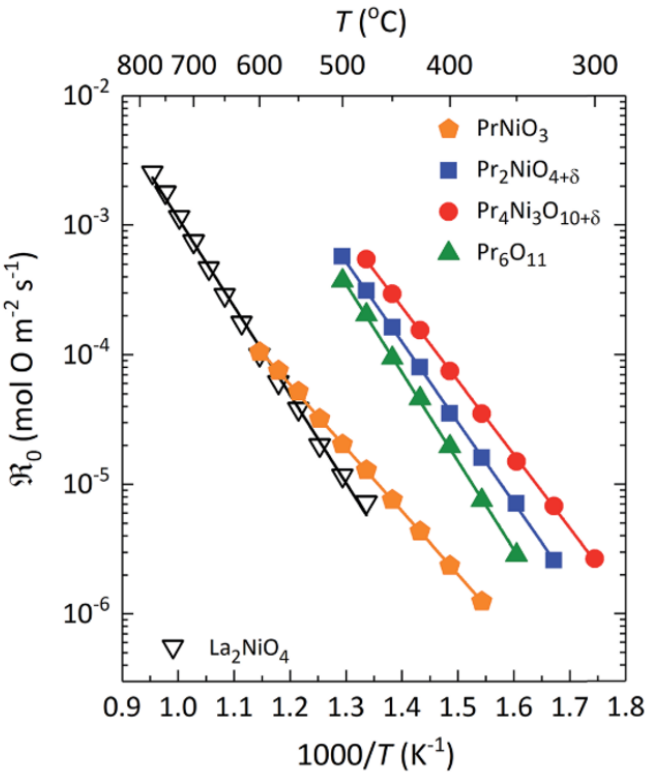


Figure 2.11: The overall surface exchange rate comparison between $PrNiO_3$, $Pr_2NiO_{4+\delta}$, $Pr_4Ni_3O_{10+\delta}$, Pr_6O_{11} and $La_2NiO_{4+\delta}$ at various temperatures under $pO_2 = 0.21$ atm. Adapted from [119] with kind permission from Royal Society of Chemistry.

On the other hand, NiO is usually expected as a highly resistive secondary phase and this is clearly demonstrated in **Figure 2.10** [118]. Hence, NiO should not contribute to the promising electrode performance after $Pr_2NiO_{4+\delta}$ air electrode was fully decomposed.

2.8 Effective medium percolation theory

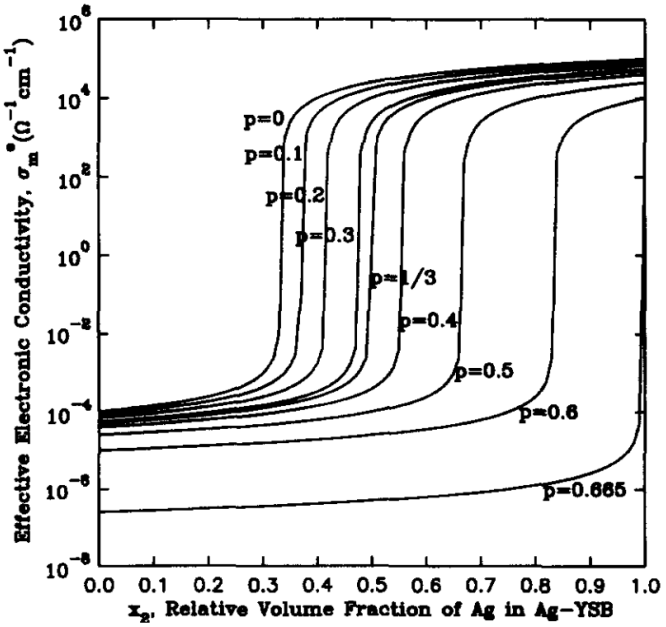
When a composite electrode is used, effective medium percolation theory (EMPT) helps with understanding the percolated network of each phase, given that one phase has a higher electronic or oxygen ionic conductivity than the other phases [120, 121]. This is achieved by solving σ_m, the effective conductivity of a porous solid, in **Equation 2.2** [120, 121]. Z is the coordination number and is equal to six in a three-dimensional composite [120, 121]. σ_k and p_k are the porous-free conductivity of phase k and the volume fraction of phase k in the system [120, 121]. The sum of each phase volume fraction should equal to one and pores should be considered as one phase in the

system with its σ_k equal to zero [120, 121]. It is worth mentioning that the calculation can only be conducted when the porous-free conductivities of each phase, including electronic and oxygen ionic conductivities, are known or can be predicted [120, 121].

$$\sum_k \frac{\sigma_m - \sigma_k}{\left(\frac{Z}{2}-1\right)\sigma_m + \sigma_k} p_k = 0 \qquad \textbf{Equation 2.2}$$

Equation 2.2 can be used to calculate the effective electronic and oxygen ionic conductivity with various volume fractions of each phase as shown in **Figure 2.12(a)** and **(b)** [121]. The vertical lines in the figures represent the percolation limit which depends on pore volume fractions (p) [121]. The amount of the target phase (Ag) in **Figure 2.12(a)** and **Figure 2.12(b),** compared to the counter phase of yttria-stabilised bismuth oxide (YSB), needs to be beyond or below this point in order to form an electronically or ionically conducting percolated network in the system, respectively [121].

(a)



(b)

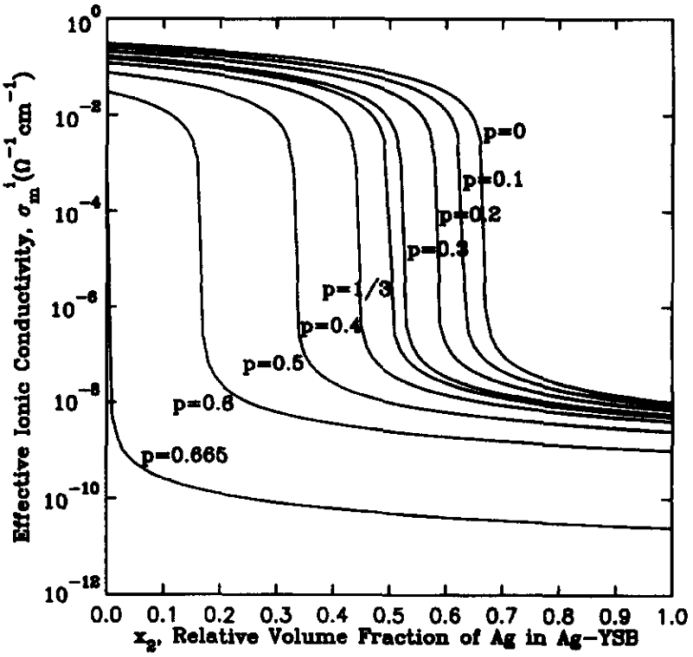


Figure 2.12: The calculated results of effective electronic conductivity **(a)** and effective ionic conductivity **(b)** in a porous Ag-YSB composite using the EMPT approach. Reproduced from [121] with kind permission from Elsevier.

Ambipolar conductivity is an important parameter which considers both the impact of the effective electronic conductivity and the effective oxygen ionic conductivity on the overall transport properties in the system [120, 121]. If there is no interaction between electronic and oxygen ionic charge carriers, then ambipolar conductivity can be estimated by **Equation 2.3** where $\sigma_e^{eff.}$ and $\sigma_i^{eff.}$ are the effective electronic conductivity and the effective oxygen ionic conductivity calculated from **Equation 2.2** [120, 121].

$$\sigma_{amp} = \sigma_e^{eff.}\sigma_i^{eff.}/(\sigma_e^{eff.} + \sigma_i^{eff.}) \qquad \textbf{Equation 2.3}$$

It is important to note that although EMPT can be used to calculate the percolation limit of each transport property, it does not consider the electrode catalytic activity and the possible gas transport limitation which will also have an impact on the final composite electrode performance [120].

2.9 Summary

Several different air electrode and electrolyte key materials were reviewed in this chapter. The fuel electrode materials, on the other hand, was introduced briefly for completeness. Both 10Sc1CeSZ and $Pr_2NiO_{4+\delta}$ were found to be promising electrolyte and air electrode material candidates when operating solid oxide cells in the intermediate temperature range of 500-800°C. Despite the promising physical properties and electrochemical properties of $Pr_2NiO_{4+\delta}$, the material was found to decompose at temperature below 900°C in air. To stabilise the material, several strategies were proposed but most compromise overall performance and introduce uncertainty in long term device performance. Interestingly, the decomposition products of $Pr_2NiO_{4+\delta}$ such as $Pr_4Ni_3O_{10+/-\delta}$, $PrNiO_{3-\delta}$ and PrO_x, and its chemical reaction with a proposed CGO barrier layer forming CGPO and NiO, have a high electrocatalytic activity towards oxygen reduction/evolution reaction in the air electrode. Therefore, making a composite electrode from these materials based on the EMPT is a promising way of developing a new air electrode which is stable and has high performance. Previous research has proven the potential of using $Pr_4Ni_3O_{10+/-\delta}$, PrO_x and CGPO as air electrode materials. It is of interest to mix $Pr_4Ni_3O_{10+/-\delta}$, the dominant electronic conductor, with high oxygen ionic conductive CGPO in particular and investigate their air electrode performance. Making a composite electrode with $Pr_4Ni_3O_{10+/-\delta}$ and PrO_x is of less interest due to the higher oxygen surface exchange rate of $Pr_4Ni_3O_{10+/-\delta}$ suggesting that the surface exchange reaction is less likely to be a rate limited process in the whole air electrode reaction.

References

[1] F. Wang, Y. Lyu, D. Chu, Z, Jin, G. Zhang, D. Wang, *Materials Science and Technology,* 35, 1551-1562, 2019.

[2] H. G. Scott , *Journal of Materials Science,* 10, 1527-1535, 1975.

[3] N. Preux, A. Rolle, R. N. Vannier, "Electrolytes and ion conductors for solid oxide fuel cells (SOFCs),"in *Functional materials for sustainable energy applications*, Editors: J. A. Kilner , S. J. Skinner, S. J. C. Irvine, P. P. Edwards, Cambridge, UK, Woodhead Publishing Limited, 370-401, 2012.

[4] A. R. West, "Basic Solid State Chemistry", Second Edition, Chichester, UK, John Wiley & Sons, Ltd, 1999.

[5] Y. Arachi, H. Sakai, O. Yamamoto, Y. Takeda, N. Imanishai, *Solid State Ionics ,* 121, 133-139, 1999.

[6] J. W. Fergus, *Journal of Power Sources,* 162, 30-40, 2006.

[7] C. N. Shyam Kumar, R. Bauri, *Journal of Physics and Chemistry of Solids,* 75, 642-650, 2014.

[8] "Database of Ionic Radii," Atomistic Simulation Group in Materials Department of Imperial College. Available: http://abulafia.mt.ic.ac.uk/shannon/ptable.php.

[9] S. Y. Gómez, D. Hotza, *Renewable and Sustainable Energy Reviews,* 61, 155-174, 2016.

[10] A. A. Jais, S. A. Muhammed Ali, M. Anwar, M. Rao Somalu, A. Muchtar, W. N. R. Wan Isahak, C. Y. Tan, R. Singh, N. P. Brandon, *Ceramics International,* 43, 8119-8125, 2017.

[11] M. A. Laguna-Bercero, S. J. Skinner, J. A. Kilner, *Journal of Power Sources,* 192, 126-131, 2009.

[12] S. Zhu, Y. Wang, Y. Rao, Z. Zhan, C. Xia, *International Journal of Hydrogen Energy,* 39, 12440-12447, 2014.

[13] T. Ishihara, H. Matsuda, Y. Takita, *Journal of the American Chemical Society,* 116, 3801-3803, 1994.

[14] M. Feng, J. B. Goodenough, *European Journal of Solid State and Inorganic Chemistry,* 31, 663-672, 1994.

[15] K. Huang, J. B. Goodenough, *Journal of Alloys and Compounds,* 303-304, 454-464, 2000.

[16] L. Zhang, S. Hu, X. Zhu, W. Yang, *Journal of Energy Chemistry,* 26, 593-601, 2017.

[17] X. Zhang, Y. Song, G. Wang, X. Bao, *Journal of Energy Chemistry,* 26, 839-853, 2017.

[18] N. Mahato, A. Banerjee, A. Gupta, S. Omar, K. Balani, *Progress in Materials Science,* 72, 141-337, 2015.

[19] S. W. Tao, P. I. Cowin, R. Lan, "Novel anode materials for solid oxide fuel cells,"in *Functional Materials for Sustainable Energy Applications*, Editors: J. A. Kilner, S. J. Skinner, S. J. C. Irvine, P. P. Edwards, Cambridge, UK, Woodhead Publishing Limited, 445-477, 2012.

[20] J. C. Grenier, J. M. Bassat, F. Mauvy, "Novel cathodes for solid oxide fuel cells,"in *Functional materials for sustainable energy applications*, Editors: J. A. Kilner, S. J. Skinner, S. J. C. Irvine, P. P. Edwards, Cambridge, UK, Woodhead Publishing Limited, 402-444, 2012.

[21] H. U. Anderson, *Solid State Ionics ,* 52, 33-41, 1992.

[22] I. Yasuda, M. Hishinuma, *Journal of Solid State Chemistry,* 123, 382-390, 1996.

[23] S. P. Jiang, J. Li, "Cathodes,"in *Solid Oxide Fuel Cells: Materials Properties and Performance*, Editors: J. W. Fergus, R. Hui, X. Li, D. P. Wilkinson, J. Zhang, Boca Raton, USA, CRC Press Taylor & Francis Group, 131-177, 2009.

[24] W. Wang, S. P. Jiang, *Solid State Ionics ,* 177, 1361-1369, 2006.

[25] G. J. la O', R. F. Savinell, Y. Shao-Horn, *Journal of The Electrochemical Society,* 156, B771-B781, 2009.

[26] J.-D. Kim, G.-D. Kim, J.-W. Moon, Y.-I. Park, W.-H. Lee, K. Kobayashi, M. Nagai, C.-E. Kim, *Solid State Ionics,* 143, 379-389, 2001.

[27] C.-C. T. Yang, W.-C. J. Wei, A. Roosen, *Materials Chemistry and Physics,* 81, 134-142, 2003.

[28] C. Sun, R. Hui, J. Roller, *Journal of Solid State Electrochemistry,* 14, 1125-1144, 2010.

[29] M. Gödickemeier, K. Sasaki, L. J. Gauckler, I. Riess, *Solid State Ionics,* 86-88, 691-701, 1996.

[30] T. Kawada, K. Masuda, J. Suzuki, A. Kaimai, K. Kawamura, Y. Nigara, J. Mizusaki, H. Yugami, H. Arashi, N. Sakai, H. Yokokawa, *Solid State Ionics,* 121, 271-279, 1999.

[31] Y. Takeda, R. Kanno, M. Noda, Y. Tomida, O. Yamamoto, *Journal of The Electrochemical Society,* 134, 2565-2661, 1987.

[32] N. H. Menzler, F. Tietz, S. Uhlenbruck, H. P. Buchkremer, D. Stover, *Journal of Materials Science,* 45, 3109-3135, 2010.

[33] A. Jun, J. Kim, J. Shin, G. Kim, *ChemElectroChem,* 3, 511-530, 2016.

[34] K. Chen, S. P. Jiang, *Journal of The Electrochemical Society,* 163, F3070-F3083, 2016.

[35] M. Sahibzada, B. C. H. Steele, K. Zheng, R. A. Rudkin, I. S. Metcalfe, *Catalysis Today,* 38, 459-466, 1997.

[36] Y. Takeda, H. Ueno, N. Imanishi, O. Yamamoto, N. Sammes, M. B. Phillipps, *Solid State Ionics,* 86-88, 1187-1190, 1996.

[37] C. Xia, W. Rauch, F. Chen, M. Liu, *Solid State Ionics,* 149, 11-19, 2002.

[38] Y. Tian, W. Wang, Y. Liu, L. Zhang, L. Jia, J. Yang, B. Chi, J. Pu, J. Li, *ACS Applied Energy Materials ,* 2, 3297-3305, 2019.

[39] A. Yan, M. Cheng, Y. Dong, W. Yang, V. Maragou, S. Song, P. Tsiakaras, *Applied Catalysis B: Environmental,* 66, 64-71, 2006.

[40] H. Zhao, Q. Li, L. Sun, *Science China Chemistry,* 54, 898-910, 2011.

[41] L. Wang, R. Merkle, J. Maier, T. Acartürk, U. Starke, *Applied Physics Letters,* 94, 071908, 2009.

[42] E. Bucher, A. Egger, G. B. Caraman, W. Sitte, *Journal of The Electrochemical Society,* 155, B1218-B1224, 2008.

[43] A. Tarancon, M. Burriel, J. Santiso, S. Skinner, J. Kilner, *Journal of Materials Chemistry,* 20, 3799-3813, 2010.

[44] S. J. Skinner, S. Cook, J. A. Kilner, "Materials for Next Generation SOFCs,"in *Solid Oxide Fuel Cells: Facts and Figures (Past, Present and Future Perspectives for SOFC Technologies)*, Editors: J. T. S. Irvine, P. Connor, London, UK, Springer, 181-202, 2013.

[45] A. A. Taskin, A. N. Lavrov, Y. Ando, *Applied Physics Letters,* 86, 091910, 2005.

[46] A. Tarancón, S. J. Skinner, R. C. Chater, F. Hernández-Ramírez, J. A. Kilner, *Journal of Materials Chemistry,* 17, 3175-3181, 2007.

[47] J.-H. Kim, F. Prado, A. Manthiram, *Journal of The Electrochemical Society,* 155, B1023-B1028, 2008.

[48] C. Zhu, X. Liu, C. Yi, D. Yan, W. Su, *Journal of Power Sources,* 185, 193-196, 2008.

[49] Q. Zhou, T. He, Y. Ji, *Journal of Power Sources,* 185, 754-758, 2008.

[50] Q. Zhou, F. Wang, Y. Shen, T. He, *Journal of Power Sources,* 195, 2174-2181, 2010.

[51] G. Amow, I. J. Davidson, S. J. Skinner, *Solid State Ionics,* 177, 1205-1210, 2006.

[52] S. Ya. Istomin, O. M. Karakulina, M. G. Rozova, S. M. Kazakov, A. A. Gippius, E. V. Antipov, I. A. Bobrikov, A. M. Balagurov, A. A. Tsirlin, A. Michau, J. J. Biendicho, G. Svensson, *RSC Advances,* 6, 33951-33958, 2016.

[53] H. Tamura, A. Hayashi, Y. Ueda, *Physica C: Superconductivity,* 258, 61-71, 1996.

[54] Y. Toyosumi, H. Ishikawa, K. Ishikawa, *Journal of Alloys and Compounds,* 408-412, 1200-1204, 2006.

[55] E. Niwa, K. Wakai, T. Hori, K. Yashiro, J. Mizusaki, T. Hashimoto, *Thermochimica Acta,* 575, 129-134, 2014.

[56] M. Yashima, N. Sirikanda, T. Ishihara, *Journal of the American Chemical Society,* 132, 2385-2392, 2010.

[57] M. Yashima, M. Enoki, T. Wakita, R. Ali, Y. Matsushita, F. Izumi, T. Ishihara, *Journal of the American Chemical Society,* 130, 2762-2763, 2008.

[58] A. Chroneos, D. Parfitt, J. A. Kilner, R. W. Grimes, *Journal of Materials Chemistry,* 20, 266-270, 2010.

[59] D. Parfitt, A. Chroneos, J. A. Kilner, R. W. Grimes, *Physical Chemistry Chemical Physics,* 12, 6834-6836, 2010.

[60] J. C. Grenier, F. Mauvy, C. Lalanne, J.-M. Bassat, F. Chauveau, J. Mougin, J. Dailly, M. Marrony, *ECS Transactions,* 25, 2537-2546, 2009.

[61] T. Nakamura, K. Yashiro, K. Sato, J. Mizusaki, *Solid State Ionics,* 180, 1406-1413, 2009.

[62] T. Nakamura, K. Yashiro, K. Sato, J. Mizusaki, *Solid State Ionics,* 181, 292-299, 2010.

[63] J.-C. Grenier, M. Pouchard, A. Wattiaux, *Current Opinion in Solid State and Materials Science,* 1, 233-240, 1996.

[64] A. Aguadero, J. A. Alonso, M. J. Martínez-Lope, M. T. Fernández-Díaz, M. J. Escudero, L. Daza, *Journal of Materials Chemistry,* 16, 3402-3408, 2006.

[65] M. Al Daroukh, V. V. Vashook, H. Ullmann, F. Tietz, I. Arual Raj, *Solid State Ionics,* 158, 141-150, 2003.

[66] H. Ullmann, N. Trofimenko, F. Tietz, D. Stöver, A. Ahmad-Khanlou, *Solid State Ionics,* 138, 79-90, 2000.

[67] W. Zhou, R. Ran, Z. Shao, *Journal of Power Sources,* 192, 231-246, 2009.

[68] A. J. Jacobson, *Chemistry of Materials,* 22, 660-674, 2010.

[69] V. V. Kharton , A. V. Kovalevsky , M. Avdeev, E. V. Tsipis, M. V. Patrakeev, A. A. Yaremchenko, E. N. Naumovich, J. R. Frade, *Chemistry of Materials,* 19, 2027-2033, 2007.

[70] E. Boehm, J.-M. Bassat, P. Dordor, F. Mauvy, J.-C. Grenier, Ph. Stevens, *Solid State Ionics,* 176, 2717-2725, 2005.

[71] X. Chen, J. Yu, S. B. Adler, *Chemistry of Materials,* 17, 4537-4546, 2005.

[72] V.V. Kharton, A. A. Yaremchenko, M. V. Patrakeev, E. N. Naumovich, F. M. B. Marques, *Journal of the European Ceramic Society,* 23, 1417-1426, 2003.

[73] S. J. Skinner, *Solid State Sciences,* 5, 419-426, 2003.

[74] S. J. Skinner, G. Amow, *Journal of Solid State Chemistry,* 180, 1977-1983, 2007.

[75] J.-H. Kim, F. Prado, A. Manthiram, *Journal of the Electrochemical Society,* 155, B1023-B1028, 2008.

[76] R. A. De Souza, J. A. Kilner, J. F. Walker, *Materials Letters,* 43, 43-52, 2000.

[77] T. Ogier, F. Mauvy, J.-M. Bassat, J. Laurencin, J. Mougin, J.-C. Grenier, *International Journal of Hydrogen Energy,* 40, 15885-15892, 2015.

[78] T. Ogier, J. M. Bassat, F. Mauvy, S. Fourcade, J. C. Grenier, K. Couturier, M. Petitjean, J. Mougin, *Fuel Cells ,* 13, 536-541, 2013.

[79] C. Ferchaud, J.-C. Grenier, Y. Zhang-Steenwinkel, M. M.A. van Tuel, F. P.F. van Berkel, J.-M. Bassat, *Journal of Power Sources journal,* 196, 1872-1879, 2011.

[80] V.V. Kharton, F.M. Figueiredo, L. Navarro, E. N. Naumovich, A. V. Kovalevsky, A. A. Yaremchenko, A. P. Viskup, A. Carneiro, F. M. B. Marques, J. R. Frade , *Journal of Materials Science,* 36, 1105-1117, 2001.

[81] A. Montenegro-Hernandez, J. Vega-Castillo, L. Mogni, A. Caneiro, *International Journal of Hydrogen Energy,* 36, 15704-15714, 2011.

[82] A. V. Kovalevsky, V. V. Kharton, A. A. Yaremchenko, Y. V. Pivak, E. N. Naumovich, J. R. Frade, *Journal of the European Ceramic Society,* 27, 4269-4272, 2007.

[83] V. Vibhu, “PhD thesis: Stability and ageing studies of Praseodymium-based nickelates as cathodes for Solid Oxide Fuel Cells,” Universite de Bordeaux, 2016.

[84] B. Philippeau, F. Mauvy, C. Mazataud, S. Fourcade, J.-C. Grenier, *Solid State Ionics,* 249-250, 17-25, 2013.

[85] K. Yamaji, H. Negishi, T. Horita, N. Sakai, H. Yokokawa, *Solid State Ionics,* 135, 389-396, 2000.

[86] J. Xue, A. Schulz, H. Wang, A. Feldhoff, *Journal of Membrane Science,* 497, 357-364, 2016.

[87] S. S. Bhoga, A. P. Khandale, B. S. Pahune, *Solid State Ionics,* 262, 340-344, 2014.

[88] E. Yu. Pikalova, D. A. Medvedev, A. F. Khasanov, *Physics of the Solid State,* 59, 694-702, 2017.

[89] V. A. Sadykov, E. Yu. Pikalova, A. A. Kolchugin, E. A. Filonova, E. M. Sadovskaya, N. F. Eremeev, A. V. Ishchenko, A. V. Fetisov, S. M. Pikalov, *Solid State Ionics,* 317, 234-243, 2018.

[90] S. J. Skinner, J. A. Kilner, *Solid State Ionics,* 135, 709-712, 2000.

[91] A. Murata, C. Hai, M. Matsuda, *Materials Letters journal,* 136, 292-294, 2014.

[92] V. Vibhu, J.-M. Bassat, A. Flura, C. Nicollet, J.-C. Grenier, A. Rougier, *ECS Transactions,* 68, 825-835, 2015.

[93] V. Vibhu, A. Rougier, C. Nicollet, A. Flura, J.-C. Grenier, J.-M. Bassat, *Solid State Ionics,* 278, 32-37, 2015.

[94] E. Dogdibegovic, Q. Cai, N. S. Alabri, W. Guan, X.-D. Zhou, *Journal of The Electrochemical Society,* 164, F99-F106, 2017.

[95] E. Dogdibegovic, W. Guan, J. Yan, M. Cheng, X.-D. Zhou, *Journal of The Electrochemical Society,* 163, F1344-F1349, 2016.

[96] M. Sakai, C. Wang, T. Okiba, H. Soga, T. Hashimoto, *Journal of Thermal Analysis and Calorimetry,* https://doi.org/10.1007/s10973-019-09190-9*,* 2019.

[97] A. V. Kovalevsky, V. V. Kharton, A. A. Yaremchenko, Y. V. Pivak, E. V. Tsipis, S. O. Yakovlev, A. A. Markov, E. N. Naumovich, J. R. Frade, *Journal of Electroceramics,* 18, 205-218, 2007.

[98] M. Sakai, C. Wang, T. Okiba, H. Soga, E. Niwa, T. Hashimoto, *Journal of Thermal Analysis and Calorimetry,* 135, 2765-2774, 2019.

[99] J. Xue, Q. Liao, W. Chen, H. J. M. Bouwmeester, H. Wang, A. Feldhoff, *Journal of Materials Chemistry A,* 3, 19107-19114, 2015.

[100] D. Ning, A. Baki, T. Scherb, J. Song, A. Fantin, X. Liu, G. Schumacher, J. Banhart, H. J. M. Bouwmeester, *Solid State Ionics,* 342, 115056, 2019.

[101] J. G. Railsback, Z. Gao, S. A. Barnett, *Solid State Ionics,* 274, 134-139, 2015.

[102] V. Vibhu, A. Rougier, C. Nicollet, A. Flura, S. Fourcade, N. Penin, J.-C. Grenier, J.-M. Bassat, *Journal of Power Sources,* 317, 184-193, 2016.

[103] V. Vibhu, A. Flura, C. Nicollet, S. Fourcade, N. Penin, J.-M. Bassat, J.-C. Grenier, A. Rougier, M. Pouchard, *Solid State Sciences,* 81, 26-31, 2018.

[104] Z. Zhang, M. Greenblatt, *Journal of Solid State Chemistry,* 117, 236-246, 1995.

[105] J. M. Bassat, C. Allancon, P. Odier, J. P. Loup, M. Deus Carvalho, A. Wattiaux, *European Journal of Solid State and Inorganic Chemistry,* 35, 173-188, 1998.

[106] E. Niwa, K. Wakai, T. Hori, K. Yashiro, J. Mizusaki, T. Hashimoto, *Thermochimica Acta,* 575, 129-134, 2014.

[107] M. A. Laguna-Bercero, H. Monzon, A. Larrea, V. M. Orera, *Journal of Materials Chemistry A,* 4, 1446-1453, 2016.

[108] M. A. Laguna-Bercero, R. Campana, A. Larrea, J. A. Kilner, V. M. Orera, *Fuel Cells,* 11, 116-123, 2011.

[109] R. Chockalingam, A. K. Ganguli, S. Basu, *Journal of Power Sources,* 250, 80-89, 2014.

[110] P. P. Dholabhai, J. B. Adams, P. A. Crozier, R. Sharma, *Journal of Materials Chemistry,* 21, 18991-18997, 2011.

[111] S. Lubke, H.-D. Wiemhofer, *Solid State Ionics,* 117, 229-243, 1999.

[112] D. L. Maricle, T. E. Swarr, S. Karavolis, *Solid State Ionics,* 52, 173-182, 1992.

[113] S. Cheng, C. Chatzichristodoulou, M. Søgaard, A. Kaiser, P. V. Hendriksen, *Journal of The Electrochemical Society,* 164, F1354-F1367, 2017.

[114] V. V. Kharton, E. V. Tsipis, A. A. Yaremchenko, J. R. Frade, *Solid State Ionics,* 166, 327-337, 2004.

[115] L. Navarrete, C. Solis, J. M. Serra, *Journal of Materials Chemistry A,* 3, 16440-16444, 2015.

[116] X. Ding, W. Zhu, G. Hua, J. Li, Z. Wu, *Electrochimica Acta,* 163, 204-212, 2015.

[117] R. Chiba, H. Aono, K. Kato, *ECS Transactions,* 57, 1831-1840, 2013.

[118] C. Nicollet, A. Flura, V. Vibhu, A. Rougier, J.-M. Bassat, J.-C. Grenier, *International Journal of Hydrogen Energy,* 41, 15538-15544, 2016.

[119] S. Saher, J. Song, V. Vibhu, C. Nicollet, A. Flura, J.-M. Bassat, H. J. M. Bouwmeester, *Journal of Materials Chemistry A,* 6, 8331-8339, 2018.

[120] V. Dusastre, J. A. Kilner, *Solid State Ionics,* 126, 163-174, 1999.

[121] Z. Wu, M. Liu, *Solid State Ionics,* 93, 65-84, 1997.

Chapter 3 Experimental methods

3.1 Introduction

Different experimental methods and materials characterisation techniques have been used in this research. This chapter aims to discuss each approach in detail including the theoretical background and the instrumental/experimental set up.

3.2 Materials synthesis

Several approaches can be used to synthesise ceramic materials. The most popular ones are the traditional solid state reaction and the more recent sol-gel method. Their differences are discussed below.

3.2.1 Solid state reaction

In general, the solid state reaction is achieved by weighing metal oxides or carbonates in a stoichiometric ratio, mixing the precursors using pestle and mortar with volatile organic solvent such as ethanol and acetone and calcining the pressed pellet mixture at a certain temperature and atmospheric condition (usually in air) [1, 2]. The last two steps are usually repeated in order to achieve a pure single phase, confirmed by X-ray diffraction [1, 2]. By applying this approach to synthesise a material, several aspects need to be considered. For example, the initial precursors can adsorb/react with steam and CO_2 easily [1-3]. This will prevent measuring the initial precursors in the correct stoichiometric ratio and hence secondary phases may be formed at the end of the synthesis process or non-stoichiometric materials result [2]. Pretreatment of the precursors at elevated temperatures to remove the adsorbed water and/or using other precursors which are less prone to react with CO_2 might be the potential solutions [1-3]. In addition, it is crucial to mix the precursors homogeneously before being thermally treated at a target temperature as it is believed that the target phase will start forming at the interface of different precursors [1]. However, no matter how well the precursor particles are mixed, the homogeneity of the mixture still remains at the particle level, which is usually in 1-10 µm scale [1]. Hence, a higher calcination temperature and a longer calcination time are usually required for cations to diffuse in order to form a single phase [1]. The diffusion path length of each cation will increase as the thickness of the target phase at the interface of the different

precursors becomes thicker over time [1]. To accelerate the synthesis process, frequently grinding the partially reacted mixtures can break the reactant/product interface and increases the opportunity for the reactants to contact with each other [1]. With respect to the calcination temperature and atmosphere, it depends on the phase diagram which indicates the thermodynamically stable phase at a certain condition [2]. If the phase diagram is not available, suggestions from literature of such compounds or analogous ones can be used as a starting point. The calcination temperature is usually below the melting temperature of the precursors but it is still high enough for cation diffusion [2]. Quenching of the sample from the calcination temperature might be required to preserve the metastable phase if the product is not kinetically stable under a normal cooling process [2].

The major drawback of the solid state reaction is that the precursors are not well mixed at an atomic level but only at a particle level [1]. This then leads to the prolonged calcination stage at a high temperature in order to overcome the cation diffusion barrier [1]. To overcome this, the sol-gel approach has been developed and is discussed next.

3.2.2 Sol-gel synthesis

There are many different sol-gel synthesis approaches but the key concept is to transform the precursors to 'sol' and then 'gel' before further thermal treatment to achieve a single phase [4]. The 'sol' is a colloidal suspension and is usually achieved by hydrolysing a dissolved precursor [4]. On the other hand, the 'gel' is a non-fluid network which can be in the form of colloidal, metal-oxane polymer, metal complex and polymer complex [4]. The main advantage of using a sol-gel approach to synthesise material is that the reactants are homogeneously mixed at an atomic level in a solution state so that the subsequent calcining time and temperature can be lower [4].

In this work, a nitrate-citrate route was applied to synthesise the materials of interest (e.g. Pr-Ni-O Ruddlesden-Popper phases and Ce-Gd-Pr-O fluorites). Various metal nitrates were used as precursors and citric acid acted as a chelating agent [4]. Some literature sources suggest that adding ammonia to control the pH of a metal citrate solution will enhance its stability and homogeneity and avoid metal hydroxide

precipitation [4-6]. However, since no precipitation was observed in the $Pr_2NiO_{4+\delta}$, $Pr_4Ni_3O_{10+/-\delta}$ and $Ce_{1-x-y}Gd_xPr_yO_{2-\delta}$ (CGPO) chemical synthesis using the nitrate-citrate route, the pH of the corresponding metal citrate solutions was not controlled. Once the appropriate stoichiometric ratios of metal nitrate precursors were dissolved in the citric acid solution, the solution was dried to become viscous and in the form of metal complex (gel) as shown in **Figure 3.1** [4]. The gel was then converted to the target metal oxides by a subsequent decomposition stage in air (600°C) and further calcining under specific temperatures and atmospheric conditions [4]. The detailed parameters to synthesise each material will be included in **Sections 4.2**, **5.2** and **6.2**.

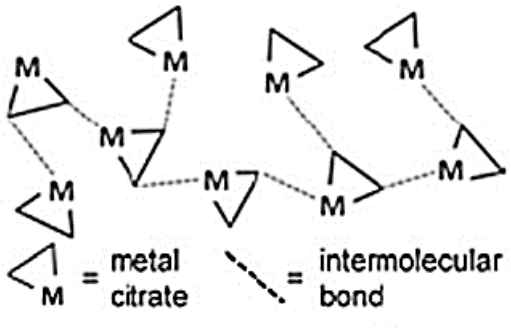


Figure 3.1: The metal complex (gel) after removing water in metal citrate solution. Reproduced from [4] published by The Royal Society of Chemistry under a Creative Commons Attribution 3.0 Unported Licence.

It is important to note that making a homogenous metal citrate solution at room temperature does not necessarily mean the homogeneity will be maintained for the rest of the synthesis stages [4, 7]. Hence, several studies have been conducted to avoid phase separation, one of which is autoignition and rapid thermal annealing [4, 7, 8]. Since the nitrates are a good oxidant and the citrate group plays the role as an organic fuel, the gel can be ignited and combusted at a relatively low temperature (~200°C) at which cation diffusion/phase separation is limited [4, 7, 8]. Although further calcination of the resulting loose powder might be required to form a target phase, the lower heat treatment to remove the organic compounds allows the preservation of the homogeneity of the mixtures before the final calcination stage [7, 8]. In combination with the rapid thermal annealing approach, the temperature range of

undesired phase separation is avoided and the final calcining temperature or time can be decreased [7, 8].

3.3 Test cell fabrication

Depending on the purpose of the investigation, a single cell or a symmetrical cell can be prepared to measure either single cell or electrode performance under a certain condition. Since the research interest is the performance of the new composite air electrodes, the symmetrical cell configuration was chosen. The major benefits for this sample configuration are that the fuel electrode will not contribute to the final electrode performance measurement and the same electrode sintering process can be applied on both electrode sides of a cell because they are made of the same electrode materials [2]. The fabricated samples will be mechanically supported by the electrolyte layer due to its greater thickness than the deposited electrodes.

3.3.1 Ball milling of the synthesised powder

Before being used for another sample preparation, most of the synthesised powders such as $Pr_4Ni_3O_{10+/-\delta}$ and $Ce_{0.75}Gd_{0.10}Pr_{0.15}O_{2-\delta}$ and the thermally pre-treated $Sc_{0.18}Ce_{0.01}Zr_{0.81}O_{2-\delta}$ (10Sc1CeSZ) commercial powder (Lot No.: H2228) from DKKK, Japan were ball milled. The main reason for this process was to break any large agglomerates forming during the previous calcination stage and to achieve a more homogeneous particle size distribution. The ball milling was conducted by mixing the powders and with zirconia milling media in ethanol and the rotation of the machine (in a rotary mill) will allow the zirconia balls to grind the powder. After ball milling, the zirconia balls were removed and the ethanol was evaporated at 80°C on a hot plate, leaving the dry ball-milled powders.

3.3.2 Electrolyte fabrication

To fabricate a dense electrolyte pellet used for symmetrical cell testing, the dry ball-milled 10Sc1CeSZ powder was firstly uniaxially pressed (739 MPa) and then isostatically pressed at 300 MPa before sintering the resulting green body at 1550°C for 5 hours in air. The density of all the sintered 10Sc1CeSZ pellets was measured by the Archimedes method (**Section 3.4.7**) with the relative density greater than 94%. In addition, the thickness of the sintered pellet was controlled to be around 1.2 mm by

grinding using SiC paper. The cross-sectional area of the electrolytes was also measured before the sample was ultrasonically cleaned and dried ready for electrode ink deposition.

3.3.3 Electrode ink fabrication

The next step is to prepare an electrode ink which consists of a mixture of the dry ball-milled powder of interest (e.g. $Pr_4Ni_3O_{10+/-\delta}$, $Ce_{0.75}Gd_{0.10}Pr_{0.15}O_{2-\delta}$, and the combination of both materials in a particular weight ratio) and a commercial ink vehicle (Fuel Cell Materials, USA, #311006). Based on previous experience [2, 9], the weight ratio of the dry ball-milled powder and the commercial ink vehicle was 2:1. The mixing was then followed by triple-roll milling of the mixtures (EXAKT 80E) to remove any powder agglomeration and to achieve a homogeneous electrode ink. The ink was collected and stored in a fridge to decrease the volatility of the organic solvent.

3.3.4 Ink deposition

The prepared electrode inks were deposited on the sintered 10Sc1CeSZ electrolyte pellets and this was usually achieved by either brush painting or screen printing. The advantages and disadvantages of each electrode deposition approach are discussed below.

3.3.4.1 Brush painting

For the brush painting method, an electrode ink was manually painted on one side of a sintered electrolyte pellet using a fine brush [2, 9]. The ink was then dried on a hot plate at around 100°C before the other side of the electrolyte pellet was brush-painted with the electrode ink [2, 9]. The advantages of this approach are that it is simple and no electrode misalignment issue will result as both sides of the electrolyte pellet were fully covered by the electrode ink. However, it is challenging to control the electrode thickness and it could lead to inhomogeneity [2, 9].

3.3.4.2 Screen printing

On the other hand, screen printing of electrodes can be achieved using a commercial screen printing machine. An electrode ink was pushed by the squeegee on one side of a mesh and the ink passed through the mesh to deposit on the aligned electrolyte pellet underneath [2, 9]. Similar to the brush painting approach, the electrode ink on

one side was dried first before depositing the electrode ink on the other side [2]. The main benefit of screen printing is that it allows the formation of a homogeneous electrode thickness but electrode alignment on each side might be a potential issue [2, 9]. This is because the electrode screen printing area is usually less than the overall cross-section area of an electrolyte pellet and the current set up of the machine requires the electrode alignment to be conducted manually. Electrode misalignment can produce significant measuring artefacts especially for half-cell measurements [10].

Brush painting was applied to deposit all the electrode inks here. Once the deposited electrode ink was dried on both sides of the sintered electrolyte, the symmetrical cells were sintered under the conditions specified in **Section 6.2**.

3.4 Materials characterisation

Different materials characterization techniques were used to evaluate samples for various purposes. The principles of each characterization technique and their experimental set up are discussed in the following sections.

3.4.1 X-ray/synchrotron source X-ray/neutron diffraction

3.4.1.1 Theoretical background

X-ray diffraction (XRD) is a technique that can identify the crystal structure of a sample. Since the wavelength of the X-ray is around one angstrom which is of the same order of magnitude as the atomic spacing found in a crystal, diffraction phenomenon will occur [11]. Bragg's law (**Equation 3.1**) is used to determine the conditions under which X-ray diffraction will occur in the manner of receiving constructive interference between the scattered X-ray from a sample [1]. λ, d_{hkl} and θ are the wavelength of the X-ray, the atomic spacing for a particular (h k l) atomic plane in a sample and the scattering angle as illustrated in **Figure 3.2(b)** [1].

$$\lambda = 2d_{hkl}sin\theta \qquad \textbf{Equation 3.1}$$

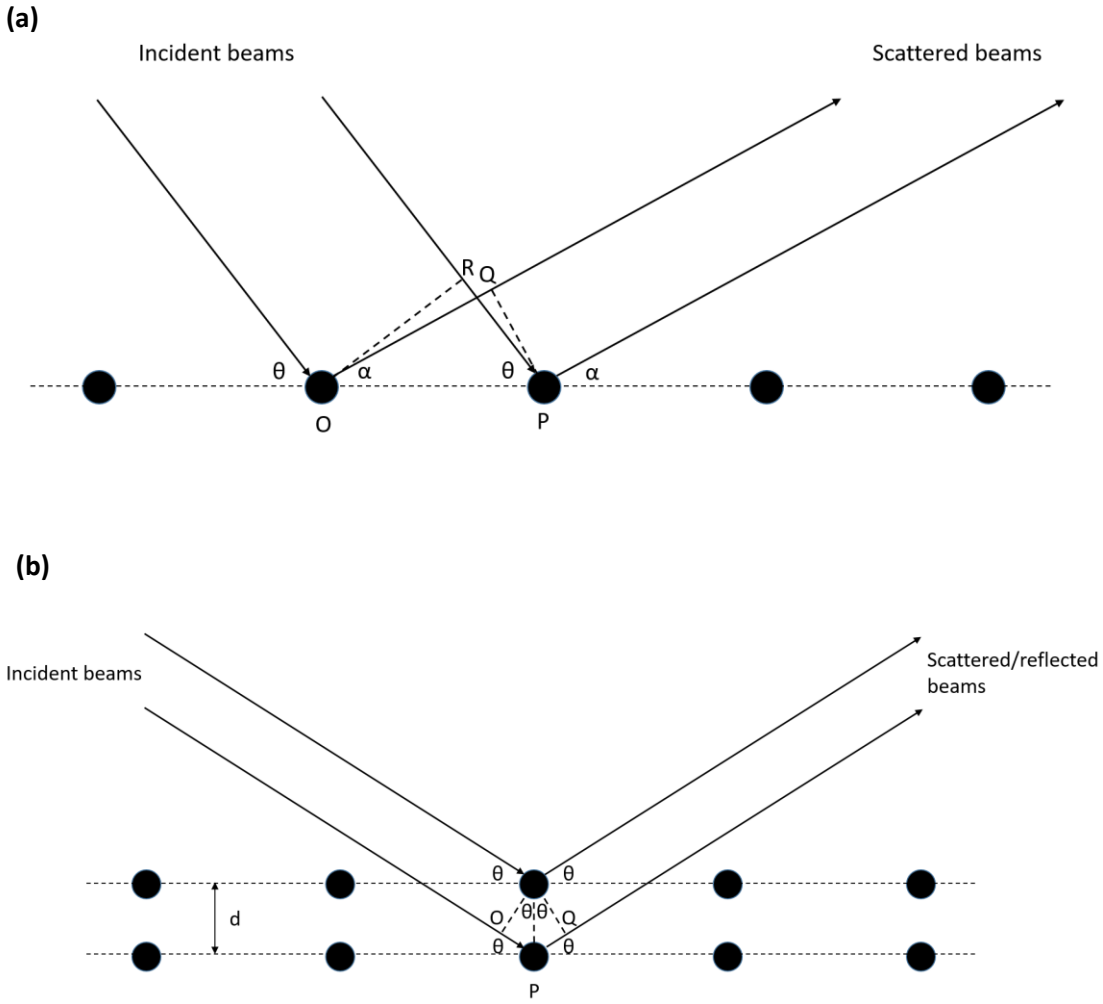


Figure 3.2: **(a)** The scenario when the incident X-ray angle (θ) is different from the scattered X-ray angle (α). **(b)** X-ray reflection from the consecutive atomic planes which are separated by distance, d.

Figures 3.2(a) and **(b)** show two possible scenarios when the incident X-ray scatters from atoms in a sample. The X-ray scattering from an atom can be in any direction with an angle of α being labelled in **Figure 3.2(a)** compared to the incident angle of θ. The path difference between the X-ray scattered by atom O and from atom P is equivalent to line OQ minus line PR and hence OP cosα- OP cosθ. This path difference will only be zero if the angle α is equal to angle θ and at such condition, these two scattered beams will be in phase, forming constructive interference. This

phenomenon can be regarded as an incident X-ray being reflected from a sample surface [1].

Now, considering the consecutive atomic planes that are beneath the surface, one with atomic plane spacing d in **Figure 3.2(b)**, the path difference between the X-ray beam reflected from the first atomic layer and the second atomic layer is OP plus PQ, which is equivalent of 2d sinθ [1]. The constructive interference of the two reflected beams will only occur if the path difference is proportional to the X-ray wavelength with an integer as suggested by Bragg's law in **Equation 3.1** [1]. The integer is an order of diffraction from a specific set of atomic planes and this value can be combined with d to from d_{hkl}.

In other scenarios, destructive interference will result from the scattered X-ray from a sample. Therefore, no signal will be detected [1]. Given that the wavelength of the X-ray source is constant, each peak position in the final diffractogram output (plotted as X-ray counts versus 2θ) indicates the atomic spacing for a specific atomic plane from a sample [1]. Depending on the crystal symmetry of the investigated material, which can be identified from the spacing between each peak, the crystal lattice parameters can be derived from the peak positions [11].

The relative peak intensities in the diffractogram output, however, is not considered in Bragg's law [1]. Therefore, the concept of the structure factor (F) which calculates the total amount of X-ray intensity scattered from a specific atomic plane with scattering angle of θ is introduced and the equation is summarised as **Equation 3.2** [1]. h, k and l are the Miller indices of an atomic plane. In a specific unit cell, it includes N atoms and j represents each atom with a fractional unit cell coordinate of x, y and z. f_j is the atomic scattering factor of atom j which is proportional to atomic number if X-rays are the radiation source [1]. Indeed, the structure factor can be used to predict the condition of systematic absences which are the result of the diffracted X-ray having destructive interference due to the lattice symmetry effect [1]. The information of systematic absences for a certain set of hkl combinations can also be used to determine the crystal structure of an unknown sample [1].

$$F_{hkl} = \sum_{j=1}^{N} f_j \exp 2\pi i(hx_j + ky_j + lz_j) \qquad \textbf{Equation 3.2}$$

3.4.1.2 Instrumentation and experimental set up

The typical laboratory based X-ray diffractometer has a Bragg-Brentano geometry in which the sample is fixed at the centre of the diffractometer and both the incident X-ray beam and the detector are moved at the same angle (θ) from a sample simultaneously [11]. The X-rays are generated by the X-ray tube and this is achieved by accelerating the electrons generated from a tungsten filament and bombarding them to a copper target [11]. At a sufficient energy, an electron from the K shell in copper will be removed by the incident electron [11]. To stabilise the state, the electrons in the outer shells (L and M) will fill the hole in the inner shell and generate X-rays with the energy equivalent to the energy difference between the two electron shells [11]. In the case of a copper target, three characteristic X-ray wavelengths are generated in the X-ray tube and they are denoted as $K_{\alpha1}$, $K_{\alpha2}$, and K_{β} [11]. Their corresponding energies are reflected in the variation of the wavelength such as 1.5406 Å, 1.5444 Å and 1.3922 Å, respectively [11]. The instrumental set up of the PANalytical X'Pert Pro MPD only removes K_{β} X-rays using a Ni filter [11]. $K_{\alpha1}$ and $K_{\alpha2}$ wavelengths, however, are difficult to separate because of the close wavelength. Therefore, two peaks with the intensity ratio of 2 to 1 will be observed in the final diffractogram for a given atomic plane [12]. The peak separation will be larger at a higher angle due to Bragg's law.

In general, a sample can be in the form of powder or solid (e.g. pellets or symmetrical cells) and different sample holders should be used. Powder samples are usually mounted on a zero background sample holder which is made of Si single crystal and is cut at a specific angle so that no diffraction from the sample holder will result in a measurable 2θ range of the diffractometer [13]. On the other hand, for solid samples, they are mounted on a sample holder with putty located at the centre. It is important to note that the surface of all different types of sample must be flattened and at the same height as the sample holders' rim to prevent sample displacement error in the final results.

In terms of the instrumental parameters, the X-ray tube was set to generate Cu K_{α} X-rays at 40 kV and 40 mA. The measurement angle in 2θ ranges from 5° to 90°/100° (2θ) with a step size of 0.017°/0.034° and time per step of 15 seconds. The small step

size and the long time per step will increase the peak resolution and the signal to background ratio in the final results [11].

3.4.1.3 In-situ x-ray diffraction

Unlike the previously introduced X-ray diffractometer which measured a sample under ambient temperature and atmosphere, an *in-situ* X-ray diffractometer (PANalytical Empyrean instrument fitted with an Anton Paar HTK1200N high temperature chamber) allows diffractograms to be collected under various non-ambient conditions, which are specified in **Section 5.2**. This technique is especially useful when investigating the chemical/structure change of a material upon heating. The instrumental configuration is still Bragg-Brentano geometry but the sample holder height is automatically adjusted at various temperatures and atmospheres to compensate for its thermal expansion effect [14]. With respect to the temperature distribution, environmental heaters are adopted in the high temperature chamber to allow homogeneous heat transport from each direction to a sample [14, 15]. The same X-ray source and filter was applied to the *in-situ* X-ray diffractometer. Each diffractogram was measured from 15° to 100° (2θ) with the step size of 0.013° and the time per step of 150.5 seconds. Auto slit mode was used to ensure that the incident X-ray coverage did not exceed the sample boundary at low 2θ and at a given temperature/atmosphere. The final diffractogram outputs were converted to as acquired under fixed slit mode before data analysis. The conversion allows the radiation volume to be constant at different 2θ and hence the correct relative peak intensities. This is required for quantitative analysis such as Rietveld refinement but has less impact on Le Bail refinement. Indeed, diffractograms were collected before and after the test to confirm that the sample was not displaced because of the sintering effect at high temperatures.

3.4.1.4 Rietveld refinement

Rietveld refinement is an approach to quantitatively analyse diffraction data. This is mainly achieved by developing a model given that an initial estimation of the crystal structure and the chemical composition for the phase of interest can be made [2]. Since both background and diffraction peaks are modelled, corresponding equations are required to consider each contribution. Depending on the software package and

the analysed data, various background functions were used for the refinement to consider the effect from detector, sample holder, air scattering, inelastic scattering, sample florescence, etc. on the final results [13]. Linear interpolation of the selected background points and a polynomial function were applied to determine the background intensity counts for Fullprof [12] and GSAS II [16], respectively. With respect to the diffraction peaks, the calculated intensity (Y_{calc}) at a specific 2θ or atomic spacing (d) value depended on the scale factor, the geometrical factor, the polarisation factor, the absorption factor, the square of the structure factor calculated from **Equation 3.2**, the previous modelled background intensity and the peak shape function [17]. A Pseudo-Voigt peak shape function, the linear combination of Gaussian and Lorentzian functions was usually used to model each of the diffraction peak shapes unless other peak shape model was specified in the text [17]. The comparison was then made between the calculated intensity (Y_{calc}) and the experimentally observed intensity (Y_{obs}) with the aim to minimise the difference by least squares method (**Equation 3.3**) [17]. This was achieved by iteratively varying parameters in the model used to calculate Y_{calc} until χ^2 is the smallest and the iteration process converged [17]. χ^2 is the goodness of fit indicator and ω_i, n and p are the weighted factor for i^{th} point, the total number of points from the experiment and the total number of variables refined, respectively [17].

$$\chi^2 = \frac{\sum_{i=1}^{n} \omega_i (Y_{obs} - Y_{calc})^2}{n-p} \qquad \textbf{Equation 3.3}$$

Other agreement factors such as profile residual (R_p) and weighted profile residual (R_{wp}) were also used and they are defined as **Equations 3.4** and **3.5**, respectively [17]. These parameters indicate the quality of refinement from data to data [2].

$$R_p = \frac{\sum_{i=1}^{n} |Y_{obs} - Y_{calc}|}{\sum_{i=1}^{n} Y_{obs}} x100\% \qquad \textbf{Equation 3.4}$$

$$R_{wp} = \left(\frac{\sum_{i=1}^{n} \omega_i (Y_{obs} - Y_{calc})^2}{\sum_{i=1}^{n} \omega_i (Y_{obs})^2}\right)^{0.5} x100\% \qquad \textbf{Equation 3.5}$$

At the end of the refinement, both the refined lattice parameters and the refined atomic parameters would result. They are the information of the crystal structure in the examined phase. Rietveld refinement can also quantify the weight fraction of each

phase if the sample is a mixture. Indeed, for most of the refined diffractograms, a difference curve of Y_{obs}-Y_{calc} is usually plotted. This curve is very useful in terms of identifying regions of poor fit and the reason is illustrated by its specific pattern around the Bragg position of interest [18].

3.4.1.5 Le Bail refinement

Le Bail refinement does not require the input of atomic parameters, which are related to the structure factor in **Equation 3.2** and hence to the relative peak intensities, as the integrated observed intensity of each point is received by an iterative fitting approach without any physical meaning [17]. Unlike the as-mentioned Rietveld refinement, lattice parameters are the only input needed in the model [17]. By fitting background, peak shape and the lattice parameters, the unit cell dimensions of the phase of interest can be retrieved after this type of refinement [17]. This data analyzing approach is very powerful and fast in terms of phase identification and lattice parameters determination but it cannot calculate the phase fraction of a mixture.

3.4.1.6 Synchrotron X-ray and neutron high resolution powder diffraction

There are several limitations of the laboratory X-ray diffractometer. For example, the X-ray source is frequently not monochromatic with both $K_{\alpha1}$ and $K_{\alpha2}$ wavelengths and the diffractometer has a relatively low resolution. These disadvantages will restrict the capability of resolving the crystal structure of a sample with subtle changes in terms of the lattice parameters and the crystal structure asymmetry. Therefore, synchrotron X-ray and neutron powder diffraction facilities were used to examine the samples.

High resolution synchrotron X-ray powder diffraction (HR-SXRPD) (Beamline I11, Diamond Light Source Ltd, UK) was applied to investigate the resulting $Ce_{1-x-y}Gd_xPr_yO_{2-\delta}$ (CGPO) lattice parameters after chemical reaction between $Pr_2NiO_{4+\delta}$ and $Ce_{0.9}Gd_{0.1}O_{2-\delta}$ (CGO10). The beamline X-ray source is monochromatic and is generated by an undulator with beam current of 300 mA [19]. The diffractometer has very high count rates and resolution ($\triangle d/d \sim 10^{-3}$-$10^{-5}$) which allows a good quality of diffractogram to be received [20]. The detailed instrumental and experimental parameters can be found in **Section 4.2**. It is important to note that neutron diffraction was not applied here because gadolinium is an intense neutron absorber [21].

In X-ray diffraction, X-ray beams are scattered by electrons and this process is so-called Thomson scattering [1]. As mentioned before, the X-ray atomic scattering factor is proportional to atomic number. Hence, the position and content of light atoms such as oxygen are hardly observable [1]. Neutrons, on the other hand, interact with atomic nuclei and the atomic scattering factor has no single dependence on atomic number [1]. High resolution powder neutron diffraction analysis was conducted at the HRPD beamline, ISIS Neutron and Muon Source, Harwell Science Campus, Didcot, UK. The aim of the experiment was to identify the crystal structure of the as-synthesised $Pr_4Ni_3O_{10+/-\delta}$ including each of the atomic positions and their occupancy, especially oxygen. ISIS has a pulsed neutron source with variable neutron wavelength generated [1, 22]. The neutron diffraction data are recorded as a function of time of flight [1, 23]. This is achieved by fixing the scattering angle (θ) and the diffraction signals are recorded based on the relationship between the atomic spacing of a particular atomic plane (d_{hkl}) and the wavelength (λ) in Bragg's law (**Equation 3.1**) [1]. Indeed, since neutron wavelength is inversely proportional to its velocity, different diffraction signals are separated by their time of flight to the detector [1]. As HRPD has a long primary flight path (~96 m) from the target, the resolution of $\triangle d/d \sim 4\text{-}5x10^{-4}$ can be achieved [23]. With respect to the detailed instrumental and experimental parameters, they can be found in **Section 5.2**.

3.4.1.7 Bond valence model

The bond valence model is an improvement of Pauling's second rule [24]. Pauling's second rule states that the sum of the bond strength from the adjacent cations is equal to the anion charge [24]. Bond strength is calculated by the ratio of cation charge to its coordination number and it is assumed that all the bond strengths are the same [1, 24]. However, in practice, the bond strength or the experimental bond valence defined by Brown, correlated to the cation-anion bond length, can be irregular [1, 24]. Therefore, Brown re-defined Pauling's second rule as **Equations 3.6** and **3.7** where S_{ij}, R_{ij}, and V_i are the experimental valence between atom i and j, the measured bond length between atom i and j and the calculated valence of atom i [24]. R_0 and B are the fitting parameters of the empirical results between bond valence and bond length [1, 24]. These values can be varied when different pairs of atoms are considered and

the database compiled by Brown was used here [24, 25]. A bond valence model was applied to calculate the Pr and Ni valences in each atomic site in $Pr_4Ni_3O_{10+/-\delta}$ given that the bond length between each Pr-O and Ni-O and the cation coordination numbers are known from the refined neutron diffraction data.

$$S_{ij} = \exp(\frac{R_0 - R_{ij}}{B}) \quad \textbf{Equation 3.6}$$

$$V_i = \sum_j S_{ij} \quad \textbf{Equation 3.7}$$

3.4.2 Scanning electron microscopy (SEM)

3.4.2.1 Theoretical background

Scanning electron microscopy (SEM) is an imaging technique which can resolve features in the micrometer and nanometer ranges [26]. Since the wavelength of an incident beam is proportional to the resolution limit, defined as the smallest distance between two adjacent points that the two separate entities can still be recognized, the resolution of electrons with wavelength ranges from ~0.012 nm to ~0.0086 nm in a SEM is much greater than visible light (~400-700 nm) in an optical microscope [1, 26].

The interaction of beam and sample is illustrated in **Figure 3.3** and can be classified as elastic scattering and inelastic scattering [26]. Backscattered electrons are the result of elastic scattering and they are generated by changing the trajectory of the primary electrons without energy loss [26]. As the amount of backscattering depends on the number of electrons in an atom and hence the atomic number, the image contrast in the backscattering electron mode is very useful in terms of distinguishing local phases constituted by different elements [26]. However, backscattered electron images do not reveal the type of element present and its concentration in a local region [26].

On the other hand, all the rest of the radiation coming from a sample shown in **Figure 3.3** are the products of inelastic scattering [26]. Only the secondary electrons and the characteristic X-rays are focused here and in **Section 3.4.3**, respectively because the corresponding techniques were used to characterise the samples. Secondary electrons are generated when the electrons in an atom are knocked off by the primary electron beam and they usually have low energy of between 2-50 eV [26]. Due to their

low energy, only the surface secondary electrons (approx. top 15 nm of the tear-drop interaction volume in **Figure 3.3**) can escape from a sample and are collected by a secondary electron detector [26]. Hence, the signals from the secondary electrons contain the information of sample topography [26]. In contrast, the 40% of the interaction volume from the top is where backscatter electrons originate, whereas the characteristic X-rays are scattered from the whole interaction volume in cubic micrometers size [26, 27].

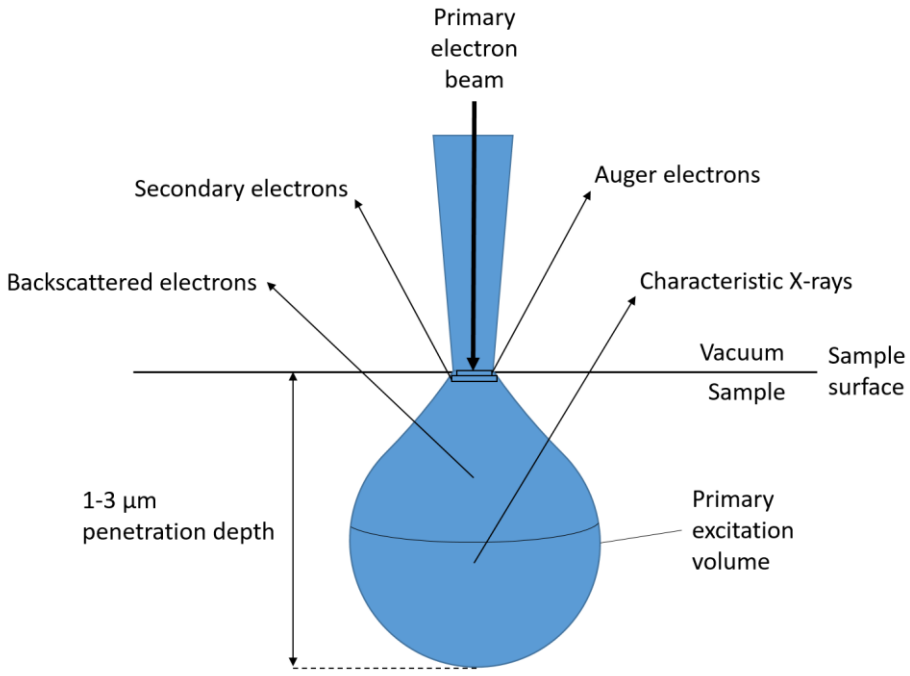


Figure 3.3: The source of signals and their corresponding interaction volume when the sample is exposed by the primary electron beam.

3.4.2.2 Instrumentation and experimental set up

The primary electrons are generated by an electron gun where the electrons are accelerated by a voltage [26]. It is important to note that the SEM chamber is under high vacuum to minimise unfavourable incident electron beam scattering effects [26]. The primary electron beam is then manipulated by the condenser lens, the aperture and the objective lens before reaching the examined sample as a spot [26]. The spot is then rastered across the sample surface to construct an electron image [26]. The spot size can be varied by several parameters such as the current in the condenser lens, the aperture size and the working distance and it has an impact on the final image resolution and the number of signals received from a sample [26]. Indeed, the

accelerating voltage will also have an impact on the interaction volume [26]. Therefore, depending on the characterisation purpose, different instrumental parameters will be used for image capturing (from secondary electrons or backscattered electrons) or elemental/chemical microanalysis (from characteristic X-rays).

In general, for high resolution sample topography investigation, low accelerating voltage and small aperture size are used to reduce the interaction volume and to decrease the spot size [26]. Moreover, a backscattered electron image was usually collected with characteristic X-ray spectra from energy dispersive spectroscopy (EDS) (**Section 3.4.3**) in order to distinguish different phases locally (from the image contrast) and to evaluate the presence of an element and its concentration in each identified phase [26]. A higher accelerating voltage and aperture size were used for this application. This is to ensure that the primary beam energy is greater than the ionisation energy of characteristic X-ray generation for most elements and sufficient X-ray signals can be received by an EDS detector [27]. The detailed instrumental parameters for the Zeiss Leo Gemini 1525 instrument used in this work for recording secondary electron images, backscatter electron images and/or SEM-EDS microanalysis can be found in **Sections 4.2**, **5.2** and **6.2**. With respect to sample preparation, samples were mounted on a SEM stub with carbon tape adhering at the bottom of the sample. If a sample was not conductive, carbon coating on the sample surface was applied and carbon tape was used to form a conductive path from the sample surface to the stub. These measures avoid potential sample charging effects.

3.4.2.3 Focused ion beam scanning electron microscope (FIB-SEM)

A focused ion beam scanning electron microscope (Helios Nanolab 600, FEI) was used to prepare transmission electron microscope lamellae. The instrument possesses an electron beam and an ion beam (Ga^+). A platinum strip was firstly deposited on the top of the excised region to avoid the erosion by the ion beam in the following milling process [26]. The sample was then milled by the gallium ion beam until the section of interest could be removed from the bulk and was transferred to a TEM grid. The cut piece was further milled by the gallium ion beam until it was electron transparent. The whole milling progress was monitored by the SEM.

3.4.3 Energy dispersive spectroscopy (EDS)

As mentioned in **Figure 3.3**, characteristic X-rays are also produced when a primary electron beam interacts with a sample. The characterization technique to capture and analyse the resulting spectrum in the form of counts/count per seconds (cps) versus X-ray energy in keV is known as energy dispersive spectroscopy (EDS) [27]. The concept of the characteristic X-ray generation is the same as the X-ray tube in a diffractometer (**Section 3.4.1.2**) but the copper target is replaced by a sample of interest which can contain elements other than copper. For primary electrons with sufficient energy, which is greater than the ionization energy of an electron shell in an atom, atom ionization will occur when an inner shell electron is removed by the primary electron [27]. This is then followed by relaxation when an outer shell electron fills the inner shell vacancy and an X-ray is emitted [27]. The energy of the X-ray is characteristic as its energy is equal to the difference between the inner shell and outer shell electron ionization energies [27]. Since the ionization energy of each electron shell in an atom is different for each element, the produced X-rays can be used to identify elements in a sample [27].

Apart from the characteristic X-rays, Bremsstrahlung X-rays will also be generated and this is due to the fact that the primary electrons are decelerated by the electric field around the nuclei of atoms in a sample [27]. Part of the energy loss is in the form of X-ray [27]. Indeed, it is more likely that the primary electron loses its energy (in a smaller amount) through several sample interactions than it loses all its energy once [27]. Therefore, in theory, the spectrum of Bremsstrahlung X-ray is a continuous curve with higher X-ray counts at low X-ray energy and vice versa [27]. However, in practice, low energy Bremsstrahlung X-rays tend to be absorbed by the sample and the detector [27]. It is important to note that the recorded EDS spectrum will be the combination of the detected characteristic X-rays and the Bremsstrahlung X-ray spectrum (background) [27].

EDS is a diverse technique which can be applied in SEM and scanning transmission electron microscopy (STEM) as the major concept is the same [27]. The main difference, however, is the sample used. For example, SEM examines thick samples that are not electron transparent whereas STEM samples must be thin (less than ~100

nm) and electron transparent [27]. Indeed, the accelerating voltage applied is quite different between SEM and STEM. The thinner the samples and the higher the accelerating voltage used in STEM allows higher spatial resolution (in the same order of the sample thickness) to be achieved compared to SEM-EDS, which is in the micron range [27].

Both qualitative and quantitative analysis can be conducted on the EDS results. Qualitative analysis is usually used to identify the presence of an element in a sample whereas quantitative analysis calculates the concentration of each element present [27]. Element line deconvolution is usually required for both types of analysis and this process is especially important when peak overlapping occurs [27]. Deconvoluting overlapping peaks can be achieved by examining the whole spectrum and identifying the X-ray lines for each family of an element as the relative intensity and energy between each family of an element are consistent and characteristic [27].

With respect to the quantitative analysis, the first step is to separate the Bremsstrahlung background intensity from the characteristic X-ray intensity at a given energy [27]. Bremsstrahlung background can be modelled by an equation which is related to Kramer's law [27]. On the other hand, the relative characteristic peak intensity between elements is not necessary to be directly proportional to their concentration [27]. Peak intensity correction must be made due to the atomic number effect (Z), the absorption effect (A) and the fluorescence effect (F) from a sample [27]. This is known as ZAF correction and is required for thick samples such as the ones used for SEM-EDS [27]. For electron transparent samples prepared for STEM-EDS, the quantitative analysis can be conducted accurately even without ZAF correction and this approach is known as the Cliff-Lorimer method [27, 28]. In other words, the relative characteristic peak intensity of each element is proportional to the real concentration [27, 28].

Finally, depending on the purpose of the experiment, EDS can be in either point mode, line scan mode or mapping mode. These modes provide the local chemical composition information in zero, one and two dimensions, respectively.

3.4.4 Electrical conductivity measurement using the van der Pauw approach

The van der Pauw approach was used to measure the electrical conductivity of dense sintered $Pr_4Ni_3O_{10+/-\delta}$ pellets at different temperatures in air. Several criteria need to be met for accurate measurement. For example, the sample must be homogeneous, thin and flat without isolated holes [29-31]. Indeed, the contact of four probes must be small and located at the edge of the sample [29, 30]. Correction factors need to be applied to the final results if there is any deviation from these criteria [32, 33].

For simplicity, a sample is illustrated as a square shape in **Figure 3.4** with contacts located at the four corners. The resistivity (sheet resistance) was measured and calculated based on **Equation 3.8** [29]. ρ, d, R_A, R_B and f are the measured resistivity (Ωm), the sample thickness (m), the resistance (Ω) derived from, for example, the voltage measured from contact 2 and 1 (V_{21}) and the DC current flowing from contact 3 to 4 (I_{34}), the resistance (Ω) derived from, for example, the voltage measured from contact 3 and 2 (V_{32}) and the current flowing from contact 4 to 1 (I_{41}) and the symmetrical factor which is with respect to the ratio of R_A and R_B, respectively. The order of R_A and R_B is not important and R_A is always greater than or equal to R_B. f is equal to one when any two adjacent contacts are symmetrical from the line drawn by the other two contacts [29, 30]. If the configuration of the probes is not symmetrical, the value of f can be read off from a published table [34]. Two sets of R_A and R_B were measured with one from $R_{21,34}$ (V_{21}/I_{34}) and $R_{32,41}$ (V_{32}/I_{41}) and the other from $R_{43,12}$ and $R_{14,23}$ [29]. The electrical conductivity measurement was regarded as being reliable if the resistivity calculated from $R_{21,34}$ and $R_{32,41}$ and the one calculated form $R_{43,12}$ and $R_{14,23}$ are within 10% of variation [29]. If the resistivity variation was acceptable, the final resistivity was recorded as the average of the two [29].

$$\rho = \frac{\pi d(R_A+R_B)f(R_A/R_B)}{ln4} \qquad \textbf{Equation 3.8}$$

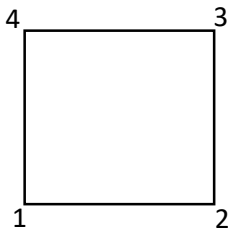


Figure 3.4: An illustration of a square sample in which its resistivity is measured by the van der Pauw approach. The probes are labelled with number and are located at the four corners.

3.4.5 AC impedance spectroscopy

3.4.5.1 Theoretical background

AC impedance spectroscopy is a popular *in-situ* characterisation technique which is commonly used in the solid oxide cell research field. Unlike the common DC approach, a small sinusoidal perturbation of AC voltage with constant magnitude (V_0) and various frequencies (ω) is introduced to a sample and the resulting current with magnitude (I_0) and phase shift (φ) is recorded [2, 35]. This allows different processes in a sample, having different time constants, to be separated and identified [2, 35]. Similar to the resistance in ohms' law, impedance can be defined as the ratio of voltage to current but its magnitude (V_0/I_0) and phase shift is frequency dependent (**Equation 3.9**) [2, 35]. It is important to note that i and ω in **Equation 3.9** are the square root of -1 and the angular frequency, respectively. Indeed, if the magnitude of impedance (|Z|) is equal to the ratio of V_0 and I_0, **Equation 3.9** can be re-written as **Equation 3.10** where Z' and Z'' indicate the real part and the imaginary part of the impedance [2].

$$Z(\omega) = \frac{V(\omega)}{I(\omega)} = \frac{V_0 e^{i\omega t}}{I_0 e^{i(\omega t+\varphi)}} = \frac{V_0}{I_0}[cos\varphi - isin\varphi] \qquad \textbf{Equation 3.9}$$

$$Z(\omega) = |Z|cos\varphi - i|Z|sin\varphi = Z' - iZ'' \qquad \textbf{Equation 3.10}$$

In general, Nyquist plots are used to present the results from AC impedance spectroscopy as shown in **Figure 3.5**. For a specific impedance value in a complex form, the real value is reflected on the x-axis whereas the y-axis shows the imaginary value. It is worth mentioning that the scale of the x-axis and y-axis in a Nyquist plot must be the same [2]. In terms of frequency, it is implicitly included in a Nyquist plot with high and low frequencies located at the low and high Z' value regions, respectively.

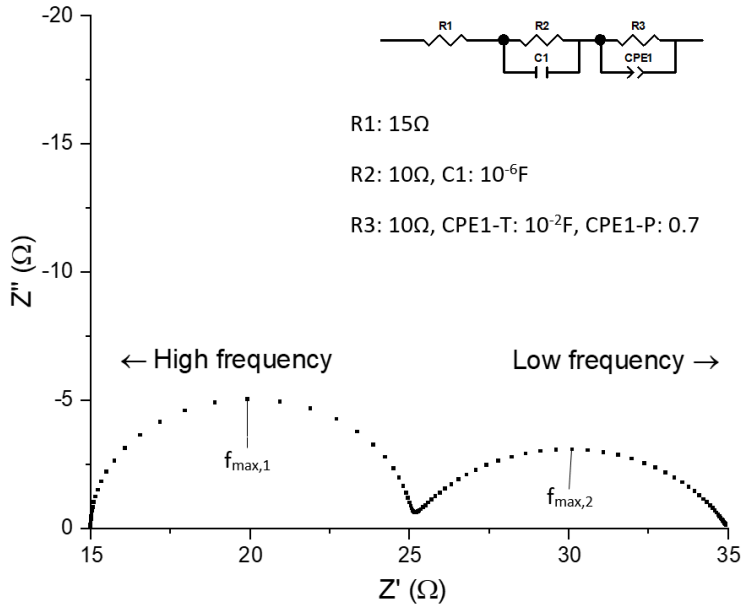


Figure 3.5: A Nyquist plot with one semi-circle and one depressed semi-circle to resemble possible results from AC impedance measurement. An equivalent circuit model used to simulate the Nyquist plot is presented and this is together with the parameters used for each circuit element. As the simulated ohmic resistance (R1) was 15 Ω, the whole Nyquist plot horizontally shifted to the right from the origin to the same magnitude.

Bode plots are another approach to present the data (**Figures 3.6(a)** and **(b)**). There are two types of Bode plot. One is plotted as the magnitude of impedance (|Z|), equivalent to the distance from the origin to a complex coordinate in the Nyquist plot, versus the standard logarithm of frequency ($\log_{10}f$) and the other is in the form of the phase shift (φ), equivalent to the angle between the x-axis and a complex coordinate from the origin in the Nyquist plot, versus the $\log_{10}f$ [2, 35]. The major advantage of Bode plots over Nyquist plots is that they are useful in terms of identifying the number of processes (semi-circles shown in a Nyquist plot) in a sample and the maximum frequency (time constant) of each process (e.g. $f_{max,1}$ and $f_{max,2}$).

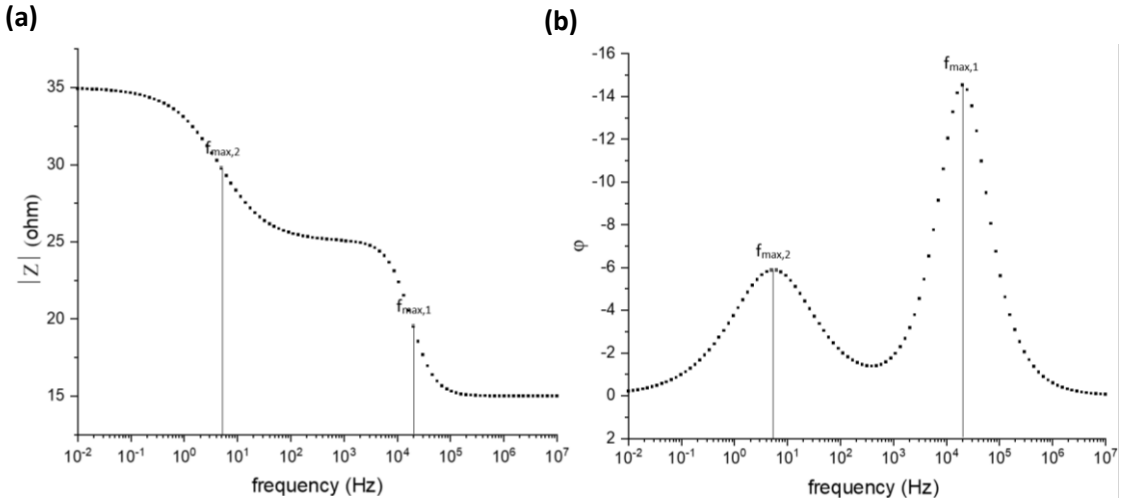


Figure 3.6: The corresponding Bode plots **(a)** in the form of the impedance magnitude over various frequencies and **(b)** in the form of the phase shift over various frequencies with respect to the Nyquist plot in **Figure 3.5**.

Figure 3.5 illustrates a simulated AC impedance result based on the equivalent circuit model and the parameters shown. In practice, the data analysis approach is in reverse order [35]. For example, the AC impedance results are recorded and the data look similar to **Figure 3.5** with several (depressed) semi-circles. They represent different processes occurring in a sample with various time constants or maximum frequency. An equivalent circuit model is then used to fit the data using the complex non-linear least squares (CNLS) approach. The parameters derived for each electric element in the model provide the information of each process such as their corresponding resistance and capacitance. ZView software package (from Scribner Associates) was used to analyse the AC impedance data.

The sample processes are usually modelled as a resistor and a capacitor connected in parallel and this equivalent circuit fits the best when a semi-circle response is observed from the data as shown in the first arc in **Figure 3.5** [2, 35]. However, in practice, a depressed semi-circle is usually observed (the second arc in **Figure 3.5**) [2, 35]. In this case, the capacitor is replaced by a constant phase element (CPE) with two parameters CPE-T and CPE-P. Given that the value of resistance (R) is available, they can be converted to capacitance (C) based on **Equation 3.11**. CPE-P is a value of between 0 and 1 and when it is equal to 1, the CPE is a pure capacitor [2, 35]. Indeed,

depending on the number of arcs present in a Nyquist plot, the equivalent circuit model is developed by connecting several R//C or R//CPE elements in series together with a resistance (corresponding to the ohmic resistance) and an inductor (if the inductance signal is observed at high frequencies and positive Z'') [2].

$$C = \frac{(RxCPE-T)^{\frac{1}{CPE-P}}}{R}$$ **Equation 3.11**

When the fitting is converged between the calculated impedances (based on the equivalent circuit model) and the measured impedances at each frequency, the ohmic resistance should be equal to the first x-intercept at high frequency in a Nyquist plot (**Figure 3.5**) and the resistance of each arc should be the same as the span of each arc on the x-axis in a Nyquist plot (**Figure 3.5**). The value of capacitance, on the other hand, is characteristic as different processes tend to have different capacitances as suggested by Irvine et al. [36]. Therefore, each observed arc can be classified to the corresponding source. With respect to the time constant (τ) of a specific process, it is equal to the product of resistance and capacitance (**Equation 3.12**) [36]. Indeed, it is crucial that the developed equivalent circuit model has physical meaning as more than one model can exist to accurately represent the data [2, 35].

$$\tau = RC$$ **Equation 3.12**

Moreover, apart from the most common R//CPE circuit to model the depressed semi-circle response from each process, Gerischer is a special circuit element which is sometimes observed as an electrode response [35, 37, 38]. As shown in **Figure 3.7**, a Gerischer element has a 45° slope in the high frequency region and a R//CPE like part in the low frequency region [38]. They indicate the oxygen ion diffusion feature and oxygen surface exchange feature, respectively in a thick electrode [37, 38]. In the equivalent circuit model (**Figure 3.7**), two parameters are used to fit the Gerischer element and they are GE-T and GE-P. The impedance equation with respect to ω of the Gerischer element is summarised in **Equation 3.13**, together with the Gerischer resistance ($R_{Gerischer}$) (**Equation 3.14**) and the time constant ($t_{Gerischer}$) (**Equation 3.15**). Hence, the corresponding capacitance of the Gerischer response can be calculated based on **Equation 3.12** [37].

$$Z(\omega) = \frac{1}{GE-T\sqrt{GE-P+i\omega}}$$ **Equation 3.13**

$$R_{Gerischer} = \frac{1}{GE-T\sqrt{GE-P}}$$ **Equation 3.14**

$$t_{Gerischer} = \frac{1}{GE-P}$$ **Equation 3.15**

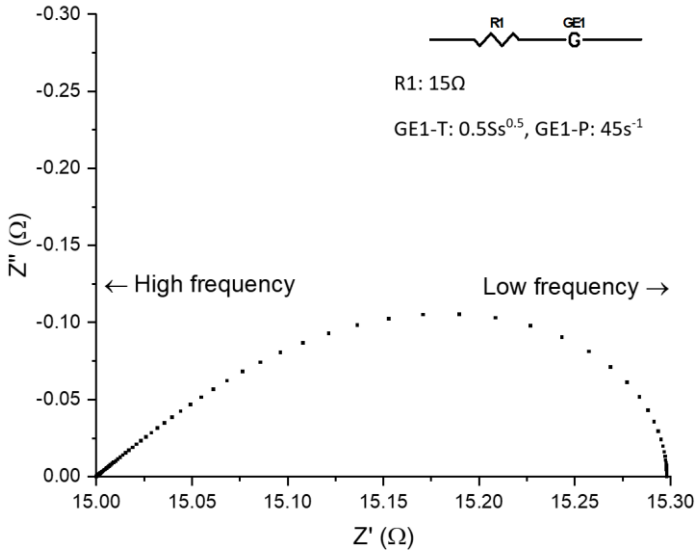


Figure 3.7: An example of a Gerischer electrode response in a Nyquist plot with the corresponding equivalent circuit model and parameters provided.

Electrode polarisation resistance (R_p) at a specific temperature in air is the most common indicator that reflects the air electrode performance. For the symmetrical cell configuration sample as mentioned in **Section 3.3**, R_p can be easily measured by summing up all the electrode resistances in an equivalent circuit model [2]. If no other process is apparent in the data except the electrode response, R_p can also be calculated as the distance between the first and the last x-intercepts in a Nyquist plot [2]. Finally, given that the cross-section area of electrodes (A) are known, the area specific resistance (ASR) can be calculated by **Equation 3.16**, where the symmetry of the sample is considered by the division of 2 [2, 39]. ASR is a normalised resistance and is used to compare the performance with other electrodes possibly measured under different dimensions.

$$ASR = \frac{R_p x A}{2}$$ **Equation 3.16**

3.4.5.2 Instrumentation and experimental set up

The sample of interest was mounted in the custom-built alumina sample holder as shown in **Figure 3.8**. Either platinum or gold mesh was used as the current collector on either side of the electrode. The physical contact between the meshes and the sample was maintained by a spring (not shown in the figure) which pulls the movable outer tube to the left. The sample holder and an extra thermocouple (not shown here) were then placed in a tube furnace which allows heating the sample to normal solid oxide cells operating temperatures. The thermocouple was located close to the sample so that the real sample temperature could be measured. Both of the platinum wires were connected to a frequency response analyser (FRA) (Solartron 1260a Impedance/Gain-Phase Analyser) which introduces an AC voltage under various frequencies and records the corresponding current signals from the sample. Detailed instrumental and experimental parameters used are discussed in **Section 6.2**.

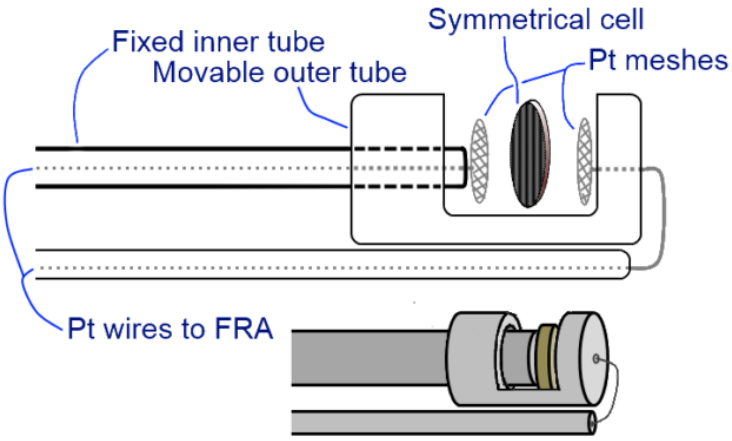


Figure 3.8: The custom-built sample holder used for AC impedance test. Au meshes were also used to replace the Pt meshes. Reproduced from [2] under a Creative Commons Attribution Non-Commercial No Derivatives licence.

3.4.5.3 Kramers-Kronig (K-K) data validity test

Before analysing AC impedance results, it is important to check if the collected data has any feature of causality, linearity and stability [35, 40]. This is achieved by performing a Kramers-Kronig data validity test [35, 40]. If the test fails, data re-acquisition is required [35]. Causality represents the direct correlation between the applied AC voltage and the recorded AC current whereas linearity means that the relationship between the applied AC voltage and the recorded AC current is linear [35].

Stability indicates that the state of the system must be in equilibrium when data is acquired [35]. If all three criteria are fulfilled, then the Kramers-Kronig relations can be established between the real part and the imaginary part of a valid impedance spectrum [35, 40]. The test result is illustrated as the difference between the measured real impedance and the converted one using the Kramers-Kronig relation from the measured imaginary impedance and vice versa over the whole frequency range [35, 40]. The smaller the differences/residuals are, the better the quality of the measured spectrum [40]. The software package of Lin-KK Tool was applied to conduct the Kramers-Kronig data validity test for the measured AC impedance spectra [40].

3.4.5.4 Distribution of relaxation time (DRT)

Distribution of relaxation time (DRT) is the most recently developed approach to analysis of AC impedance data. It converts the impedance data (Z(ω)) from the frequency domain to the time domain by solving **Equation 3.17** where $R_{ohmic,}$ τ, f and γ are the ohmic resistance, the time constants, the frequencies and the function that describes the time relaxation characteristics of the processes observed from the impedance data [41]. The main advantage of applying DRT is its higher frequency resolution (>5Hz), compared to the data in the frequency domain in which the characteristic frequency of any two adjacent processes need to be at least two to three orders of magnitude (e.g. >100Hz) in order to be recognised [42]. However, care must be taken when using the DRT approach as more than one solution exists when solving **Equation 3.17** [41, 43]. Therefore, depending on the inversion methods chosen, careful selection of the processing parameter is required and the resulting peaks must be attributed to a corresponding physical processes [42, 43]. The free Matlab toolbox, called DRTtools [41], was used to interpret the AC impedance data and the detailed methodology can be found in the same reference.

$$Z(f) = R_{ohmic} + \int_{-\infty}^{\infty} \frac{\gamma(\ln(\tau))}{1+i2\pi f\tau} dln\tau \qquad \textbf{Equation 3.17}$$

3.4.6 Inductively coupled plasma atomic emission spectroscopy (ICP-AES)

Inductively coupled plasma atomic emission spectroscopy (ICP-AES) is capable of evaluating the concentration of each element in a sample in the sensitivity of part per million (ppm) level [2]. This is achieved by using an argon based plasma source

produced by electromagnetic induction [2]. It atomises a sample introduced as an aqueous mist [2]. Atoms are then lost and received electrons when interacting with the plasma and they emit an optical radiation with the characteristic wavelength corresponding to a specific element [2]. The measured intensity of a specific wavelength in the target sample can be compared with the intensity from the reference samples which the elemental concentrations are known [2]. Hence, the concentration of the element in the target sample can be measured.

Two types of samples are prepared and they are the sample to be tested and the reference samples. As the measurement from the ICP-AES (Thermo Scientific iCAP 6000 Series) is the most accurate when an element concentration is between 1-20 ppm, the samples were prepared to ensure that the concentration for the element of interest is within this range. To prepare the tested sample, weighed powder (e.g. synthesised $Pr_2NiO_{4+\delta}$) was dissolved in a dilute nitric acid solution. Commercial praseodymium and nickel ICP standards (Sigma-Aldrich) with known concentration were used to prepare reference samples of various ppm concentrations. The quality of the prepared reference samples were examined as a plot of the intensity counts versus the concentration and a straight line should result for both praseodymium and nickel [2]. The concentration of praseodymium and nickel based on their measured intensities from the tested sample can be calculated by interpolation from these reference plots. It is important to note that the measured values of praseodymium and nickel are in ppm level. To convert them to the unit of moles for praseodymium and nickel atomic ratio calculation, they need to be divided by the corresponding atomic weight [2].

3.4.7 Archimedes density testing

The density of the sintered pellets such as 10Sc1CeSZ electrolyte, $Ce_{0.75}Gd_{0.1}Pr_{0.15}O_{2-\delta}$ (CGPO) and $Pr_4Ni_3O_{10+/-\delta}$, which were prepared for AC impedance or DC electrical conductivity measurement, were evaluated using an Archimedes balance (Sartorius CP124S). Based on the Archimedean principle where the volume of an object is equal to the volume of the displaced liquid (distilled water here) in which the object is immersed, the density of the object can be measured if its mass and the volume of the displaced liquid can be measured [44]. Since the volume of the displaced liquid

can be calculated from the buoyancy force (G), the difference between the weights of the sample in air (W_{dry}) and when it is immersed in liquid, and the density of liquid (ρ_{fl}), **Equation 3.18** was derived to calculate the density of the sintered pellets ($\rho_{measured}$) [44]. In **Equation 3.18**, extra factors such as air buoyancy in terms of air density (ρ_{air}) and the additional buoyancy effect caused by the wires of the weighing assembly (D) are also considered to eliminate any instrumental errors [44]. Indeed, before weighing the sample in water, the sample was boiled in water for a few minutes to ensure that all the open pores were filled with water.

$$\rho_{measured} = \frac{W_{dry} \cdot [\rho_{fl} - \rho_{air}]}{DG} + \rho_{air} \qquad \textbf{Equation 3.18}$$

The measured solid density was then compared with the theoretical density ($\rho_{theoretical}$) calculated from **Equation 3.19** where Z, MW, V_c and N_A are the number of formula unit in a single unit cell, the molecular weight of a formula unit, the unit cell volume from Inorganic Crystal Structure Database (ICSD) and Avogadro's number [1].

$$\rho_{theoretical} = \frac{Z \cdot MW}{V_c N_A} \qquad \textbf{Equation 3.19}$$

3.4.8 Electrode adherence testing

Electrode adherence testing was used to determine electrode sintering temperature. This was achieved by pressing a piece of Scotch tape on the surface of a sintered electrode and then the tape was removed from it [2, 45]. If the electrode sintered well on an electrolyte pellet, then no electrode residue should be left on the sticky side of the tape [2]. Otherwise, the test failed and demonstrated the unsatisfactory electrode adherence on the electrolyte. Further modification of the sample preparation process, such as higher sintering temperature, would need to be applied. Nevertheless, material chemical compatibility and material stability should also be considered when optimising the electrode sintering temperatures. All the symmetrical cells with various electrodes were prepared based on the electrode sintering conditions that passed the Scotch tape test before being used for the following electrode performance test and the long term (7 days) performance test.

3.4.9 Iodometric titrations

Unlike neutron diffraction and thermogravimetric analysis which allow *in-situ* measurement of material oxygen content under various atmospheres and temperatures, iodometric titration measures the oxygen content of an as-received powder. The synthesised $Pr_4Ni_3O_{10+/-\delta}$ powder (~0.05 g) was dissolved in concentrated hydrochloric acid (37 vol.%) (~25 mL) in an airtight glassware of which the inner environment was flushed with argon to remove any potential oxidant [9, 46]. Since the content of Ni^{3+} in $Pr_4Ni_3O_{10+/-\delta}$ is proportional to the oxygen content in the material, the real quantity of Ni^{3+} was measured indirectly based on the following three equations (**Equations 3.20**, **3.21** and **3.22**) [9, 46].

$$2Ni^{3+}_{(aq)} + 2Cl^{-}_{(aq)} \rightarrow 2Ni^{2+}_{(aq)} + Cl_{2(g)} \qquad \textbf{Equation 3.20}$$

$$Cl_{2(g)} + 2I^{-}_{(aq)} \rightarrow 2Cl^{-}_{(aq)} + I_{2(aq)} \qquad \textbf{Equation 3.21}$$

$$I_{2(aq)} + 2S_2O^{2-}_{3(aq)} \rightarrow 2I^{-}_{(aq)} + S_4O^{2-}_{6(aq)} \qquad \textbf{Equation 3.22}$$

Ni^{+3} acted as an oxidant which oxidised the chloride ions originating from hydrochloric acid to form chlorine gas (**Equation 3.20**) [9, 46]. The produced chlorine gas was then flowed with argon and bubbled through the potassium iodide solution (~0.1 M). The iodide ion was then oxidised by the chlorine gas and iodine was formed (**Equation 3.21**) [9, 46]. It is worth mentioning that under conditions when both iodine and excess iodide ions are present, they will be in equilibrium with the triiodide ion (I_3^-) [9]. However, aqueous iodine is used in the equations for simplicity. At the end of the chemical reaction, the reacted potassium iodine solution was titrated by sodium sulphate solution (~0.01 M) using starch solution as an indicator (**Equation 3.22**) [9, 46]. The titration finished when the titrated solution colour changed from dark brown to transparent [9]. The amount of Ni^{3+} in the material (in mole) is the same as the amount of sodium sulphate consumed (in mole) [9]. Therefore, the oxygen content in the as-synthesised $Pr_4Ni_3O_{10+/-\delta}$ can be calculated [9]. The experiment was conducted at least three times to check for the reproducibility [46].

3.5 Summary

An introduction to the experimental methods used, including the corresponding theoretical background, was discussed in this chapter. It clearly explains the general approaches used for the following research. The detailed experimental set up and the parameters used in each study will be included in **Sections 4.2**, **5.2** and **6.2**.

References

[1] A. R. West, "Basic Solid State Chemistry", Second Edition, Chichester, UK, John Wiley & Sons, Ltd, 1999.

[2] R. Woolley, "PhD thesis: Ruddlesden-Popper Phases as Solid Oxide Fuel Cell Cathodes: Electrochemical Performance and In Situ Characterisation", Imperial College London, 2014.

[3] T. Nomura, S. Nishimoto, Y. Kameshima, M. Miyake, *Journal of the Ceramic Society of Japan,* 120, 534-538, 2012.

[4] A. E. Danks, S. R. Hall, Z. Schnepp, *Materials Horizons,* 3, 91-112, 2016.

[5] T. Chen, Y. Zhou, C. Yuan, M. Liu, X. Meng, Z. Zhan, C. Xia, S. Wang, *Journal of Power Sources,* 269, 812-817, 2014.

[6] T. Chen, M. Liu, C. Yuan, Y. Zhou, X. Ye, Z. Zhan, C. Xia, S. Wang, *Journal of Power Sources,* 276, 1-6, 2015.

[7] P. Barboux, P. Griesmar, F. Ribot, L. Mazerolles, *Journal of Solid State Chemistry,* 117, 343-350, 1995.

[8] J. M. Bassat, C. Allancon, P. Odier, J. P. Loup, M. Deus Carvalho, A. Wattiaux, *European Journal of Solid State and Inorganic Chemistry,* 35, 173-188, 1998.

[9] M. A. Yatoo, "PhD thesis: Ruddlesden-Popper Phase Materials for Solid Oxide Fuel Cells: Performance and Structural Studies", Imperial College London, 2019.

[10] S. B. Adler, *Chemical Reviews,* 104, 4791-4843, 2004.

[11] "X-ray diffraction," mySCOPE Microscopy Australia. Available: https://myscope.training/legacy/xrd.

[12] J. Rodriguez-Carvajal, *Physica B.,* 192, 55-69, 1993.

[13] V. K. Pecharsky, P. Y. Zavalij, "Fundamentals of Powder Diffraction and Structural Characterization of Materials", Second Edition, New York, USA, Springer Science+Business Media, LLC, 2009.

[14] "X-Ray diffraction (XRD)," Anton Paar. Available: https://wiki.anton-paar.com/en/x-ray-diffraction-xrd/#validation-by-thermal-lattice-expansion.

[15] “HTK 1200N- oven heater,” Malvern Panalytical. Available: https://www.malvernpanalytical.com/en/products/category/x-ray-components/non-ambient-chambers/htk-1200n/.

[16] B. H. Toby, R. B. Von Dreele, *Journal of Applied Crystallography,* 46, 544-549, 2013.

[17] J. Rodríguez-Carvajal, *An Introduction of the program: Fullprof 2000,* Gif-sur-Yvette, France: Laboratoire Léon Brillouin (CEA-CNRS), 2001.

[18] L. B. McCusker, R. B. Von Dreele, D. E. Cox, D. Louer, P. Scardi, *Journal of Applied Crystallography,* 32, 36-50, 1999.

[19] “Diffraction,” Diamond Light Source. Available: https://www.diamond.ac.uk/Instruments/Techniques/Diffraction.html.

[20] “I11: High Resolution Powder Diffraction,” Diamond Light Source. Available: https://www.diamond.ac.uk/Instruments/Crystallography/I11.html.

[21] E. S. Nikova, Y. A. Salamatov, E. A. Kravtsov, V. I. Bodnarchuk, V. V. Ustinov, *Physica B: Condensed Matter,* 552, 58-61, 2019.

[22] “What is ISIS Neutron and Muon Source?,” Science & Technology Facilities Council. Available: https://www.isis.stfc.ac.uk/Pages/What-does-ISIS-Neutron-Muon-Source-do.aspx.

[23] “High Resolution Powder Diffraction,” Science & Technology Facilities Council. Available: https://www.isis.stfc.ac.uk/Pages/Hrpd.aspx.

[24] I. D. Brown, “The Chemical Bond in Inorganic Chemistry: The Bond Valence Model”, Volume 27 of IUCr Monographs on Crystallography, Second Edition, Oxford, UK, Oxford University Press, 2016.

[25] I. D. Brown, “Bond valence parameters,” International Union of Crystallography. Available: https://www.iucr.org/resources/data/data-sets/bond-valence-parameters.

[26] “Scanning Electron Microscopy,” mySCOPE Microscopy Australia. Available: https://myscope.training/#/SEM.

[27] “Energy Dispersive Spectroscopy,” mySCOPE Microscopy Australia. Available: https://myscope.training/#/EDS.

[28] E. Metcalfe, J. Broomfeld, *Journal De Physique,* 45, C2 407-410, 1984.

[29] M. B. Heaney, “Electrical Conductivity and Resistivity,” in *Electrical Measurement, Signal Processing, and Displays*, Editior: J. G. Webster, Boca Raton, USA, CRC Press, 7 1-14, 2003.

[30] L. J. van der Pauw, *Philips Technical Review,* 26, 220-224, 1958/59.

[31] M. Yamashita, *Japanese Journal of Applied Physics,* 25, 563-567, 1986.

[32] M. Reveil, V. C. Sorg, E. R. Cheng, T. Ezzyat, P. Clancy, M. O. Thompson, *Review of Scientific Instruments,* 88, 094704 1-12, 2017.

[33] S. H. N. Lim, D. R. McKenzie, M. M. M. Bilek, *Review of Scientific Instruments,* 80, 075109 1-4, 2009.

[34] A. A. Ramadan, R. D. Gould, A. Ashour, *Thin Solid Films,* 239, 272-275, 1994.

[35] B. A. Boukamp, *Introduction to Electrochemical Impedance Spectroscopy,* Lille, France: International workshop on impedance spectroscopy applied to the study of porous electrodes for electrochemical applications, 2018. Available: https://research.utwente.nl/en/activities/introduction-to-electrochemical-impedance-spectroscopy-tutorial.

[36] J. T. S. Irvine, D. C. Sinclair, A. R. West, *Advanced Materials,* 2, 132-138, 1990.

[37] S. B. Adler, J. A. Lane, B. C. H. Steele, *Journal of The Electrochemical Society,* 143, 3554-3564, 1996.

[38] A. Flura, C. Nicollet, V. Vibhu, A. Rougier, J.-M. Bassat, J.-C. Grenier, *Electrochimica Acta,* 231, 103-114, 2017.

[39] T. Ogier, F. Mauvy, J.-M. Bassat, J. Laurencin, J. Mougin, J.-C. Grenier, *International Journal of Hydrogen Energy,* 40, 15885-15892, 2015.

[40] "Kramers-Kronig Validity Test Lin-KK for Impedance Spectra," Karlsruhe Institute of Technology. Available: http://www.iam.kit.edu/wet/english/Lin-KK.php.

[41] T. H. Wan, M. Saccoccio, C. Chen, F. Ciucci, *Electrochimica Acta,* 184, 483-499, 2015.

[42] X. Zhang, Y. Song, G. Wang, X. Bao, *Journal of Energy Chemistry,* 26, 839-853, 2017.

[43] B. A. Boukamp, *Distribution Function of Relaxation Times for SOFC electrodes,* Lille, France: International workshop on impedance spectroscopy applied to the study of porous electrodes for electrochemical applications, 2018. Available: https://research.utwente.nl/en/activities/distribution-function-of-relaxation-times-for-sofc-electrodes-tut.

[44] *Sartorius YDK03-Density Determination Kit User Manual, Sartorius,* Gottingen, Germany.

[45] R. J. Wolley, S. J. Skinner, *Journal of Power Sources,* 243, 790-795, 2013.

[46] C. D. Ling, D. N. Argyriou, G. Wu, J. J. Neumeier, *Journal of Solid State Chemistry,* 152, 517-525, 1999.

Chapter 4 Chemical compatibility between $Pr_2NiO_{4+\delta}$ and $Ce_{0.9}Gd_{0.1}O_{2-\delta}$ under solid oxide cell sintering and operating temperatures

4.1 Introduction

As mentioned in **Section 2.5.4**, the electrode performance of $Pr_2NiO_{4+\delta}$ was reported to be the best among the other lanthanide nickelate candidates and was even comparable to the conventional $La_{0.6}Sr_{0.4}Fe_{0.8}Co_{0.2}O_{3-\delta}$ (LSCF) air electrode material [1, 2]. However, introduction of a $Ce_{1-x}Gd_xO_{2-\delta}$ (CGO) barrier layer at the air electrode and conventional zirconia electrolyte interface was usually required to avoid the formation of insulating $Pr_2Zr_2O_7$ (**Sections 2.5.4** and **2.5.5**) [2, 3]. CGO barrier layer also enhanced the electrochemical performance of symmetrical cells by improving the adherence of an air electrode [2]. $Pr_2NiO_{4+\delta}$/CGO/$Zr_{1-x}Y_xO_{2-\delta}$(YSZ) was proved to have a better electrode performance than the state-of-the-art LSCF/CGO/YSZ symmetrical cell [2].

Despite the high performance of $Pr_2NiO_{4+\delta}$/CGO/$Zr_{1-x}Y_xO_{2-\delta}$(YSZ), it was not stable and the reasons for degradation can be categorised based on the following mechanisms: 1) The chemical reaction between $Pr_2NiO_{4+\delta}$ and CGO to from $Ce_{1-x-y}Gd_xPr_yO_{2-\delta}$ (CGPO) phases [4, 5]. 2) The decomposition of $Pr_2NiO_{4+\delta}$ at temperature below 900^{o}C under an oxidative atmosphere and the formation of $Pr_4Ni_3O_{10+/-\delta}$, the high order RP phase, and PrO_x [6]. Nevertheless, it is interesting to find that the degradation processes had no apparent negative impact on the overall electrochemical performance which might suggest the activation of the resulting degradation products towards the electrode performance [4, 5].

Several investigations have been conducted to investigate the decomposition products [3, 4, 5, 7], but the mechanism and formation kinetics of the various phases and the proper quantification of the actual CGPO composition are still unclear. In this chapter, a systematic approach and a combination of different materials characterisation techniques were applied to reveal each chemical product formed from the reaction between $Pr_2NiO_{4+\delta}$ and CGO under normal electrode sintering and operating temperatures.

4.2 Detailed experimental procedures

A nitrate-citrate route was used to synthesise $Pr_2NiO_{4+\delta}$ [2]. This was achieved by mixing the correct stoichiometric ratio of $Pr(NO_3)_3.6H_2O$ (Aldrich) and $Ni(NO_3)_2.6H_2O$ (Alfa Aesar), which have purity greater than 99.9%, with excess citric acid solution (10 wt.% of citric acid (Aldrich)). Due to the hygroscopic nature of the nitrate precursors, their actual water contents were evaluated by measuring the weight difference before and after the decomposition at 600°C for several hours in air, resulting in the formation of Pr_6O_{11} and NiO, respectively. Citric acid acted as a chelating agent in this wet chemistry approach. Water was evaporated from the resulting solution by heating on a hot plate until the formation of a gel. The gel was then decomposed at 600^{o}C for 12 hours in air to obtain a precursor powder which was further calcined at 1075^{o}C for 8 hours in air to generate the final product.

The samples used for chemical compatibility tests were prepared by mixing the synthesised $Pr_2NiO_{4+\delta}$ powder and $Ce_{0.9}Gd_{0.1}O_{2-\delta}$ (CGO10) (Fuel Cell Materials, USA) powder in 4:1 weight ratio using a pestle and mortar with an addition of ethanol. Some of the samples were then uniaxially and isostatically pressed to form a pellet. The samples in loose powder and pressed pellet forms were thermally treated at 1100^{o}C, the normal sintering temperature, between 2 and 12 hours in air. Finally, the pressed samples which were previously heated at 1100^{o}C for 12 hours in air were further thermally treated at 800^{o}C for 24 hours in air (in pressed pellet form) to evaluate any additional phase change at the conditions resembling normal solid oxide cell operating temperatures.

The laboratory powder X-ray diffractometer (PANalytical X'Pert Pro MPD with a Cu K_α source) was used to analyse any phase change of the samples after each thermal treatment, applying the same instrumental parameters mentioned in **Section 3.4.1.2**. All the samples were manually ground into powder before the examination. Fullprof software suite [8] was then applied to conduct Rietveld/Le Bail refinement of the diffraction data. The Pr and Ni ratio of the synthesised $Pr_2NiO_{4+\delta}$ was confirmed by using inductively coupled plasma atomic emission spectroscopy (ICP-AES, Thermo Scientific iCAP 6000 Series).

To distinguish any subtle phase changes, high resolution synchrotron X-ray powder diffraction (HR-SXRPD) (Beamline I11, Diamond Light Source Ltd, UK with X-ray wavelength of 0.824874(10) Å and 2θ zero shift of 0.004266(2)°) was used to examine selected ground samples after the thermal treatment at room temperature. The ground samples were loaded in a borosilicate glass capillary (0.5 mm inner diameter) to the height of around 40-50 mm. The open end of the capillary was then sealed by wax. The total scanning time of each sample was the same and was set to be 3600 seconds.

In addition, scanning transmission electron microscopy (STEM) energy dispersive X-ray spectroscopy (EDS) mapping (Titan 80/300 TEM/STEM with Bruker Quantax EDS) was used to determine the CGPO chemical compositions after heating the pressed samples at 1100^{o}C for 2 and 12 hours in air. The commercial CGO10 powder was also examined to validate the experimental parameters and the following data quantification approach. The experimental parameters of the STEM EDS mapping were 300 kV accelerating voltage, 4.5 kV field emission electron gun (FEG) extraction voltage, 99 µA FEG emission current, 15° tilting of the stage, with total STEM EDS scanning time of 20 minutes for each site of interest. ESPRIT software (Bruker) was used to analyse the data via the process of element identification, background determination, element line deconvolution and element quantification applying the Cliff-Lorimer approach. The samples used for STEM EDS mapping was prepared by drying the suspended powder in analytical grade isopropanol on the TEM copper grid and fabricating electron transparent lamella using the focused ion beam scanning electron microscope (FIB-SEM, FEI Helios NanoLab 600) (5 kV, 2.8 nA) for the powder and the sintered samples, respectively.

The particle size of each phase in the thermally untreated sample was identified by the scanning electron microscope (SEM) equipped with the energy dispersive X-ray spectroscopy detector (EDS) (Zeiss Leo Gemini 1525 with Inca X-act EDS) (EHT of 20 kV, aperture size of 60 µm).

4.3 Phase identification of the synthesised materials and the thermally untreated powder mixture

The Rietveld refinement result of the as-synthesised $Pr_2NiO_{4+\delta}$ powder is shown in **Figure 4.1** with the data obtained from laboratory based X-ray diffraction (XRD). The synthesised $Pr_2NiO_{4+\delta}$ phase presented here was best described by the orthorhombic *Fmmm* space group and had lattice parameters determined to be a = 5.3946(1) Å, b = 5.4524(1) Å and c = 12.4445(1) Å. There was no evidence of any secondary phase being present within the instrument detection limits. ICP-AES, which has ppm level of element detection sensitivity, was further applied to examine the cation ratio (Pr:Ni) of the synthesised $Pr_2NiO_{4+\delta}$. The result with the ratio of 1.99(2) indicated excellent agreement to the target stoichiometric ratio of 2 in the system.

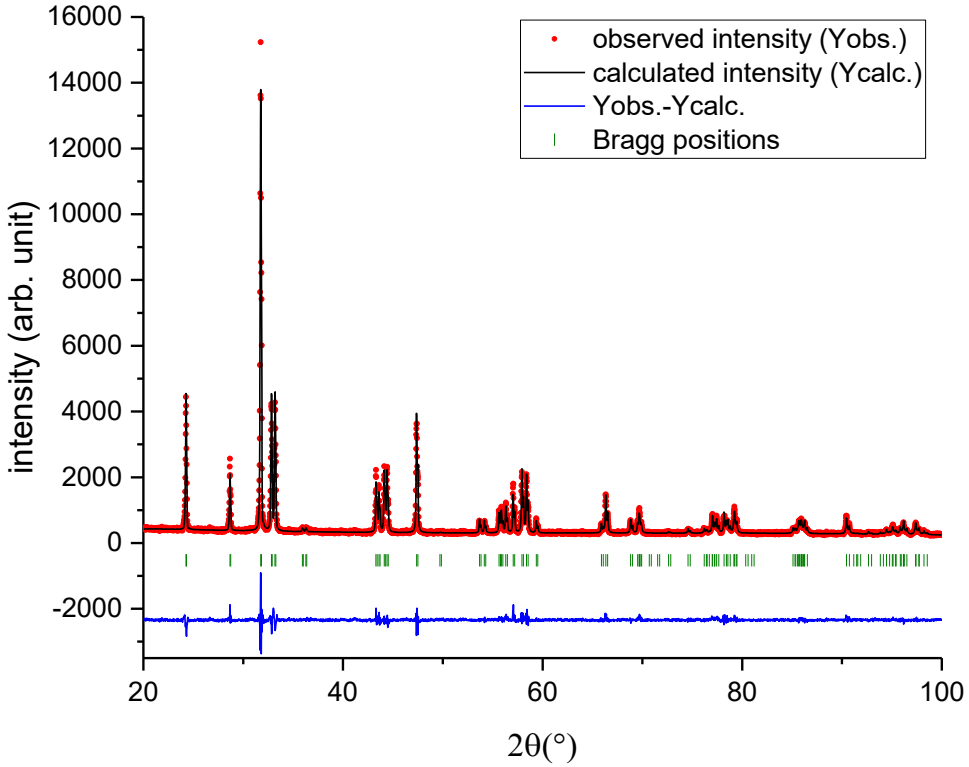


Figure 4.1: Rietveld refinement of the as-synthesised $Pr_2NiO_{4+\delta}$ powder based on the laboratory based XRD. The figure demonstrates that a single phase was received with acceptable goodness of fit (χ^2=2.74, R_{wp}= 7.57%, R_p= 5.96%). Reproduced from Tsai et al. [9].

Given that $Pr_2NiO_{4+\delta}$ was successfully synthesised, it was mixed with CGO10 powder, ready for the following chemical compatibility tests. As mentioned in **Section 4.2**, both XRD and HR-SXRPD were used to identify phase changes after samples were heated

under various conditions. Therefore, the diffractogram of the untreated sample must be evaluated first and was used as a reference to compare with other diffraction data after a certain thermal treatment. This is especially important when analyzing data from HR-SXRPD as its resolution is high enough to examine small phase changes. In **Figure 4.2**, HR-SXRPD data of the thermally untreated $Pr_2NiO_{4+\delta}$ and CGO10 powder mixture in 4:1 weight ratio was analysed by Le Bail refinement because only the peak positions and the space group of each phase were of interest. It is worth mentioning that $Pr_2NiO_{4+\delta}$ can no longer be modelled with the *Fmmm* space group in the HR-SXRPD data due to the observation of peak splitting. Broux et al. [10] suggested that there is a monoclinic distortion of the crystal structure and $Pr_2NiO_{4+\delta}$ was best indexed by the *C*2/*m* space group. Since the $Pr_2NiO_{4+\delta}$ crystal structure distortion was subtle and this was reflected from the small deviation of β lattice parameter in **Table 4.1** from 90°, $Pr_2NiO_{4+\delta}$ appeared to be an orthorhombic phase under low-resolution laboratory X-ray diffraction (**Figure 4.1**). Indeed, in **Figure 4.2**, there were some differences between the observed intensity and the calculated intensity, especially in the regions where the $Pr_2NiO_{4+\delta}$ Bragg positions are located. Based on the shape of the difference curve, the reason was attributed to the full width at half maximum (FWHM) mismatch which might be caused by the anisotropic line broadening feature of the $Pr_2NiO_{4+\delta}$ phase [11]. On the other hand, there was no change of the CGO10 crystal symmetry in the HR-SXRPD data and the same space group of *Fm*-3*m* was used in the refinement. Besides $Pr_2NiO_{4+\delta}$ and CGO10, no other secondary phase was observed in the HR-SXRPD diffractogram of the untreated sample (**Figure 4.2**). The corresponding lattice parameters of each phase are presented in **Table 4.1**.

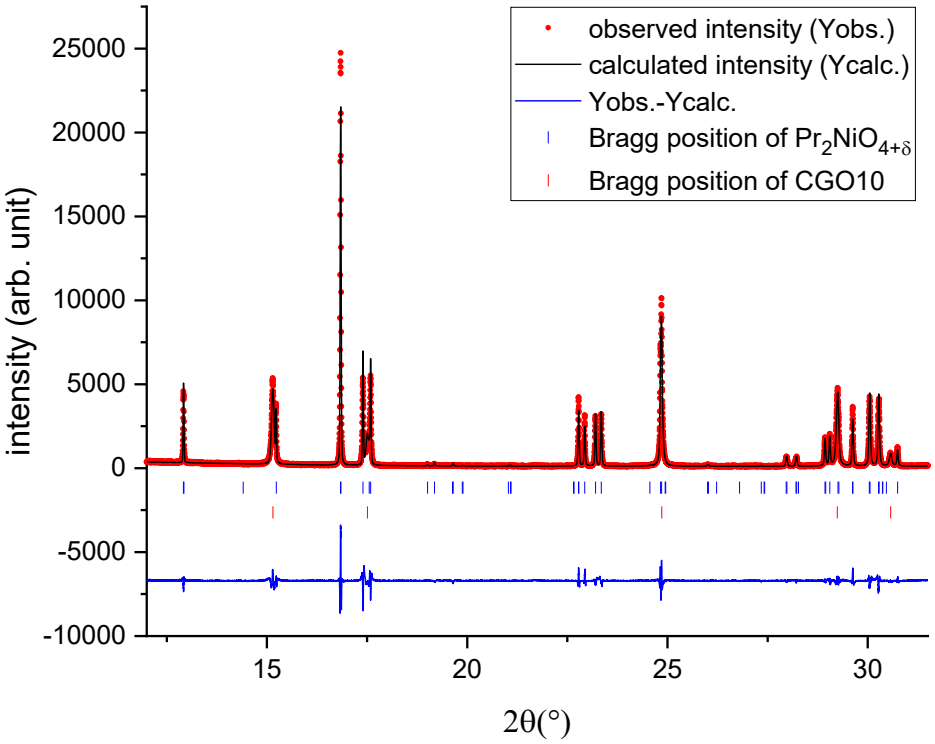


Figure 4.2: HR-SXRPD data of the untreated $Pr_2NiO_{4+\delta}$/CGO10 composite powder analysed by Le Bail refinement. The figure highlights the peak position of each phase with acceptable goodness of fit (χ^2=4.90, R_{wp}=12.1, R_p=8.86). Reproduced from Tsai et al. [9].

Table 4.1: The corresponding refined lattice parameters from **Figure 4.2** for $Pr_2NiO_{4+\delta}$ and CGO10. Reproduced from Tsai et al. [9].

Phase	Lattice parameters (Å)
$Pr_2NiO_{4+\delta}$ (Monoclinic, *C*2/*m*)	a = 5.3950(1), b = 12.4474(1), c = 5.4538(1), β = 89.943(1)°
CGO10 (Cubic, *Fm*-3*m*)	a = b = c = 5.4197(1)

In addition, the investigation of the particle size of each phase before the compatibility test was conducted. This was achieved using SEM in the backscattered electron imaging mode as shown in **Figure 4.3**. **Figure 4.3(a)** displays the low magnification image of the untreated $Pr_2NiO_{4+\delta}$ and CGO10 mixed powders. Two size ranges of particle were observed, with one group of particles in the micron size range (5-15 µm) and the other in the sub-micron size range (0.3-0.7 µm), forming a bimodal particle size distribution. EDS data were collected from multiple spots, as labelled in **Figure 4.3(b)**, to identify the phase(s) corresponding to each particle size range. The micron

size particles were found to be composed of $Pr_2NiO_{4+\delta}$ as only Pr and Ni signals were detected **Figure 4.4(a)**. On the other hand, Ce, Gd, Pr and Ni signals were observed from the sub-micron size particles **Figure 4.4(b)**. Hence, these sub-micron particles were identified as the CGO10 particles. The observation of Pr and Ni signals in these regions is mainly because of the difference between the particle size (sub-micron range) and the spatial resolution of EDS (around 1 μm^3). Therefore, part of the $Pr_2NiO_{4+\delta}$ particle below the CGO particle was detected. Overall, **Figure 4.3** indicates that $Pr_2NiO_{4+\delta}$ and CGO10 particles are of micron and sub-micron size, respectively.

It is important to note that no ball milling was applied to the synthesized $Pr_2NiO_{4+\delta}$ powder to further decrease the particle size to less than 1 µm. The variation of $Pr_2NiO_{4+\delta}$ particle size might influence the kinetics of the chemical reaction with CGO10 [3]. Indeed, it is unclear if phase or structural change of $Pr_2NiO_{4+\delta}$ material will occur under ball milling condition and hence, further investigation is required.

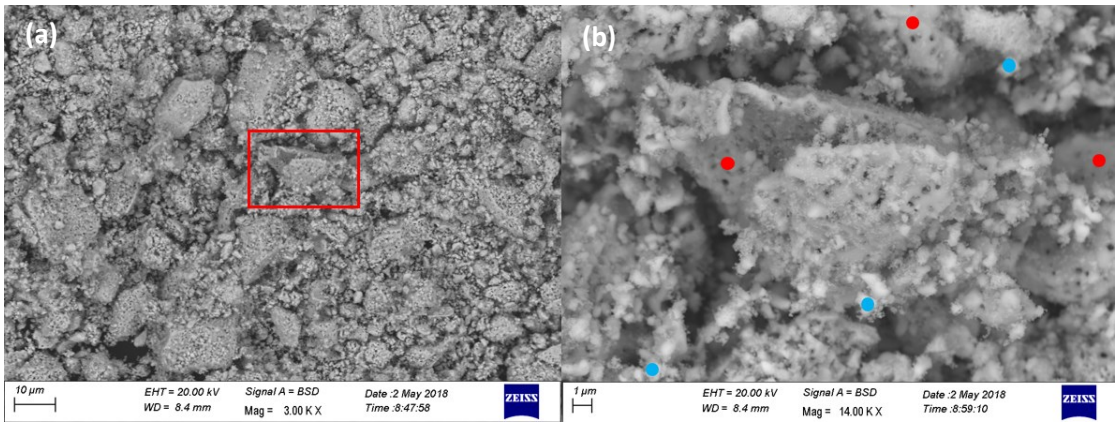
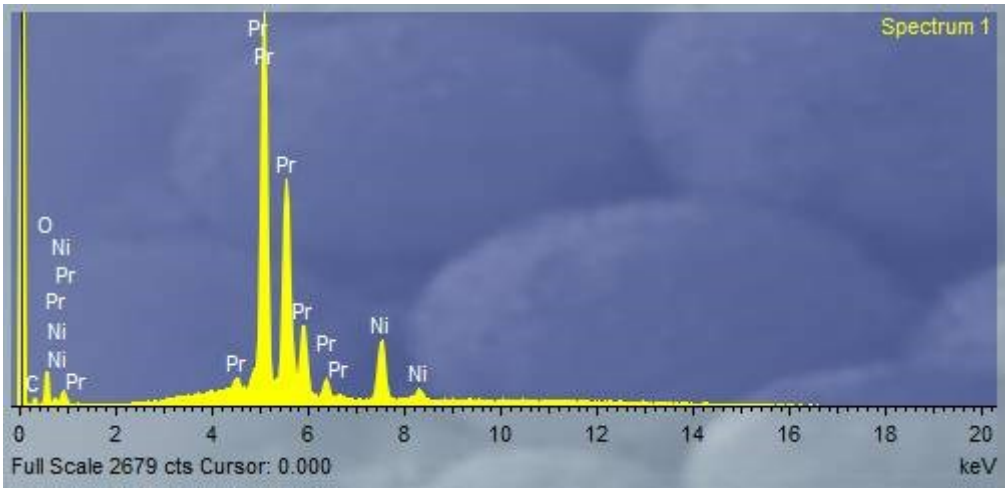


Figure 4.3: **(a)** The low magnification of the backscattered image showing bimodal distribution of particle size. **(b)** The magnification image of the red square region in **Figure 4.3(a)**. Point EDS was conducted at each location with red dots being identified as $Pr_2NiO_{4+\delta}$ and blue dots were CGO10. The corresponding EDS spectrum of red dots and blue dots can be found in **Figure 4.4(a)** and **(b)**. Reproduced from Tsai et al. [9].

(a)



(b)

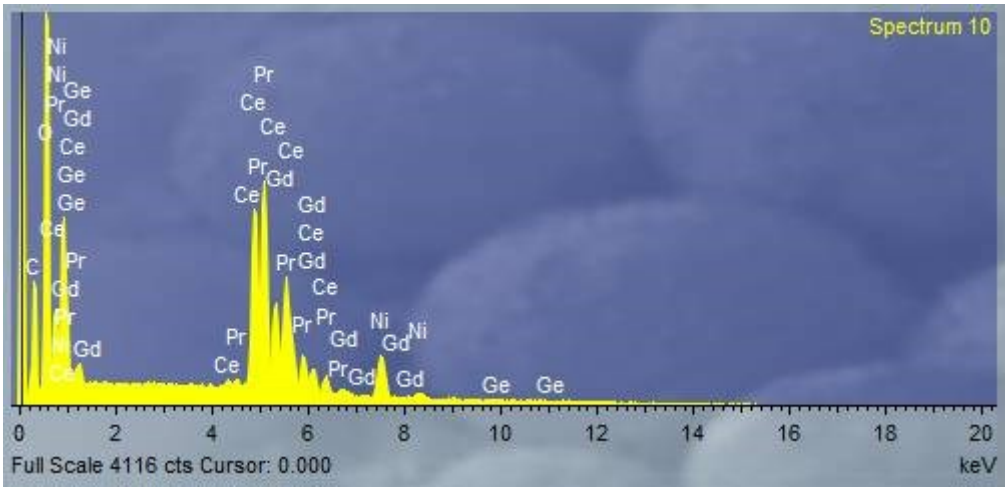


Figure 4.4: EDS spectrum corresponding to **(a)** red dots ($Pr_2NiO_{4+\delta}$) and **(b)** blue dots (CGO10) in **Figure 4.3(b).** The observed Ge signal in **Figure 4.4(b**) might be due to the presence of an impurity at the local regions.

4.4 Thermal treatment of the composites at cell sintering conditions

The chemical reaction of the samples thermally treated at 1100^{o}C for periods between 2 and 12 hours in both the loose powder and pressed pellet forms were first investigated using laboratory X-ray diffraction (**Figures 4.5(a)** and **4.6(a)**). The data obtained from the loose powder samples after thermal treatment were initially modelled with one substituted ceria phase (CGPO) in the Le Bail refinement as shown in **Figure 4.7**, but a poor fit was obtained in the two theta region corresponding to the substituted ceria phases (422) reflection in the X-ray diffractogram. This indicates that more than one substituted ceria phase was present in the system after the thermal

treatment. Therefore, one more substituted ceria phase was introduced in the Le Bail refinement and the improvement of the overall fitting was observed in the region of the (422) reflections, as shown in **Figure 4.5(b)**. On the other hand, the laboratory XRD data obtained from the thermally treated pressed pellet samples fit well with one substituted ceria phase (**Figure 4.6(b)**) although the small feature on the left shoulder of the main peak ((422) of CGPO) suggests the presence of more than one substituted ceria phase. Overall, the analysis results of each sample processed at different sintering times are summarised in **Figures 4.8(a)** and **(b)**. For the loose powder samples, considering that the substituted ceria phases had lattice parameters of 5.4185(4) Å (on average) and less than 5.4110(1) Å (depending on the total sintering time), they were classified as the unreacted CGO10 and the newly formed CGPO phases, respectively. It is known that the introduction of praseodymium into the fluorite structure of the substituted ceria will decrease the lattice parameters due to the smaller Pr^{+4} ionic radius (0.960 Å) compared with Ce^{+4} (0.970 Å) and Gd^{+3} (1.053 Å) [4, 12]. Indeed, the refined substituted ceria from the thermally treated dense pellet samples were regarded as the CGPO phase(s) due to the relatively small average lattice parameter of 5.4071(9) Å (for the samples heated between 2 and 12 hours). Overall, the relatively low quantity of the unreacted CGO10 phase and the relatively low CGPO lattice parameters in the pressed pellet samples compared to the loose powder samples indicate that the extent of the praseodymium diffusion into the unreacted CGO10 was more extensive in the pressed pellet samples. In addition, it is worth mentioning that NiO was observed in each of the thermally treated samples regardless of the sample type (**Figures 4.5(a)** and **4.6(a)**). This demonstrates that the source of Pr incorporated into the CGO10 originated from the partial decomposition of $Pr_2NiO_{4+\delta}$ [4].

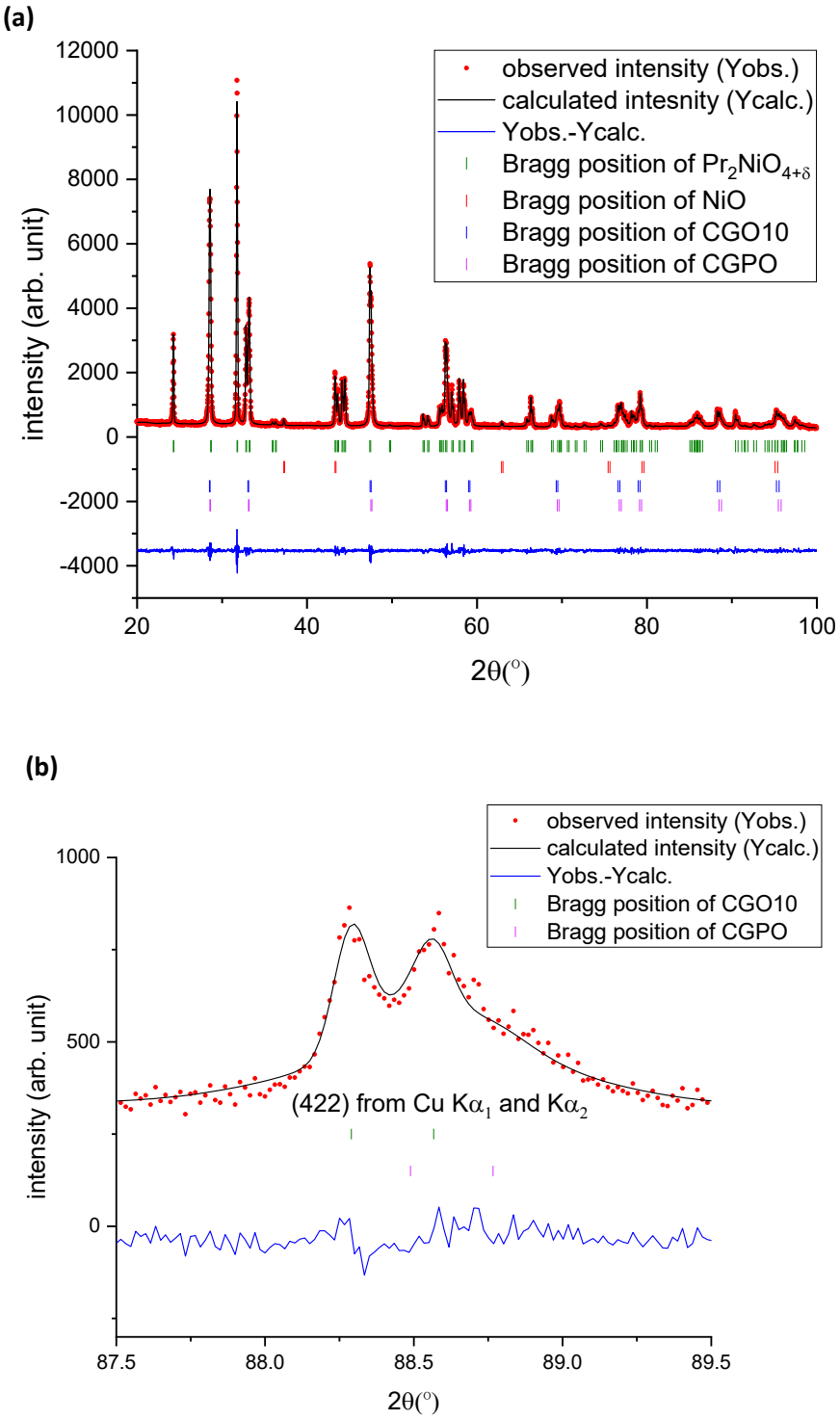


Figure 4.5: **(a)** Laboratory XRD data analysis results of the thermally treated (1100°C, 12 hours, air) $Pr_2NiO_{4+\delta}$ and CGO10 mixture in loose powder form using Le Bail refinement with both CGO10 and CGPO phases included in the model. The goodness of fit parameters are χ^2=1.97, R_{wp}=5.97% and R_p=4.69%. **(b)** The magnification of **Figure 4.5(a)** highlights the presence of the unreacted CGO10 and the newly formed CGPO phases at (422) reflection.

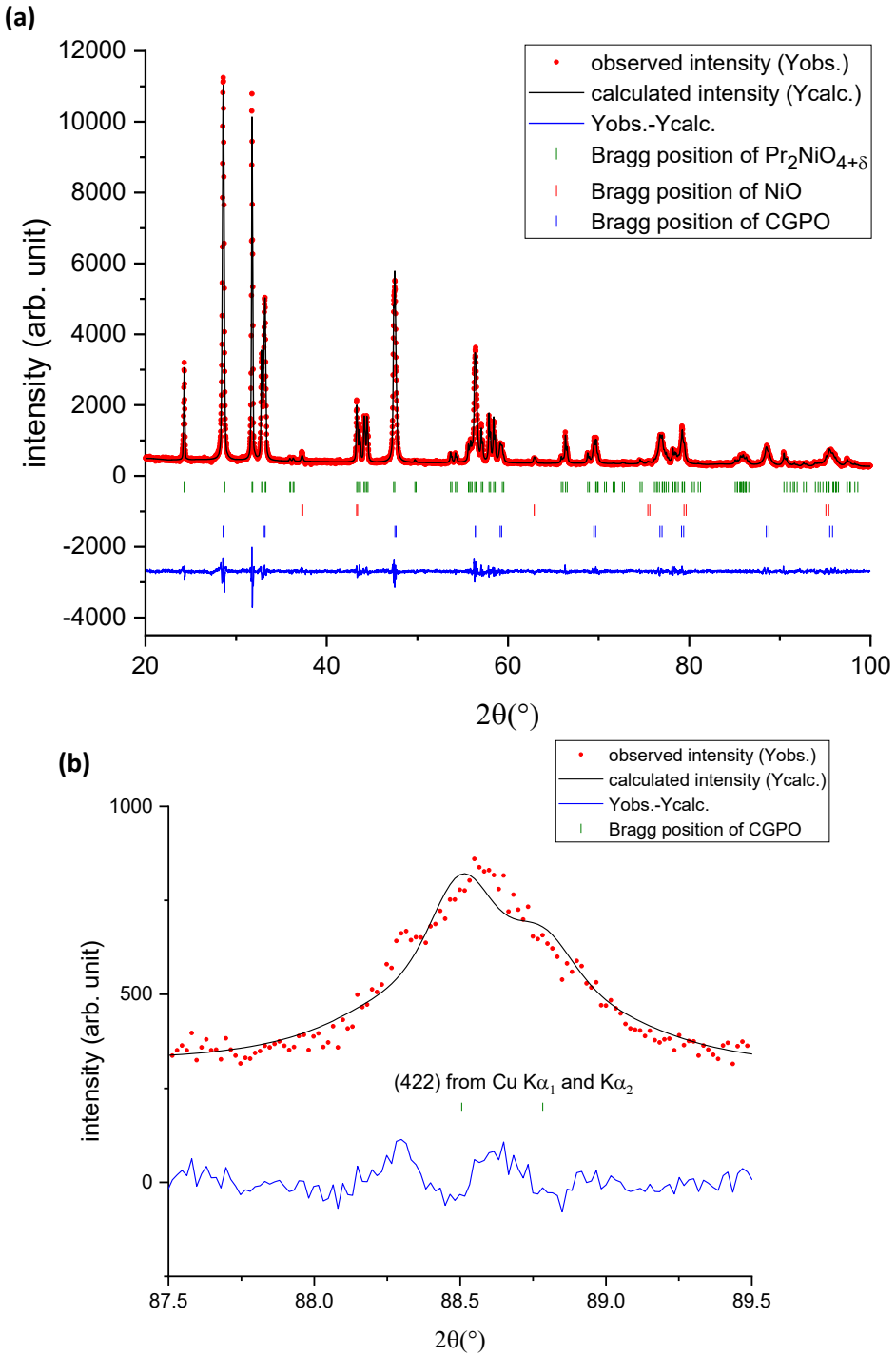


Figure 4.6: **(a)** Laboratory XRD data analysis results of the thermally treated (1100°C, 6 hours, air) $Pr_2NiO_{4+\delta}$ and CGO10 mixture in pressed pellet form using Le Bail refinement with one CGPO phase included in the model. The goodness of fit parameters are χ^2=2.14, R_{wp}=6.02% and R_p=4.72%. **(b)** The magnification of **Figure 4.6(a)** shows the extra unindexed peak at the left shoulder of the CGPO (422) reflection which highlights the presence of more than one substituted ceria phase. Reproduced from Tsai et al. [9].

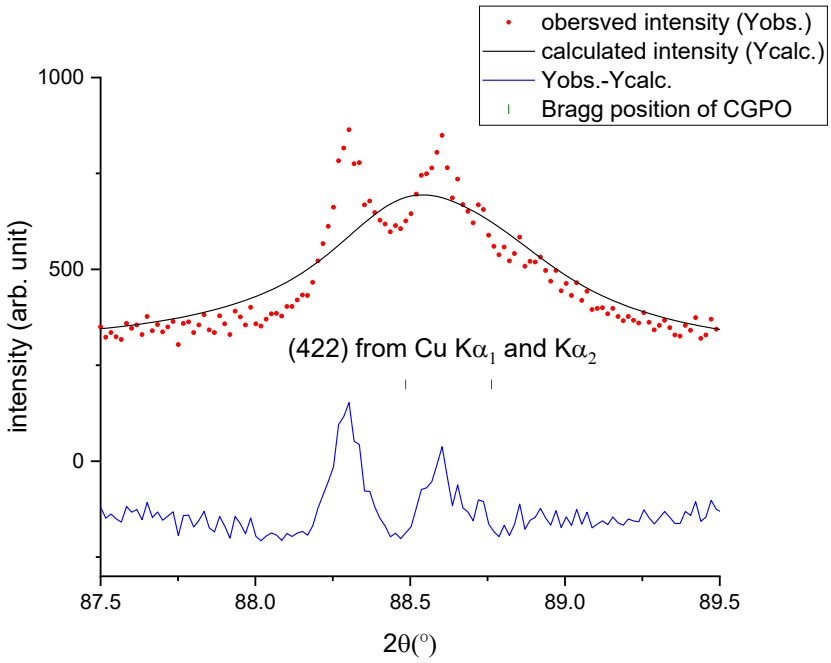
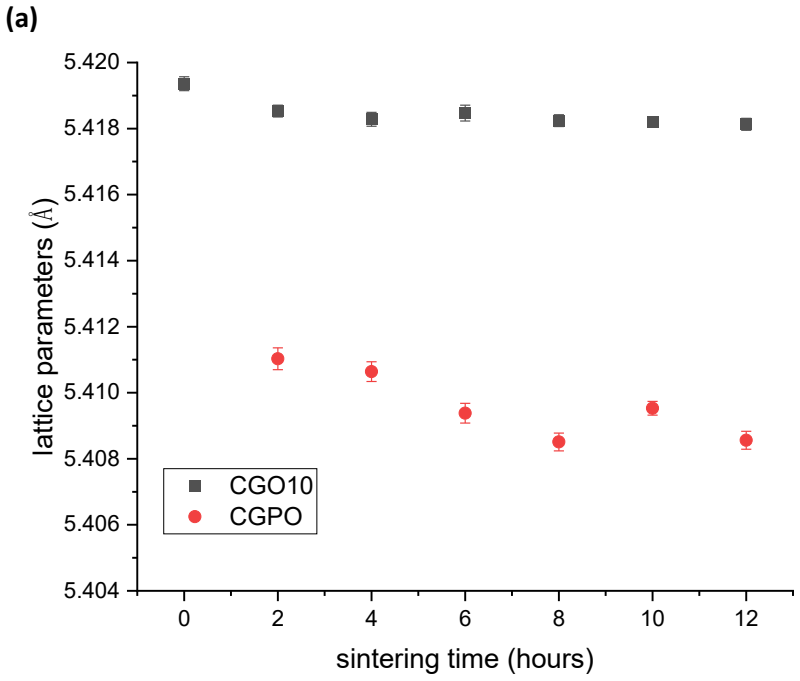


Figure 4.7: Laboratory XRD data obtained in the 2θ region corresponding to the (422) substituted ceria reflection. The figure demonstrates that a single CGPO phase cannot model the data for the $Pr_2NiO_{4+\delta}$:CGO10 sample thermally treated at 1100°C for 12 hours under air in loose powder form.



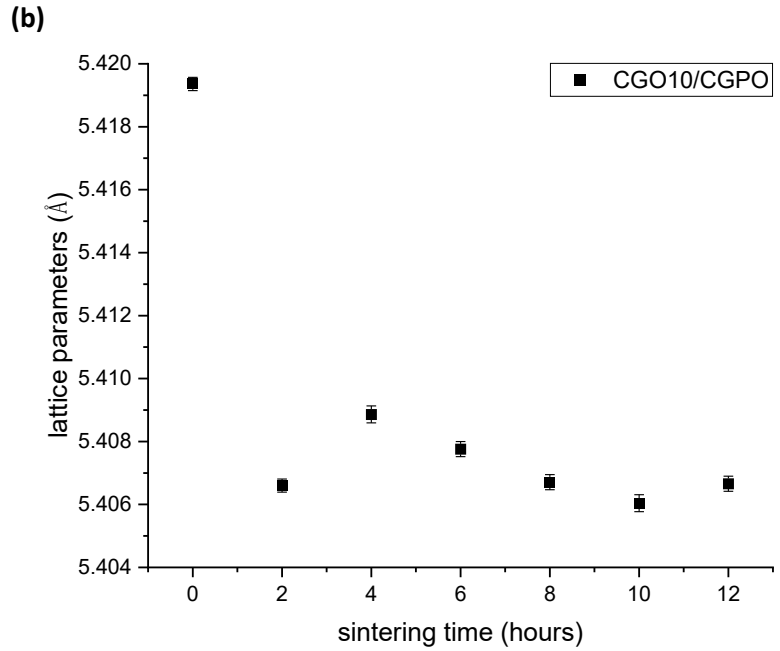


Figure 4.8: The summary of the CGO10/CGPO lattice parameters after thermal treatment at 1100°C between 0 and 12 hours under air in **(a)** loose powder form and **(b)** pressed pellet form. The data were obtained from the laboratory based X-ray diffractometer. The error bar in each point represents three estimated standard deviations.

To have a better understanding of the resulting substituted ceria phases and to identify the presence of the unreacted CGO10, HR-SXRPD was applied to examine the selected samples. The results of the samples that were thermally treated at 1100^{o}C for 6 hours and 12 hours in either loose powder form or pressed pellet forms are presented in **Figure 4.9**. Based on the previous Le Bail refinement results of the untreated powder mixtures HR-SXRPD data (**Figure 4.2**), CGO10 and $Pr_2NiO_{4+\delta}$ have peaks at 2θ=30.57^{o} (222) and 30.74^{o} (080), respectively. **Figure 4.9** shows the presence of the unreacted CGO10 and $Pr_2NiO_{4+\delta}$ in each of the thermally treated samples. The newly formed CGPO phases were indexed in the *Fm*-3*m* space group and identified from the broad feature at 2θ~30.64^{o}, between the $(222)_{CGO}$ and $(080)_{Pr2NiO4+\delta}$ reflections. In terms of the relative quantity of CGO10 and CGPO, a direct correlation was observed. For example, the relative increase of CGPO content has a corresponding decrease of CGO10 content in the system. On the other hand, no clear change in the diffraction patterns for the $Pr_2NiO_{4+\delta}$ was observed among each sample,

which may be due to the fact that only a small portion of $Pr_2NiO_{4+\delta}$ in the initial composition of $Pr_2NiO_{4+\delta}$:CGO10 = 4:1 weight ratio was decomposed and reacted with the CGO10. Generally, a higher and smaller quantity of the unreacted CGO10 and the newly formed CGPO, respectively was observed in the loose powder samples when compared to the pressed pellet samples with the same thermal treatment conditions. This can be attributed to the magnitude of particles contact in each type of sample and obviously the particles in the pressed pellet samples are more compact than the loose powder ones, resulting in the chemical reaction facilitation [7]. In addition, these results proved that the praseodymium diffusion towards the CGO10 phase was time dependent as more newly formed CGPO was produced for the samples heated for 12 hours compared to those heated for only 6 hours at 1100^{o}C. Overall, to quantify the results, the integrated peak intensity of the CGO10 (222) and CGPO (222) reflections was calculated in each sample. They were 48, 32, 28 and 25 for CGO10 and 12, 29, 50 and 70 for CGPO in the sample order of being thermally treated at 1100^{o}C for 6 and 12 hours under air in loose powder and pressed pellet forms, respectively. It is important to note that although the as-mentioned quantification were based on the raw data without normalising the intensities (**Figure 4.9**), they did reflect the relative amount of CGO10 and CGPO from sample to sample. This is because the examined radiation volume and the total scanning time were the same for each sample (**Section 4.2**).

Based on the results of the Le Bail refinement on each of the HR-SXRPD data, the lattice parameters of the newly formed CGPO were determined to be 5.4084(1) Å, 5.4067(1) Å, 5.4087(1) Å and 5.4076(1) Å for the thermally treated loose powder samples for 6 hours and 12 hours at 1100^{o}C and for the pressed pellet samples heated under the same conditions, respectively. Indeed, **Figure 4.9** shows that the FWHM of the CGO10 peak is different from the newly formed CGPO in each sample. Detailed calculations verify that the FWHM of the CGO10 (222) peaks were about 0.04^o and they were compared with the FWHM of the CGPO (222) peaks at 2θ around 30.64^o, which were about 0.10^o. The much larger FWHM at the CGPO region could indicate that more than one phase of the newly formed CGPO was produced and this was confirmed by the STEM EDS mapping results presented later.

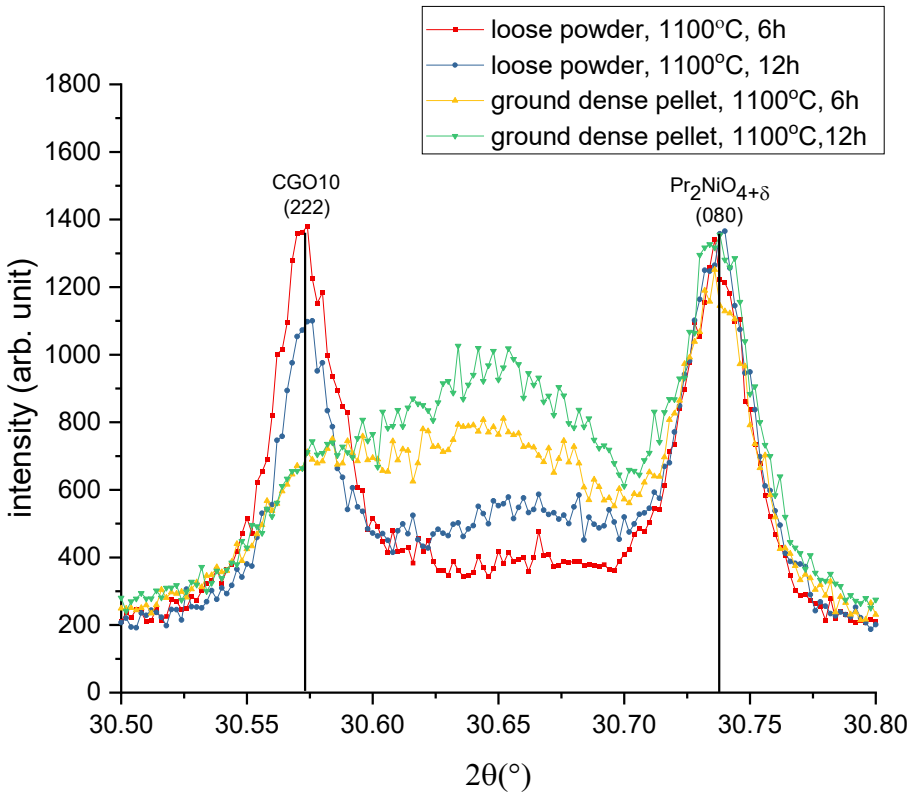


Figure 4.9: A selected region of the HR-SXRPD data which illustrates the relative change of the quantity of CGO10, $Pr_2NiO_{4+\delta}$ and the newly formed CGPO after different thermal treatment conditions in various sample forms. The CGPO phases with (222) reflection locate at 2θ between 30.57° and 30.70°. Reproduced from Tsai et al. [9].

Moreover, similar to the observation from the laboratory XRD data, the detection of NiO and the higher 2θ value for the resulting substituted ceria phases demonstrates the praseodymium diffusion and the degradation of $Pr_2NiO_{4+\delta}$. It is interesting to point out that two NiO phases with a slight difference in lattice parameters were detected in the HR-SXRPD data for each sample as shown in **Figure 4.10**. The lattice parameters for each of the indexed peaks corresponding to the (220) reflection were 4.1795(1) Å and 4.1751(1) Å. The slight variation of the lattice parameters might be induced by local microstrain from the adjacent $Pr_2NiO_{4+\delta}$ and CGPO phases as shown in the STEM EDS mapping (**Figures 4.12(a)** and **(b)**). Moreover, PrOx was not observed in any of the samples which is inconsistent with Laguna-Bercero et al.'s results [4]. It is suspected that the variation is due to the difference of particle size used in the experiments, although further investigation is required to verify this. Besides the previously

identified phases, no other secondary phase was observed in each of the thermally treated samples.

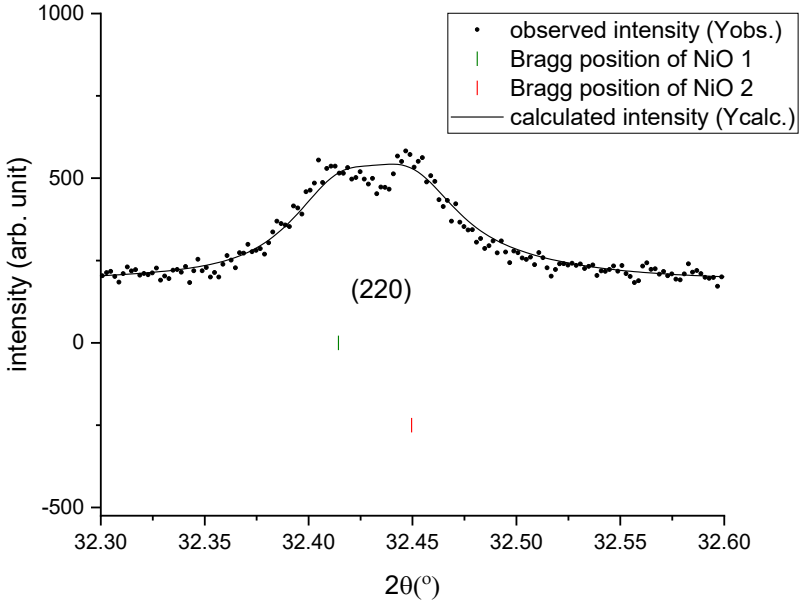


Figure 4.10: The presence of two NiO phases in the HR-SXRPD data for the $Pr_2NiO_{4+\delta}$:CGO10 sample (ground dense pellet) which was thermally treated at 1100°C for 12 hours in air.

Before applying the STEM EDS mapping technique to evaluate the lamella prepared from the sintered samples, commercial CGO10 powder was examined first as a reference to ensure that the experimental parameters used for STEM EDS mapping and the following data quantification approach were reliable. **Figure 4.11** illustrates the selected regions from the sub-micron size CGO10 particles for data quantification with the results being summarized in **Table 4.2**. Despite the relative error of 10%, the quantified Ce and Gd molar ratio matched to the nominal stoichiometric ratio of CGO10. Therefore, the same evaluation approach was conducted on the electron transparent lamella of the sintered samples to identify the chemical composition of the resulting substituted ceria phase(s). The large relative errors shown here might be due to the relatively small x-ray counts compared to the statistical fluctuations of random errors [13].

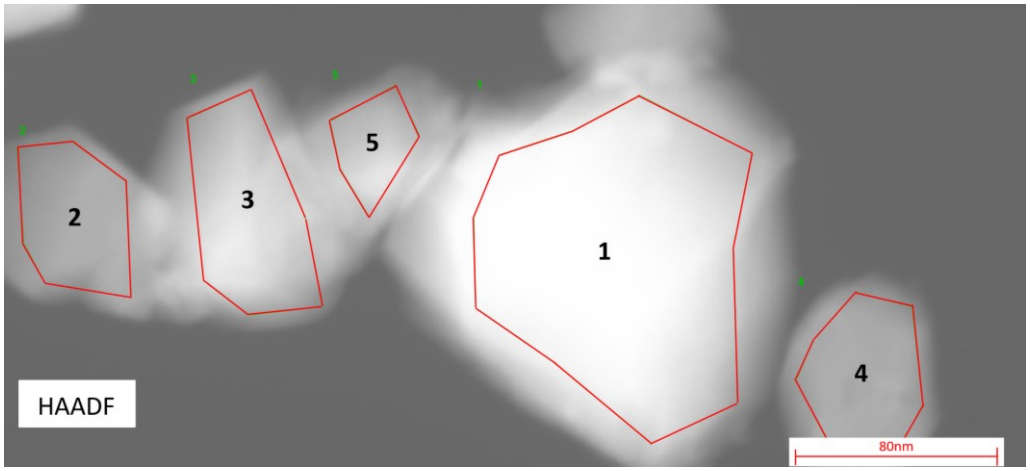


Figure 4.11: The high-angle annular dark-field (HAADF) image of the CGO10 commercial powder mounted on a TEM copper grid. The STEM EDS mapping data at the selected regions were quantified and the results are presented in **Table 4.2**.

Table 4.2: Composition of the commercial CGO10 powder, corresponding to the areas in **Figure 4.11**.

Region	Normalised atomic % of Ce site of $CeO_{2-\delta}$	
	Ce	Gd
1	89±9	11±1
2	88±9	12±2
3	89±9	11±1
4	89±9	11±2
5	89±9	11±2

Figure 4.12 shows the HAADF image and Ni, Ce and Pr elemental maps of the sample sintered at 1100^{o}C for 12 hours in air. According to the distribution of each element (**Figures 4.12(b)**, **(c)** and **(d)**), regions of $Pr_2NiO_{4+\delta}$, NiO and substituted ceria phase were identified. Consistency in terms of $Pr_2NiO_{4+\delta}$ and substituted ceria grain sizes were observed when compared with the previous SEM results (**Figure 4.3**). NiO was located close to the interface between $Pr_2NiO_{4+\delta}$ and the substituted ceria phase regions (labelled as the blue curve in **Figure 4.12(a)**), confirming the chemical reaction mechanism of praseodymium diffusion from the $Pr_2NiO_{4+\delta}$ phase to the CGO10 direction leaving NiO at the original site. This mechanism was further supported by the trend of praseodymium signal intensity which was strong in the $Pr_2NiO_{4+\delta}$ region and attenuated in the substituted ceria phase region. An inverse correlation between

the praseodymium intensity in the substituted ceria phase regions and the distance from the interface was observed. In agreement with the HR-SXRPD results, the hypothesis that more than one CGPO phase formed after sintering was verified by the STEM EDS mapping.

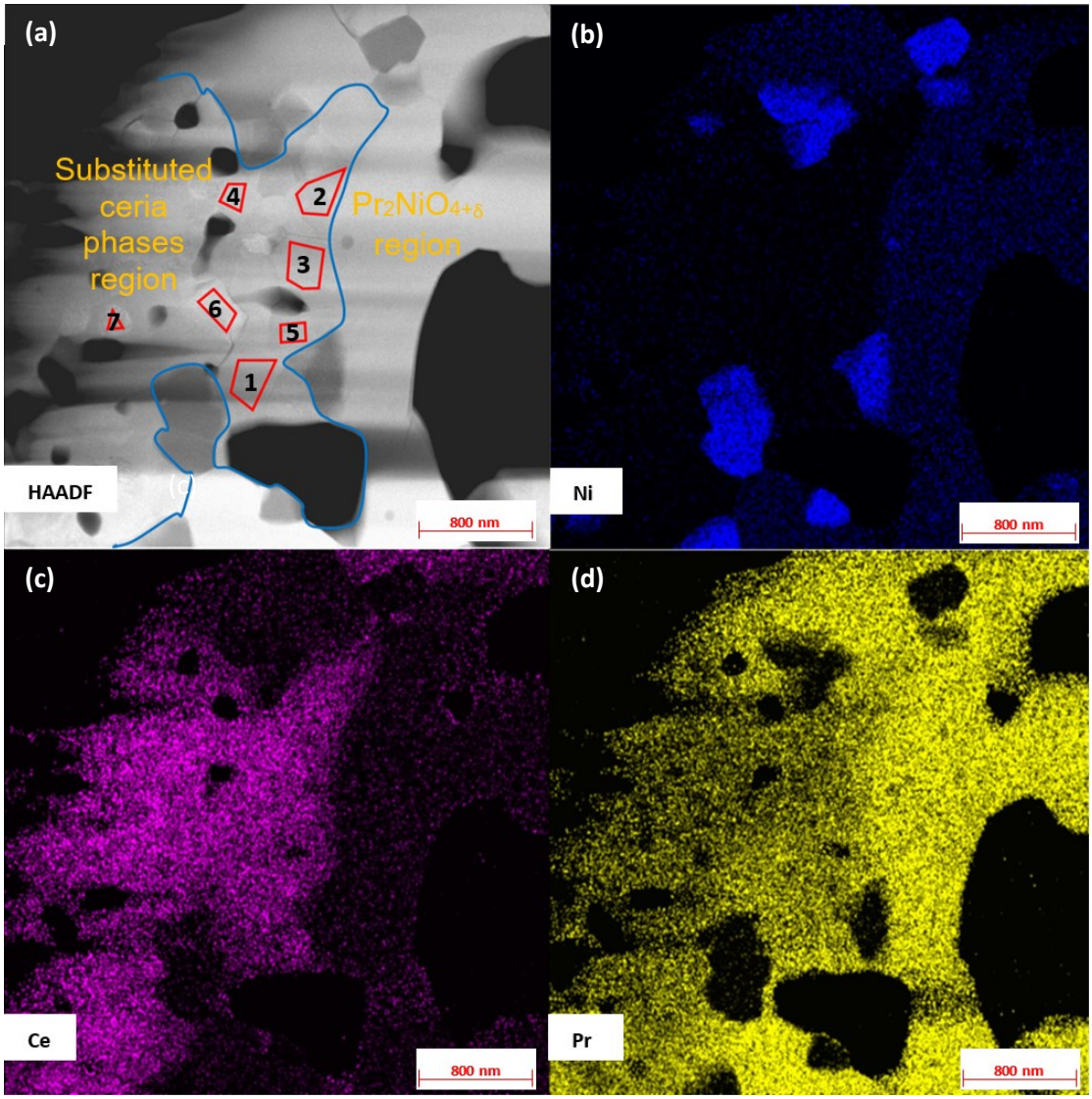


Figure 4.12: The STEM EDS mapping results from a TEM lamella which originates from a $Pr_2NiO_{4+\delta}$:CGO10 pressed pellet sample being heated at 1100°C for 12 hours in air. **(a)** HAADF image. The blue curve indicates the interface between the $Pr_2NiO_{4+\delta}$ and the substituted ceria phases. **(b)** Ni elemental map. **(c)** Ce elemental map. **(d)** Pr elemental map. Reproduced from Tsai et al. [9].

Table 4.3: The chemical composition of each CGPO site correspond with the regions identified in **Figure 4.12(a)**, where 1 represents the closest region to the $Pr_2NiO_{4+\delta}$/substituted ceria interface and 7 is the furthest. Reproduced from Tsai et al. [9].

Region	Normalised atomic % of Ce site of $CeO_{2-\delta}$		
	Ce	Pr	Gd
1	37±4	61±7	2.2±0.6
2	36±4	61±6	3.3±0.6
3	43±5	54±6	4±1
4	59±7	37±5	4±1
5	47±6	49±6	4±1
6	46±5	50±6	5±1
7	59±9	35±6	7±2

Table 4.3 summarizes the chemical composition of each of the CGPO phases in the substituted ceria phase regions. The selected areas for CGPO elemental quantification are labelled in **Figure 4.12(a)**. In general, there was a higher praseodymium ratio in CGPO if the grain was located closer to the $Pr_2NiO_{4+\delta}$ and CGO10 interface and vice versa. This higher ratio of praseodymium was compensated by the lower cerium and gadolinium ratio in the system. In addition, it is important to note that unreacted CGO10 was also observed within the same sample, consistent with the HR-SXRPD results, as shown in the selected areas of **Figure 4.13(a)** where praseodymium was deficient (**Figure 4.13(b)**). On closer inspection of the resulting EDS spectra from the corresponding selected areas, no praseodymium signal was detected. The normalized cation ratio between cerium and gadolinium in each area is presented in **Table 4.4**, which was observed to be close to the nominal stoichiometric ratio of CGO10. Interestingly, **Figure 4.13** suggests that the external praseodymium diffused faster at the grain boundaries in the substituted ceria phase regions than within the bulk as a stronger signal of praseodymium was detected at the grain boundaries. This observation helps with understanding the main praseodymium diffusion pathway from the interface at the sintering conditions employed. The praseodymium diffusion from the grain boundaries to the substituted ceria bulk is believed to be the rate-limiting step of the chemical reaction.

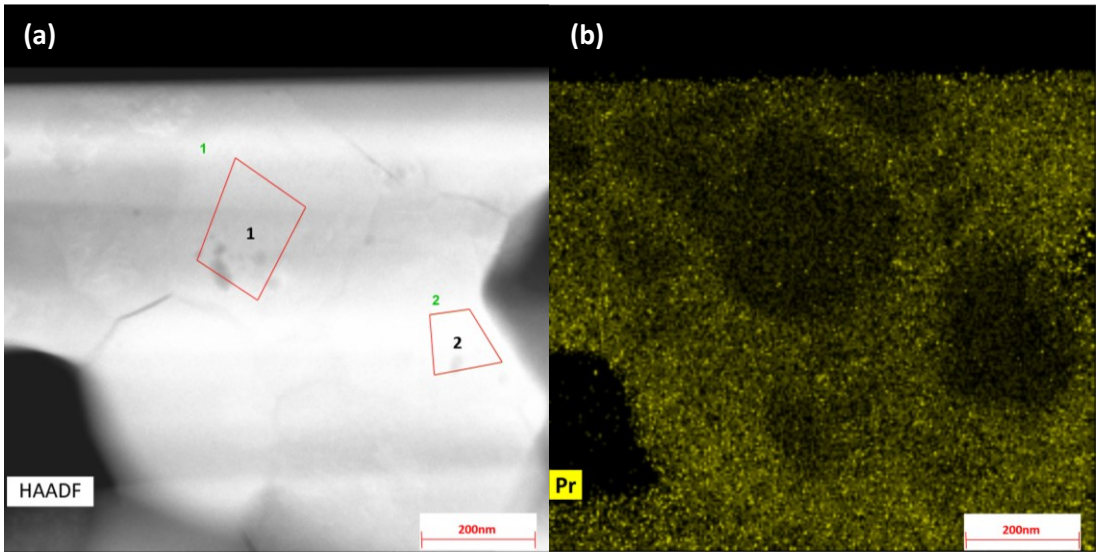


Figure 4.13: STEM EDS mapping for a TEM lamella prepared from the $Pr_2NiO_{4+\delta}$:CGO10 pressed pellet sample heat treated at 1100°C for 12 hours in air. The selected areas are the unreacted CGO10 regions without the Pr signals **(a)** HAADF image. **(b)** Pr elemental map.

Table 4.4: Composition of the unreacted CGO10 regions, corresponding to the areas in **Figure 4.13**.

Region	Normalised atomic % of Ce site of $CeO_{2-\delta}$	
	Ce	Gd
1	88±9	12±1
2	89±9	11±1

Furthermore, STEM EDS mapping was conducted to examine the sample after being heated at 1100^{o}C for 2 hours in air as shown in **Figure 4.14**. **Figure 4.14(a)** shows the regions of $Pr_2NiO_{4+\delta}$ and substituted ceria phases based on the Ni elemental map (**Figure 4.14(b)**). The selected area in **Figure 4.14(a)** was about 400 nm away from the interface and its normalised atomic percentages of Ce, Pr and Gd were 63(6), 29(3) and 8(1). This is compared with the results of region 6 of the sample heated at 1100^{o}C for 12 hours in air in **Table 4.3.** The much larger praseodymium ratio found in the samples sintered at a longer time suggests that more praseodymium was incorporated in the substituted ceria phase located at a similar distance away from the interface.

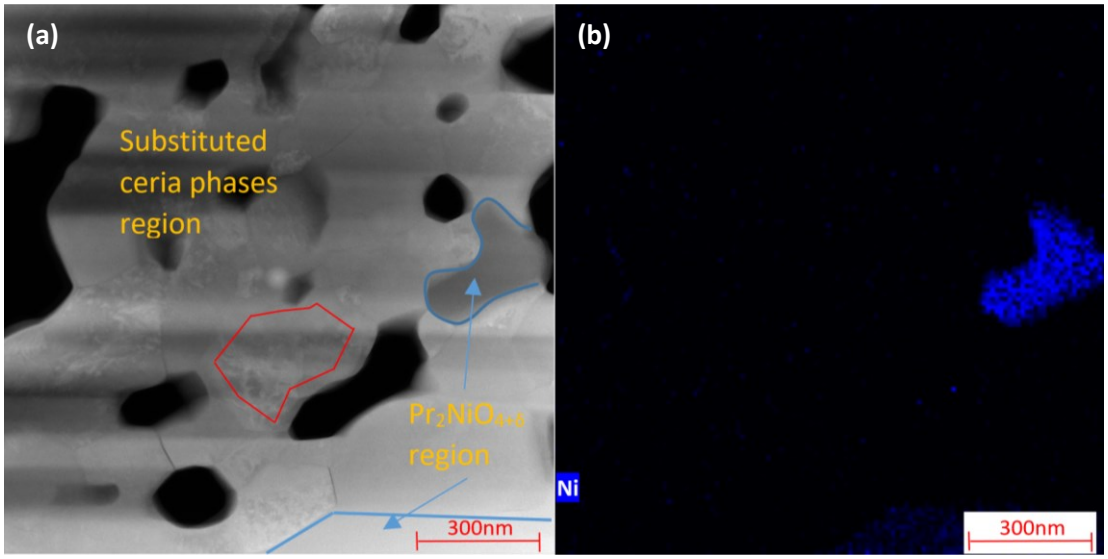


Figure 4.14: STEM EDS mapping for a TEM lamella prepared from the $Pr_2NiO_{4+\delta}$:CGO10 pressed pellet sample heat treated at 1100°C for 2 hours in air. **(a)** HAADF image. **(b)** Ni elemental map.

Overall, compared to the diffusion of praseodymium, the diffusion of cerium, gadolinium and nickel to the counter phase was insignificant. Combining the results from laboratory XRD, HR-SXRPD and STEM EDS mapping, no other secondary phases such as PrO_x, CeO_2 or $Ce_{1-x}Pr_xO_{2-\delta}$ were observed. A series of CGPO solid solutions formed under the sintering conditions detailed through incorporation of praseodymium into the CGO10 phase. Therefore, the proposed chemical reaction is as follows (**Equation 4.1**):

$$Pr_2NiO_{4+\delta} + aCe_{0.9}Gd_{0.1}O_{2-\delta} \rightarrow y/2Pr_2NiO_{4+\delta} + bCe_{0.9}Gd_{0.1}O_{2-\delta} + cCe_{1-x-y}Gd_xPr_yO_{2-\delta} + y/2NiO \quad \textbf{Equation 4.1}$$

where a, b, c, x, y, z are to be determined and could take a wide range of values, depending on the sample forms, the distance from an interface and the sintering time.

4.5 Thermal treatment of the composites at cell operating temperature

To investigate if there were any chemical reactions happening at conditions resembling solid oxide cell operating temperatures, the ground sample previously heated at 1100°C for 12 hours under air in pressed pellet form was further pressed into a new pellet and was ready for further thermal treatment at 800°C for 24 hours in static air. The laboratory XRD data were analysed using the Le Bail refinement

technique as shown in **Figure 4.15**. The evidence of the presence of each phase in **Figure 4.15** is illustrated in **Figure A1**.

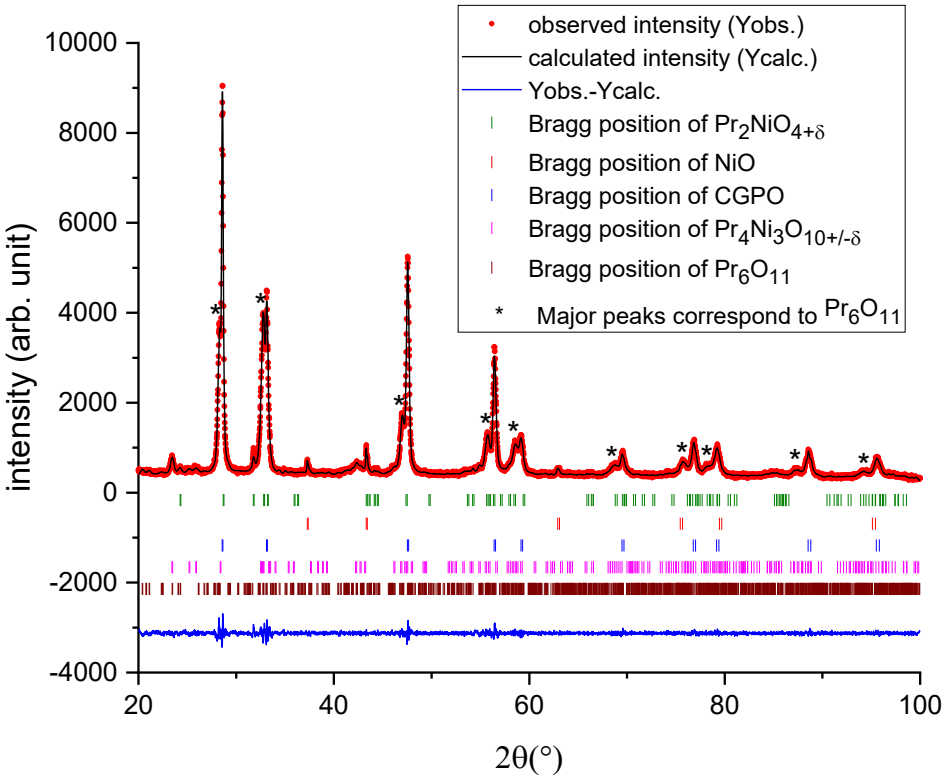


Figure 4.15: Laboratory XRD data analysis results of the $Pr_2NiO_{4+\delta}$:CGO10 pressed pellet sample, which was previously sintered at 1100°C for 12 hours in air and was further heated at 800°C for 24 hours in air, using Le Bail refinement. The figure highlights a significant decompositon of $Pr_2NiO_{4+\delta}$ to $Pr_4Ni_3O_{10+/-\delta}$ and Pr_6O_{11}. The goodness of fit parameters were χ^2=1.41, R_{wp}=4.78% and R_p=3.73%. Reproduced from Tsai et al. [9].

When comparing **Figure 4.15** with the laboratory XRD data of the same sample before further heat treatment (i.e. only heated at 1100°C for 12 hours in the pressed pellet form) (**Figure 4.16**), there was a significant decrease of the $Pr_2NiO_{4+\delta}$ phase and a corresponding increase of Pr_6O_{11} and $Pr_4Ni_3O_{10+/-\delta}$ phases. Indeed, no apparent change in the substituted ceria phase lattice parameters was observed (**Figure 4.17(a)**). The increased background evident in **Figure 4.17(a)** at 2θ= 87.5° was attributed to the presence of Pr_6O_{11} in the system after further thermal treatment at 800°C for 24 hours in air. Due to the limited resolution of the laboratory X-ray diffractometer, the unreacted CGO10 minor phase cannot be fully detected (**Figure 4.17(a)**), unlike in the

earlier HR-SXRPD data (**Figure 4.9**). Therefore, a CGO10 phase was not included in the Le Bail refinement models shown in **Figures 4.15** and **4.16**. In addition, **Figure 4.17(b)** illustrates that there was no obvious increase in the amount of NiO before and after the further thermal treatment at 800^{o}C for 24 hours. Again, similar to the statement for **Figure 4.9**, the intensities were not normalised in **Figure 4.17(b)** when making the comparison of two diffractograms because the examined radiation volume and the total scanning time were the same for both measurements (**Section 4.2**). The final lattice parameters of each phase after further heating at 800^{o}C for 24 hours is summarised in **Table 4.5**. Overall, the results indicate that unlike the observations under the sintering conditions, no diffusion of praseodymium into the substituted ceria phases was observed at 800^{o}C. However, the decomposition of $Pr_2NiO_{4+\delta}$ to Pr_6O_{11} and $Pr_4Ni_3O_{10+/-\delta}$ occurred. This result is consistent with the previous report by Kovalevsky et al. [6] where the $Pr_2NiO_{4+\delta}$ stability was investigated which concluded that $Pr_2NiO_{4+\delta}$ started to decompose at temperatures below 900^{o}C in air, and also with Saher et al.'s [14] results when investigating the phase change of $Pr_2NiO_{4+\delta}$ after heating their sample at 750^{o}C for 128 hours for oxygen permeation test. It is worth mentioning that no $PrNiO_{3-\delta}$ was detected in the current research although its presence was reported by both Philippeau et al. [7], who heated a $Pr_2NiO_{4+\delta}$ and CGO10 mixture in 1:1 weight ratio at 1150°C for 1 hour and at 800°C for 5 days in air, and Saher et al. [14], who investigated the single phase $Pr_2NiO_{4+\delta}$ material. The difference between these results might be due to the various lengths of thermal treatment time (e.g. 24 hours in this study versus 5 days in Philippeau et al. [7]) and /or the weight ratio difference in the composite between the studies.

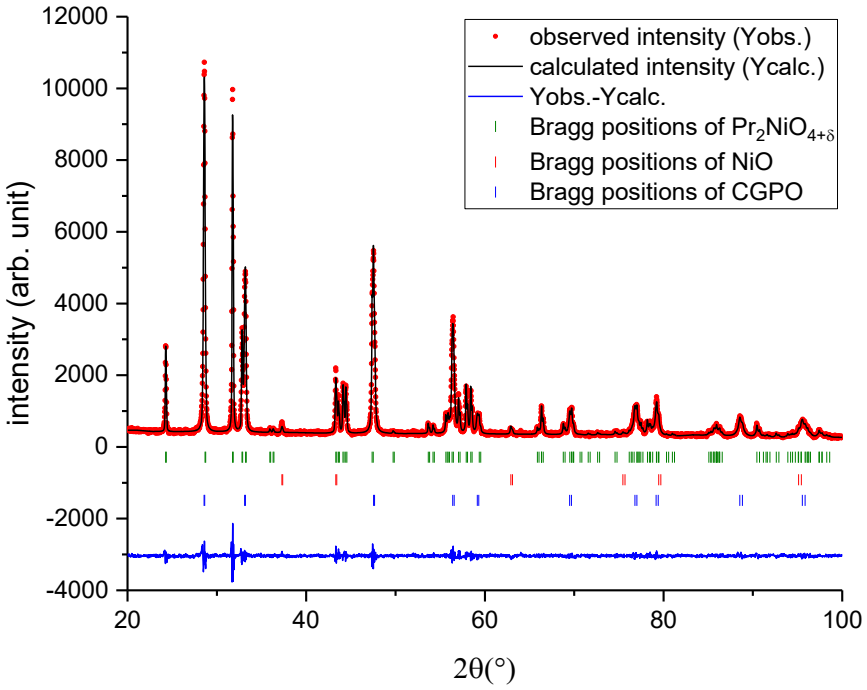


Figure 4.16: Laboratory XRD data analysis results of the $Pr_2NiO_{4+\delta}$:CGO10 pressed pellet sample, which was sintered at 1100°C for 12 hours in air, using Le Bail refinement. The goodness of fit parameters were χ^2=2.21, R_{wp}=6.22% and R_p=4.83%. Reproduced from Tsai et al. [9].

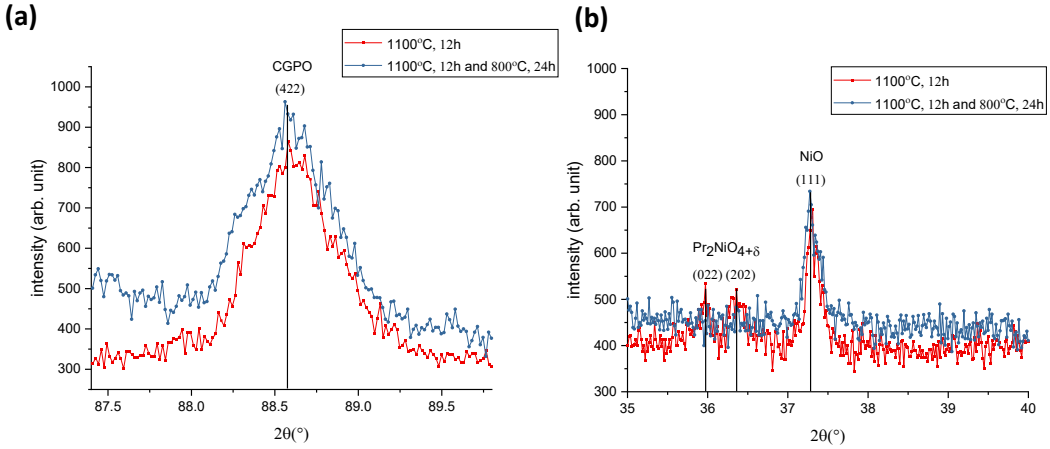


Figure 4.17: **(a)** Comparisons between the CGPO peak position before (red) and after (blue) further heating at 800°C for 24 hours in air. **(b)** The change of NiO content before (red) and after (blue) the as-mentioned heat treatment. All the data were measured using a laboratory based X-ray diffractometer. Reproduced from Tsai et al. [9].

Table 4.5: The refined lattice parameters corresponding to the data in **Figure 4.15**. Reproduced from Tsai et al. [9].

Phase	Lattice parameters (Å)	Phase	Lattice parameters (Å)
$Pr_2NiO_{4+\delta}$ (*Fmmm*)	a=5.3910(1), b=5.4535(1), c=12.4430(1)	$Pr_4Ni_3O_{10+/-\delta}$ (*Fmmm*)	a=5.3718(1), b=5.4607(1), c=27.5251(2)
NiO (*Fm*-3*m*)	a=b=c=4.1750(1)	Pr_6O_{11} (*P*1 *21/c 1*)	a=6.6849(1), b=11.6019(1), c=12.8251(1), β=99.970(1)°
CGPO (*Fm*-3*m*)	a=b=c=5.4065(1)		

As shown in **Figure 4.9**, there was evidence of the co-existence of CGO10 and CGPO after thermal treatment at 1100°C in the high resolution synchrotron X-ray diffraction data. However, **Figure 4.15** can only confirm the presence of one substituted ceria phase in the system as it is challenging to distinguish the CGO10 from the CGPO phases because of the resolution limitation of the laboratory X-ray diffractometer. Nevertheless, at such low thermal treatment temperature (e.g. 800°C) compared to the sintering temperatures which are usually greater than 1000°C, it is reasonable to assume that there is no significant praseodymium diffusion towards the unreacted CGO10 and the amount of the unreacted CGO10 should be almost constant after the further annealing stage. Therefore, it is expected that both CGO10 and CGPO phases co-exist at the operating temperatures of the cells.

The chemical reaction at the solid oxide cell operating temperature can be deduced as follows (**Equation 4.2**), after the previous chemical reaction under the sintering condition:

$$y/2Pr_2NiO_{4+\delta} + bCe_{0.9}Gd_{0.1}O_{2-\delta} + cCe_{1-x-y}Gd_xPr_yO_{2-\delta} + y/2NiO \rightarrow \alpha Pr_2NiO_{4+\delta} + bCe_{0.9}Gd_{0.1}O_{2-\delta} + cCe_{1-x-y}Gd_xPr_yO_{2-\delta} + y/2NiO + \beta Pr_4Ni_3O_{10+/-\delta} + \gamma Pr_6O_{11}$$ **Equation 4.2**

where b, c, are the ratios of the ceria based phases and α, β, γ are the unknown ratios of the $Pr_2NiO_{4+\delta}$ degradation phases.

Based on the results of this research and of the previous studies [3-6, 14] it is clear that $Pr_2NiO_{4+\delta}$ will decompose to the higher order Ruddlesden-Popper phase at solid oxide cell operating temperatures and that CGPO will form under sintering temperatures (assuming sintering is at 1100°C or above). However, the formation of

the new phases might have the potential to be an air electrode candidate possessing high and stable performance [4, 5]. This work clearly shows the chemical reactions that occurred at different stages of the thermal treatment and has identified the chemical composition of the series of ceria phases obtained under the cell sintering conditions. These results further demonstrate the importance of controlling sample processing and operating conditions and the requirement to carefully analyse the diffraction data of ceria based composite electrodes to identify the presence of cation diffusion.

4.6 Summary

The reactivity investigation between $Pr_2NiO_{4+\delta}$ and $Ce_{0.9}Gd_{0.1}O_{2-\delta}$ (CGO10), used as a composite air electrode material in solid oxide cells, shows a significant phase interaction under sintering conditions (1100^{o}C in air). $Pr_2NiO_{4+\delta}$ partially decomposed, with praseodymium diffusion towards the CGO10 site to form a new $Ce_{1-x-y}Gd_xPr_yO_{2-\delta}$ (CGPO) phase. Based on the observations from both XRD and STEM EDS mapping, the chemical composition after the sintering stage comprised $Pr_2NiO_{4+\delta}$, $Ce_{0.9}Gd_{0.1}O_{2-\delta}$,NiO and a series of $Ce_{1-x-y}Gd_xPr_yO_{2-\delta}$ phases with various stoichiometries. No other potential secondary phases were detected. The STEM EDS mapping results indicated that the newly formed CGPO phases were mainly located close to the $Pr_2NiO_{4+\delta}$ grains with a high ratio of praseodymium being incorporated into the substituted ceria, and the praseodymium ratio decreased with the increase in distance from the interface between $Pr_2NiO_{4+\delta}$ and CGO10. Praseodymium diffusion was also found to be faster in the grain boundaries and when the particles were in close contact with each other. For a substituted ceria located at a certain distance from the $Pr_2NiO_{4+\delta}$ and CGO10 interface, more praseodymium incorporation will result at a longer sintering time. Besides praseodymium, cation diffusion of other species was not significant.

Further degradation of $Pr_2NiO_{4+\delta}$ was observed when treating the sample under the typical cell operating temperature (800^{o}C in air). $Pr_2NiO_{4+\delta}$ was converted to $Pr_4Ni_3O_{10+/-\delta}$, the higher order Ruddlesden-Popper phase, and Pr_6O_{11} but no further evolution of CGPO phases was detected. There was also no apparent change of NiO content before and after the thermal treatment.

It is therefore proposed that a composite air electrode consisting of $Pr_4Ni_3O_{10+/-\delta}$ and CGPO should have a more stable performance thermodynamically, as the $Pr_4Ni_3O_{10+/-\delta}$ phase is stable under operating conditions, in contrast to the $Pr_2NiO_{4+\delta}$ phase. The preparation of $Pr_4Ni_3O_{10+/-\delta}$ and its physical properties investigation are discussed in **Chapter 5**, whereas the composite air electrode performance and the long term (7 days) performance stability are discussed in **Chapter 6**.

References

[1] T. Ogier, J. M. Bassat, F. Mauvy, S. Fourcade, J. C. Grenier, K. Couturier, M. Petitjean, J. Mougin, *Fuel Cells,* 13, 536-541, 2013.

[2] T. Ogier, F. Mauvy, J.-M. Bassat, J. Laurencin, J. Mougin, J.-C. Grenier, *International Journal of Hydrogen Energy,* 40, 15885-15892, 2015.

[3] A. Montenegro-Hernandez, J. Vega-Castillo, L. Mogni, A. Caneiro, *International Journal of Hydrogen Energy,* 36, 15704-15714, 2011.

[4] M. A. Laguna-Bercero, H. Monzon, A. Larrea, V. M. Orera, *Journal of Materials Chemistry A,* 4, 1446-1453, 2016.

[5] V. Vibhu, "PhD thesis: Stability and aging studies of praseodymium-based nickelates as cathodes for solid oxide fuel cells", Universite de Bordeaux, 2016.

[6] A. V. Kovalevsky, V. V. Kharton, A. A. Yaremchenko, Y. V. Pivak, E. V. Tsipis, S. O. Yakovlev, A. A. Markov, E. N. Naumovich, J. R. Frade, *Journal of Electroceramics,* 18, 205-218, 2007.

[7] B. Philippeau, F. Mauvy, C. Mazataud, S. Fourcade, J.-C. Grenier, *Solid State Ionics,* 249-250, 17-25, 2013.

[8] J. Rodriguez-Carvajal, *Physica B.,* 192, 55-69, 1993.

[9] C.-Y. Tsai, C. M. McGilvery, A. Aguadero, S. J. Skinner, *International Journal of Hydrogen Energy,* 44, 31458-31465, 2019.

[10] T. Broux, C. Prestipino, M. Bahout, S. Paofai, E. Elkaïm, V. Vibhu, J. C. Grenier, A. Rougier, J. M. Bassat, O. Hernandez, *Dalton Transactions,* 45, 3024-3033, 2016.

[11] L. B. McCusker, R. B. Von Dreele, D. E. Cox, D. Louer, P. Scardi, *Journal of Applied Crystallography,* 32, 36-50, 1999.

[12] M. Heidenreich, Ch. Kaps, A. Simon, F. Schulze-Kuppers, S. Baumann, *Solid State Ionics,* 283, 56-67, 2015.

[13] "Energy Dispersive Spectroscopy," mySCOPE Microscopy Australia. Available: https://myscope.training/#/EDS.

[14] S. Saher, J. Song, V. Vibhu, C. Nicollet, A. Flura, J.-M. Bassat, H. J. M. Bouwmeester, *Journal of Materials Chemistry A,* 6, 8331-8339, 2018.

Chapter 5 Synthesis kinetics and physical properties of $Pr_4Ni_3O_{10-\delta}$

5.1 Introduction

Material synthesis of $Pr_4Ni_3O_{10+/-\delta}$ has been demonstrated to be challenging as high temperatures and long calcination times under an oxidising atmosphere are usually required to thermally treat the precursor [1-3]. One of the approaches to prepare $Pr_4Ni_3O_{10+/-\delta}$ is to decompose $Pr_2NiO_{4+\delta}$, which is much easier to synthesise [4], but the secondary phase of Pr_6O_{11} will be produced simultaneously. For most papers investigating $Pr_4Ni_3O_{10+/-\delta}$, only the synthesis conditions and the material preparation methods are disclosed. However, the synthesis kinetics of $Pr_4Ni_3O_{10+/-\delta}$ have not been previously discussed. In this chapter, the reasons for the high temperature and long duration calcination under an oxidising atmosphere are explained.

In addition, most papers indexed $Pr_4Ni_3O_{10+/-\delta}$ as having an orthorhombic *Fmmm* crystal structure [1-3] using laboratory based X-ray diffraction. However, when comparing to the recent neutron diffraction studies of $La_4Ni_3O_{10+\delta}$ and $Nd_4Ni_3O_{10-\delta}$ in which their space groups were demonstrated to be *Bmab*/*Cmca* [5, 6] and $P2_1/a$ [7], respectively, it was considered worthwhile reinvestigating and confirming if $Pr_4Ni_3O_{10+/-\delta}$ is orthorhombic or belongs to the crystal structure with lower symmetry. This is because the ionic radius of praseodymium is between lanthanum and neodymium. Indeed, the most recent study from Zhang et al. [8] suggests that, according to high resolution synchrotron X-ray and neutron powder diffraction data, $Pr_4Ni_3O_{10+/-\delta}$ has a monoclinic crystal structure with space group of $P2_1/a$. However, only the lattice parameters were reported without including the detailed information of the structural model.

The defect chemistry of $Pr_4Ni_3O_{10+/-\delta}$ and its relationship with the electrical performance is also of interest. There are inconsistencies with respect to the reported oxygen content of $Pr_4Ni_3O_{10+/-\delta}$ in the literature because both oxygen hyper- and hypo-stoichiometry were reported [1-3]. Vibhu et al. [1, 9] observed that $Pr_4Ni_3O_{10+\delta}$ always possessed oxygen hyperstoichiometry with an oxygen content varying between ~10.02 and ~10.14, depending on the temperatures and atmospheres used. On the other hand, $Pr_4Ni_3O_{10-\delta}$ was observed to possess slight ($Pr_4Ni_3O_{9.9}$) and more apparent

oxygen deficiency ($Pr_4Ni_3O_{9.85}$) by Bassat et al. [2] when heating the sample in air and by Zhang et al. [3], respectively. It is worth mentioning that the oxygen non-stoichiometry for all the reported values were measured using thermogravimetric analysis (TGA) but neutron diffraction has never been used to determine the oxygen occupancy at a certain atomic site and hence the oxygen stoichiometry.

With respect to the electrical conductivity measurement of $Pr_4Ni_3O_{10+/-\delta}$, a dense sintered sample is usually required. This is also the case if the oxygen ionic conductivity of $Pr_4Ni_3O_{10+/-\delta}$ is measured using the common approach of oxygen isotopic exchange and secondary ion mass spectroscopy (SIMS). However, it is difficult to densify higher order Ruddlesden-Popper (RP) phases as $Ln_2NiO_{4+\delta}$ (Ln=La, Pr and Nd) will result at high sintering temperatures. It is likely that the previously reported electrical conductivity of $Pr_4Ni_3O_{10+/-\delta}$ has been underestimated because the samples had relatively low density of 70% [1] and >80% [2].

Overall, a systematic study has been conducted to correlate $Pr_4Ni_3O_{10+/-\delta}$ crystal structure and its oxygen content to its transport properties. The change of the crystal structure was also evaluated on increasing temperature in air using *in-situ* X-ray diffraction (XRD). Indeed, $Pr_4Ni_3O_{10+/-\delta}$ was successfully densified using a new approach with the aim to obtain a more accurate electrical conductivity measurement.

5.2 Detailed experimental procedures

A nitrate-citrate route was used to synthesise $Pr_4Ni_3O_{10+/-\delta}$ [2]. This was achieved by weighing the correct stoichiometric ratio of $Pr(NO_3)_3.6H_2O$ (Aldrich, 99.9% purity) and $Ni(NO_3)_2.6H_2O$ (Alfa Aesar, 99.9985% purity) and dissolving them in a citric acid solution with ~10 wt.% of citric acid. As both $Pr(NO_3)_3.6H_2O$ and $Ni(NO_3)_2.6H_2O$ are hygroscopic, their actual water content were measured indirectly by the weight difference before and after the decomposition process at 600°C in air for several hours, resulting in the decomposed products of Pr_6O_{11} and NiO, respectively. The dissolved precursors in the citric acid solution were mixed by a magnetic stirrer and the excess water was removed by heating the solution on a hot plate until gel was formed. Gel decomposition was then conducted at 600°C in air for 12 hours. The final step was to calcine the resulting solid precursor under various conditions in terms of temperatures,

atmospheres and times in order to form a single phase $Pr_4Ni_3O_{10+/-\delta}$. Ball milling was applied to the synthesised $Pr_4Ni_3O_{10+/-\delta}$ powder to reach a homogenous particle size of 1-3 μm before the powder was measured or was further processed.

In the $Pr_4Ni_3O_{10+/-\delta}$ synthesis kinetics study, the phase formation after each thermal treatment stage was monitored by a laboratory X-ray diffractometer (XRD) (PANalytical X'Pert Pro MPD with a Cu K_α source), applying the same instrumental parameters mentioned in **Section 3.4.1.2**. Full analysis of the XRD data was achieved with the Fullprof software suite [10] using Rietveld refinement of the as-synthesised $Pr_4Ni_3O_{10+/-\delta}$ powder.

The synthesised $Pr_4Ni_3O_{10+/-\delta}$ powder was also examined by time-of-flight high resolution powder neutron diffraction (HRPD) using the facility at the ISIS Neutron and Muon Source, Harwell Science Campus, Didcot, UK. This technique allows measurement of oxygen stoichiometry and identifying any subtle orthorhombic/monoclinic peak splitting. The sample was placed in a vanadium can and the experiment was executed at room temperature under vacuum. With respect to the instrumental parameters, the data collection conditions are 30-130 ms window and 80 μA. Data analysis was conducted by Rietveld refinement using GSAS II [11]. Several simulated diffraction patterns including the *Fmmm*, *Bmab* and *C2/m* space groups were also constructed for comparisons.

In terms of $Pr_4Ni_3O_{10+/-\delta}$ oxygen content investigation, the value was not only derived from the Rietveld refinement results of the neutron diffraction data, but it was also measured by iodometic titration. The iodometric titration experimental procedure has been discussed in **Section 3.4.9**.

A dense sintered $Pr_4Ni_3O_{10+/-\delta}$ pellet was prepared for electrical conductivity measurement. The sample preparation approach was similar to that suggested by Vibhu [9] but with lower sintering temperature to reduce NiO and/or PrO_x secondary phase residuals after a post-annealing stage. Post-annealing of the sintered pellet under an oxidising atmosphere is usually required to convert a $Pr_2NiO_{4+\delta}$/NiO mixture produced in the sintering stage to $Pr_4Ni_3O_{10+/-\delta}$ [9, 12]. The detailed fabrication procedure is as follows: the uniaxially pressed (500 MPa, 2 minutes) and isostatically

pressed (300 MPa, 2 minutes) $Pr_4Ni_3O_{10+/-\delta}$ green body was firstly sintered at 1150°C for 12 hours under oxygen with 2°C min^{-1} heating rate from room temperature. The sample was then slowly cooled (0.1°C min^{-1}) to 1050°C and post-annealling at this temperature for up to 108 hours under oxygen. The laboratory X-ray diffractometer (XRD) (PANalytical X'Pert Pro MPD with a Cu K_α source), scanning electron microscopy (SEM) (Zeiss Leo Gemini 1525) in backscattered electron mode (EHT of 20kV and aperture size of 60 µm) and energy dispersive spectroscopy (EDS) (Oxford Instruments Inca X-act) were applied to evaluate the phase of the sintered pellet after post-annealing. Archimedes method (**Section 3.4.7**) was then conducted to measure the density of the sample and the value of greater than 90% with respect to the theoretical density was achieved. Indeed, the van der Pauw approach (**Section 3.4.4**) was used to measure the electrical conductivity of the sintered dense $Pr_4Ni_3O_{10+/-\delta}$ pellet in the measurement range from room temperature to 815°C in air. Since there was a deviation between the probe position on the sample and the sample edge, a geometric correction factor was included in the calculation to consider this effect [13].

In addition, in order to evaluate if there was a phase change or crystal structure change of $Pr_4Ni_3O_{10+/-\delta}$ with increasing temperature from 35°C to 1000°C in air, laboratory *in-situ* XRD (PANalytical Empyrean instrument fitted with an Anton Paar HTK1200N high temperature chamber and using Ni filtered Cu K_α radiation) was used to collect the diffraction data of a powder sample at each temperature step. Le Bail refinement using the Fullprof software suite [10] was applied to analyse the data and the results were compared with the measured electrical conductivity change over temperatures.

5.3 The synthesis kinetics of $Pr_4Ni_3O_{10+/-\delta}$

Most literature studies reported that $Pr_4Ni_3O_{10+/-\delta}$ was synthesised at high temperatures of between 1000-1097°C under oxygen atmosphere [1-3]. However, none of these studies have explained the reasons for the suggested synthesis conditions. Vibhu et al. [1] demonstrated that $Pr_4Ni_3O_{10+\delta}$ was stable when heating at temperatures up to 1050°C in air before it was chemically transformed to $Pr_2NiO_{4+\delta}$ and NiO. Therefore, the solid precursor was firstly attempted to calcine at temperatures below this threshold in air. As mentioned in **Section 5.2**, a two-stage

process was conducted here including the decomposition stage and the calcination stage. As shown in **Figure 5.1**, the resulting phase(s) after each thermal treatment was examined by XRD. After the decomposition stage at 600°C for 12 hours in air, the resulting solid precursors were a mixture of Pr_6O_{11} and NiO. For the small features located at around 26°, 31° and 34° two theta, they were suspected to be PrO_x compounds. The solid precursors were then further calcined at specific temperatures ranging from 900°C to 1050°C in air for a certain amount of time with the aim of producing the $Pr_4Ni_3O_{10+/-\delta}$ phase. No new phase was formed when the calcination was conducted at 900°C for 24 hours in air. However, a small amount of $Pr_2NiO_{4+\delta}$ phase was observed at a higher calcination temperature of 950°C for 24 hours in air. There was an insignificant increase of $Pr_2NiO_{4+\delta}$ content when the calcination time was extended to 72 hours under the same conditions. Indeed, at a higher calcination temperature of 1000°C and 1050°C for 24 hours in air, more $Pr_2NiO_{4+\delta}$ was produced and this corresponded with the decrease in the amount of Pr_6O_{11} and NiO phases in the system. At the end of the reaction (e.g. in the case of 1050°C), NiO always remained because the initial weighed stoichiometric ratio of $Pr(NO_3)_3.6H_2O$ and $Ni(NO_3)_2.6H_2O$ was to synthesise $Pr_4Ni_3O_{10+/-\delta}$ but not $Pr_2NiO_{4+\delta}$. It is important to note that apart from the sample further calcined at 950°C for the extended amount of time, a fresh sample was always used for the calcination condition investigation in air. Overall, although the imposed calcination time is longer here, there is a general consistency between the observed results and those reported by Railsback et al. [14]. Railsback et al. [14] attempted to synthesise $Pr_2NiO_{4+\delta}$ by heating the nitrate solutions for 4 hours at 900°C, 950°C, 1000°C and 1100°C. The only slight deviation is that Railsback et al. [14] did not observe the presence of $Pr_2NiO_{4+\delta}$ at 950°C and this might be because of the calcination time differences.

Nevertheless, Bassat et al. [2] proved that $Pr_4Ni_3O_{10}$ can be formed when specially prepared solid precursors were calcined at around 967°C for 4 days in air. For this approach, the solid precursors were prepared from slowly heating the dried gel from a nitrate-citrate route until it was auto-ignited at much lower temperatures compared to the decomposition temperature of 600°C [2, 15]. This allows the homogeneity of the amorphous oxide mixture to be maintained before calcination and hence

$Pr_4Ni_3O_{10+/-\delta}$ can be produced at the lower calcination temperature [2, 16]. On the other hand, it is likely that there were some degrees of oxide phase separation after the proposed decomposition stage although the resulting solid precursor might have particle size in submicron ranges [2, 16]. It is believed that the formation of $Pr_4Ni_3O_{10+/-\delta}$ was restricted by the cation interdiffusion between praseodymium and nickel due to the limited formation of Pr-Ni-O phase at temperatures less than 950°C in this research. This explanation can be further verified by increasing the calcination temperature to facilitate cation diffusion so that the diffusion length is greater than the heterogeneity distance [16].

Moreover, Kovalevsky et al. [17] reported that $Pr_2NiO_{4+\delta}$ started to decompose to $Pr_4Ni_3O_{10-\delta}$ and Pr_6O_{11} at temperature less than 900°C in air. Considering the as-mentioned Vibhu et al. [1] observation that the thermal stability of $Pr_4Ni_3O_{10+\delta}$ was at temperatures less than 1050°C in air, it seems that there is an overlapping temperature region of thermodynamical stability between $Pr_4Ni_3O_{10+/-\delta}$ and $Pr_2NiO_{4+\delta}$ phases. This condition is similar to the homologous La-Ni-O system [12].

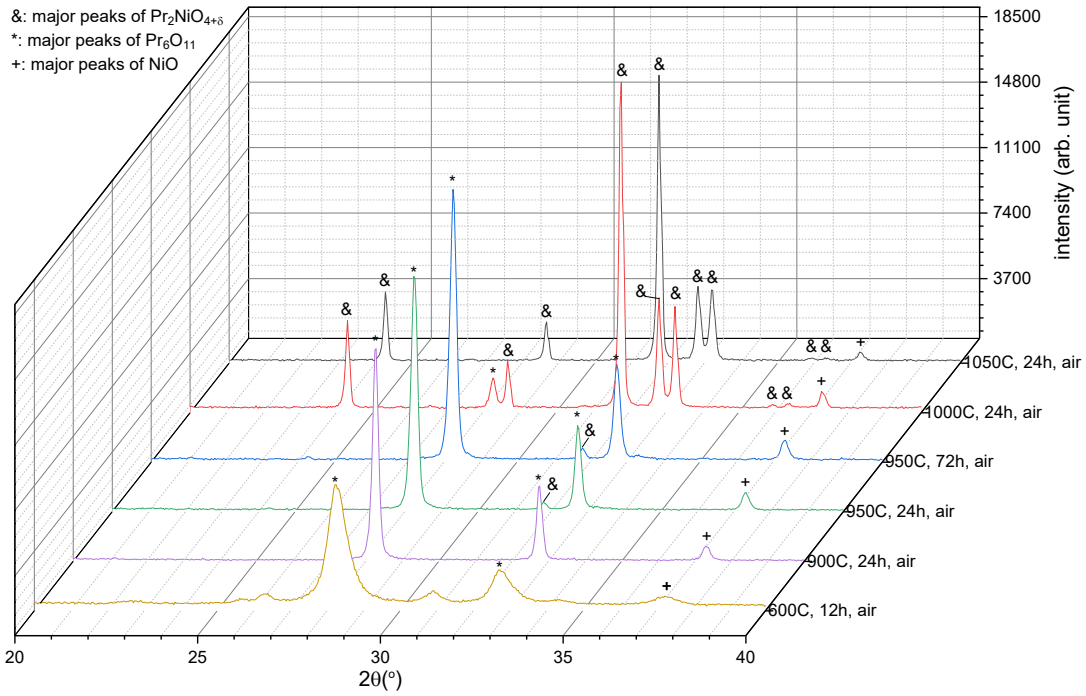


Figure 5.1: The XRD data shows the change of phases after the decomposition stage (600°C, 12 hours, air) and after further calcination stage at various conditions in air. Reproduced from Tsai et al. [18].

The next step is to increase the calcination temperature in order to overcome the limitation of cation diffusion. Nevertheless, it is crucial to maintain the temperature to be within the thermodynamically stable range of $Pr_4Ni_3O_{10+/-\delta}$. Vibhu et al. [1] found that the boundary of the temperature range was higher under oxidising conditions. For example, no phase transition of $Pr_4Ni_3O_{10+\delta}$ to $Pr_2NiO_{4+\delta}$ and NiO would occur when the temperature was below 1120°C in oxygen. The reason for the higher $Pr_4Ni_3O_{10+/-\delta}$ stabilisation under oxidising condition can be summarised by **Equation 5.1**, where the $Pr_4Ni_3O_{10+/-\delta}$ is the oxidised product of $Pr_2NiO_{4+\delta}$. This can be further reflected by its higher average nickel valence than the one of $Pr_2NiO_{4+\delta}$ [17, 19]. In **Equation 5.1**, d, δ and x indicate the amount of oxygen content in Pr_2NiO_4, $Pr_4Ni_3O_{10}$, and praseodymium oxide, respectively. The investigation of oxygen non-stoichiometry in the synthesised $Pr_4Ni_3O_{10+/-\delta}$ is discussed later in **Section 5.5**.

$$3Pr_2NiO_{4+d} \xrightarrow{O_2} Pr_4Ni_3O_{10+/-\delta} + 2PrO_x \qquad \textbf{Equation 5.1}$$

Several calcination conditions were attempted under oxygen flow. The decomposed solid precursors were firstly calcined at 1000°C for various amount of time with intermediate grinding in each thermal cycle of 12 hours. This allows the unreacted materials to be mixed homogeneously [1-3]. **Figure 5.2(a)** illustrates the phase formation and the phase content change in each thermal cycle. It is obvious that $Pr_4Ni_3O_{10+/-\delta}$ was produced gradually with corresponding decrease of PrO_x and NiO quantity but the change was insignificant after the calcination time was greater than 48 hours. The residual PrO_x and NiO were always observed and **Figure 5.2(b)** compares the PrO_2 content in the sample after the total calcination time of 48 and 60 hours. PrO_x was composed of Pr_6O_{11} and PrO_2 but more PrO_2 was present in the remaining PrO_x residue at a longer overall calcination time under oxygen. The results indicate that $Pr_4Ni_3O_{10+/-\delta}$ synthesis was again restricted kinetically and hence the calcination temperature should be further increased.

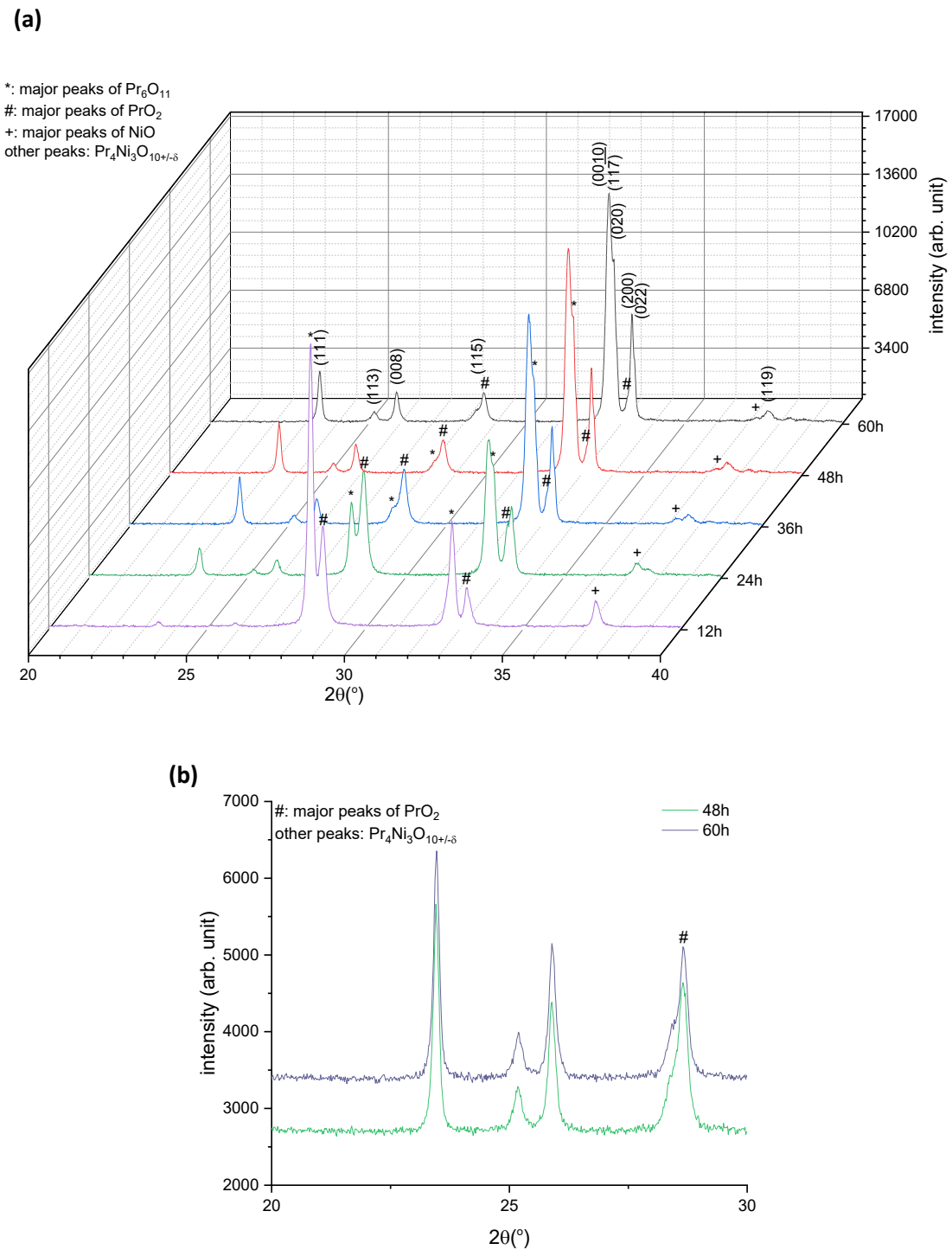


Figure 5.2: (a) The XRD data shows the change of phases at various total calcination time at 1000°C in oxygen. **(b)** The snapshot of the XRD data which illustrates an insignificant change of PrO_2 content when increasing the total calcination time from 48 hours to 60 hours at 1000°C in oxygen. Reproduced from Tsai et al. [18].

Figure 5.3 shows the phase change in each thermal cycle of 12 hours when the calcination temperature was raised to 1050°C under oxygen. It is important to note that fresh decomposed solid precursors were used here. Unlike the previous results when calcining at 1000°C under oxygen, $Pr_2NiO_{4+\delta}$ was initially formed in the first two thermal cycles but the content was slowly decreased after further calcination. This indicates that $Pr_2NiO_{4+\delta}$ is a metastable phase under these calcination conditions. The overall calcination terminated when no $Pr_2NiO_{4+\delta}$ was observed from the laboratory XRD results and this was when the total calcination time was 84 hours (**Figure 5.4**). Indeed, no other secondary phases such as PrO_x and NiO were observed. Further extending the calcination time to 96 hours had no detectable impact on the synthesised $Pr_4Ni_3O_{10+/-\delta}$ phase.

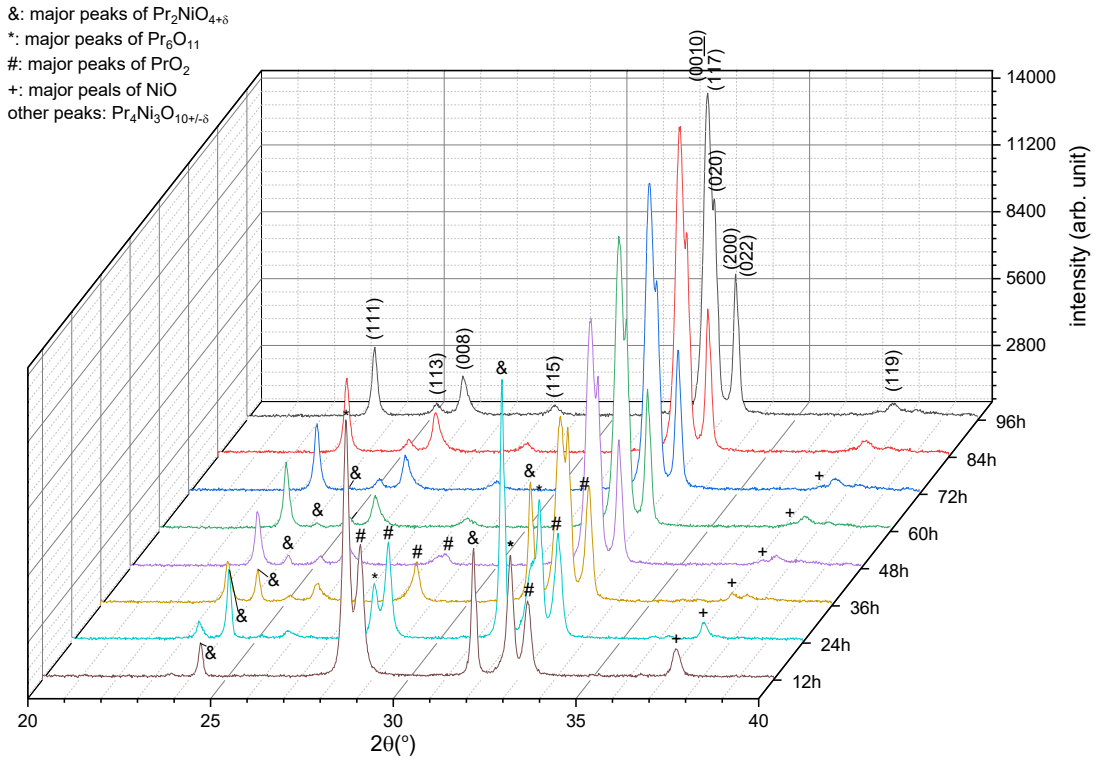


Figure 5.3: The XRD data shows the change of phases at various total calcination time at 1050°C in oxygen. $Pr_4Ni_3O_{10+/-\delta}$ miller indices were labelled and the figure highlights that no secondary phase was observed after calcining for more than 84 hours. Reproduced from Tsai et al. [18].

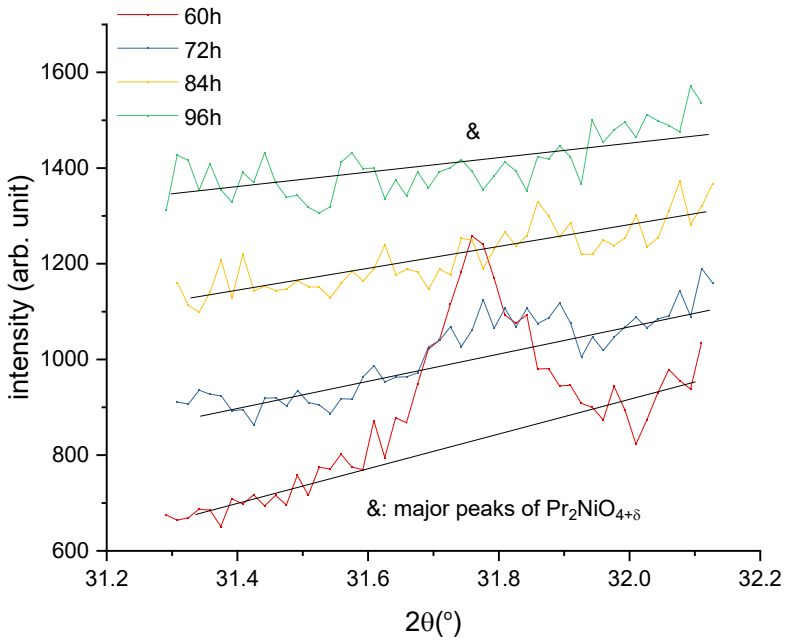


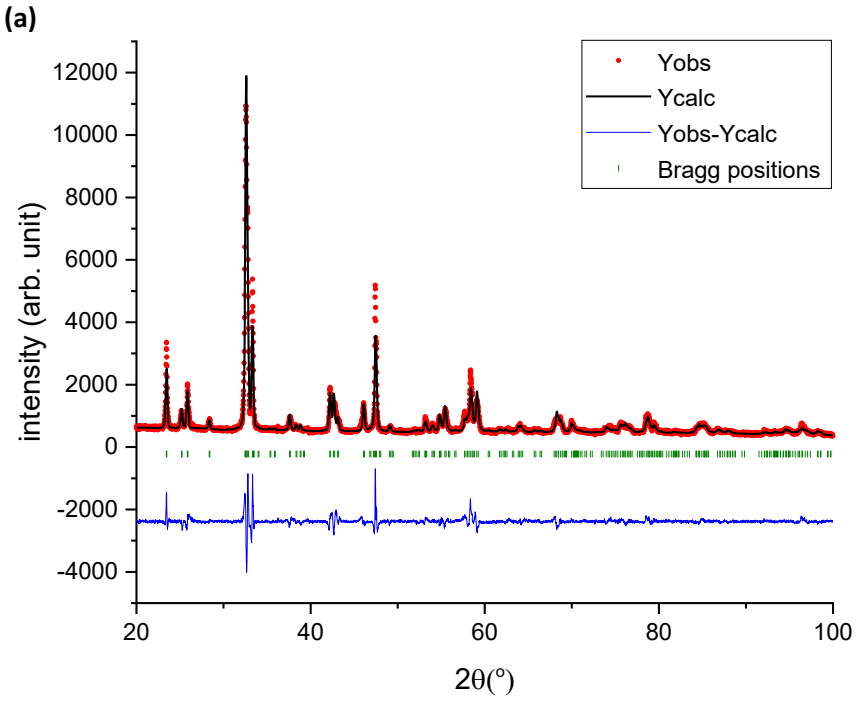
Figure 5.4: The gradual decrease of $Pr_2NiO_{4+\delta}$ secondary phase when increasing the total calcination time from 60 hours to 96 hours at 1050°C in oxygen. The background fit of each diffractogram was indicated by the straight lines. Reproduced from Tsai et al. [18].

The investigation of $Pr_4Ni_3O_{10+/-\delta}$ calcination condition demonstrated that the chemical synthesis is kinetically limited and hence a higher calcination temperature and a prolonged calcination time under oxygen are required. The calcination results under oxygen are in agreement with Laffez et al.'s [20] observation from *in-situ* XRD. The PrO_x and NiO mixture started forming $Pr_4Ni_3O_{10+/-\delta}$ at 1000°C in oxygen and at 1050°C, $Pr_4Ni_3O_{10+/-\delta}$ became the major phase [20]. However, further increasing the temperature to over 1100°C led to the phase decomposition towards $Pr_2NiO_{4+\delta}$ and NiO [20]. Indeed, although the calcination temperature of 1050°C used here under oxygen is slightly greater than the one reported by Vibhu et al. [1] of 1000°C, the overall calcination time is still shorter than the one suggested by Bassat et al. [2] (5 days at 1097°C) and Zhang et al. [3] (5-6 days at 1050°C). The deviations might be due to the variation of the synthesis equipment and probably the homogeneity of the decomposed solid precursors.

5.4 Re-evaluation of the crystal structure of $Pr_4Ni_3O_{10+/-\delta}$

As discussed in **Section 5.1**, $Pr_4Ni_3O_{10+/-\delta}$ was usually indexed as orthorhombic *Fmmm* [1-3] but this identification might be an initial approximation as suggested by Bassat et al. [2]. To confirm, the crystal structure of the synthesised $Pr_4Ni_3O_{10+/-\delta}$ powder was resolved next.

Figure 5.5(a) presents the Rietveld refinement results of the laboratory XRD data. In general, the synthesised $Pr_4Ni_3O_{10+/-\delta}$ fitted well with a calculated model based on the *Fmmm* space group. However, there were some deviations between the model and the experimental data and they were reflected on the resulting difference curve (Y_{obs}-Y_{calc}) and the parameters of goodness-of-fit (e.g. χ^2, R_{wp} and R_p). For example, **Figure 5.5(b)** illustrates the observations of asymmetric peak broadening at ~46° and peak intensity mismatch at ~47.5° two theta. For the feature at ~47.5° two theta, the difference curve shape indicates that the calculated peak possessed a larger full width at half maximum (FWHM) than the experimental data and this might suggest the presence of more than one Bragg position in these regions [21]. When both phenomena in **Figure 5.5(b)** were considered, $Pr_4Ni_3O_{10+/-\delta}$ might possess a less symmetric crystal structure.



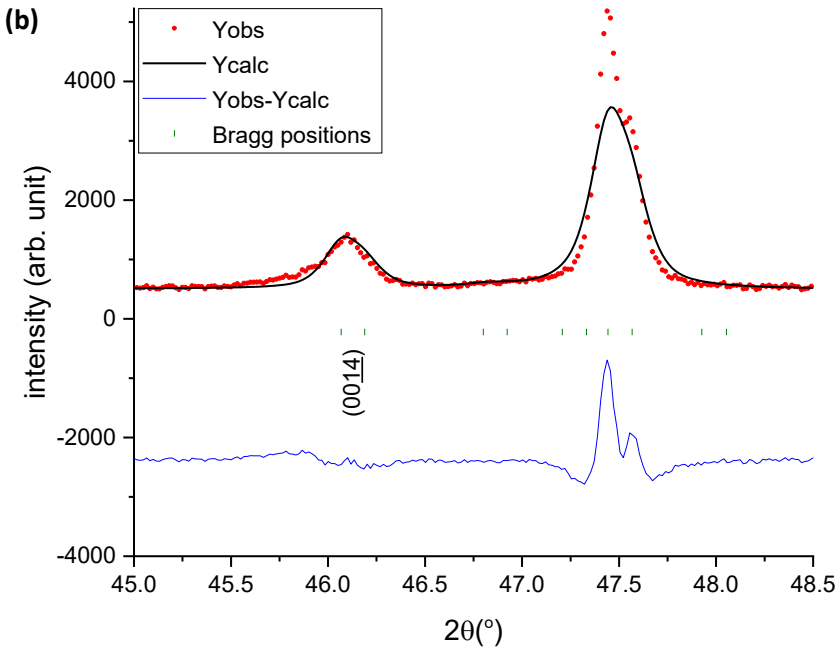


Figure 5.5: (a) Laboratory XRD data analysis results of the as-synthesised $Pr_4Ni_3O_{10+/-\delta}$ powder using Rietveld refinement. The goodness of fit parameters are χ^2=6.54, R_{wp}= 9.81% and R_p= 7.23%. **(b)** The selected region in **Figure 5.5(a)** which highlights the asymmetric peak broadening issue at ~46° and the peak shape mismatch at ~47.5°. These issues can be easily observed from the Y_{obs}-Y_{calc} curve. Reproduced from Tsai et al. [18].

From the results shown in **Figures 5.5(a)** and **(b)**, they appear a potential of crystal symmetry lowering but laboratory XRD cannot clearly distinguish peak splitting. Hence, a high resolution neutron diffraction was applied to resolve this. Before refining the structure model using the neutron diffraction data, the experimental results were compared with several simulated diffraction patterns corresponding to the potential space groups. These did not only include the as-mentioned *Fmmm* space group but also the *Bmab*, *C*2/*m* and *P*2$_1$/*a* space groups which were reported to be the crystal structures of the homologous $La_4Ni_3O_{10+\delta}$ [5], $La_4Co_3O_{10+\delta}$ [22] and $Nd_4Ni_3O_{10-\delta}$ [7] phases, respectively. The comparisons are illustrated in **Figure 5.6(a)**. However, for the reason of simplicity in terms of presentation, the simulated diffraction pattern of *P*2$_1$/*a* was not shown but the final Rietveld refinement results are. For the peaks corresponding to (214) and (01$\underline{1}$0) in *P*2$_1$/*a* and *Bmab* structure models, they were unindexed in the simulated diffraction patterns of *Fmmm* and *C2/m* models. Indeed, **Figure 5.6(b)** shows evidence of peak splitting for the reflections with the (hkl) and (h0l) conditions in the atomic spacing range from 1.96 Å to 2.15 Å. All the evidence

indicates that the crystal structure of $Pr_4Ni_3O_{10-\delta}$ is monoclinic with the space group of $P2_1/a$.

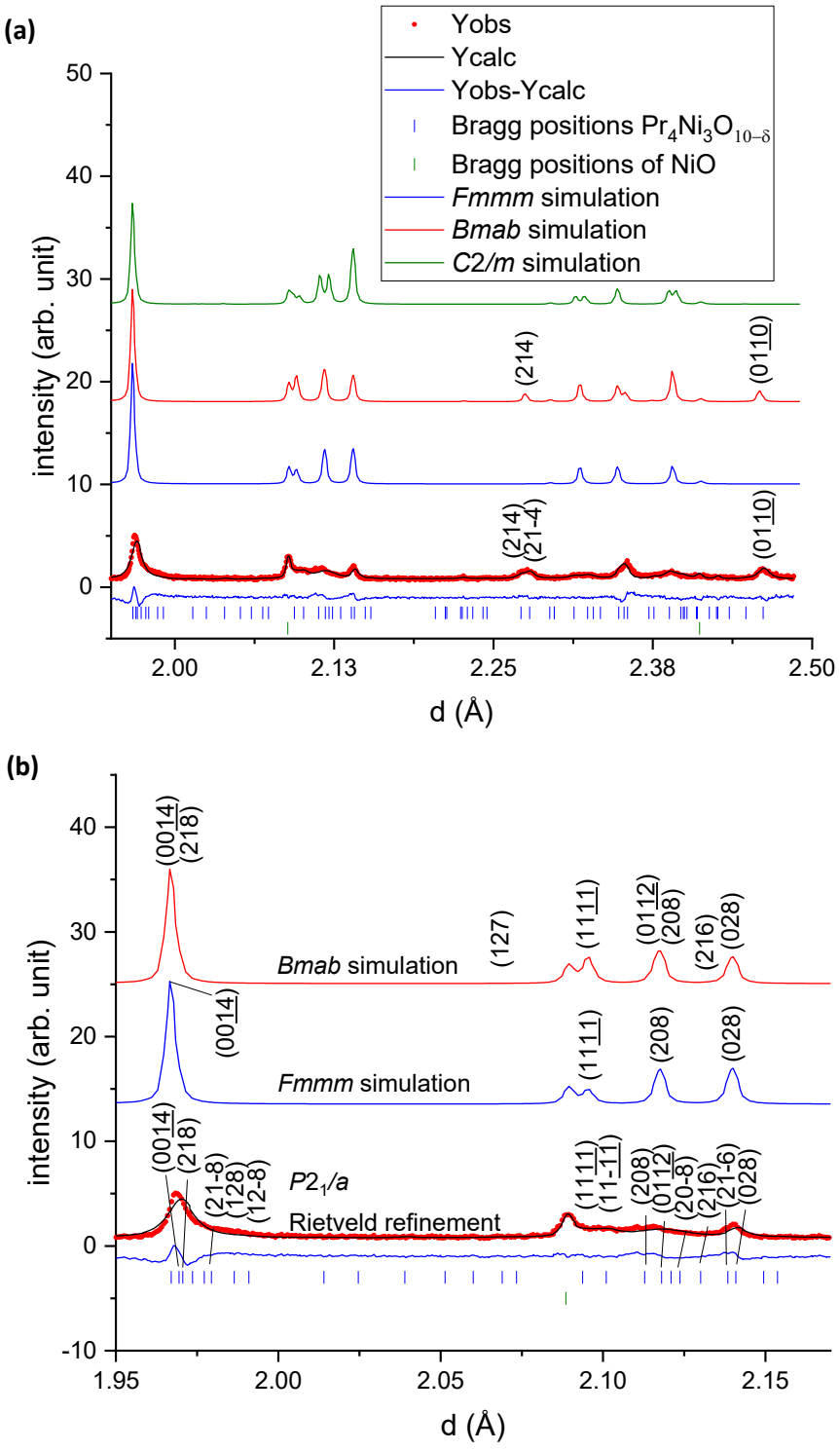


Figure 5.6: (a) The comparison between the simulated *Fmmm*, *Bmab* and *C*2/*m* patterns and Rietveld refinement results of $Pr_4Ni_3O_{10-\delta}$ based on $P2_1/a$ space group. **(b)** The confirmation of the monoclinic distortion due to the evidence of peak splitting and the presence of extra peaks not indexed by either *Bmab* and *Fmmm*. Reproduced from Tsai et al. [18].

The full Rietveld refinement result obtained for the $Pr_4Ni_3O_{10-\delta}$ neutron diffraction data is displayed in **Figure 5.7**. In the calculated model, the lattice parameters and the atomic parameters were not only refined but other parameters such as the scale factor, the background parameters, the phase fraction, the isotropic domain size parameters and the generalised microstrain parameters were also considered. Indeed, all the praseodymium in various atomic coordinates were set to have the same thermal displacement (U_{iso}). This was also applied to the U_{iso} of the nickel positions to reduce the total number of the refined parameters and to ensure a physically plausible model was used. Both **Figures 5.6** and **5.7** show that the cubic NiO with *Fm-3m* space group was present as the secondary phase whereas the monoclinic $Pr_4Ni_3O_{10-\delta}$ was the major phase. The calculated weight percentages for each phase were 1.1(1) and 98.9(3), respectively.

In addition, there was an observation of a peak shape mismatch indicated by the difference curve (Y_{obs}-Y_{calc}) at ~1.97 Å in **Figures 5.6** and **5.7**. Despite refining all the as-mentioned parameters, the issue was not resolved. Combining with the peak shape mismatch evidence in the other regions, they led to the relatively poor goodness-of-fit (R_{wp}= 6.77%, R_p= 6.12%). After several attempts, it seems that the system includes more than one monoclinic $Pr_4Ni_3O_{10-\delta}$ phase with slightly different lattice parameters and atomic parameters. Therefore, two monoclinic $Pr_4Ni_3O_{10-\delta}$ phases were introduced into the model for Rietveld refinement as shown in **Figures 5.8(a)** and **(b)**, which resulted in a better goodness of fit (R_{wp}= 5.68%, R_p= 5.21%). Nevertheless, the global convergence could never be achieved despite the introduction of constraints and restraints. It is believed that the similar refined parameters of the two monoclinic phases caused the refinement to be challenging. Therefore, the lattice parameters and the atomic parameters from the refinement results with one monoclinic $Pr_4Ni_3O_{10-\delta}$ phase represents the average values in the system.

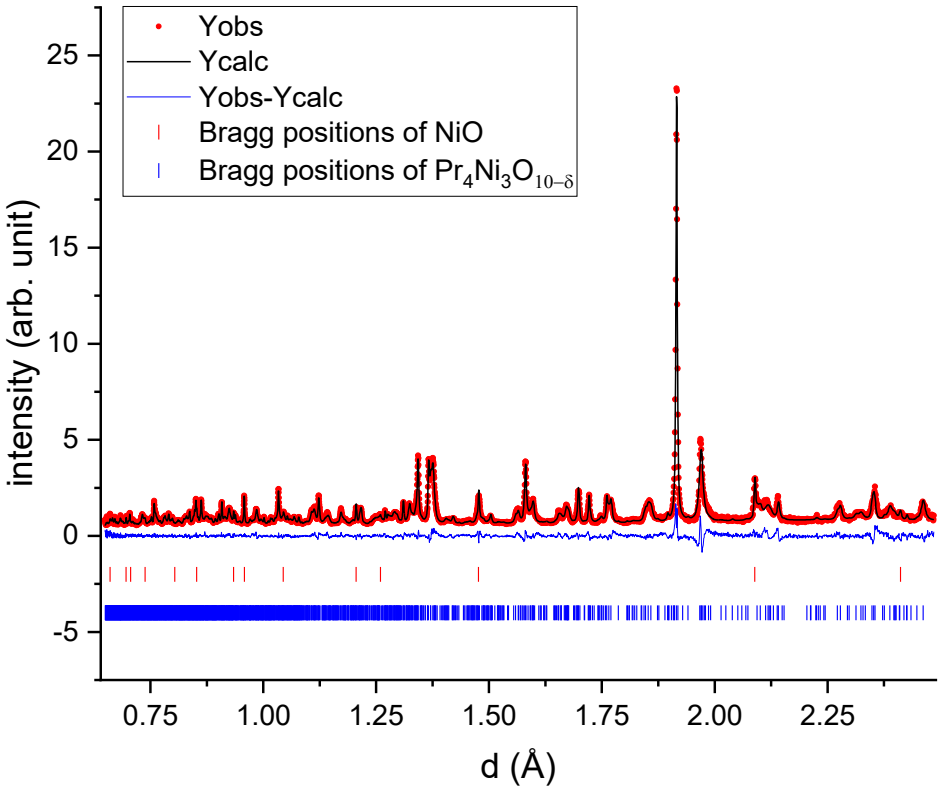
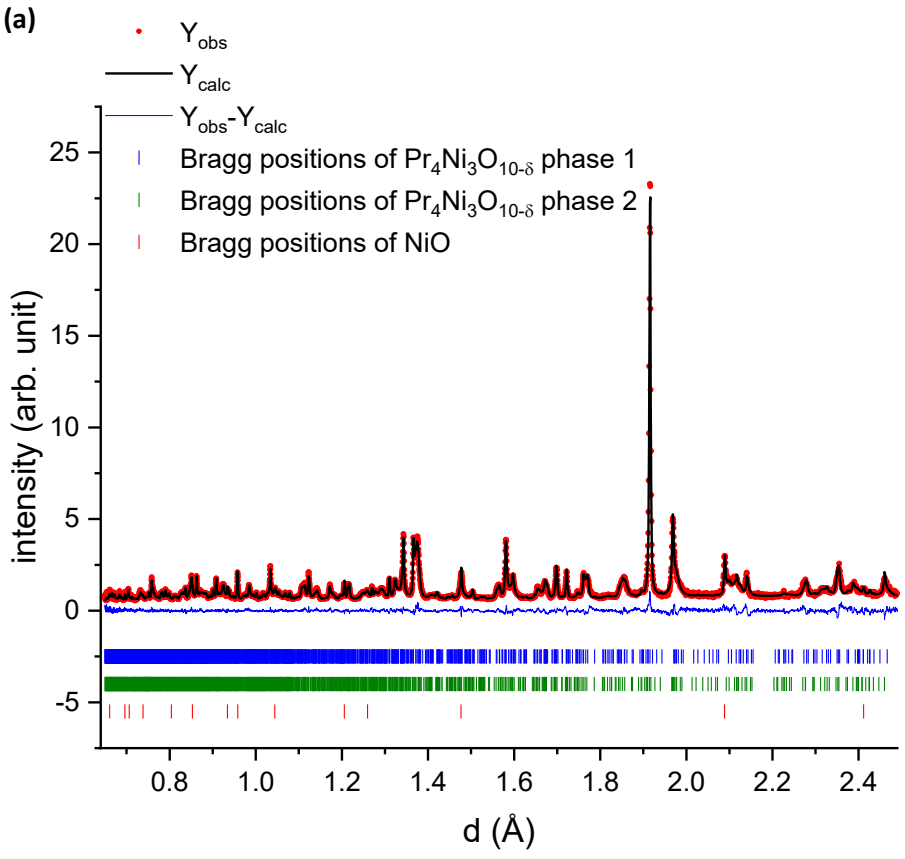


Figure 5.7: Neutron diffraction data analysis results of the as-synthesised $Pr_4Ni_3O_{10-\delta}$ powder using Rietveld refinement. The goodness of fit parameters are R_{wp}= 6.77%, R_p= 6.12%. Reproduced from Tsai et al. [18].



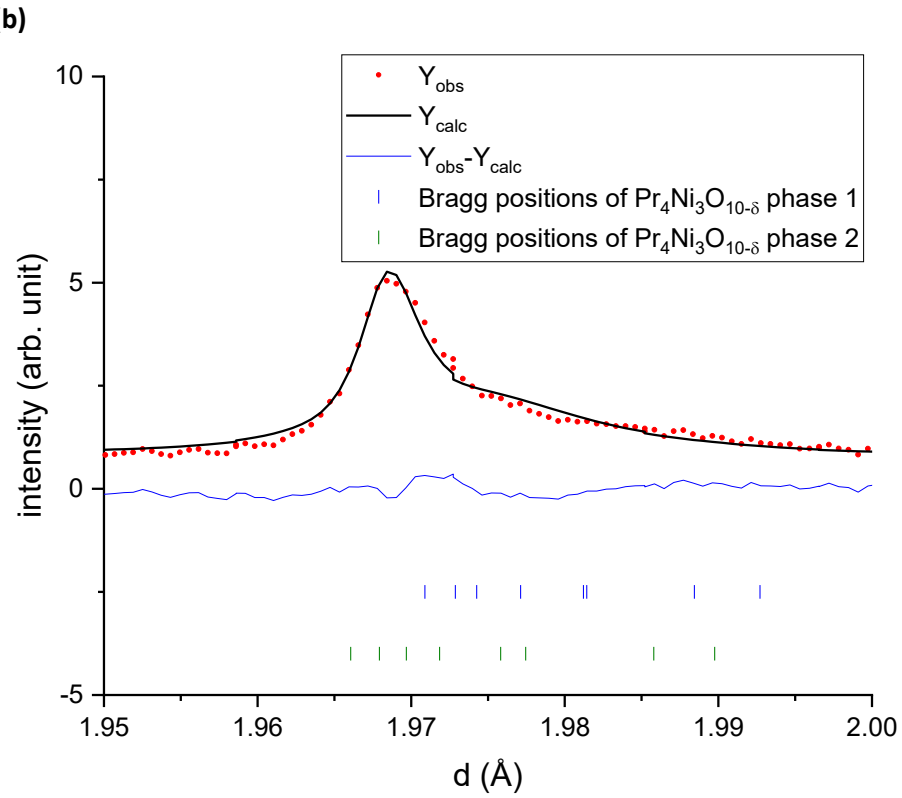


Figure 5.8: (a) Neutron diffraction data analysis results of the as-synthesised $Pr_4Ni_3O_{10-\delta}$ using Rietveld refinement with two $P2_1/a$ monoclinic phases introduced in the model. The goodness of fit parameters are R_{wp}= 5.68% and R_p= 5.21%. (b) Evidence of the improved fitting of the peak at d ~ 1.97 Å.

The summary of the refined lattice and atomic parameters are tabulated in **Table 5.1**. Compared to the reported *a* and *b* lattice parameters of $Pr_4Ni_3O_{10-\delta}$ from Zhang et al. [3], the refined *a* and *b* values were 5.3705(1) Å and 5.4637(1) Å, respectively. The deviations were in the range of three standard deviations with respect to the reported values. However, the refined *c* parameters of 27.5728(8) Å was out of range when compared to the reported 27.528(7) Å [3]. These observations were also consistent when comparing with the $Pr_4Ni_3O_{10+/-\delta}$ lattice parameters measured from high resolution synchrotron X-ray powder diffraction at room temperature [8]. The elongation of the *c* parameter might be because of the variation of the atomic spacing measured by X-ray and neutron sources. However, since no such large deviation was observed in *a* and *b* parameters, the larger *c* parameter might be attributed to the slight A-site and B-site deficiency and oxygen vacancy content in the synthesised

$Pr_4Ni_3O_{10-\delta}$. **Table 5.1** shows that Pr4, Ni2, O2 and O9 (with atomic positions defined in **Figure 5.9**) had occupancy less than one. The overall praseodymium to nickel atomic ratio in the system can be recalculated given that the weight fractions of NiO and $Pr_4Ni_3O_{10-\delta}$, more correctly presented by $Pr_{3.94(4)}Ni_{2.94(2)}O_{9.72(7)}$, were known. The calculated ratio was 3.9:3.1 and this approached the target value of 4:3.

Table 5.1: Refined lattice and atomic parameters for the $Pr_4Ni_3O_{10-\delta}$ phase corresponding to the data presented in **Figure 5.7**. The parentheses labelled adjacent to each atom are the corresponding Wyckoff site. Reproduced from Tsai et al. [18].

Lattice parameters	a= 5.3705(1)Å b= 5.4637(1)Å c= 27.5728(8)Å ß= 90.303(3)°				
Atomic coordinates	x	y	z	Frac.	100 x U_{iso}(Å^2)
Pr1 (4e)	0.009(4)	0.014(3)	0.299(1)	1	0.8(1)
Pr2 (4e)	0.512(4)	0.004(4)	0.799(1)	1	0.8(1)
Pr3 (4e)	0.036(3)	-0.015(3)	0.434(1)	1	0.8(1)
Pr4 (4e)	0.484(3)	0.010(3)	0.926(1)	0.94(4)	0.8(1)
Ni1 (2b)	0	0.5	0.5	1	0.6(1)
Ni2 (2a)	0	0	0	0.88(3)	0.6(1)
Ni3 (4e)	-0.003(2)	-0.002(2)	0.138(1)	1	0.6(1)
Ni4 (4e)	0.482(2)	0.010(2)	0.640(1)	1	0.6(1)
O1 (4e)	0.285(3)	0.299(3)	0.492(1)	1	1.5(4)
O2 (4e)	0.272(3)	0.223(3)	0.992(1)	0.91(5)	0.1(3)
O3 (4e)	0.013(3)	0.066(2)	0.075(1)	1	1.0(3)
O4 (4e)	0.488(3)	0.067(2)	0.564(1)	1	1.4(3)
O5 (4e)	0.245(3)	0.259(4)	0.150(1)	1	1.2(3)
O6 (4e)	0.750(3)	0.251(4)	0.648(1)	1	0.8(3)
O7 (4e)	0.013(3)	-0.032(2)	0.217(1)	1	1.4(3)
O8 (4e)	0.488(3)	-0.069(2)	0.714(1)	1	0.7(2)
O9 (4e)	0.756(3)	0.255(4)	0.867(1)	0.81(5)	0.1(4)
O10 (4e)	0.281(3)	0.252(4)	0.373(1)	1	2.0(4)

Figure 5.9 illustrates the $Pr_{3.94(4)}Ni_{2.94(2)}O_{9.72(7)}$ crystal structure and the atomic position of each ion. O2 and O9 sites were the only locations where oxygen vacancies were located. They were in the same perovskite tri-layers (Ni3-Ni2-Ni3) where praseodymium deficiency (Pr4) and nickel deficiency (Ni2) were observed. It is likely that there was formation of defect associates and its impact on the material physical

properties requires further investigation. Indeed, none of the apical oxygen pointing towards the rock salt layers, such as O7 and O8, had occupancy less than one. Oxygen transport pathways might occur within the perovskite layers, in particular close to the O2 and O9 sites.

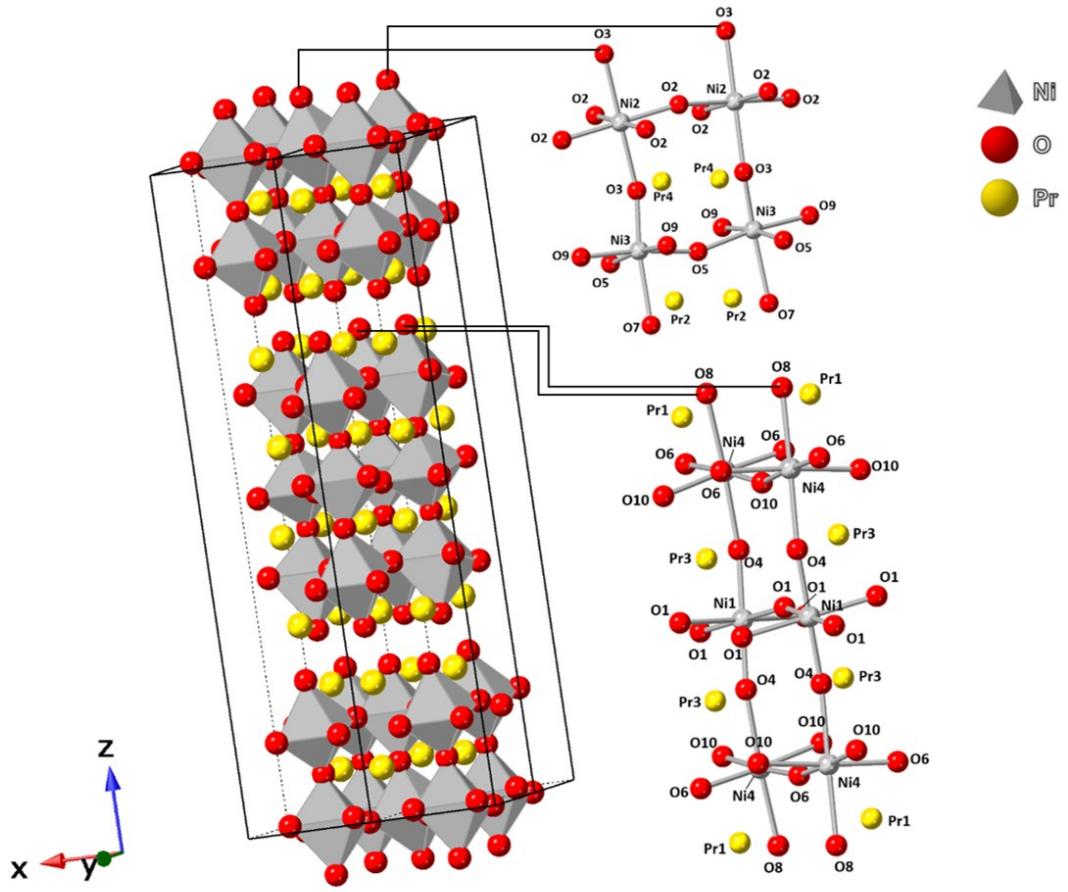


Figure 5.9: The illustration of the refined monoclinic crystal structure with space group of $P2_1/a$ based on the parameters used in **Table 5.1**. The figure was plotted using CrystalMaker software package. Reproduced from Tsai et al. [18].

The interatomic bond distances and the bond angles of Ni-O-Ni of the refined $Pr_{3.94(4)}Ni_{2.94(2)}O_{9.72(7)}$ were summarised in **Table A1**. The bond distances of Pr-O were between 2.27 Å and 3.21 Å. In general agreement with the reported $Nd_4Ni_3O_{10-\delta}$ crystal structure [7], the coordination number of the praseodymium located within the perovskite tri-layers such as Pr3 and Pr4 was 12. On the other hand, for the praseodymium adjacent to the rock salt layers such as Pr1 and Pr2, the coordination

number was 9. In terms of the bond distances of Ni-O, they were between 1.77 Å and 2.21 Å. Ni3-O7 and Ni4-O8 had the highest two bond distances and they indicate the elongation of apical oxygen in the NiO_6 octahedra towards the direction of the rock salt layers. Olafsen et al. [7] suggested that this might result in a charge ordering effect. Indeed, the deviations of Ni-O-Ni bond angles from 180° in **Table A1** (e.g. range between 157° and 173°), reflect that the crystal structure possesses NiO_6 octahedra with strong distortion.

The bond valence sum calculations were also conducted here to evaluate the cation valence in $Pr_{3.94(4)}Ni_{2.94(2)}O_{9.72(7)}$. The detailed concept of the method is discussed in **Section 3.4.1.7**. Overall, all four praseodymium positions in the crystal structure had valence around 3 (e.g. between 2.8 and 3.2). The results are in agreement with Vibhu et al. [1] who suggested that Pr^{+4} was unstable in the crystal structure due to its smaller cation size than Pr^{+3}. On the other hand, the calculated nickel valences of Ni1, Ni2, Ni3 and Ni4 were 3.3, 2.6, 3.0 and 2.6, respectively. Recalling the crystal structure in **Figure 5.9**, each perovskite tri-layer such as Ni3-Ni2-Ni3 and Ni4-Ni1-Ni4 had high and low nickel valences positioned alternatively. This indicates that the crystal structure possessed an anisotropic electron conduction pathway.

5.5 The oxygen content of the synthesised $Pr_4Ni_3O_{10-\delta}$

With respect to the oxygen content of the synthesised $Pr_4Ni_3O_{10-\delta}$, it was calculated to be 9.72(7) from the Rietveld refinement results of the neutron diffraction data in **Table 5.1**. To verify this value, a fresh sample was used in iodometric titration and the oxygen content was measured to be 9.65(1), which was within one standard deviation of the previous 9.72(7).

Compared to the oxygen content measurement based on TGA in the literature, Zhang et al. [3] observed a significant oxygen deficiency in $Pr_4Ni_3O_{10-\delta}$ but they suspected that the result was partially caused by the presence of impurity phases in the samples. On the other hand, Bassat et al. [2] showed that $Pr_4Ni_3O_{10\pm\delta}$ could be either oxygen hyper- or hypo-stoichiometry with δ varied between -0.1 and 0.1. Both powder synthesis conditions and thermal treatment history had an impact on the final oxygen content in $Pr_4Ni_3O_{10\pm\delta}$ [2]. These observations were in contrast to Vibhu et al.'s [1]

results which showed that $Pr_4Ni_3O_{10+\delta}$ had oxygen content always greater than 10. However, it would not exceed 10.14 [1]. In general, it is believed that the stacking of the perovskite layers in higher order RP phases such as $Pr_4Ni_3O_{10+/-\delta}$ allows the perovskite/rock salt interfacial strain to be relieved progressively by the mixed valence of $Ni^{2+/3+}$ [2]. Hence, there is no need to accommodate significant amounts of oxygen interstitials in the rock salt layer as with $Pr_2NiO_{4+\delta}$, where δ can be as high as 0.21-0.22, to mitigate the bond length differences between Pr-O and Ni-O [2, 4]. This leads to the result that $Pr_4Ni_3O_{10+/-\delta}$ possesses a near stoichiometric oxygen content [2, 3]. The resulting high oxygen deficiency in the synthesised sample might be because of the presence of A-site and B-site deficiency in the crystal structure.

5.6 The electrical conductivity of $Pr_4Ni_3O_{10+/-\delta}$ and *in-situ* XRD results

Before implementing the electrical conductivity measurement on $Pr_4Ni_3O_{10+/-\delta}$, a sintered pellet of 91.7% of theoretical density was prepared and its phase was examined by laboratory XRD after post-annealing at 1050°C under oxygen for different amounts of time as shown in **Figure 5.10**. For the initial 36 to 84 hours, there was a significant decrease of $Pr_2NiO_{4+\delta}$ and NiO content but the NiO residue was always present even when the post-annealing time was increased from 84 to 108 hours. The final amount of NiO was calculated to be 3.1(2) wt.% and NiO was also observed in the backscattered electron image (**Figure 5.11**) and the corresponding EDS results (**Table 5.2**). In **Figure 5.11**, the darker grey spots (e.g. sites of interest 1, 3 and 6) were identified as NiO because they had lower praseodymium to nickel atomic ratio summarised in **Table 5.2**. The presence of a praseodymium signal in the EDS spectra was due to the fact that the spatial resolution of EDS, around 1 μm^3, was greater than the NiO particle size. For the rest of the investigated spots (e.g. sites of interest 2, 4 and 5), they had lower grey scale in the backscatter electron image (**Figure 5.11**), indicating that the average atomic number of these phases were greater than NiO. Indeed, their corresponding praseodymium to nickel atomic ratios were close to the target value of 4:3 (around 1.3). Hence, they were regarded as the $Pr_4Ni_3O_{10+/-\delta}$ phase. Overall, considering that NiO had low quantity and it did not form a percolated network at the $Pr_4Ni_3O_{10+/-\delta}$ grain boundaries (**Figure 5.11**), its impact on the following $Pr_4Ni_3O_{10+/-\delta}$ electrical conductivity measurements should be less of concern.

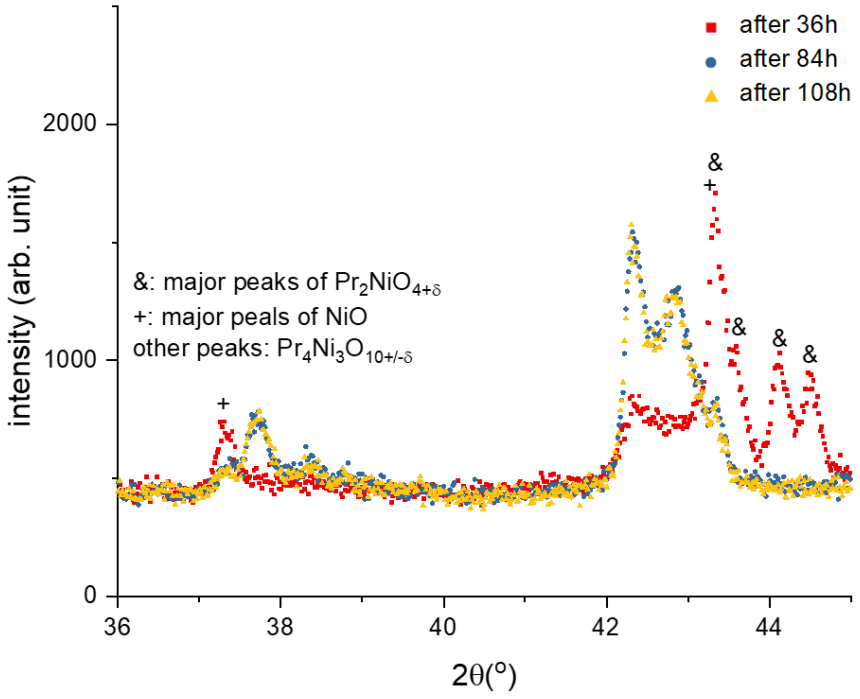


Figure 5.10: The change of the phase after post-annealing the sintered $Pr_4Ni_3O_{10+/-\delta}$ pellet for various amount of time at 1050°C under oxygen flow. Reproduced from Tsai et al. [18].

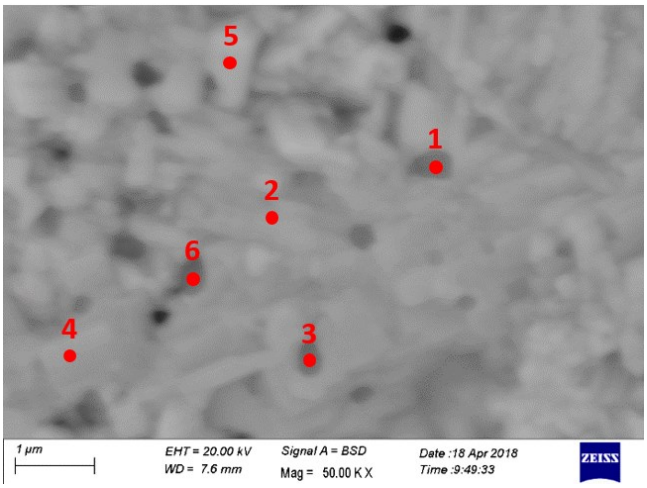


Figure 5.11: The backscattered electron image highlights the presence of secondary phase, which was later identified as NiO using EDS (**Table 5.2**), on the post-annealing (1050°C, 108 hours, oxygen) sintered $Pr_4N_3O_{10+/-\delta}$ pellet. Reproduced from Tsai et al. [18].

Table 5.2: The EDS results of each site of interest in **Figure 5.11**. Reproduced from Tsai et al. [18].

Site of interest	Pr	Ni	Pr:Ni ratio	Comments
1	36.0	64.0	0.6	NiO
2	58.1	41.9	1.4	$Pr_4Ni_3O_{10+/-\delta}$
3	38.3	61.7	0.6	NiO
4	55.9	44.1	1.3	$Pr_4Ni_3O_{10+/-\delta}$
5	56.8	43.2	1.3	$Pr_4Ni_3O_{10+/-\delta}$
6	48.1	51.9	0.9	NiO

The results of $Pr_4Ni_3O_{10+/-\delta}$ electrical conductivity measurement from room temperature to ~815°C in air were plotted in **Figure 5.12**, together with the previously reported values in the literature [1, 2]. The decreasing trend of the electrical conductivity with increasing temperature showed that $Pr_4Ni_3O_{10+/-\delta}$ possessed a metallic behaviour. Vibhu et al. [1] suggested that this was mainly because of the electron mobility reduction at higher temperatures as the concentration change of Ni^{+3} was almost insignificant. For example, it only decreased from 73% to 70% when heating the sample from room temperature to 800°C in air [1]. At 700°C in air, the measured $Pr_4Ni_3O_{10+/-\delta}$ electrical conductivity was 235 Scm^{-1} and this was greater than the reported 86 Scm^{-1} and ~56 Scm^{-1} from Vibhu et al. [1] and Bassat et al. [2] using samples with desnity of ~70% and >80%, respectively. This is the highest measured electrical conductivity from $Pr_4Ni_3O_{10+/-\delta}$, thanks to the prepared dense pellet which was greater than 90% of theoretical density. Indeed, compared to the $Pr_2NiO_{4+\delta}$ electrical conductivity measured under the same conditions, which was ~105 Scm^{-1} [1], $Pr_4Ni_3O_{10+/-\delta}$ had electrical conductivity of at least two times greater. It is believed that the electrical conductivity of $Pr_4Ni_3O_{10+/-\delta}$ would be even greater if the sintered pellet approached 100% dense, with a value estimated to be between 275 to 322 Scm^{-1} at 700°C in air depending on the exponent used in **Equation 5.2** (e.g. n=1.5 or 3) [23]. $\sigma_{expected}$, $\sigma_{measured}$ and n are the expected electrical conductivity, the measured electrical conductivity based on the porosity in a sample and the exponent range reported in literature, respectively [23, 24]. The estimated electrical conductivities for pore-free $Pr_4Ni_3O_{10+/-\delta}$ as a function of temperature were also plotted in **Figure 5.12** for comparison. It is important to note that the calculation was an approximation as

the exponent in **Equation 5.2** varied significantly for different materials and the exponent corresponding to $Pr_4Ni_3O_{10+/-\delta}$ was unknown [23, 24].

$$\sigma_{expected} = \frac{\sigma_{measured}}{(1-porosity)^n} \; where \; 1.5 < n < 3 \qquad \textbf{Equation 5.2}$$

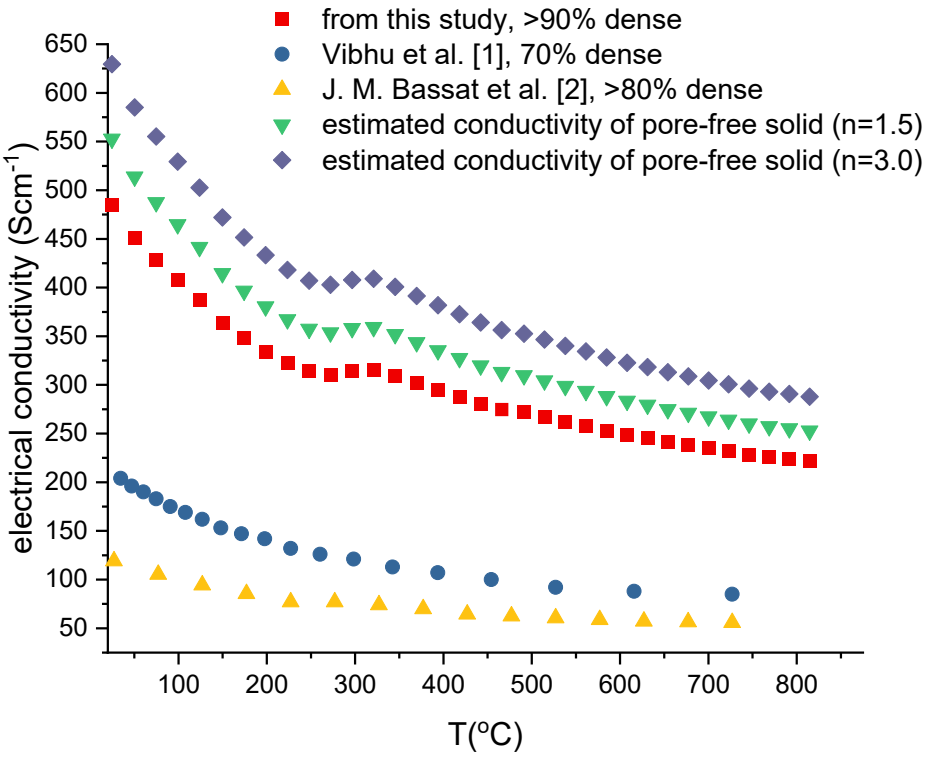
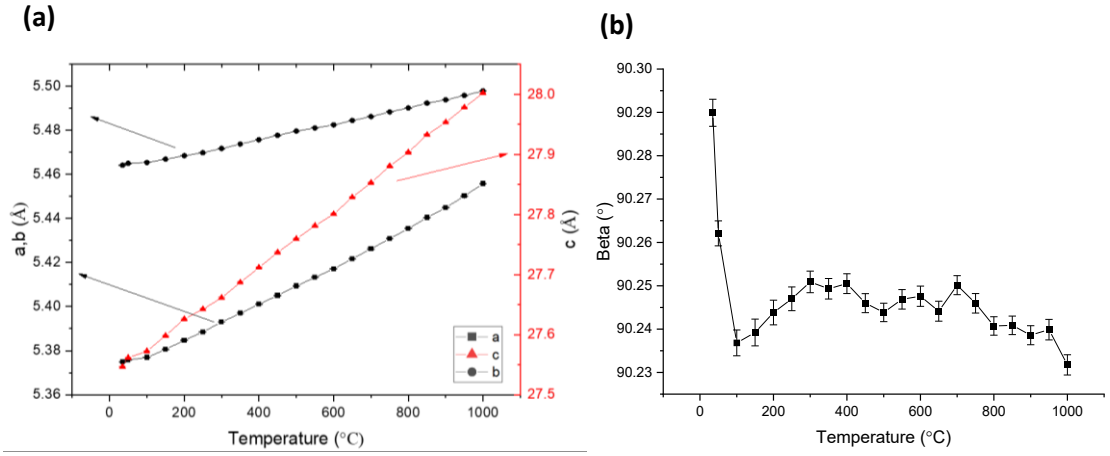


Figure 5.12: Comparison of $Pr_4Ni_3O_{10+/-\delta}$ electrical conductivity from this study with data reported from other literature sources, and with the estimated values when the solid is pore-free using **Equation 5.2**. All the measurement were conducted in air at different temperatures. The size of the measurement errors are smaller than the labels. Adapted from Tsai et al. [18].

Furthermore, **Figure 5.12** shows the presence of an anomaly occuring at ~300°C in air. To understand the reason behind it, *in-situ* XRD was applied to monitor the $Pr_4Ni_3O_{10-\delta}$ crystal structure change at increasing temperatures from 35°C to 1000°C in air. These results were then compared with the electrical conductivity measurements especially at ~300°C. As illustrated in **Figures 5.13(a)** and **(b)** and **Figures 5.14(a)** and **(b)**, $Pr_4Ni_3O_{10-\delta}$ was in the same space group of $P2_1/a$ over the examined temperature ranges. Although there was a slight mismatch of FWHM causing the higher χ^2 in the results of Le Bail refinement (**Figures 5.14(a)** and **(b)**), each calculated Bragg position aligned well with the experimental peaks. Both of these observations can be easily

supported by the shape of the difference cureves (Y_{obs}-Y_{calc}) [21]. The observed peak shape mismatch is due to the use of a Pseudo-Voigt peak shape function in the refinement and this peak shape function is poor to cope with anisotropic line broadening and possible stacking faults which have been observed in higher order Ruddlesden-Popper phases [8, 21]. However, it was found that this issue had a minor impact on determining the $Pr_4Ni_3O_{10-\delta}$ peak positions and hence the lattice parameters at each temperature. Indeed, the summary of lattice parameters (e.g. *a*, *b* and *c*) in **Figure 5.13(a)** does not reflect any anomaly at ~300°C but shows a linearly increasing trend when heating the sample. This is in contrast to the beta angle in which an abrupt change was observed at ~300°C in **Figure 5.13(b)**. This change is also reflected in the variation of the linear slope at the same temperature in **Figure 5.13(c)**. Overall, this indicates that there is a crystal structure rearrangement and this is in agreement with the observed anomaly in the electrical conductivity measurements. Nevertheless, the sudden change of beta angle at temperatures less than 100°C is uncertain and was not reflected in the electrical conductivity results shown in **Figure 5.12**. In addition, two anomalies were detected by Bassat et al. [2] at ~277.7°C and ~477°C when measuring $Pr_4Ni_3O_{10+/-\delta}$ electrical conductivity in air. The first anomaly is similar to the observation in **Figure 5.12** but no others were found at temperatures above 300°C.



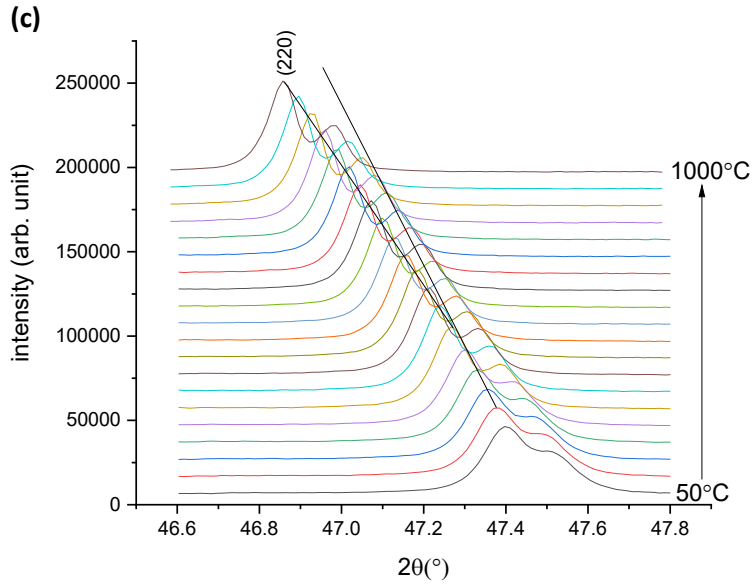
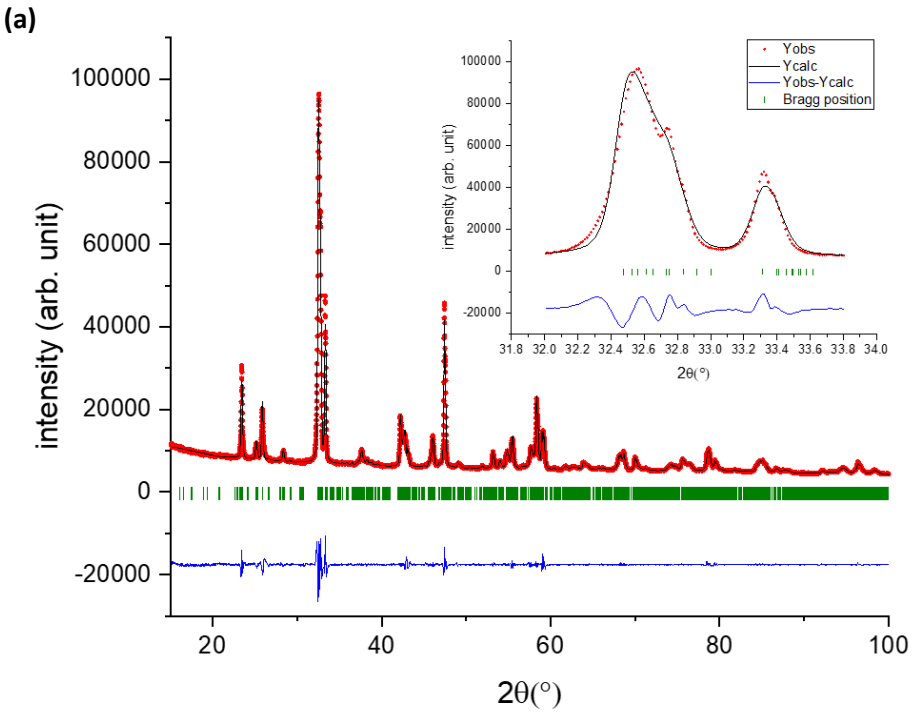


Figure 5.13: **(a) (b)** The change of the $Pr_4Ni_3O_{10-\delta}$ lattice parameters from 35°C to 1000°C in air. The *in-situ* XRD data were analysed using Le Bail refinement. The error bar in each point represents three estimated standard deviations. **(c)** The figure highlights the small distortion of the crystal structure at ~300°C in air. Each diffractogram was placed on top of each other along the heating direction from 50°C to 1000°C in air with temperature step size of 50°C. Reproduced from Tsai et al. [18].



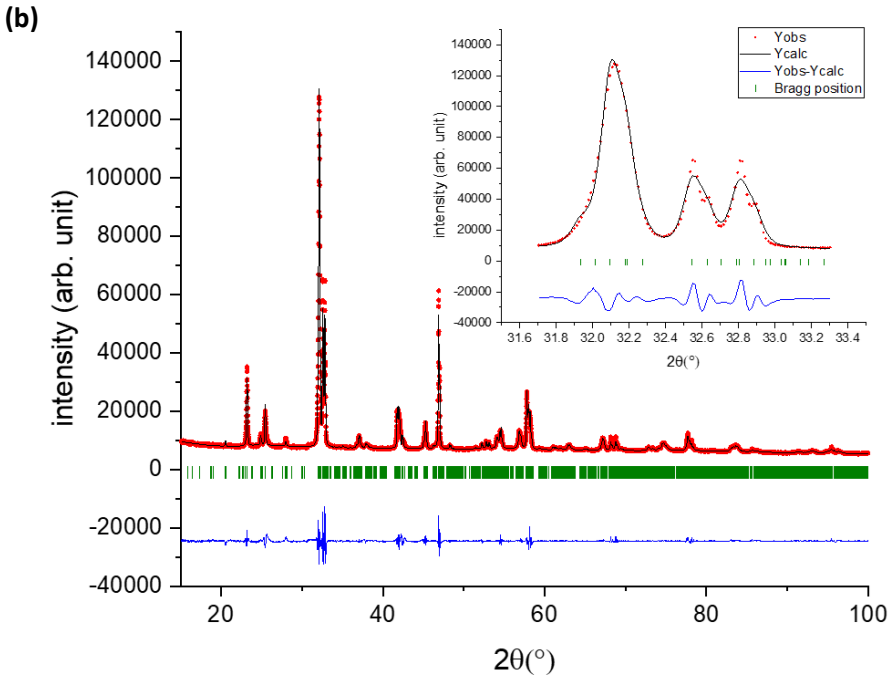


Figure 5.14: The *in-situ* XRD data analysis of the as-synthesised $Pr_4Ni_3O_{10-\delta}$ powder at **(a)** 35°C and **(b)** 1000°C in air using Le Bail refinement. The goodness of fit parameters are χ^2=11.9, R_{wp}= 3.96%, R_p= 2.39% and χ^2=16.3, R_{wp}= 4.44%, R_p= 2.73%, respectively. The evidence of peak shape mismatch is shown in the insets and they are the reasons for the relatively poor fit of the calculated model. Reproduced from Tsai et al. [18].

5.7 Summary

In this chapter, the synthesis kinetics of $Pr_4Ni_3O_{10-\delta}$ were investigated, together with other physical properties of the synthesised $Pr_4Ni_3O_{10-\delta}$ such as the crystal structure, the oxygen non-stoichiometry and the electrical conductivity.

$Pr_4Ni_3O_{10-\delta}$ was successfully synthesised when calcining the decomposed solid precursors under an oxygen atmosphere at 1050°C for at least 84 hours. Intermediate grindings were required to minimise the residuals of secondary phases. The synthesis reaction was found to be limited kinetically at lower temperatures by cation diffusion. The introduction of oxygen flow in the calcination stage allows the $Pr_4Ni_3O_{10-\delta}$ thermodynamically stable temperature boundary to be extended to a higher temperature compared to the conditions under air. Therefore, the kinetic limitation was overcome by the high calcination temperature and time.

From the high resolution neutron powder diffraction results, the synthesised $Pr_4Ni_3O_{10-\delta}$ was demonstrated to be best indexed by the monoclinic $P2_1/a$ space group,

rather than the commonly reported orthorhombic *Fmmm* space group. This was due to the asymmetric peak broadening and peak splitting observed in the diffractogram. The Rietveld refinement also showed that the sample had slight A-site and B-site deficiency and oxygen hypostoichiometry with chemical formula of $Pr_{3.94(4)}Ni_{2.94(2)}O_{9.72(7)}$. The calculated oxygen content here was consistent with the measured results from iodometric titrations. In contrast to the other reported $Pr_4Ni_3O_{10-\delta}$ lattice parameters, $Pr_{3.94(4)}Ni_{2.94(2)}O_{9.72(7)}$ had a greater *c* value of 27.5728(8) Å. Indeed, all the cation and oxygen vacancies were located at the same perovskite tri-layers in the unit cell. It would be interesting to understand the presence of vacancy clusters and/or the oxygen transport mechanism locally. In addition, praseodymium was calculated to have ~+3 valence in the crystal structure whereas Ni contained mixed average valence of +2.6 and ~+3 in each perovskite tri-layer. The alternative location of mixed Ni valence might contribute to the conducting pathway of electrons in the crystal structure.

Finally, due to the prepared dense pellet which was higher than 90% with respect to the theoretical density, the highest electrical conductivity of $Pr_4Ni_3O_{10+/-\delta}$ was received from room temperature to 815°C in air. The measured electrical conductivity of 235 Scm^{-1} at ~700°C in air was about 3-4 times greater than the previously reported values. The overall electrical conductivity of $Pr_4Ni_3O_{10+/-\delta}$ as a function of temperature possessed metallic behaviour but an anomaly was observed at ~300°C. This was later confirmed by *in-situ* XRD to be due to a small crystal structure rearrangement. $Pr_4Ni_3O_{10-\delta}$ was also demonstrated to have no macroscopic phase change at conditions between room temperature and 1000°C in air.

References

[1] V. Vibhu, A. Rougier, C. Nicollet, A. Flura, S. Fourcade, N. Penin, J.-C. Grenier, J.-M. Bassat, *Journal of Power Sources,* 317, 184-193, 2016.

[2] J. M. Bassat, C. Allancon, P. Odier, J. P. Loup, M. Deus Carvalho, A. Wattiaux, *European Journal of Solid State Inorganic Chemistry,* 35, 173-188, 1998.

[3] Z. Zhang, M. Greenblatt, *Journal of Solid State Chemistry,* 117, 236-246, 1995.

[4] E. Boehm, J.-M. Bassat, P. Dordor, F. Mauvy, J.-C. Grenier, Ph. Stevens, *Solid State Ionics,* 176, 2717-2725, 2005.

[5] C. D. Ling, D. N. Argyriou, G. Wu, J. J. Neumeier, *Journal of Solid State Chemistry,* 152, 517-525, 1999.

[6] V. I. Voronin, I. F. Berger, V. A. Cherepanov, L. Ya. Gavrilova, A. N. Petrov, A. I. Ancharov, B. P. Tolochko, S. G. Nikitenko, *Nuclear Instruments and Methods in Physics Research A,* 470, 202-209, 2001.

[7] A. Olafsen, H. Fjellvag, B. C. Hauback, *Journal of Solid State Chemistry,* 151, 46-55, 2000.

[8] J. Zhang, H. Zheng, Y.-S. Chen, Y. Ren, M. Yonemura, A. Huq, J. F. Mitchell, arXiv:1904.10048v1, 2019.

[9] V. Vibhu, "PhD thesis: Stability and aging studies of praseodymium-based nickelates as cathodes for solid oxide fuel cells", Universite de Bordeaux, 2016.

[10] J. Rodriguez-Carvajal, *Physica B.,* 192, 55-69, 1993.

[11] B. H. Toby, R. B. Von Dreele, *Journal of Applied Crystallography,* 46, 544-549, 2013.

[12] Y. Adachi, N. Hatada, K. Hirota, M. Kato, T. Uda, *Journal of the American Ceramic Society,* 102, 7077-7088, 2019.

[13] S. H. N. Lim, D. R. McKenzie, M. M. M. Bilek, *Review of Scientific Instruments,* 80, 075109, 2009.

[14] J. G. Railsback, Z. Gao, S. A. Barnett, *Solid State Ionics,* 274, 134-139, 2015.

[15] A. E. Danks, S. R. Hall, Z. Schnepp, *Materials Horizons,* 3, 91-112, 2016.

[16] P. Barboux, P. Griesmar, F. Ribot, L. Mazerolles, *Journal of Solid State Chemistry,* 117, 343-350, 1995.

[17] A. V. Kovalevsky, V. V. Kharton, A. A. Yaremchenko, Y. V. Pivak, E. V. Tsipis, S. O. Yakovlev, A. A. Markov, E. N. Naumovich, J. R. Frade, *Journal of Electroceramics,* 18, 205-218, 2007.

[18] C.-Y. Tsai, A. Aguadero, S. J. Skinner, *Journal of Solid State Chemistry,* 289, 121533, 2020.

[19] A. V. Kovalevsky, V. V. Kharton, A. A. Yaremchenko, Y. V. Pivak, E. N. Naumovich, J. R. Frade, *Journal of the European Ceramic Society,* 27, 4269-4272, 2007.

[20] P. Laffez, Q. Simon, Y. Kikuchi, R. Retoux, F. Giovannelli, A. Yamamoto, *Thin Solid Films,* 693, 137705, 2020.

[21] L. B. McCusker, R. B. Von Dreele, D. E. Cox, D. Louer, P. Scardi, *Journal of Applied Crystallography,* 32, 36-50, 1999.

[22] O. H. Hansteen, H. Fjellvåg, *Journal of Solid State Chemistry,* 141, 212-220, 1998.

[23] V. Dusastre, J. A. Kilner, *Solid State Ionics,* 126, 163-174, 1999.

[24] C. E. Baumgartner, R. H. Arendt, C. D. Iacovangelo, B. R. Karas, *Journal of the Electrochemical Society,* 131, 2217-2221, 1984.

Chapter 6 Evaluation of the electrochemical performance of $Pr_4Ni_3O_{10-\delta}$ and CGPO composite electrodes

6.1 Introduction

The motivation of making a composite electrode with $Pr_4Ni_3O_{10-\delta}$ and $Ce_{1-x-y}Gd_xPr_yO_{2-\delta}$ has been discussed in **Chapters 2** and **4**. Indeed, the results from **Chapter 4** show that various chemical compositions of $Ce_{1-x-y}Gd_xPr_yO_{2-\delta}$ were produced after sintering $Pr_2NiO_{4+\delta}$ and $Ce_{0.9}Gd_{0.1}O_{2-\delta}$ (CGO10). The content of praseodymium in the newly formed $Ce_{1-x-y}Gd_xPr_yO_{2-\delta}$ is directly related to the distance from the interface of CGO10 and $Pr_2NiO_{4+\delta}$. Given that $Pr_4Ni_3O_{10-\delta}$ was synthesized using the approach suggested in **Chapter 5**, the only question left is what the chemical composition of $Ce_{1-x-y}Gd_xPr_yO_{2-\delta}$ that should be used for the proposed composite air electrodes is.

Several studies have demonstrated that co-doping gadolinium and praseodymium in CeO_2 can increase the oxygen ionic conductivity, compared with the single doping cases as co-doping enhances oxygen ion mobility [1-3]. Since the main purpose of introducing $Ce_{1-x-y}Gd_xPr_yO_{2-\delta}$ is to enhance the effective oxygen ionic conductivity in the composite air electrode, the total doping level and the ratio between gadolinium and praseodymium need to be optimized to maximize the oxygen ionic conductivity of $Ce_{1-x-y}Gd_xPr_yO_{2-\delta}$. As mentioned in **Section 2.7.2**, from the simulated model of Dholabhai et al. [1], the maximum oxygen ionic conductivity can be reached when the total dopant level is around 25 mol.% at the cerium site. Exceeding this range, the oxygen ionic conductivity will decrease because of the formation of associated defects between the acceptor dopants and the oxygen vacancies and/or the repulsion of the increasing oxygen vacancies in the system [1]. From all of the literature reviewed to date that report the oxygen ionic conductivity of different $Ce_{1-x-y}Gd_xPr_yO_{2-\delta}$ chemical compositions, $Ce_{0.75}Gd_{0.1}Pr_{0.15}O_{2-\delta}$ showed the highest oxygen ionic conductivity of 0.055 Scm^{-1} at 700°C in air [2-8].

The other advantages of including praseodymium in the ceria phase is its ability to conduct electrons. This is mainly due to the +3/+4 mixed valence of praseodymium [3, 9-11]. The electronic conductivity of $Ce_{1-x-y}Gd_xPr_yO_{2-\delta}$ is proportional to the amount of

praseodymium in the system and can be explained by the percolation theory mentioned in **Section 2.8** [3, 12]. Cheng et al. [3] found that the electronic conductivity percolation threshold of $Ce_{0.9-x}Gd_{0.1}Pr_xO_{2-\delta}$ at temperature between 500°C and 1000°C was when x had a value of around 0.12. However, it is important to note that the high praseodymium content in ceria will result in a high overall thermal expansion coefficient as praseodymium is partially reduced at ~500°C [3, 12, 13]. Therefore, the ionic radius of Pr^{+4} changes from 0.960 Å to 1.260 Å of Pr^{+3} [13]. The total thermal expansion coefficient (TEC) of $Ce_{0.75}Gd_{0.1}Pr_{0.15}O_{2-\delta}$ is $21.5x10^{-6}$ K^{-1} between 200-900°C which is much greater than the target TEC of $10.8\text{-}13.5x10^{-6}$ K^{-1} from the conventional electrolytes (**Section 1.3.1**) [3].

Overall, the issue of TEC mismatch of $Ce_{0.75}Gd_{0.1}Pr_{0.15}O_{2-\delta}$ can be significantly mitigated if the other material in the composite (e.g. $Pr_4Ni_3O_{10-\delta}$) has a much lower TEC value, which was reported to be $10x10^{-6}$ K^{-1} between room temperature and 1000°C in air [14, 15]. It can be concluded that $Ce_{0.75}Gd_{0.1}Pr_{0.15}O_{2-\delta}$ is the best chemical composition in terms of oxygen ionic conductivity, electronic conductivity and thermal expansion coefficients. Hence, $Ce_{0.75}Gd_{0.1}Pr_{0.15}O_{2-\delta}$ will be used and mixed with $Pr_4Ni_3O_{10-\delta}$ to form a composite electrode. The aim of this chapter is to identify the electrochemical performance and the long term (7 days) stability of the $Pr_4Ni_3O_{10-\delta}$-$Ce_{0.75}Gd_{0.1}Pr_{0.15}O_{2-\delta}$ composite electrodes.

6.2 Detailed experimental procedures

$Pr_4Ni_3O_{10-\delta}$ was synthesized using the same approach and annealing conditions as described in **Section 5.2**. $Ce_{0.75}Gd_{0.1}Pr_{0.15}O_{2-\delta}$ (CGPO) and other chemical compositions such as $Ce_{0.9-x}Gd_{0.1}Pr_xO_{2-\delta}$ (x=0, 0.30 and 0.45) were also synthesized using the citrate-nitrate route. A stoichiometric ratio of $Ce(NO_3)_3.6H_2O$ (Alfa Aesar), $Pr(NO_3)_3.6H_2O$ (Aldrich) and $Gd(NO_3)_3.6H_2O$ (Aldrich) with purity greater than 99.5% were mixed and dissolved in a citric acid solution (~10 wt.% citric acid, Sigma-Aldrich). Due to the hygroscopic nature of each precursor, the water content of each precursor was determined by measuring the weight before and after the decomposition at 600°C for several hours in air. After decomposition, each precursor formed CeO_2, Pr_6O_{11} and Gd_2O_3, respectively, confirmed by a laboratory X-ray diffractometer (PANalytical X'Pert Pro MPD with a Cu K_α source). The mixed nitrate solution was heated on a hot

plate until a gel was formed. The gel was then transferred to an oven for decomposition at 600°C for 12 hours in air before any further thermal treatment in air at higher temperatures.

Electrode inks with $Pr_4Ni_3O_{10-\delta}$-$Ce_{0.75}Gd_{0.1}Pr_{0.15}O_{2-\delta}$ weight ratios ranging from 100:0 wt.%, 75:25 wt.%, 50:50 wt.%, 25:75 wt.% and 0:100 wt.%, and the sintered 10Sc1CeSZ electrolyte pellets were prepared as described earlier in **Section 3.3.2**. The electrode inks were brush painted onto each side of the sintered electrolyte pellets before sintering for 2 hours in air at 950°C for 100:0 and 0:100 wt.% ratios and at 900°C for the rest of the symmetrical cells. The electrode sintering temperatures were determined by the Scotch tape test results (**Section 3.4.8**). The platinum paste (Gwent Group, Code No. C51002P6) or gold paste (Gwent Group, Code No. C2090908D1) were then brush-painted on the sintered electrodes and heated for 2 hours at 900°C and 700°C, respectively to act as a current collector of a symmetrical cell. Indeed, platinum paste was also used as the current collector for the sintered 10Sc1CeSZ and CGPO samples. The approach used to prepare the CGPO pellet was similar to that used for the 10Sc1CeSZ electrolyte pellets, although the sintering temperature was lower (1300°C for 4 hours in air).

AC impedance spectroscopy was used to examine the electrical conductivity of the sintered 10Sc1CeSZ and CGPO pellets and the electrochemical performance of each composite electrode. The impedance responses were measured using a Solartron 1260a Impedance/Gain-Phase Analyser under OCV condition with frequency range from 10MHz to 0.01Hz, measuring 30 points per decade, 1s integration time and AC amplitude of 100mV. For 10Sc1CeSZ and CGPO sintered pellets, the measurements were conducted from 500°C to 800°C and between 200°C and 800°C with temperature step size of 25°C, respectively. For the composite electrode, the temperature range of interest was between 600°C and 800°C with the same temperature step size. For the long term durability test (7 days) the furnace temperature was fixed at 700°C and the impedance responses were recorded every 30 minutes. A DC bias test was set up by introducing a 100mV DC polarization to the sample for 7 days at 700°C but impedance data were not recorded. This experiment was conducted to check if the electrical bias

will have any impact on $Pr_4Ni_3O_{10-\delta}$ degradation. All of the above measurements were undertaken in static laboratory air.

The laboratory X-ray diffractometer (PANalytical X'Pert Pro MPD with a Cu K_α source) with the same instrumental parameters mentioned in **Section 3.4.1.2** was used to identify phases within a sample after initial materials synthesis, after chemical compatibility tests, and before and after the AC impedance tests. The temperature and atmosphere conditions of each of the test are specified in the following sections. Le Bail refinement and Rietveld refinement of the XRD data were conducted using the FullProf software suite [16].

Particle sizes of the ball-milled powders and the electrode microstructures before and after the AC impedance test were examined by scanning electron microscopy (Zeiss Leo Gemini 1525, EHT of 5 keV, aperture size of 30 µm). Any Energy Dispersive X-ray Spectroscopy (EDS) analysis (Inca X-act EDS, Oxford Instruments) in the form of point mode or line scan, had EHT and aperture setting of 20 keV and 120 µm, respectively.

6.3 Chemical synthesis and phase identification

Figure 6.1(a) compares the $Ce_{0.75}Gd_{0.1}Pr_{0.15}O_{2-\delta}$ powder XRD results obtained from a sample after the decomposition stage at 600°C for 12 hours in air and after further thermal treatment at 700°C and then 900°C for several hours in air. The results show that $Ce_{0.75}Gd_{0.1}Pr_{0.15}O_{2-\delta}$ was fully formed after the decomposition stage. The relatively broader peaks after the decomposition stage compared to the resulting sharper ones after further thermal treatment indicate the increase of the crystallite size. This can be reflected by the full width at half maximum (FWHM) change of peak (111) at 2θ~28.5° before and after further thermal treatment. The initial FWHM was 0.84° whereas subsequent FWHM was 0.26°. The purpose of the further thermal treatment was to produce shaper peaks in the XRD data so that the following lattice parameter calculation had greater accuracy. The sharper the peaks were, the much easier for the Fullprof software to identify the exact peak positions. Based on the results of Le Bail refinement, **Figure 6.1(b)**, the synthesized $Ce_{0.75}Gd_{0.1}Pr_{0.15}O_{2-\delta}$ has a cubic fluorite structure with space group *Fm*-3*m* with lattice parameters of a = b =c 5.4157(1) Å. This value is consistent with the results from Cheng et al. [3].

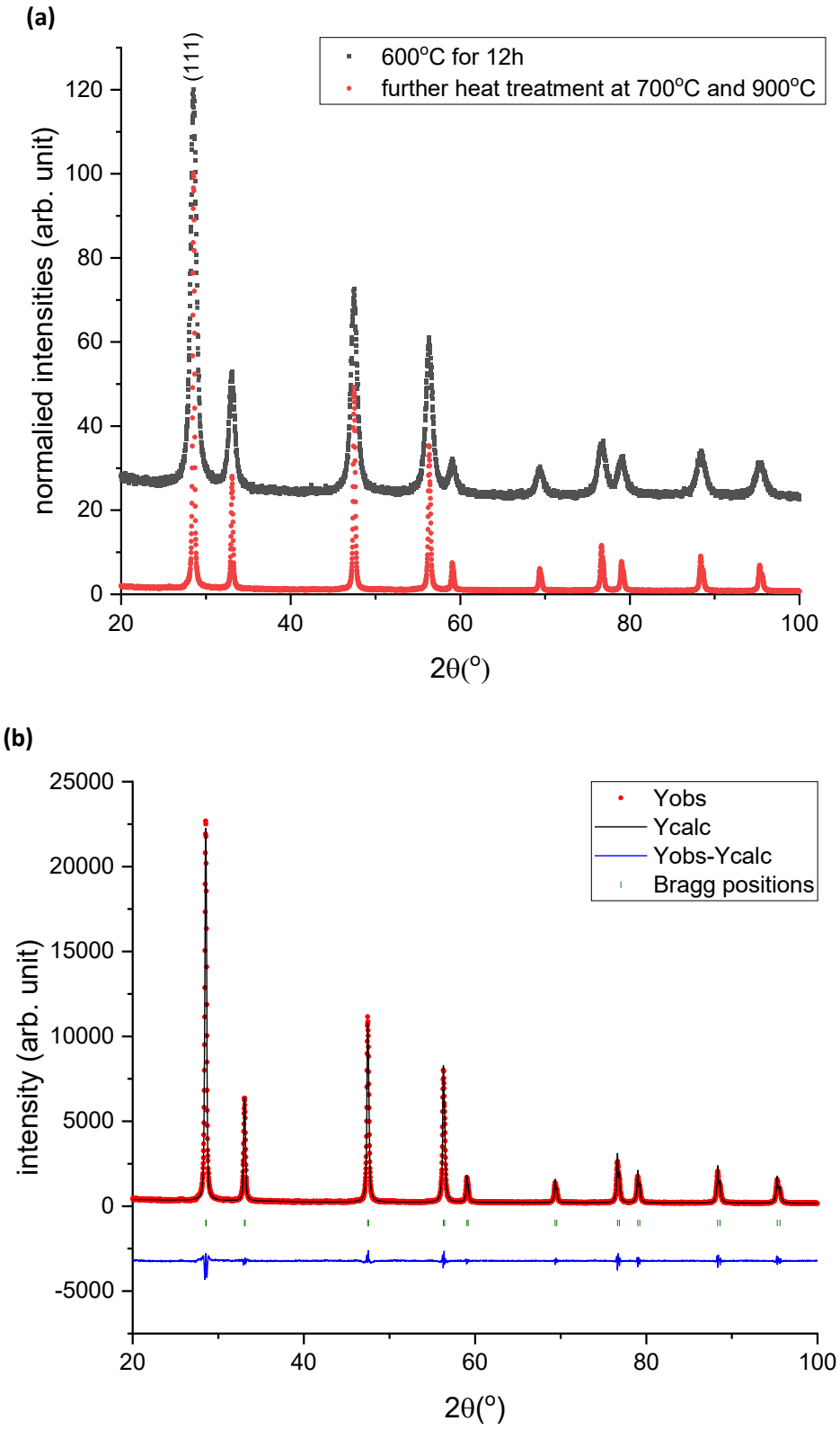


Figure 6.1: **(a)** Evolution of the $Ce_{0.75}Gd_{0.1}Pr_{0.15}O_{2-\delta}$ peak shape on heating. The figure highlights a sharpening of the peaks after further heating to 700°C and 900°C in air. **(b)** Le Bail refinement of the synthesised $Ce_{0.75}Gd_{0.1}Pr_{0.15}O_{2-\delta}$ experiencing further thermal treatment. χ^2=2.56, R_{wp}= 7.14%, R_p= 5.52%.

Several other $Ce_{0.9-x}Gd_{0.1}Pr_xO_{2-\delta}$ compositions (x=0, 0.30 and 0.45) were also synthesised and their lattice parameters were compared with $Ce_{0.75}Gd_{0.1}Pr_{0.15}O_{2-\delta}$ and $Ce_{0.9}Gd_{0.1}O_{2-\delta}$ as summarized in **Figure 6.2**. It is important to note that each of the $Ce_{0.9-x}Gd_{0.1}Pr_xO_{2-\delta}$ phases has the same space group and a solid solution was formed when introducing praseodymium into $Ce_{0.9}Gd_{0.1}O_{2-\delta}$. The decrease of the lattice parameters with increasing praseodymium content in the system can be explained by the smaller Pr^{+4} ionic radius (0.960 Å) compared with the one of Ce^{+4} (0.970 Å) as suggested in **Section 4.4** [13]. The same observations have been reported in several studies regarding the praseodymium substituted/doped ceria $Ce_{1-x}Pr_xO_{2-\delta}$ and $Ce_{1-x-y}Gd_xPr_yO_{2-\delta}$ [3, 12, 13]. It can be concluded that the praseodymium sites are tetravalent in $Ce_{0.9-x}Gd_{0.1}Pr_xO_{2-\delta}$ at room temperature under air, as expected, and that the $Ce_{0.9-x}Gd_{0.1}Pr_xO_{2-\delta}$ solid solutions obey Vegard's law [3, 13]. Indeed, considering the as-mentioned lattice parameters of $Ce_{0.75}Gd_{0.1}Pr_{0.15}O_{2-\delta}$ which were in agreement with the reported value of Cheng et al. [3], the lattice parameters of $Ce_{0.9}Gd_{0.1}O_{2-\delta}$ were also consistent with the literature [17]. Therefore, it is suggested that the synthesized $Ce_{0.75}Gd_{0.1}Pr_{0.15}O_{2-\delta}$ had the correct chemical composition.

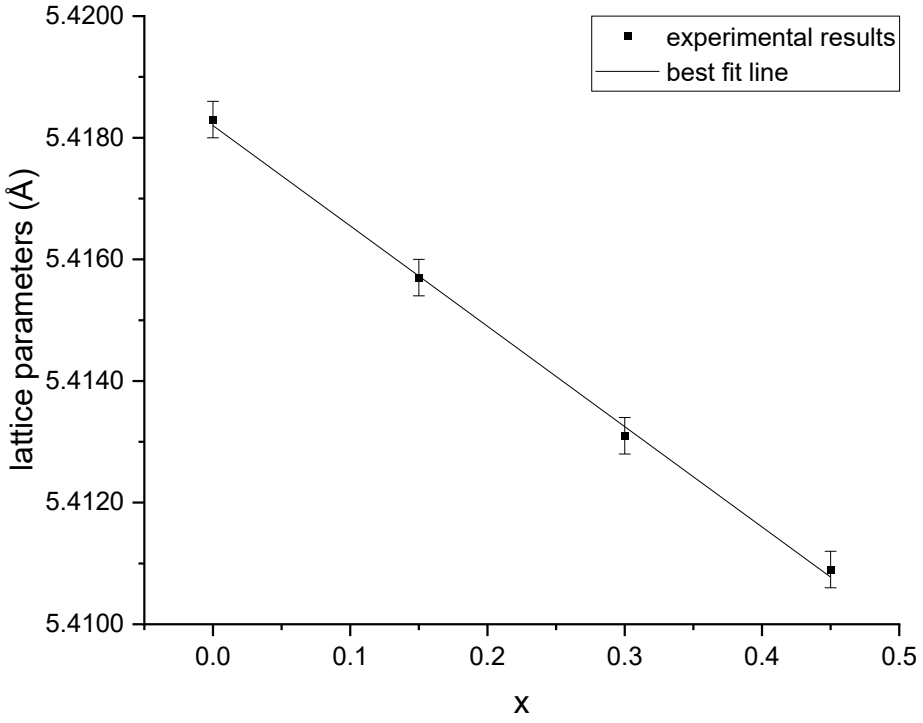
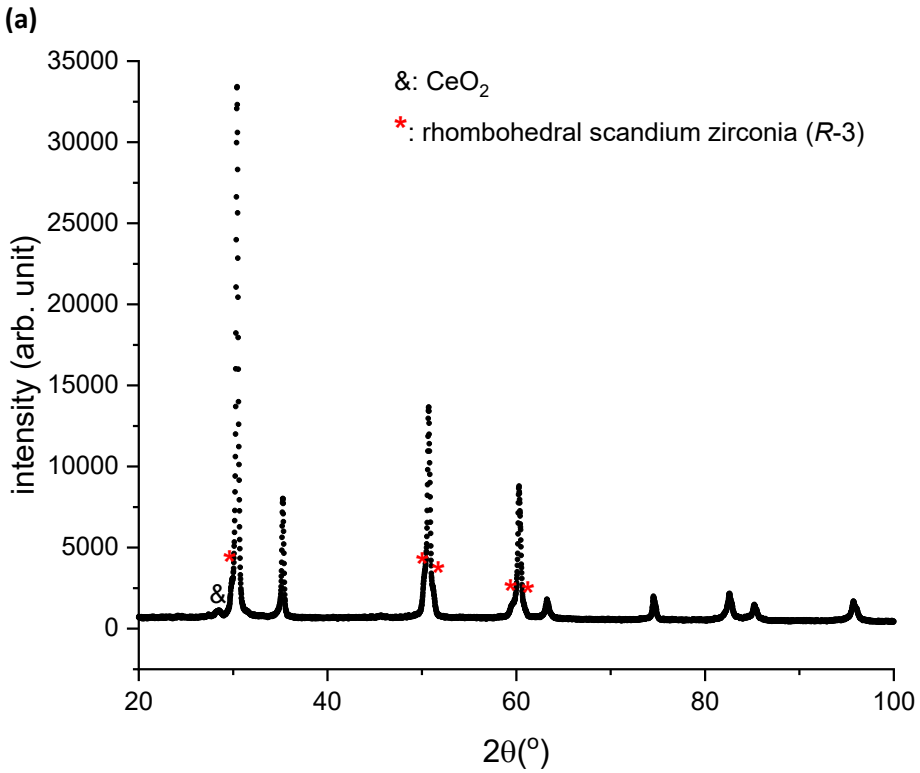


Figure 6.2: The change of lattice parameters for $Ce_{0.9-x}Gd_{0.1}Pr_xO_{2-\delta}$ with various x which equals to 0, 0.15, 0.30 and 0.45. The error bar in each point represents three estimated standard deviations.

The phase of the as-received 10Sc1CeSZ powder from DKKK, Japan (Lot No.: H2228) was firstly examined by XRD and the results are shown in **Figure 6.3(a)**. It is apparent that the as-received powder was not in the form of a pure cubic (*Fm*-3*m*) phase but other secondary phases such as rhombohedral (*R*-3) scandium zirconate and ceria were also present. To form a single cubic phase, the as-received powder was thermally treated at 1500°C for 5 hours in air and the corresponding XRD results are illustrated in **Figure 6.3(b)**. Within the detection limit of XRD, the pure cubic *Fm*-3*m* 10Sc1CeSZ was received with the lattice parameters determined to be a = b = c = 5.0926(1) Å. This thermally treated powder was then used for the following chemical compatibility test (**Section 6.4**) and the electrolyte pellet fabrication (**Section 3.3.2**)



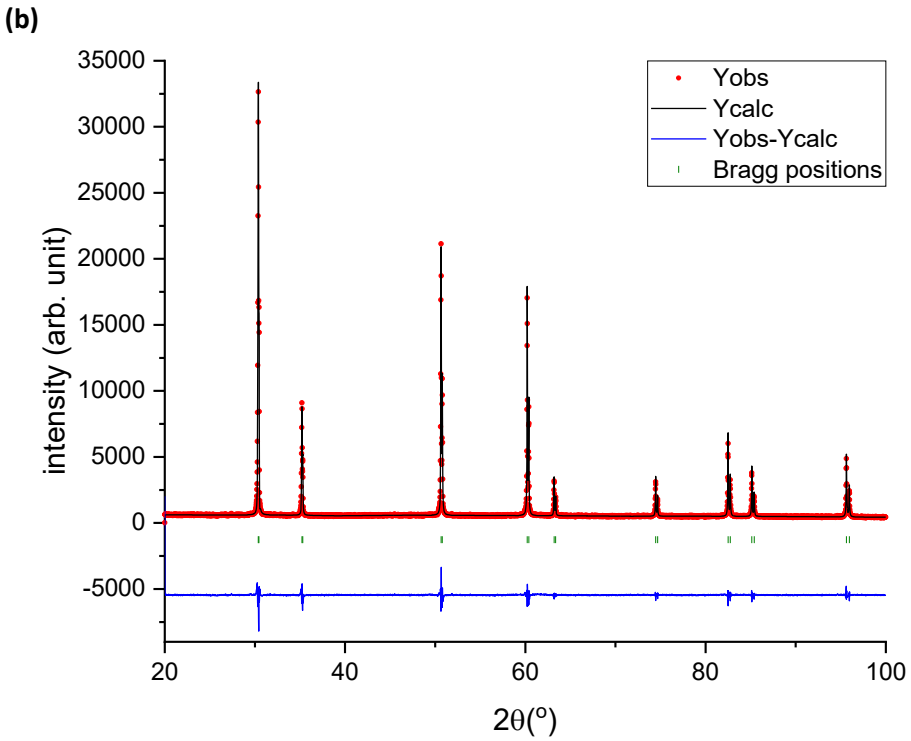


Figure 6.3: **(a)** The XRD data of the as-received 10Sc1CeSZ powder. **(b)** Le Bail refinement of the thermally treated 10Sc1CeSZ powder at 1500°C for 5 hours in air. χ^2=3.20, R_{wp}= 6.71%, R_p= 4.95%.

6.4 Chemical compatibility test of electrode and electrolyte components

The investigation of the chemical compatibility between the 10Sc1CeSZ electrolyte, $Pr_4Ni_3O_{10-\delta}$ and $Ce_{0.75}Gd_{0.1}Pr_{0.15}O_{2-\delta}$ (CGPO) composite electrode components is important as the results will have an impact on the performance and the long term stability of these composite air electrodes. The pressed pellet samples in the form of 1:1 weight ratio of combinations $Pr_4Ni_3O_{10-\delta}$, CGPO and 10Sc1CeSZ were prepared in the same manner as those discussed in **Section 4.2**. The powders used for the test were ball-milled and these were the same as the ones used to make the electrode inks and for the electrolyte fabrication. Based on the results in **Chapter 4** for $Pr_2NiO_{4+\delta}$ and $Ce_{0.9}Gd_{0.1}O_{2-\delta}$ which indicated that pressed pellet samples will facilitate the extent of chemical reaction (if there is any), pressed pellet samples were used in this investigation.

Figures 6.4, **6.5** and **6.6** summarise the chemical compatibility test results of 10Sc1CeSZ-$Pr_4Ni_3O_{10-\delta}$, 10Sc1CeSZ-CGPO and $Pr_4Ni_3O_{10-\delta}$-CGPO, respectively before and after being thermally treated at the electrode sintering condition of 950°C for 2

hours in air and being further heated at the highest operating temperature of 800°C for 24 hours in air. Indeed, these results were compared with the fresh pressed pellet samples being directly heated at 700°C for 7 days in air, conditions that resemble the test conditions used in the long term test. It is interesting to observe that no chemical reaction occurred between $Pr_4Ni_3O_{10-\delta}$ and 10Sc1CeSZ under both sintering and operating conditions (**Figure 6.4**). This is compared to the results from Montenegro-Hernandez et al. [18] who observed the formation of $Pr_2Zr_2O_7$, Pr_6O_{11} and $Pr_4Ni_3O_{10-\delta}$ when heating the mixture of the n=1 Ruddlesden-Popper phase $Pr_2NiO_{4+\delta}$ and $Zr_{0.92}Y_{0.08}O_{1.96}$ (YSZ) at 900°C in air for several hours. As the decomposition of $Pr_2NiO_{4+\delta}$ was firstly detected before the formation of $Pr_2Zr_2O_7$, Montenegro-Hernandez et al. [18] suspected that $Pr_2Zr_2O_7$ was produced by the reaction of $Pr_2NiO_{4+\delta}$ decomposition products, either Pr_6O_{11} or $Pr_4Ni_3O_{10-\delta}$ with YSZ. The results in **Figure 6.4** indicate that the higher thermodynamic stability of $Pr_4Ni_3O_{10-\delta}$ at temperatures below 950°C in air increases its chemical compatibility with 10Sc1CeSZ, the zirconia-based electrolyte material.

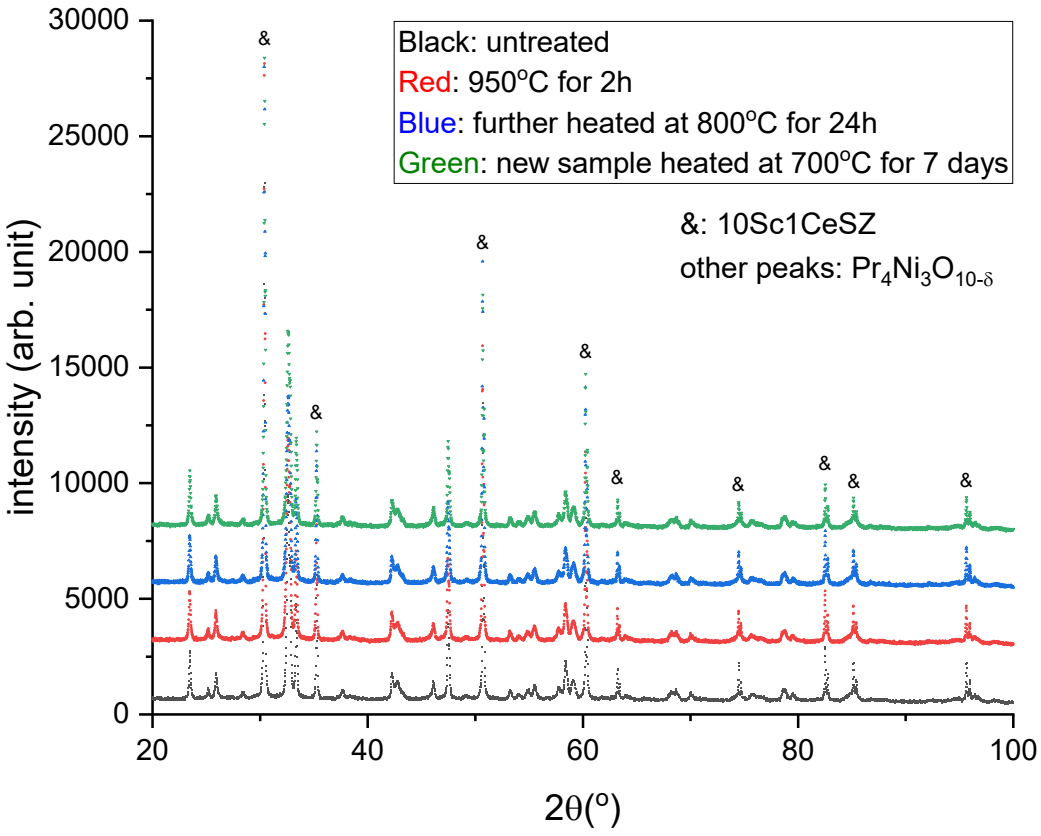


Figure 6.4: The XRD results of the chemical compatibility test between 10Sc1CeSZ and $Pr_4Ni_3O_{10-\delta}$ at various conditions in air.

With respect to the chemical compatibility test between CGPO and 10Sc1CeSZ, **Figure 6.5** shows that there were no new peaks observed but that there was a change of the relative peak intensities between the original 10Sc1CeSZ and CGPO peaks before and after the thermal treatment. For example, the most apparent change can be found at 2θ approximately equal to 28.5° and 30.5° which correspond to CGPO (111) and 10Sc1CeSZ (111). The area ratios between these two peaks (10Sc1CeSZ:CGPO) are 0.36(1), 0.60(2), 0.58(2) and 0.49(1) for the untreated sample, the sintered sample at 950°C for 2 hours, the further heat treated sample at 800°C for 24 hours and a fresh sample after being heated at 700°C for 7 days, respectively. The increase of 10Sc1CeSZ content and the corresponding decrease of CGPO content suggests that there is a diffusion of cations such as cerium, gadolinium and/or praseodymium from CGPO to 10Sc1CeSZ to form a solid solution. This cation diffusion happened under high temperature sintering conditions (e.g. 950°C for 2 hours in air) but its impact was less certain after further heat treatment at 800°C for 24 hours in air because there is no apparent difference between the 10Sc1CeSZ: CGPO peak area ratio for these two XRD results. The similar peak area ratio for the sample before and after further heat treatment (e.g. 0.60(3) versus 0.58(2)) might be due to the fact that the two samples originated from two different batches and the one that experienced further heat treatment was not handled between the two heating stages. It was, however, heated directly at a lower temperature of 800°C. Since the particle contact was not changed for this sample, it was suspected that the lower heating temperature limited the cation diffusion length exceeding the thickness of the newly formed secondary phases at the particle interface of 10Sc1CeSZ and CGPO. Indeed, to confirm if cation diffusion occurs within the operating temperature range, a fresh mixture of CGPO and 10Sc1CeSZ prepared as a pressed pellet was heated at 700°C for 7 days in air. The obvious 10Sc1CeSZ:CGPO peak ratio change of 0.49(1) was observed and this was compared with the untreated sample of 0.36(1) and the sintered sample of 0.60(3). The results indicate that the cation diffusion was mainly driven by temperature and then time.

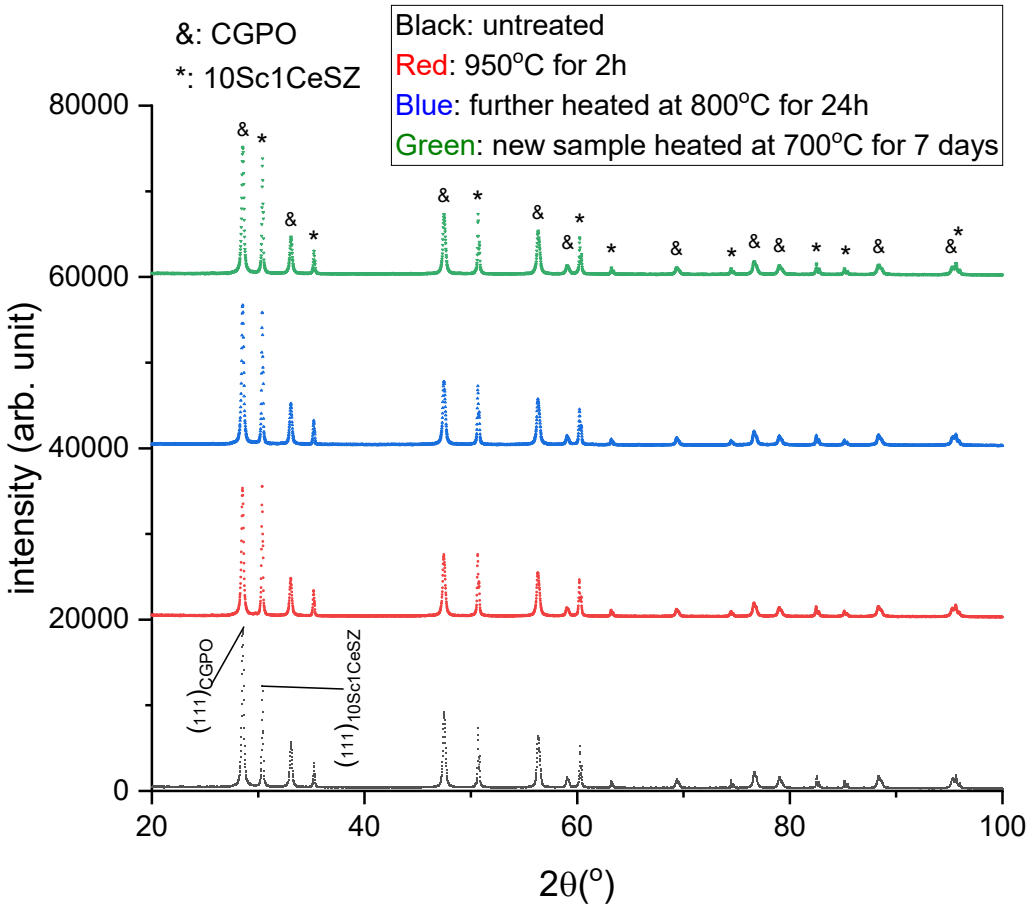


Figure 6.5: The XRD results of the chemical compatibility test between 10Sc1CeSZ and CGPO at various conditions in air.

The chemical compatibility test results of $Pr_4Ni_3O_{10-\delta}$-CGPO can be found in **Figure 6.6**. **Figure 6.6(a)** and **(b)** show that NiO was formed under the electrode sintering conditions of 950°C for 2 hours in air, but the amount of NiO present did not change after further heat treatment at 800°C for 24 hours in air. The total amount of NiO determined from the XRD results was calculated to be ~5.5 wt.% from Rietveld refinement in both cases. The lattice parameters of the CGPO phase were calculated to be a = 5.4135(1) Å and 5.4132(1) Å, respectively, compared to the initial CGPO lattice parameter of a = 5.4157(1) Å. Considering the presence of NiO, these results indicate that there was diffusion of praseodymium from $Pr_4Ni_3O_{10-\delta}$ to CGPO to form a new solid solution with lower lattice parameters because the ionic radius of Pr^{+4} (0.960 Å) is smaller than Ce^{+4} (0.970 Å) and Gd^{+3} (1.053 Å) [13]. Despite no direct evidence, it is possible that the chemical reaction of $Pr_4Ni_3O_{10-\delta}$ and CGPO was similar

to the one of $Pr_2NiO_{4+\delta}$ and $Ce_{0.9}Gd_{0.1}O_{2-\delta}$ discussed in **Section 4.4**. This can be reflected by the broader CGPO peaks in the diffraction data after sintering compared to the result from the untreated sample. CGPO phase could represent a distribution of composition and the praseodymium content in the composition might depend on the initial location of each CGPO phase from the $Pr_4Ni_3O_{10-\delta}$/CGPO interface. The small deviation of each newly formed CGPO phase from the initial CGPO chemical composition could be resolved by a high resolution diffraction technique but it is not considered here. Apparently, laboratory based XRD cannot distinguish these subtle changes and hence the resulting CGPO lattice parameters after thermal treatment are the average values of all possible compositions. In addition, to mitigate the chemical reaction between $Pr_4Ni_3O_{10-\delta}$ and CGPO under sintering conditions, it was proposed to decrease the sintering temperature to 900°C. In **Figure 6.6(b)**, there is an apparent decrease of NiO content for the fresh sample thermally treated at 900°C for 2 hours in air. The NiO content and the average CGPO lattice parameters were calculated to be 3.5(3) wt.% and a = 5.4148(1) Å from the Rietveld refinement. Finally, a 7 days long term $Pr_4Ni_3O_{10-\delta}$-CGPO chemical compatibility test was conducted at 700°C in air using a fresh sample. No formation of NiO content was observed. Hence, it can be concluded that the chemical reaction between $Pr_4Ni_3O_{10-\delta}$ and CGPO only occurs at temperatures greater than 900°C in air, and so processing and operation of any devices should be maintained below this temperature.

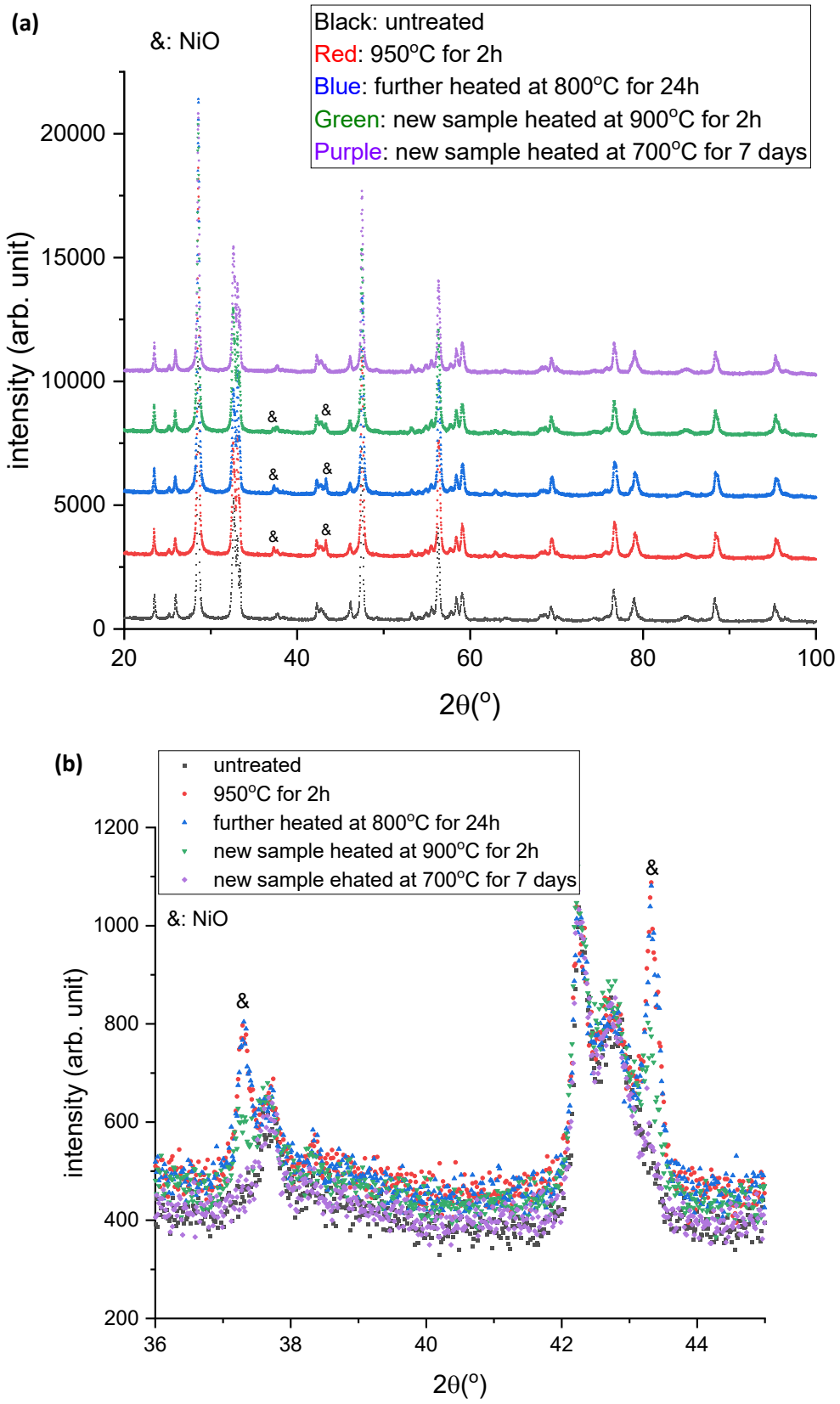


Figure 6.6: **(a)** The XRD results of the chemical compatibility test between $Pr_4Ni_3O_{10-\delta}$ and CGPO at various conditions in air. **(b)** The variation of NiO content before and after each different type of thermal treatment.

6.5 As-sintered electrodes

The air electrode sintering conditions for each composition have been discussed in **Section 6.2**. The XRD results of the as-sintered electrode are illustrated in **Figure 6.7**, which shows the relative change of the peak intensity between $Pr_4Ni_3O_{10-\delta}$ (117) at 32.7°/(200) at 33.3° and CGPO (111) at 28.5°/(200) at 33.1° for various $Pr_4Ni_3O_{10-\delta}$-CGPO compositions. The peak located at 30.4° corresponds to 10Sc1CeSZ (111) electrolyte. The presence of the 10Sc1CeSZ signal was due to the incomplete coverage of the electrolyte but not because of the smaller electrode thickness than the X-ray penetration depth. The latter statement was confirmed by the calculation in **Section 6.9**.

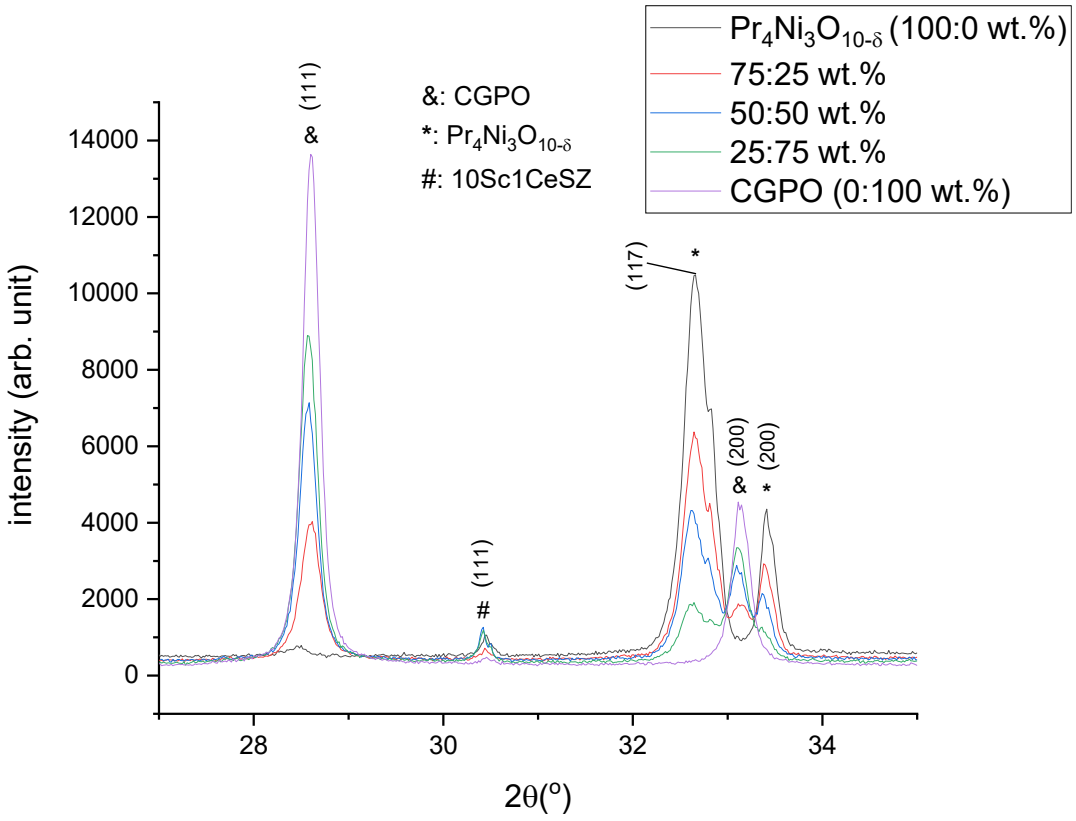
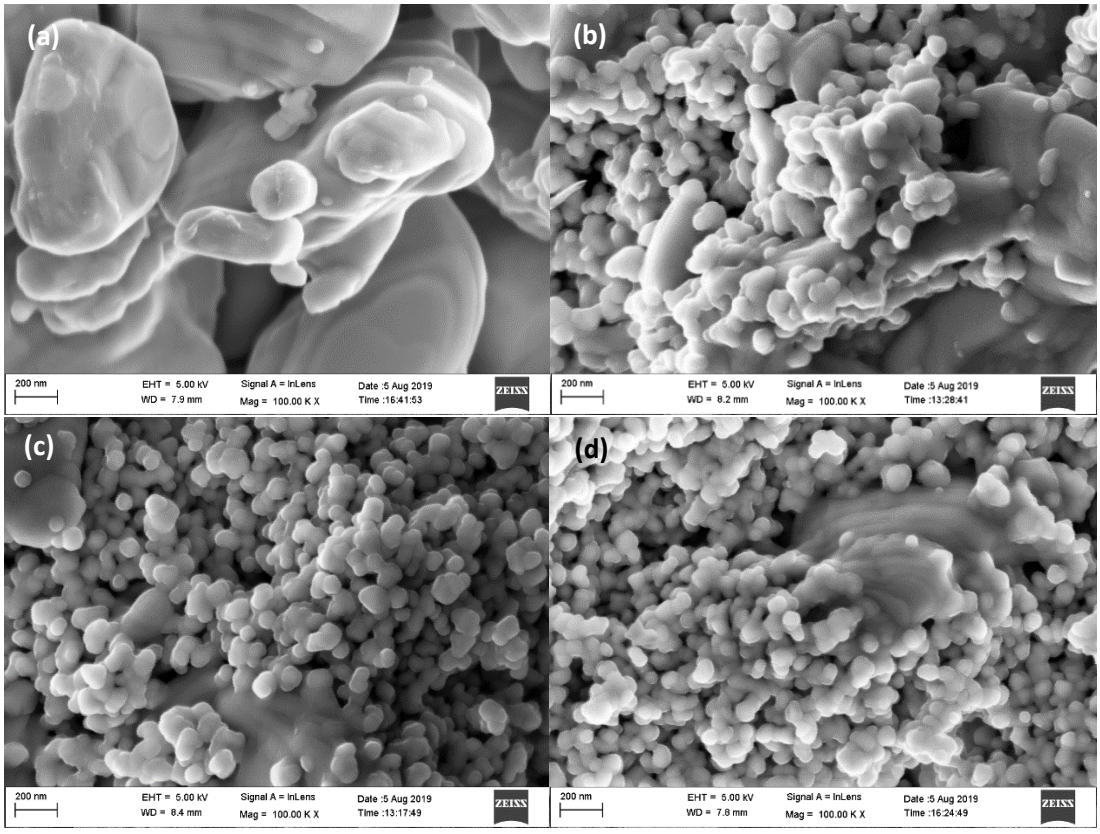


Figure 6.7: The XRD results of the as-sintered electrodes with various $Pr_4Ni_3O_{10-\delta}$ and CGPO compositions.

Moreover, the microstructure of the as-sintered electrodes was also recorded and these images are included in **Figures 6.8(a)-(e)**. It is important to note that before capturing the electron images, each of the as-sintered electrode samples were further

heat treated at 900°C for 2 hours in air, to resemble the thermal conditions experienced during the platinum paste/current collector sintering process. Therefore, any further change of the electrode microstructure in the following post-mortem tests can be attributed to the phenomenon occurring under test/operating conditions. The phase/relative content of $Pr_4Ni_3O_{10-\delta}$ and CGPO in **Figure 6.8** can be easily identified based on their initial particle size, shown in **Figures 6.9(a)** and **(b)**, after the synthesized powder was ball-milled and dried. The initial particle size of $Pr_4Ni_3O_{10-\delta}$ and CGPO were ~1 µm and ~80 nm, respectively. Apparently, there was an increase of CGPO particle size towards ~110 nm after the sintering processes. The change of $Pr_4Ni_3O_{10-\delta}$ particle size, on the other hand, was less significant.



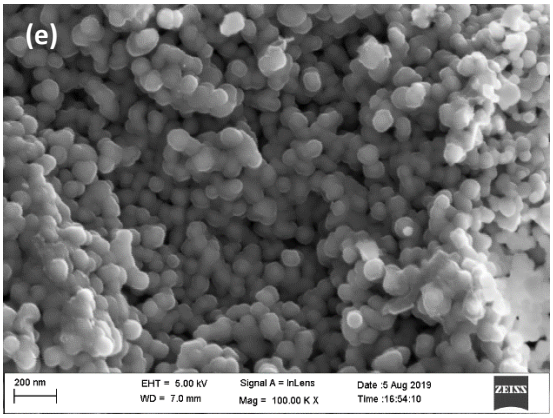


Figure 6.8: The electrode microstructure of the as-sintered $Pr_4Ni_3O_{10-\delta}$:CGPO electrodes. **(a)** 100:0 wt.%. **(b)** 75:25 wt.%. **(c)** 50:50 wt.%. **(d)** 25:75 wt.%. **(e)** 0:100 wt.%.

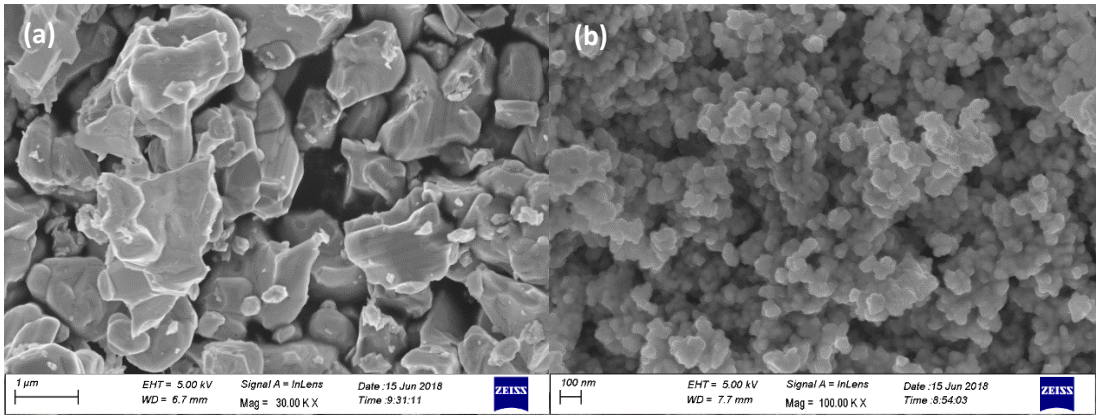


Figure 6.9: Secondary electron images show the particle size of (a) $Pr_4Ni_3O_{10-\delta}$ and (b) CGPO after ball-milling.

6.6 Electrochemical performance of the composite electrode with various compositions

To verify the quality of the AC impedance spectroscopy data the Kramer-Kronig (K-K) data validity test (**Section 3.4.5.3**) was used prior to further processing and analysis of the data. It is important that the physical states in a sample must be in equilibrium during AC impedance measurements, otherwise, the resulting data is not reliable. The K-K tests of all the AC impedance data measured at different temperatures for symmetrical cells with various composite electrodes have similar results to **Figure 6.10**. The relative residuals of the imaginary and the real components were both less than 1% which indicates that the measured AC impedance data is of good quality. It should

be noted that the data corresponding to the inductance part of the response (primarily due to the instrument and connections) was not considered in the K-K test.

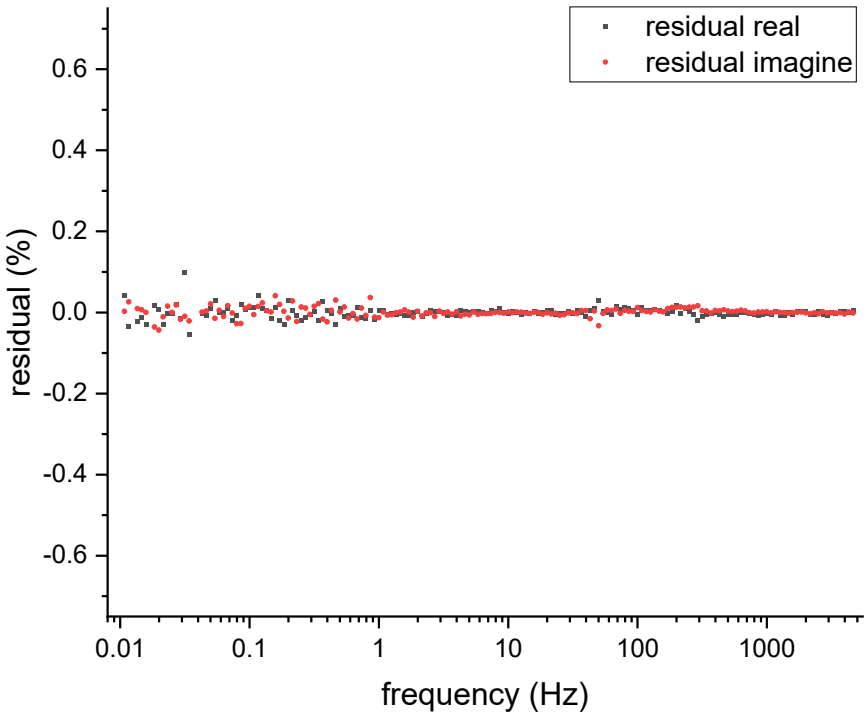


Figure 6.10: Kramer-Kronig test for the AC impedance data of a 50:50 wt.% composite electrode measured at 686°C in air.

The equivalent circuit models used to fit the AC impedance raw data for different composite electrodes measured at ~686°C in air are displayed in **Figure 6.11**. The goodness of fit indicator, the weighted sum of squares, the values of each component in the equivalent circuit models for different composite electrodes at various temperatures and their corresponding area specific resistances (ASR) are also included in **Table 6.1**. It is important to note that the minimum number of circuit elements were added to the models to receive an acceptable fit with reasonable physical meaning.

Figure 6.11 illustrates the change of the arc shape in the Nyquist plots at low frequency regions from a compressed semicircle for $Pr_4Ni_3O_{10-\delta}$ electrode to a Gerischer element for the 75:25 wt.% and 50:50 wt.% and to a compressed semicircle again for 25:75 wt.% and CGPO electrodes. These indicate the change of the rate limiting step(s) in the electrochemical reactions occurring at various composite electrode compositions. The shapes of the compressed semicircle (R//CPE) and the

Gerischer element (G) have already been discussed in **Section 3.4.5.1**. In general, there are two known electrode reactions that will lead to the Gerischer response [19-21]. The first one is when the electrode reactions are co-limited by both bulk oxygen diffusion (D*) and oxygen exchange processes at the electrode surface (k) [20]. Otherwise, the electrode reactions are co-limited by slow surface adsorption and surface diffusion [21]. It is worth mentioning that the first scenario usually occurs with mixed ionic and electronic conducting (MIEC) air electrodes and the second scenario was observed from the purely electronic conducting fuel electrode [20, 21]. Due to the fact that the composite electrode materials are MIECs and the AC impedance results are measured under normal air electrode operating conditions, it can be concluded that the Gerischer response observed in the 75:25 wt.% and 50:50 wt.% composite electrodes indicates the oxygen bulk diffusion and surface exchange co-limiting electrode reactions.

With respect to 25:75 wt.% composite electrode, it was found that the R//CPE circuit fit better than the Gerischer element so R//CPE was used to simulate the response of the electrochemical reaction. This indicates that there was a change of electrode reaction rate limiting step when more CGPO was included in the composite electrode composition. It is likely that the electrode reaction rate limiting step of the 25:75 wt.% composite is similar to that of the CGPO.

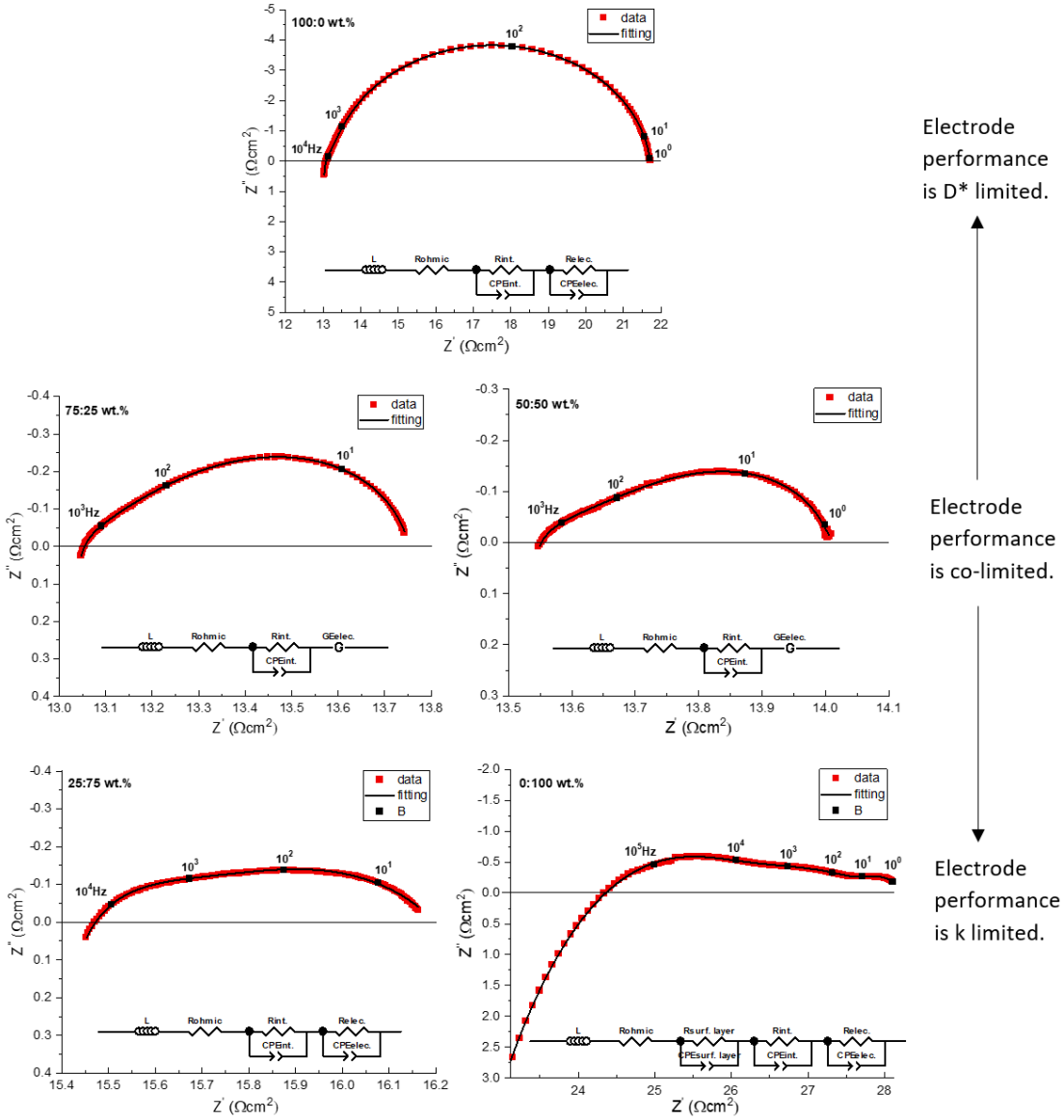


Figure 6.11: Fitting the AC impedance data (measured at ~686°C in air) of each composite electrode (including pure $Pr_4Ni_3O_{10-\delta}$ and pure CGPO electrodes) with the corresponding proposed equivalent circuit model. L, R_{ohmic}, $R_{surf.\ layer}$ /$CPE_{surf.\ layer}$, $R_{int.}$/$CPE_{int.}$, $R_{elec.}$/$CPE_{elec.}$ and $GE_{elec.}$ are inductor, ohmic resistance, resistance/constant phase element of surface layer, resistance/constant phase element of interface, resistance/constant phase element of electrode and Gerischer element corresponding to an electrode response, respectively.

Table 6.1: The AC impedance fitting summary of each composite electrode (including pure $Pr_4Ni_3O_{10-\delta}$ and pure CGPO electrodes).

Electr-ode	Tempe-rature (°C)	$R_{surf.\ layer}$ (Ω)	$CPE_{surf.\ layer}$-T (F)	$CPE_{surf.\ layer}$-P	Calculat-ed $C_{surf.\ layer}$ (F)	$R_{int.}$ (Ω)	$CPE_{int.}$- T (F)	$CPE_{int.}$-P	Calcula-ted $C_{int.}$ (F)	$R_{elec.}$ (Ω)	$CPE_{elec.}$-T (F)/ $GE_{elec.}$-T ($Ss^{0.5}$)	$CPE_{elec.}$-P/ $GE_{elec.}$-P (s^{-1})	Calculated $C_{elec.}$ (F)	ASR (Ωcm^2)	ASR error (Ωcm^2)	Weighted sum of squares
$Pr_4Ni_3O_{10-\delta}$	637					0.68	$1.53x10^{-2}$	0.52	$2.09x10^{-4}$	13.83	$3.35x10^{-4}$	0.94	$2.39x10^{-4}$	9.38	0.06	$3.20x10^{-3}$
	686					0.35	$1.18x10^{-2}$	0.57	$1.82x10^{-4}$	6.40	$3.15x10^{-4}$	0.94	$2.15x10^{-4}$	4.36	0.02	$1.48x10^{-3}$
	735					0.19	$1.03x10^{-2}$	0.61	$1.82x10^{-4}$	3.78	$3.40x10^{-4}$	0.93	$2.04x10^{-4}$	2.56	0.02	$2.67x10^{-3}$
	784					0.16	$8.39x10^{-3}$	0.65	$2.29x10^{-4}$	1.97	$3.50x10^{-4}$	0.93	$2.02x10^{-4}$	1.38	0.03	$5.78x10^{-3}$
75:25 wt.%	637					0.16	$5.92x10^{-1}$	0.43	$2.56x10^{-2}$	1.08	0.18	27.88	$3.33x10^{-2}$	0.81	0.01	$1.10x10^{-3}$
	686					0.10	$6.08x10^{-1}$	0.49	$3.66x10^{-2}$	0.46	0.25	73.64	$2.94x10^{-2}$	0.37	0.01	$2.28x10^{-4}$
	735					0.08	$3.52x10^{-1}$	0.58	$2.65x10^{-2}$	0.19	0.37	189.70	$2.71x10^{-2}$	0.18	0.01	$3.65x10^{-4}$
	784					0.06	$3.69x10^{-1}$	0.59	$2.64x10^{-2}$	0.09	0.51	468.40	$2.36x10^{-2}$	0.10	0.01	$1.05x10^{-3}$
50:50 wt.%	637					0.18	$2.39x10^{-1}$	0.47	$6.92x10^{-3}$	0.63	0.39	16.71	$9.50x10^{-2}$	0.53	0.01	$4.54x10^{-3}$
	686					0.14	$4.85x10^{-1}$	0.41	$8.92x10^{-3}$	0.25	0.58	46.61	$8.48x10^{-2}$	0.25	0.01	$6.17x10^{-4}$
	735					0.11	$5.13x10^{-1}$	0.42	$8.60x10^{-3}$	0.10	0.89	120.80	$8.07x10^{-2}$	0.14	0.01	$6.37x10^{-4}$
	784					0.09	$4.29x10^{-1}$	0.45	$8.21x10^{-3}$	0.04	1.48	317.00	$8.30x10^{-2}$	0.08	0.01	$1.29x10^{-3}$
25:75 wt.%	638					0.75	$4.50x10^{-2}$	0.40	$1.20x10^{-4}$	0.39	$1.38x10^{-1}$	0.68	$3.41x10^{-2}$	0.74	0.13	$2.37x10^{-3}$
	687					0.44	$3.17x10^{-2}$	0.42	$9.36x10^{-5}$	0.27	$1.10x10^{-1}$	0.64	$1.48x10^{-2}$	0.46	0.11	$1.13x10^{-3}$
	736					0.28	$2.35x10^{-2}$	0.49	$1.28x10^{-4}$	0.19	$6.98x10^{-2}$	0.66	$7.95x10^{-3}$	0.31	0.07	$4.18x10^{-4}$
	784					0.22	$1.78x10^{-2}$	0.53	$1.38x10^{-4}$	0.14	$3.97x10^{-2}$	0.71	$4.86x10^{-3}$	0.24	0.09	$6.67x10^{-4}$
CGPO	636.9	13.55	$1.52x10^{-5}$	0.52	$6.60x10^{-9}$	2.78	$2.63x10^{-2}$	0.43	$8.79x10^{-4}$	0.81	$2.46x10^{-1}$	0.90	$2.07x10^{-1}$	11.06	0.49	$2.78x10^{-3}$
	686	8.17	$3.67x10^{-5}$	0.48	$5.57x10^{-9}$	1.29	$2.15x10^{-2}$	0.45	$2.66x10^{-4}$	0.29	$2.67x10^{-1}$	0.90	$2.00x10^{-1}$	6.29	0.76	$2.93x10^{-3}$
	735	4.53	$4.75x10^{-5}$	0.48	$5.78x10^{-9}$	0.85	$1.21x10^{-2}$	0.45	$4.87x10^{-5}$	0.10	$3.76x10^{-1}$	0.89	$2.46x10^{-1}$	3.53	0.04	$2.21x10^{-3}$
	783.8	3.11	$4.11x10^{-5}$	0.48	$2.89x10^{-9}$	0.53	$4.55x10^{-3}$	0.54	$2.55x10^{-5}$	0.05	$7.58x10^{-1}$	0.71	$1.99x10^{-1}$	2.38	0.06	$3.10x10^{-3}$

To understand the electrode reaction rate limiting step for $Pr_4Ni_3O_{10-\delta}$ and CGPO, it is crucial to introduce the characteristic thickness (L_c), which is the ratio of D* and k [20, 22]. The D* and k values of $Pr_4Ni_3O_{10-\delta}$ were reported to be $4x10^{-9}$ cm^2s^{-1} and $1x10^{-7}$ cms^{-1}, respectively at 700°C in pO_2 = 0.21 bar by Vibhu [23] using the technique of isotopic exchange depth profile (IEDP) and secondary ion mass spectrometry analysis (SIMS). As discussed in **Sections 2.7.1** and **2.7.3**, Vibhu [23] suggested that part of the reason for the one order of magnitude lower D* and k values compared to the coefficients measured for $Pr_2NiO_{4+\delta}$ is because of the presence of small impurities such as NiO in the sintered pellet. On the other hand, Saher et al. [24] reported a promising $Pr_4Ni_3O_{10-\delta}$ oxygen exchange value, even higher than $Pr_2NiO_{4+\delta}$ and Pr_6O_{11} at temperatures below 500°C and at pO_2 of 0.21 bar, using the pulse isotopic exchange (PIE) technique (**Figure 2.11**). The oxygen exchange measurement from PIE should be more accurate as powder is used and there is no secondary phase issue. Indeed, if in reality $Pr_4Ni_3O_{10-\delta}$ has relatively low D* compared to its k, then the IEDP plus SIMS technique will never receive a precise k value of the material but a precise D* value [25]. This is because the oxygen exchange process is limited by the oxygen diffusion in the bulk material [25]. Therefore, the k value measured from PIE will be more reliable. Assuming that the slopes of the oxygen exchange rate versus temperature (**Figure 2.11**) are constant for both $Pr_4Ni_3O_{10-\delta}$ and $Pr_2NiO_{4+\delta}$, the exchange rate of $Pr_4Ni_3O_{10-\delta}$ will be similar to (but still slightly higher than) the one of $Pr_2NiO_{4+\delta}$ at 700°C. Using the reported k value of $Pr_2NiO_{4+\delta}$ at 700°C and pO_2 = 0.21 bar, $2x10^{-6}$ cms^{-1} [23], and the previous $Pr_4Ni_3O_{10-\delta}$ D* value of $4x10^{-9}$ cm^2s^{-1}, the calculated L_c is 20 µm. Since this L_c value is slightly lower than the real $Pr_4Ni_3O_{10-\delta}$ electrode thickness of ~22 µm, it indicates that the electrode reaction of $Pr_4Ni_3O_{10-\delta}$ is oxygen diffusion (D*) limited.

For the CGPO electrode, it is believed that the real D* and k values are similar to $Ce_{1-x}Pr_xO_{2-\delta}$. At 670°C in air, the D* and k values of $Ce_{0.9}Pr_{0.1}O_{2-\delta}$ (CPO10) and $Ce_{0.8}Pr_{0.2}O_{2-\delta}$ (CPO20) are $1.34x10^{-8}$ cm^2s^{-1} and $3.73x10^{-8}$ cms^{-1} and $1.01x10^{-8}$ cm^2s^{-1} and $4.59x10^{-8}$ cms^{-1}, respectively [22]. The corresponding L_c values for CPO10 and CPO20 are $3.58x10^3$ µm and $2.20x10^3$ µm [22]. As both values are much greater than the CGPO electrode thickness of ~26 µm, the CGPO electrode reaction is surface exchange (k) limited. Overall, it is interesting to observe the gradual change of the electrode

reaction rate limiting step(s) from oxygen diffusion limited in the $Pr_4Ni_3O_{10-\delta}$ electrode, to oxygen diffusion and surface exchange co-limited in 75:25 wt.% and 50:50 wt.% composite electrodes and then to surface exchange limited in the 25:75 wt.% and CGPO electrodes.

Moreover, as shown in **Table 6.1**, there is a significant difference in electrode capacitance ($C_{elec.}$) between $Pr_4Ni_3O_{10-\delta}$, composite electrodes and CGPO. $Pr_4Ni_3O_{10-\delta}$ has the smallest electrode capacitance whereas CGPO has the largest. These phenomena can be explained by the relatively low oxygen stoichiometry change occurring in the $Pr_4Ni_3O_{10-\delta}$ electrode when compared to CGPO. Chen et al. [22] also observed the large chemical capacitance of ~10^{-2} F for CPO10 air electrodes and these results are consistent with the current observation in the CGPO electrodes. Indeed, the increase of electrode capacitance from the $Pr_4Ni_3O_{10-\delta}$ to the composite electrodes indicates the increase of the active region from the electrode/electrolyte interface [20]. The enlargement of the active area in the composite electrodes decreases electrode resistance ($R_{elec.}$) and improves the overall electrode performance.

Apart from the electrochemical reaction component in the proposed equivalent circuit models, the other component which is common to all the electrodes is the interface. The main reason for attributing this component to interface transport is because of the $CPE_{int.}$-P values which are close to 0.5. This suggests that these arcs have a diffusive nature. Since the oxygen bulk diffusion in the electrode materials have been considered, the other possibilities are gas diffusion, oxygen ion or electron diffusion at the electrode/electrolyte interface or the electrode/platinum current collector interface. As the resistances of this arc decrease with increasing temperature, it is clear that this arc is not the response of gas diffusion but the diffusive process occurs at the interface. It is uncertain which interface contributes to this arc in the different composite electrodes (e.g. 75:25 wt.%, 50:50 wt.% and 25:75 wt.%). However, based on the electronic and oxygen ionic conductivities of $Pr_4Ni_3O_{10-\delta}$ and CGPO, it is suspected that the $Pr_4Ni_3O_{10-\delta}$ and CGPO interface resistances ($R_{int.}$) are caused by the charge transfer across the electrode/electrolyte and electrode/platinum current collector, respectively.

The main difference between the CGPO equivalent circuit model from the others is the presence of a new arc in the high frequency region with capacitance of 10^{-9} F. The only possible responses at such low capacitance originate either from the grain boundaries of 10Sc1CeSZ/CGPO or the surface layer at the electrode/electrolyte interface. The electrical conductivity measurements of 10Sc1CeSZ and CGPO using AC impedance spectroscopy show that the grain boundary responses will disappear at temperatures greater than 600°C in air. This is consistent with the results in the literature for both materials [26, 27]. Since the arcs were still observed at temperatures above 600°C, these arcs were attributed to a new surface layer forming at the electrode/electrolyte interface. This is related to the previous chemical compatibility tests (**Section 6.4**) between 10Sc1CeSZ and CGPO which demonstrate a new scandium stabilized zirconia solid solution formed after the heat treatment under both the sintering and operating conditions. Indeed, the CPE $_{\text{surf. layer}}$-P of CGPO, **Table 6.1**, is close to 0.5 and this indicates the oxygen ion diffusion through the surface layer. Interestingly, the surface layer responses were not observed in the composite electrodes (75:25 wt.%, 50:50 wt.% and 25:75 wt.%) in spite of the presence of CGPO. It seems that $Pr_4Ni_3O_{10-\delta}$ avoids the formation of the continuous surface layer at the electrode/electrolyte interface.

Overall, the summary of the electrode performance for various composite electrodes can be found in **Figure 6.12**. 50:50 wt.% shows the best results and the ASRs are less than 0.15 Ωcm^2, the target electrode performance defined in **Section 1.2.2**, at temperatures greater than 711°C in air. It is believed that the target value can be reached at an even lower temperature if the composite electrode microstructure is further optimised. For example, decreasing the $Pr_4Ni_3O_{10-\delta}$ particle size to enhance the overall number of electrochemically active sites in the composite electrode. The test results were reproducible when a fresh sample (50:50 wt.%) prepared in the same manner was tested under the same conditions. Indeed, 75:25 wt.% provides a promising electrode performance but its ASR values are slightly higher than those of the 50:50 wt.% at each temperature. 25:75 wt.%, on the other hand, has a comparable electrode performance to the 50:50 wt.% and 75:25 wt.% composites at temperature below 660°C but the performance is significantly worse at higher temperature. This is

reflected by its activation energy of 0.68 eV compared to ~1.06 eV and 1.19 eV for the 50:50 wt.% and 75:25 wt.% compositions, respectively. The lower overall activation energy of 25:75 wt.% is mainly due to the much lower activation energy in the electrode component (0.60 eV) than 1.53 eV for the 50:50 wt.% and 1.38 eV for the 75:25 wt.%. This represents the change of the electrode reaction mechanism in 25:75 wt.% materials but the detail is uncertain. The pure $Pr_4Ni_3O_{10-\delta}$ and CGPO electrodes have a much worse electrode performance than the composite electrodes even if the surface layer component is not considered in the ASR of CGPO. The improved CGPO electrode performance (without surface layer) compared with $Pr_4Ni_3O_{10-\delta}$ might be due to its smaller particle size which enlarges the active surface area of the electrode. Overall, **Figure 6.12** demonstrates the benefit of mixing the two phases to form a composite electrode.

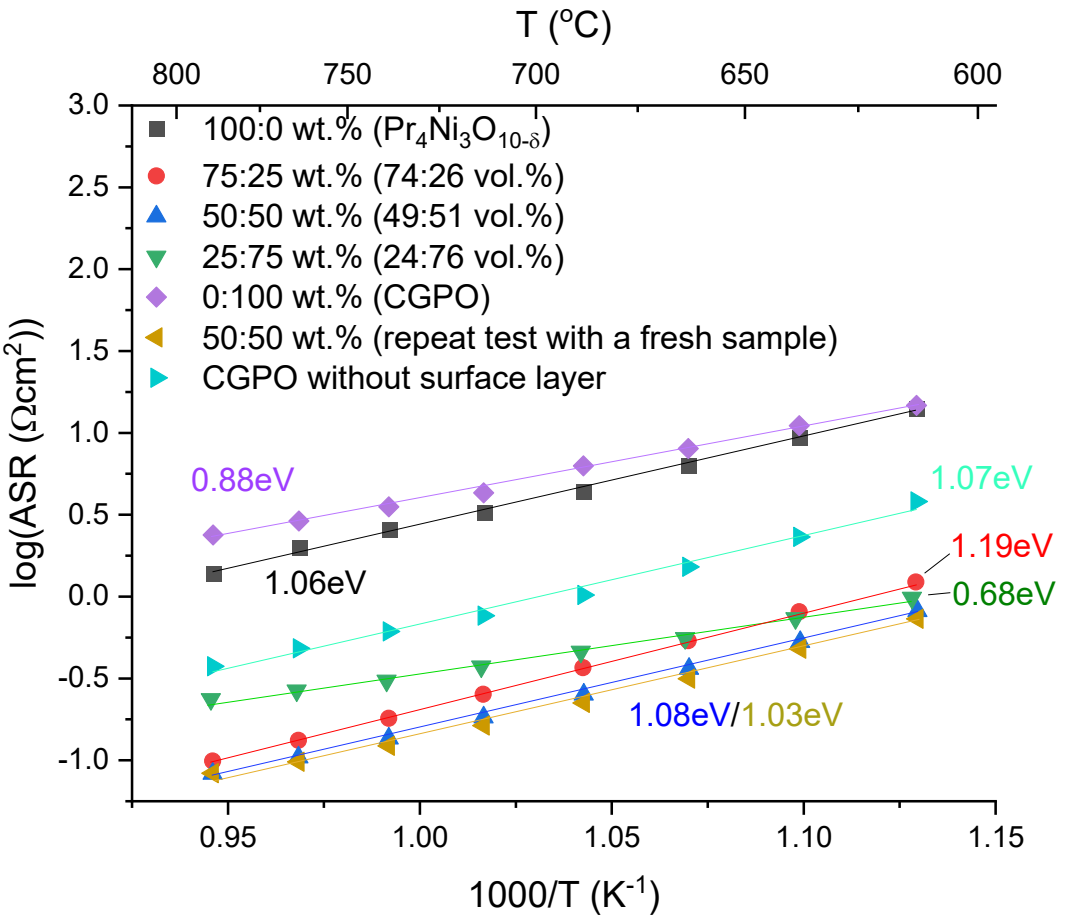


Figure 6.12: The ASR versus temperature plot for each of the composite electrode. The figure highlights the decrease in ASR on increasing the CGPO composition, with the lowest values reported for the 50:50 wt.% compositions.

Effective medium percolation theory introduced in **Section 2.8** can be used to explain why the 50:50 wt.% composition provides the best electrode results compared to the other compositions and the end-member $Pr_4Ni_3O_{10-\delta}$ and CGPO electrodes. Given that the electronic and oxygen ionic conductivities of $Pr_4Ni_4O_{10}$ and CGPO are known (**Table 6.2**), the effective electronic and oxygen ionic conductivity can be calculated for various $Pr_4Ni_3O_{10-\delta}$, CGPO and pore volume fractions in an electrode. As shown in **Figures 6.13(a)** and **(b)**, the percolation threshold for $Pr_4Ni_3O_{10-\delta}$ to form a percolated electronic conducting network or for CGPO to form a percolated oxygen ionic conducting network is when the relative volume fraction of $Pr_4Ni_3O_{10-\delta}$ is greater than 0.47 and less than 0.50, respectively. The relative volume fraction does not consider the porosity but the volume ratio between $Pr_4Ni_3O_{10-\delta}$ and CGPO. The electrode porosity will shift the percolation thresholds but the changes are relatively small. Indeed, the more apparent percolation threshold in the effective electronic conductivity is due to the significant electronic conductivity difference between $Pr_4Ni_3O_{10-\delta}$ and CGPO (**Table 6.2**). In terms of the ambipolar conductivity as defined in **Section 2.8**, the highest value is reached when the $Pr_4Ni_3O_{10-\delta}$ relative volume fraction is between 0.375 and 0.475, depending on the volume fraction of porosity (**Figure 6.13 (c)**). All the calculated results in **Figure 6.13** indicate that 50:50 wt.% (49:51 vol.%) composite electrode should present the best electrode results as it has the percolating conducting networks for both electrons and oxygen ions from the platinum current collector to the 10Sc1CeSZ electrolyte. This is consistent with the results presented above.

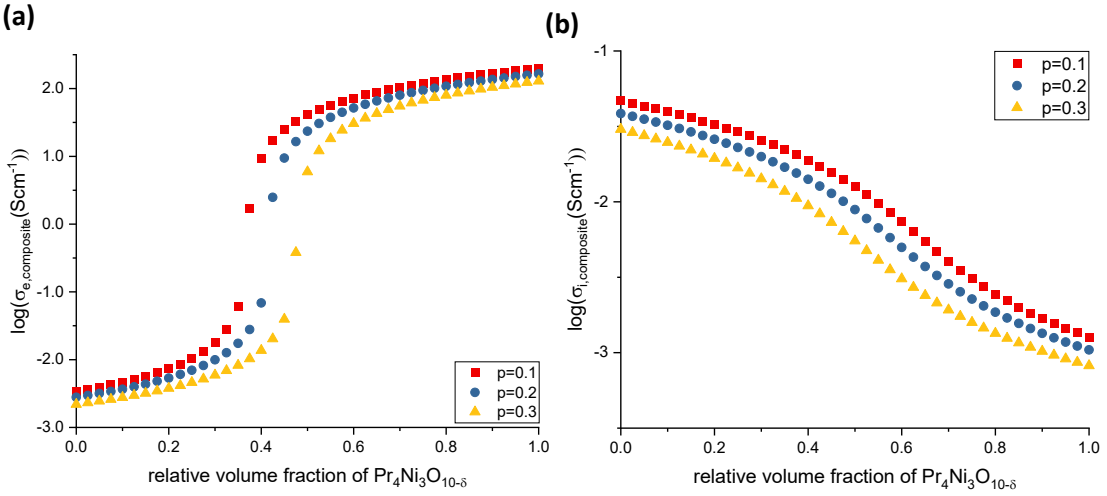
In practice, it is believed that the percolation of the CGPO network can be formed more easily than $Pr_4Ni_3O_{10-\delta}$ at the same relative volume fraction of each phase as the initial particle size of CGPO (~80 nm) is much smaller than that of $Pr_4Ni_3O_{10-\delta}$ (~1 µm) (**Figure 6.9**) [28]. This explains why the 75:25 wt.% also shows a promising electrode performance despite the lower content of CGPO than in the 50:50 wt.% optimal composition. Although the previous percolation calculation assumes that the particle size of both phases are the same and it is known that the particle size ratio between $Pr_4Ni_3O_{10-\delta}$ and CGPO, which deviates from one, will shift the percolation thresholds,

the calculation estimates that the best relative $Pr_4Ni_3O_{10-\delta}$ relative volume fraction is between 0.4 and 0.6 [28, 29].

The other approach to confirm the percolation of $Pr_4Ni_3O_{10-\delta}$ is to examine the ohmic resistance of the symmetrical cells with various composite electrodes. Since the electrical conductivity of 10Sc1CeSZ was measured at different temperatures, any extra unexpected ohmic resistance values are evidence of the non-percolated $Pr_4Ni_3O_{10-\delta}$ network in the composite electrodes. The differences between the real and the estimated ohmic resistance at 784 °C were 0.28 Ω, 0.51 Ω and 2.05 Ω for 75:25 wt.%, 50:50 wt.% and 25:75 wt.% symmetrical cells, respectively. Considering that the small ohmic resistance deviations are likely due to the measured dimensional errors for each of the sintered 10Sc1CeSZ pellets, it is clear that the $Pr_4Ni_3O_{10-\delta}$ percolation network was broken in the 25:75 wt.% composition electrode. This effect was reflected in its electrode performance results which were significantly worse than 50:50 wt.% and 75:25 wt.% electrodes.

Table 6.2: Electronic conductivity and oxygen ionic conductivity of $Pr_4Ni_3O_{10-\delta}$ and $Ce_{0.75}Gd_{0.1}Pr_{0.15}O_{2-\delta}$ at 700°C under pO_2 of 0.21 bar. The values are based on the data reported in **Section 5.6**, [3] and [23].

	Electronic conductivity (Scm^{-1})	Oxygen ionic conductivity (Scm^{-1})
$Pr_4Ni_3O_{10-\delta}$	235	1.49×10^{-3}
$Ce_{0.75}Gd_{0.1}Pr_{0.15}O_{2-\delta}$	0.004	0.055



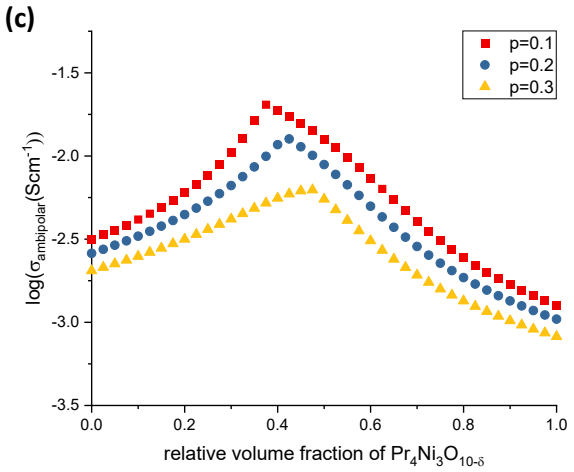


Figure 6.13: The change in **(a)** effective electronic conductivity, **(b)** effective ionic conductivity and **(c)** ambipolar conductivity at various relative volume fractions of $Pr_4Ni_3O_{10-\delta}$ in the $Pr_4Ni_3O_{10-\delta}$:CGPO composite electrode system. The calculation is based on the input data from **Table 6.2** and the effective medium percolation theory mentioned in **Section 2.8**.

6.7 Post-mortem test of the composite electrodes

Post-mortem tests were conducted on the symmetrical cells after the electrode performance measurements were complete. The key foci were to investigate any change of electrode phase and microstructure induced through the cell operation. **Figure 6.14** illustrates the XRD results of the electrode layer after manually removing the majority of the applied platinum current collector with abrasive SiC paper. Surprisingly, apart from the presence of $Pr_4Ni_3O_{10-\delta}$, CGPO, 10Sc1CeSZ, some NiO and Pt phases, Pr_9O_{16} and $Pr_{10}O_{18}$ were also observed in the $Pr_4Ni_3O_{10-\delta}$, 75:25 wt.%, 50:50 wt.% and 25:75 wt.% samples. The observation of NiO in the $Pr_4Ni_3O_{10-\delta}$ sample (100:0 wt.%), together with the presence of Pr_9O_{16} and $Pr_{10}O_{18}$, provides evidence of $Pr_4Ni_3O_{10-\delta}$ decomposition. The decomposition of $Pr_4Ni_3O_{10-\delta}$ might be due to the presence of the platinum current collector as no such decomposition was observed in the previous chemical compatibility tests (**Section 6.4**). Indeed, possible chemical reaction between $Pr_4Ni_3O_{10-\delta}$ and Pt to form Pr_2NiPtO_6 double perovskite was not found [30]. Detailed investigations on the major factor which causes the decomposition and its mechanism will be discussed in **Section 6.9**. It is important to note that the quantitative comparisons for the amount of secondary phases formed for $Pr_4Ni_3O_{10-\delta}$ and the composite electrode samples cannot be made as it is likely that

part of the Pr_9O_{16}, $Pr_{10}O_{18}$ and NiO were removed when the platinum current collector was removed.

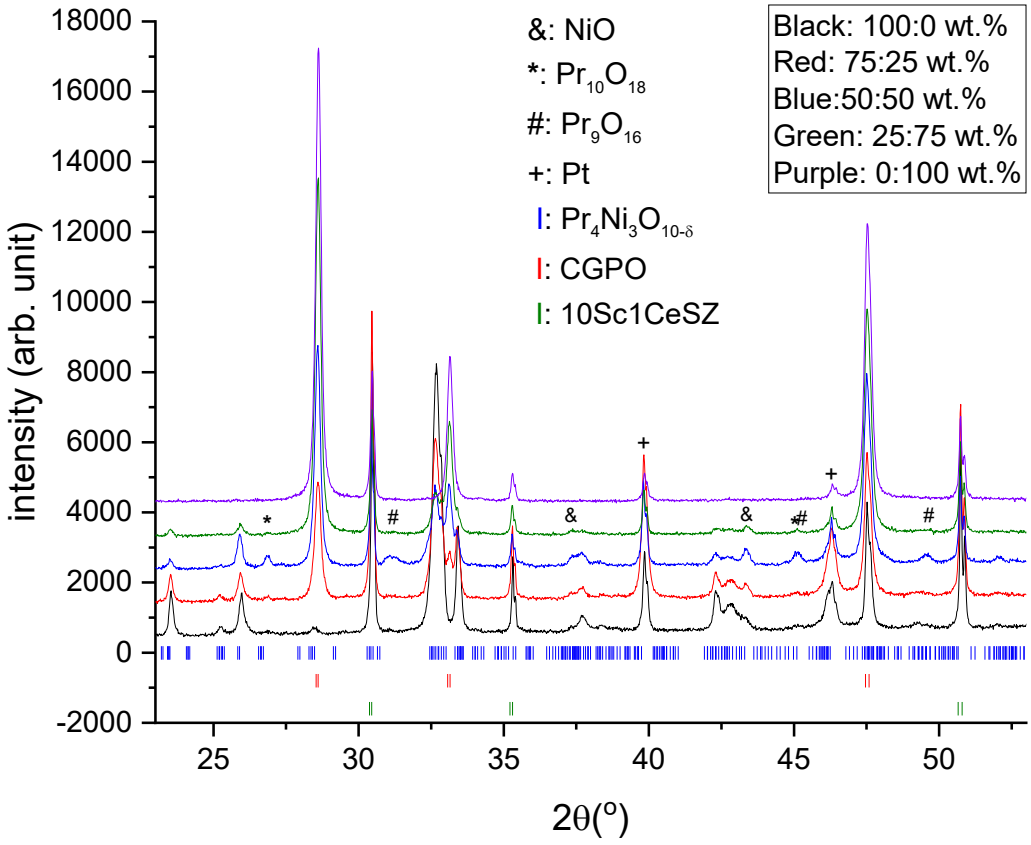
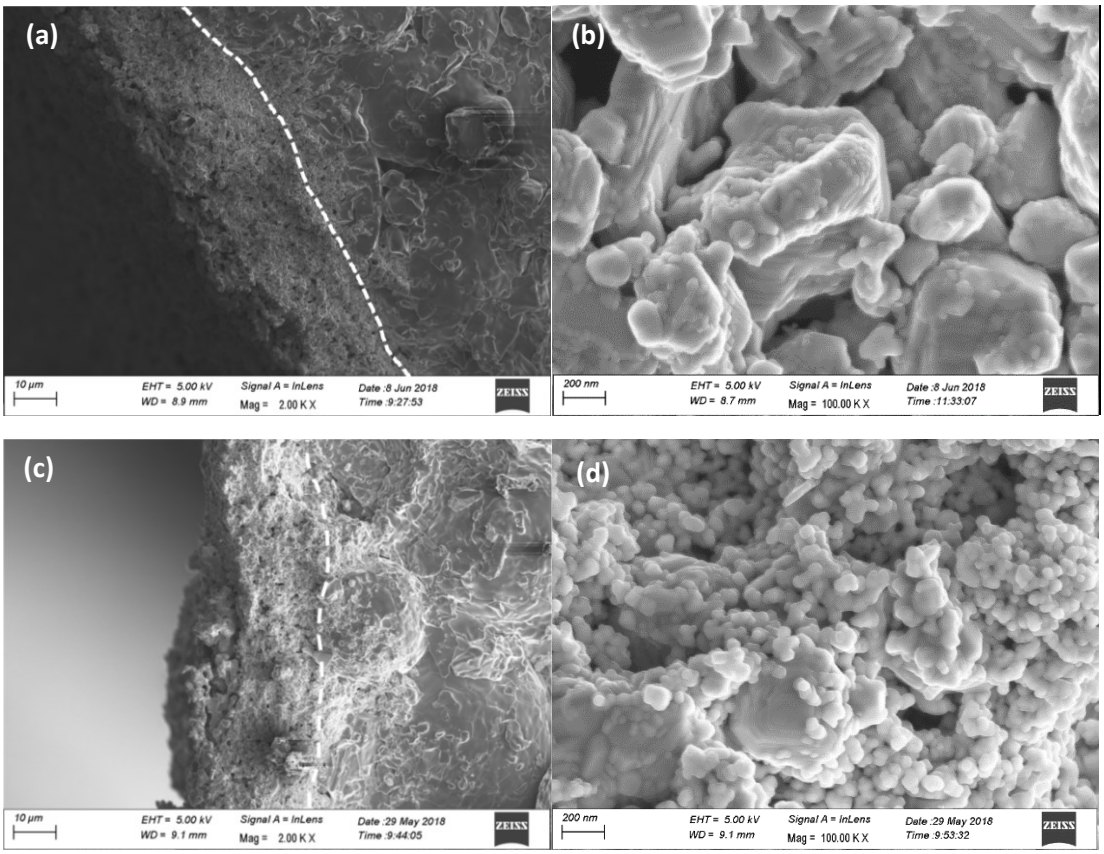


Figure 6.14: The post-mortem XRD results of each composite electrode (including pure $Pr_4Ni_3O_{10-\delta}$ and pure CGPO electrodes) after the electrode performance test under OCV.

With respect to the electrode microstructure after the AC impedance tests, **Figure 6.15** shows the electrode cross-section for each of the symmetrical cell obtained by secondary electron microscopy. The electrode thicknesses were determined to be 22 µm (**Figure 6.15(a)**), 20 µm (**Figure 6.15(c)**), 29 µm (**Figure 6.15(e)**), 19 µm (**Figure 6.15(g)**) and 26 µm (**Figure 6.15(i)**) for $Pr_4Ni_3O_{10-\delta}$, 75:25 wt.%, 50:50 wt.%, 25:75 wt.% and CGPO cells, respectively. An inhomogeneous electrode thickness can be observed in almost all samples because of the uneven 10Sc1CeSZ electrolyte surface and the brush painted electrodes. The large 10Sc1CeSZ grains/particles observed in the electrolyte region are mainly due to the as-mentioned powder pretreatment at 1500°C for 5 hours in air in order to receive a pure cubic phase of 10Sc1CeSZ. Although ball-milling was applied to the thermally treated powder, the particle size of 10Sc1CeSZ cannot be reduced to the initial submicron range. It then leads to the lower density of the sintered 10Sc1CeSZ pellets (~94%) despite sintering at a high

temperature of 1550°C for several hours in air. Overall, it is believed that the artifacts of the lower density electrolyte and the inhomogeneous electrode thickness should have little impact on investigating the electrode performance for the composite electrodes. This is because the electrical conductivity of the sintered 10Sc1CeSZ pellets were measured individually to distinguish the electrolyte and electrode responses in the AC impedance measurements and gas leakage is of less concern in the symmetrical cell tests as both electrodes in a symmetrical cell experience the same atmosphere. Indeed, the rough 10Sc1CeSZ surface provides a good contact with the electrodes at the interface (**Figures 6.15(a)**, **(c)**, **(e)**, **(g)** and **(i)**) and **Figure 6.12** demonstrates that the reproducible electrode performance measurement can be reached for the proposed sample preparation approach. Moreover, no apparent particle growth, especially CGPO, was observed in **Figures 6.15(b)**, **(d)**, **(f)**, **(h)** and **(j)** when comparing to the as-sintered electrodes in **Figures 6.8(a)-(e)**. However, it was found that the shape of the CGPO particles in **Figure 6.8(a)-(e)** was more spherical. This might be due to the fact that the images were taken on the sample surface rather than the electrodes' cross-section. Therefore, the CGPO particle growth was less restricted by the adjacent particles, unlike the case in **Figure 6.15(b)**, **(d)**, **(f)**, **(h)** and **(j)**.



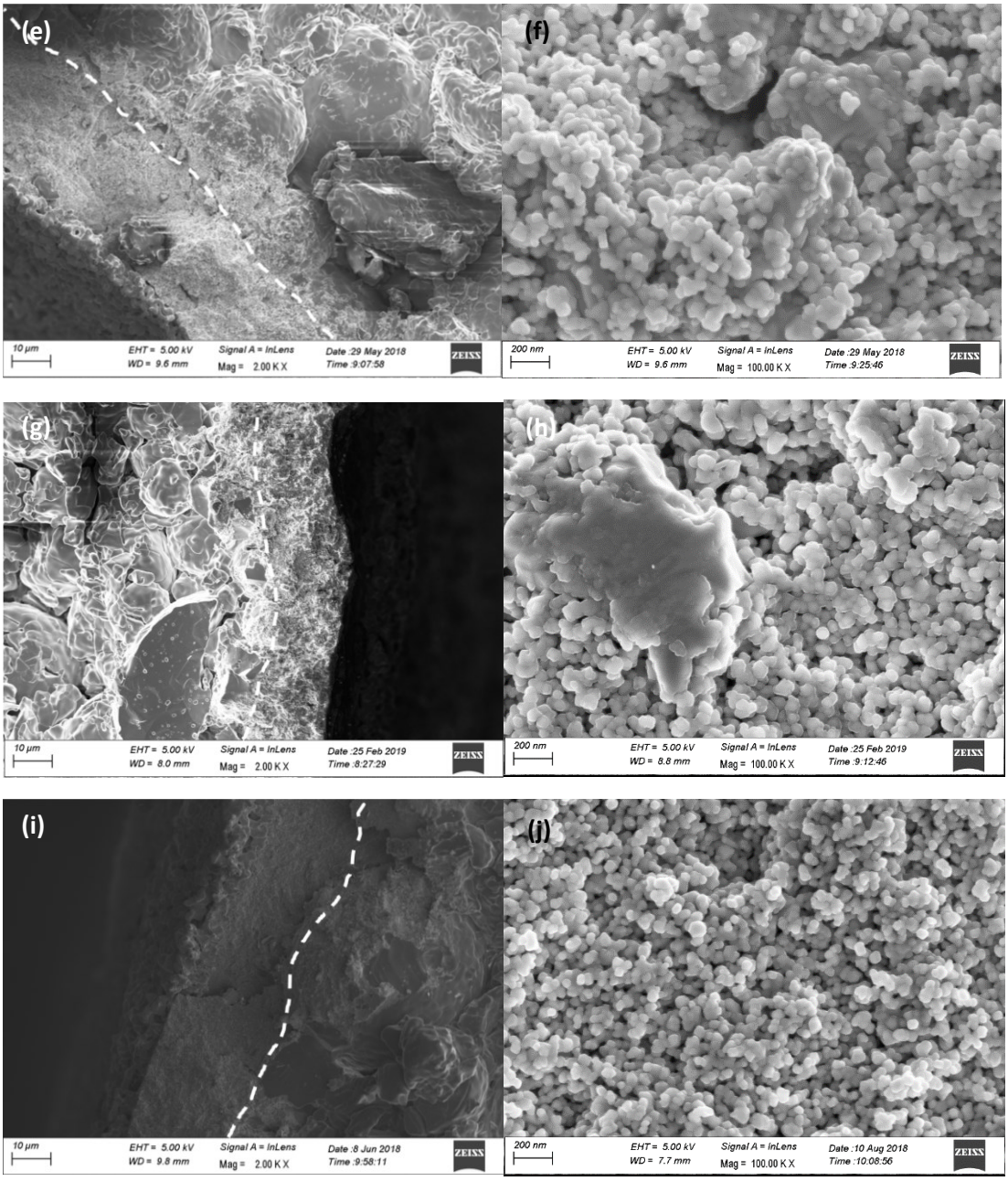
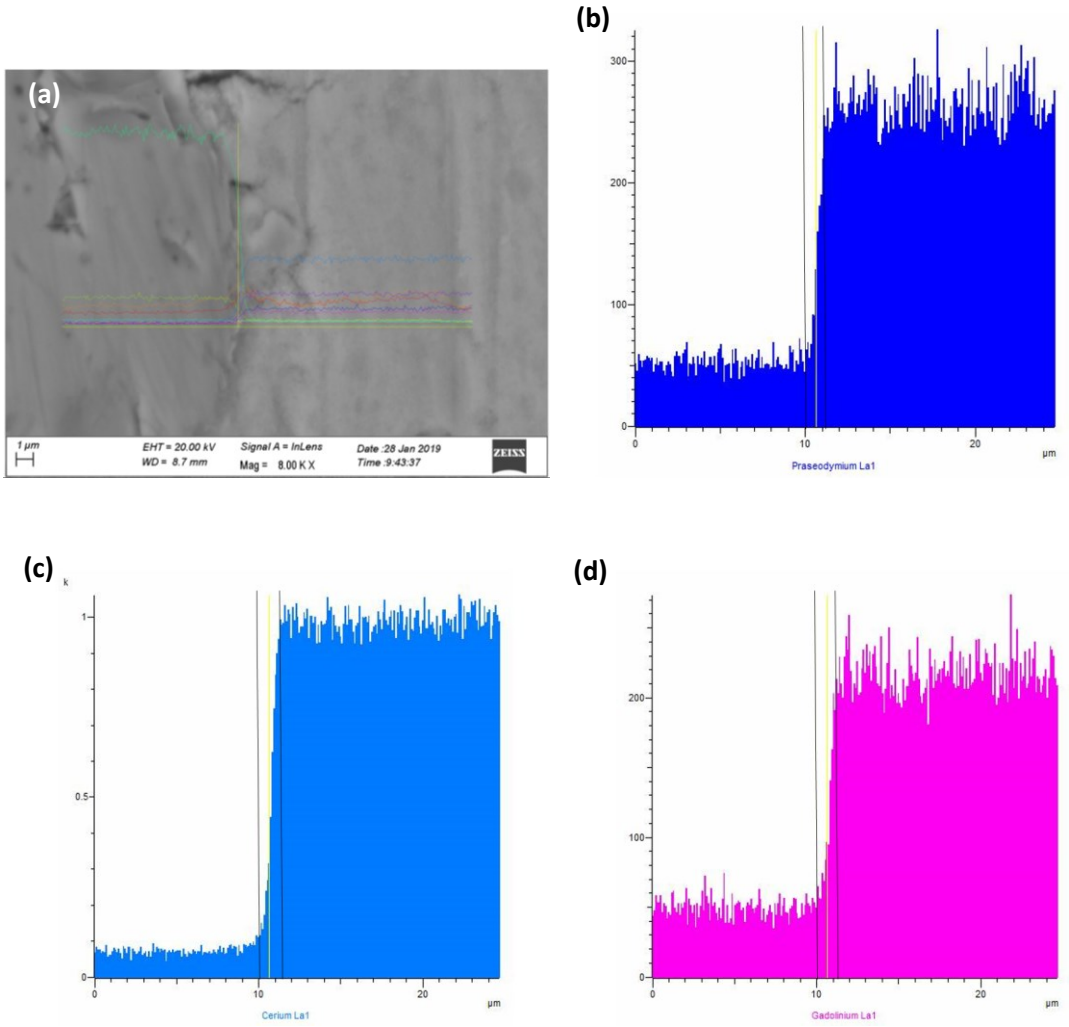


Figure 6.15: Analysis of the electrode microstructure of **(a) (b)** $Pr_4Ni_3O_{10-\delta}$, **(c) (d)** 75:25 wt.%, **(e) (f)** 50:50 wt.%, **(g) (h)** 25:75 wt.% and **(i) (j)** CGPO after the electrode performance tests under OCV. The figures highlight the excellent adhesion and robust structure. The white dashed lines in **Figure 6.15(a)**, **(c)**, **(e)**, **(g)** and **(i)** illustrate the composite air electrode/electrolyte interface.

To investigate the chemical composition and the thickness of the newly formed surface layer at the interface between the CGPO electrode and 10Sc1CeSZ electrolyte an EDS line scan technique was used, characterizing the sample after the electrode

performance test. The results are shown in **Figures 6.16(a)-(f)**. The elements of interest were praseodymium, cerium, gadolinium, scandium and zirconium. The average intensities on the left hand side in **Figures 6.16(b)-(d)** were attributed to the background signals and they were compared with the intensity on the right hand side which correlated to the real quantity of each element. This is opposite for scandium and zirconium plots in **Figures 6.16(e)** and **(f)**, respectively. The yellow and black vertical lines in **Figures 6.16(a)-(f)** represent the location of the interface and the diffusion length of each element. Since the diffusion length of each element is ~1.2 µm, which is within the detection limit of EDS, the chemical composition and the thickness of the newly formed surface layer cannot be resolved.



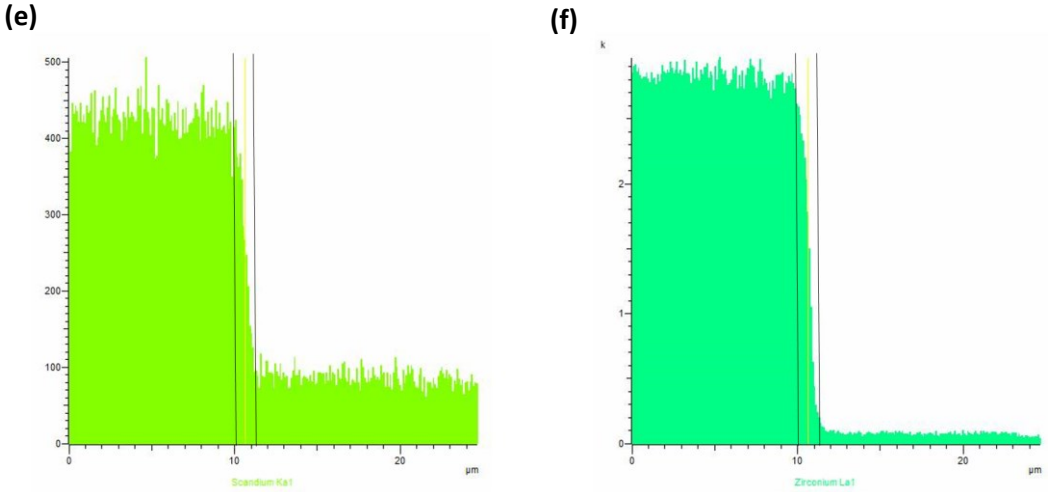


Figure 6.16: The EDS line scan results of CGPO (0:100) symmetrical cell cross-section after the electrode performance test under OCV. **(a)** The interface of CGPO electrode and electrolyte was examined by EDS line scan. The corresponding signals (counts) to location plots for **(b)** praseodymium, **(c)** cerium, **(d)** gadolinium, **(e)** scandium, and **(f)** zirconium are illustrated with annotation linking to **Figure 6.16(a)**.

6.8 7-day electrode performance

7-day electrode performance tests were conducted for the 50:50 wt.% composite electrode with platinum as the current collector, as this composition presented the best electrode performance, at ~685°C for 7 days in air. The main purpose of this experiment was to investigate the composite electrode performance stability over time and investigate any electrode degradation. By using the same equivalent circuit model of 50:50 wt.% in **Figure 6.11**, **Figure 6.17(a)** shows an increase of the overall electrode ASR (ASR_{total}) over time. The ASR_{total} increased from 0.20 to 0.45 Ωcm^2 (~122%) in 7 days. Such obvious electrode performance degradation was unexpected as it was previously believed that the composite electrode of $Pr_4Ni_3O_{10-\delta}$ and CGPO should be more thermodynamically stable than the $Pr_2NiO_{4+\delta}$ analogue. To understand which component(s) contributes to the increase of the overall electrode ASR (ASR_{total}), the change in the interface ASR ($ASR_{int.}$) and the ASR attributed to a gerischer element ($ASR_{elec.}$) over time were also examined (**Figure 6.17(a)**). Compared with $ASR_{int.}$ which shows an initial rise and then reaches a plateau, there was a continuous increase of $ASR_{elec.}$ over time. Indeed, with respect to the ohmic resistance (ASR_{ohmic}) (**Figure 6.17(b)**), the initial sudden decrease and then increase of the value over time might

represent the improvement of the contact resistance between the platinum current collector and the composite electrode and the formation of new scandium stabilized zirconia solid solutions as indicated in **Section 6.4**. However, the change of ASR_{ohmic} is relatively small over time (less than 2%).

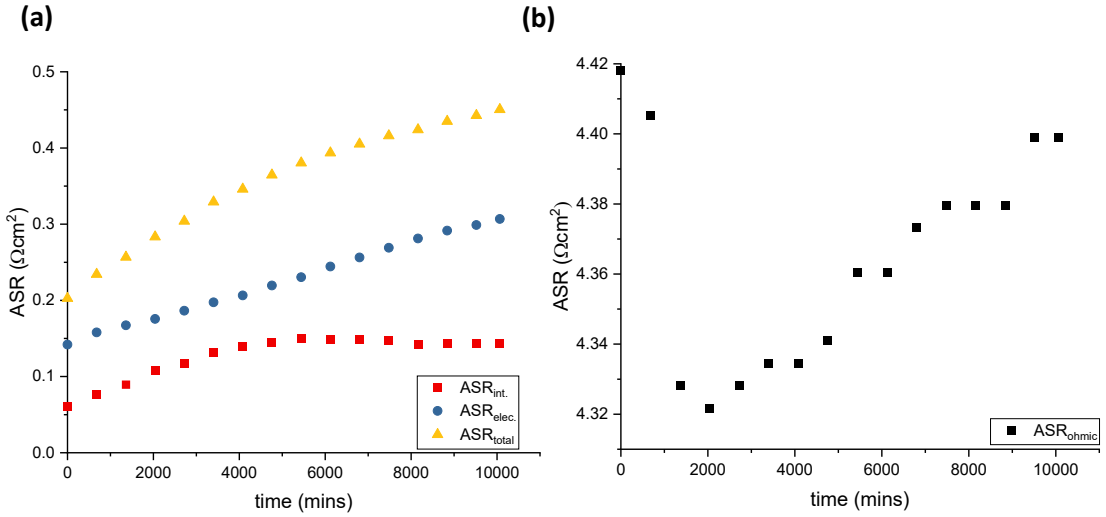


Figure 6.17: The 7-day performance of the 50:50 wt.% composite electrode with platinum as the current collector. **(a)** The change of the electrode ASR over time. **(b)** The change of the ohmic ASR over time.

Both XRD and SEM were applied to examine the phase evolution and the electrode microstructure of the sample after the 7-day performance test. Again, the platinum current collector was manually removed by SiC paper before conducting XRD. Similar to the previous XRD results presented in **Figure 6.14** for electrodes containing $Pr_4Ni_3O_{10-\delta}$, the presence of Pr_9O_{16}, $Pr_{10}O_{18}$ and NiO were also observed after the 7-day performance test as shown in **Figure 6.18**. However, there was no significant change of the electrode microstructure (**Figure 6.19**) when comparing to the microstructure of the as-sintered electrode in **Figure 6.8(c)**. Again, as mentioned in **Section 6.7**, the deviation of CGPO particles shape in **Figure 6.19** from **Figure 6.8(c)** might be because of the local steric restriction imposed by the adjacent particles within the composite electrode.

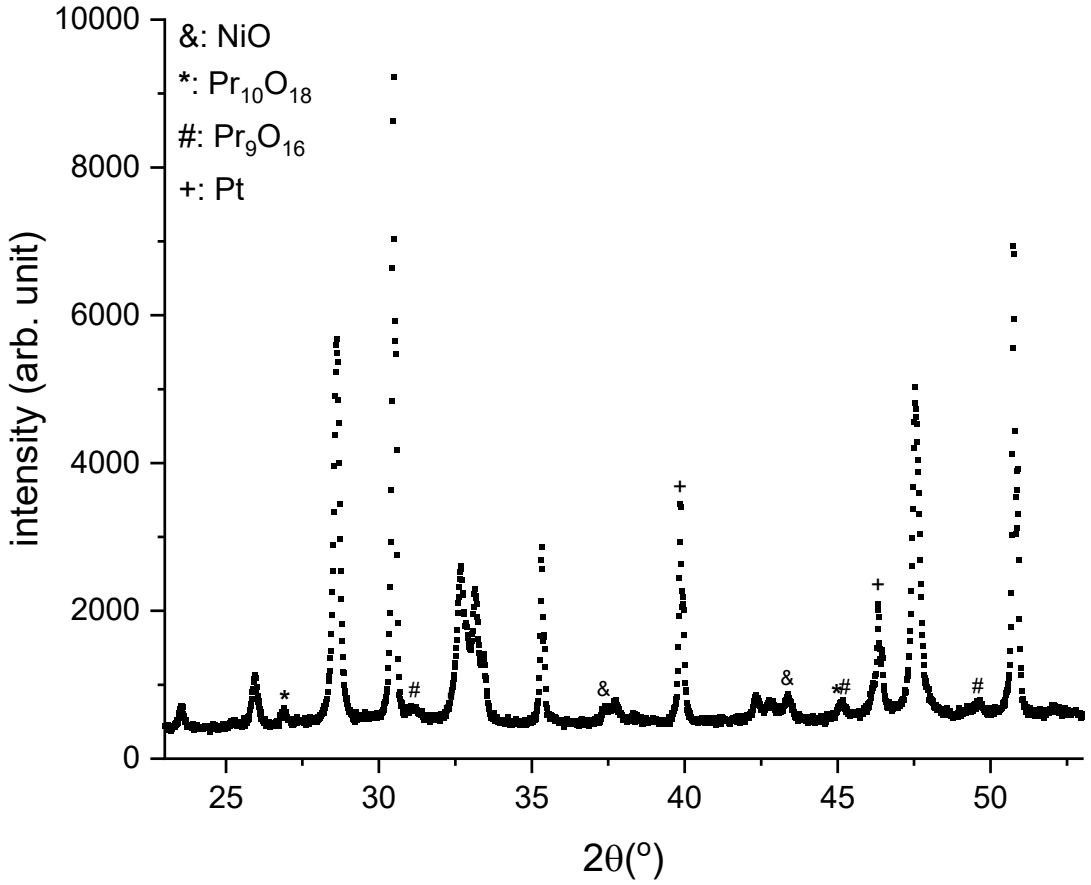


Figure 6.18: The XRD results of the sample (50:50 wt.%) using platinum as the current collector after the 7-day performance test. The chosen 2θ range best describes the presence of the secondary phases compared to the other 2θ regions where peak overlapping is significant.

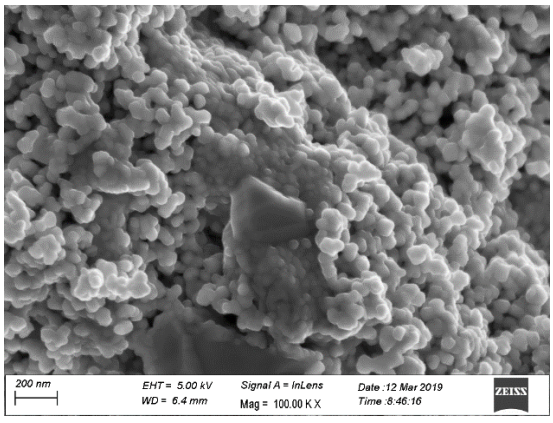


Figure 6.19: The cross-section electrode microstructure of the sample (50:50 wt.%) using platinum as the current collector after the 7-day performance test.

Other current collectors such as gold paste were also used for the 7-day performance test. Due to its relatively low melting point of 1064°C compared to platinum (1768°C), the gold paste sintering temperature was reduced to 700°C for 2 hours in air. To resemble the thermal history and hence the electrode microstructure for the previous samples where platinum paste was used as the current collector, the 50:50 wt.% electrode ink for the new samples were sintered at 900°C for 4 hours in air before depositing the gold paste on top of it.

The same equivalent circuit model of 50:50 wt.% (**Figure 6.11**) was again used to fit the 7-day performance test results but the $ASR_{int.}$ and $ASR_{elec.}$ are about twice and three times greater than the initial 50:50 wt.% composite electrode obtained when using platinum as the current collector. In addition, the $CPE_{int.}$-P is around 0.3 which is a significant deviation from the previously observed value of around 0.5. It seems that there was a new process introduced which contributes to the ASR_{total} here. To deconvolute the extra response in the system, a new fresh sample was prepared with a gold current collector and its electrode performance was measured on increasing temperature in air. In addition, a distribution of relaxation time (DRT) with regularization parameter of 1×10^{-2} was used to separate electrochemical responses that have similar time constants (**Section 3.4.5.4**). **Figure 6.20(a)** compares the DRT results between the 7-day performance test sample and the newly prepared sample which both used gold as the current collector. The similarity in peak positions and peak areas for both samples indicate again that the electrode performance measurement is reproducible. The slight deviation might be due to the small temperature difference (e.g. ~685°C in the 7-day performance test sample versus ~680°C for the newly prepared sample) when measuring the electrode performance. Moreover, **Figure 6.20(a)** illustrates the difference when platinum and gold were used as the current collector. The time constant of the interface component (the peaks in the far left) for the sample with a platinum current collector was larger than the sample where gold was the current collector, whereas it is opposite for the Gerischer response (the peaks in the far right). The resistance/area of the Gerischer response for the sample with a gold current collector was also much larger than the sample with a platinum current

collector. In addition, an extra peak was observed in the middle between the peaks in the far left and right when a gold current collector was used.

In order to attribute the middle peak observed in the samples measured with a gold current collector, the freshly prepared sample was heated from 680°C to 803°C in air and the AC impedance was measured every ~25°C. The corresponding DRT results are displayed in **Figure 6.20(b)**. It is interesting to observe that there is almost no change of the middle peak time constant on increasing temperature. Indeed, the middle peak areas/resistances are almost constant at temperatures greater than 778°C. Below this temperature, the middle peaks have a slightly greater resistance and this extra area might be contributed by the asymmetric feature of the adjacent Gerischer peak [31]. This contribution is much smaller at the higher temperatures and hence the resistance of the middle peak can be identified.

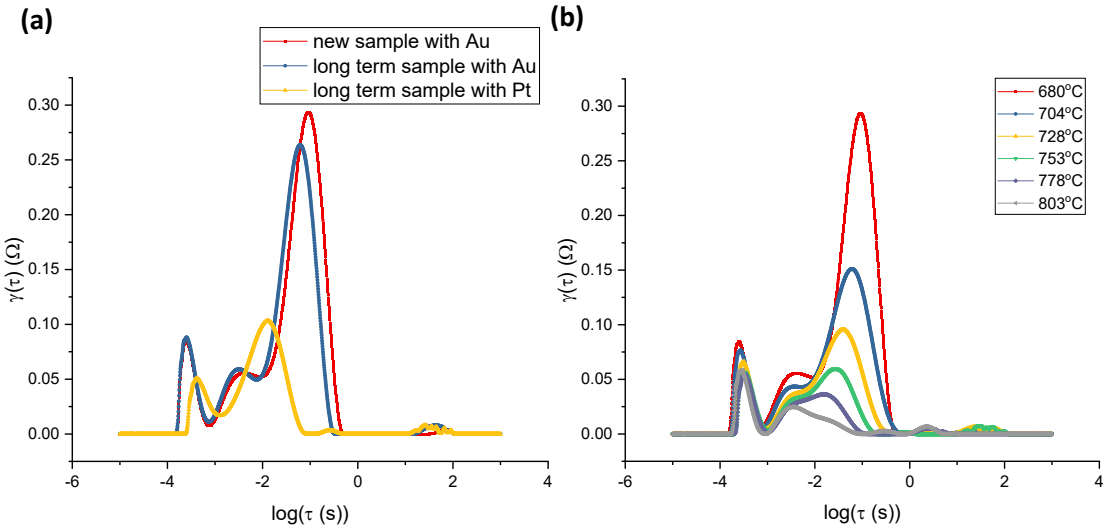


Figure 6.20: **(a)** The DRT results of the newly prepared sample using gold as the current collector (measured at ~680°C in air) and the 7-day performance test samples using either gold or platinum as the current collector (measured at ~685°C in air). **(b)** The change of the DRT results at various temperatures for the newly prepared sample using gold as the current collector.

By introducing the gas diffusion component (R//CPE) in the equivalent circuit model for the samples with gold current collector, the $ASR_{int.}$ value became similar to that determined for the samples with platinum current collectors, and $CPE_{int.}$-P had a value close to 0.5. **Figure 6.21(a)** shows the summary of 50:50 wt.% composite electrode 7-

day performance when using gold as the current collector. Overall, there is no significant change of the total electrode ASR (ASR_{total}) and the ASR of each component ($ASR_{int.}$, $ASR_{gas\ diffusion}$ and $ASR_{elec.}$). The initial decrease of $ASR_{elec.}$ can be related to the change observed in the ohmic ASR (**Figure 6.21(b)**). This might be again because of the enhancement of the interface between the composite electrode and the gold current collector. The slight increasing trend of $ASR_{gas\ diffusion}$ over time might suggest the densification of the gold current collector as discussed next. Indeed, despite small magnitude (less than 1.5%), the increase of ohmic resistance over time might be caused by cation interdiffusion between 10Sc1CeSZ and CGPO. The lower ohmic ASR in **Figure 6.21(b)** compared to that in **Figure 6.17(b)** is because of the electrolyte thickness variation between the two samples.

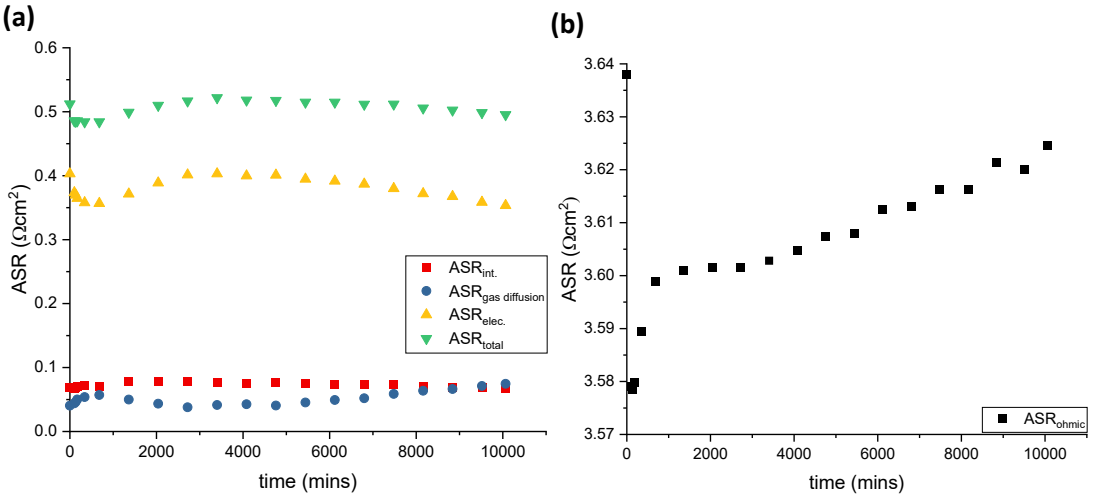


Figure 6.21: The 7-day performance of the 50:50 wt.% composite electrode with gold as the current collector. **(a)** The change of the electrode ASR over time. **(b)** The change of the ohmic ASR over time.

Figure 6.22(a) shows the secondary electron image of the gold current collector and this is compared with that obtained from the sample with a platinum current collector (**Figure 6.22(b)**) after the 7-day performance test. It is apparent that the gold current collector has much less porosity than the platinum and this leads to the observed gas diffusion resistance in the electrode as air flow to the composite electrode is restricted. **Figure 6.22(c)** is the backscattered electron image of the sample with a gold current collector. Both the contrast (**Figure 6.22(c)**) and the EDS results (**Figure 6.23(a)** and **(b)**)

demonstrate that the top dense layer is gold and the bottom porous layer is the composite electrode.

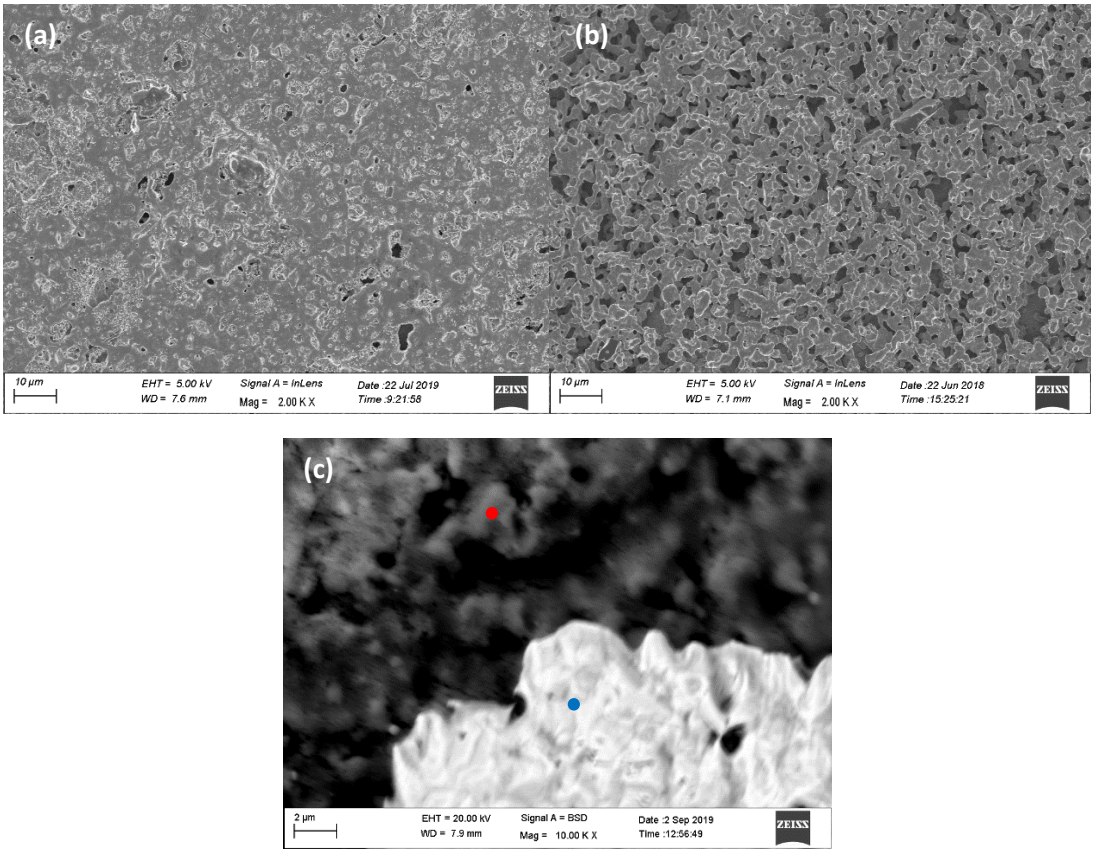
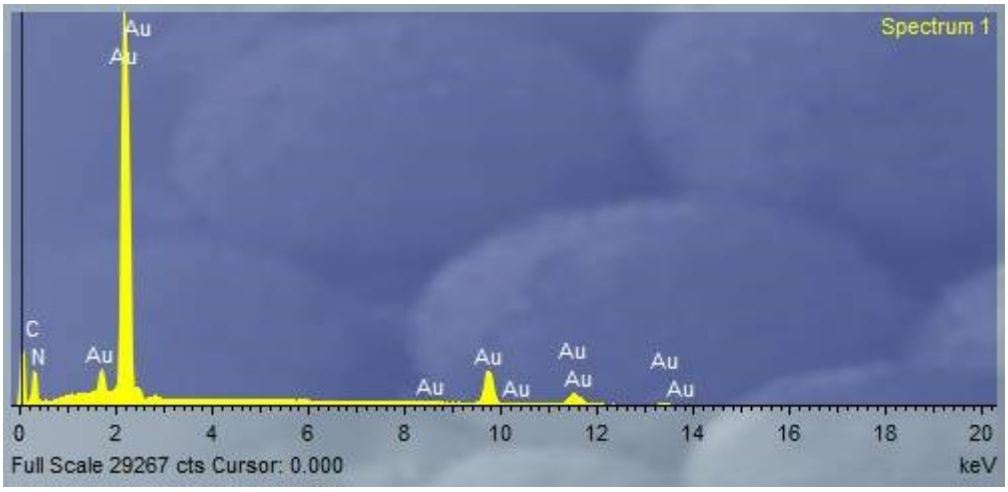


Figure 6.22: The top-down microstructure of the gold current collector **(a)** and the platinum current collector **(b)** for the samples after 7-day performance test. **(c)** The backscattered image of the 7-day performance test sample using gold as the current collector. The brighter part at the bottom is gold whereas the darker one at the top is the composite electrode. This was confirmed by the point mode EDS at the location of blue dot and red dot, respectively (**Figure 6.23**).

(a)



(b)

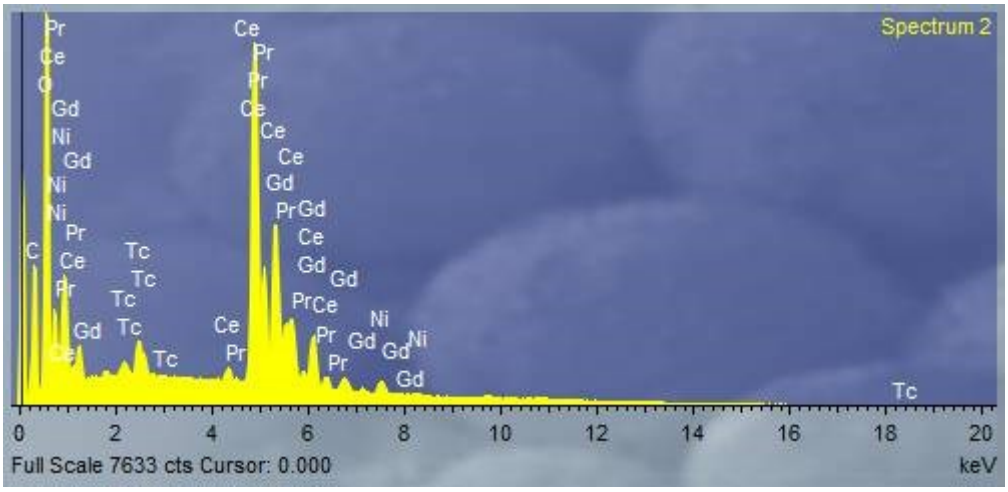


Figure 6.23: EDS spectrum correspond to **(a)** the blue dot (Au current collector) and **(b)** the red dot (the $Pr_4Ni_3O_{10-\delta}$:CGPO composite air electrode) in **Figure 6.22(c).** The observed Tc signal in **Figure 6.23(b**) might be due to the presence of an impurity at the local regions.

Furthermore, the change of the interface component time constant (**Figure 6.20(a)**) when comparing the samples using gold and platinum as the current collector suggests that the response can be attributed to the charge transfer process at the composite electrode/current collector interface as there is no change of materials and configuration at the electrode/electrolyte interface between these two samples. The variation of the $Pr_4Ni_3O_{10-\delta}$ decomposed products might also play a role here. For example, unlike **Figure 6.18** in which Pr_9O_{16} and $Pr_{10}O_{18}$ were observed from the platinum current collecting sample, Pr_7O_{12} was found in the sample with a gold current collector after the 7-day performance test (**Figure 6.24**). The peak at 2θ around 31.4°

in the XRD pattern (**Figure 6.24**) was unindexed and it might be attributed to an unknown phase. Indeed, the variation of the Gerischer electrode component for these two samples, especially the resistance, might be because of the change of the effective oxygen diffusion coefficient (D*) and the effective surface exchange coefficient (k) in the gold sample since no apparent electrode microstructure change was observed between the 7-day performance test sample using either platinum (**Figure 6.19**) or gold (**Figure 6.25**) as the current collector. As mentioned before, the dense gold layer will limit the air flow to the active sites of the composite electrode. Therefore, it is very likely that the local oxygen partial pressure at the active sites will be deviated from 0.21 bar. This will then change the effective D* and k and hence the electrode performance [20].

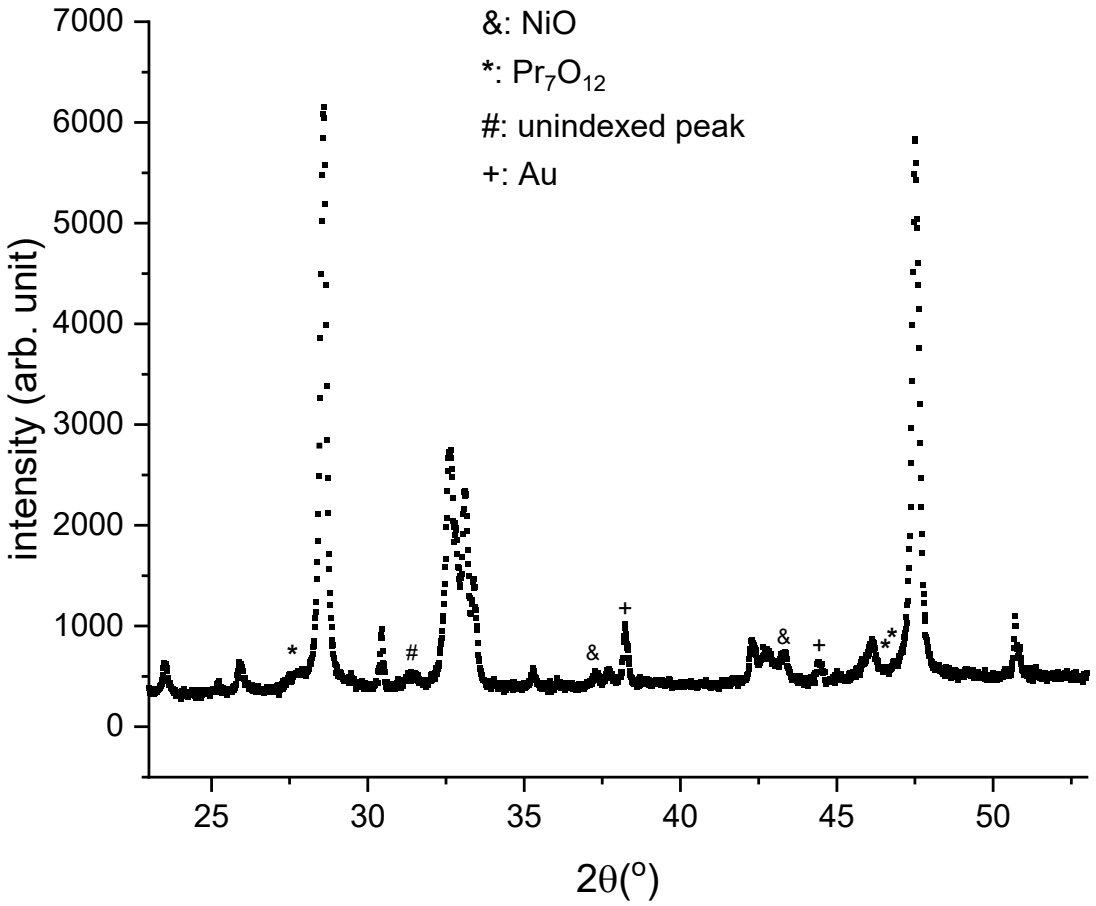


Figure 6.24: The XRD results of the sample (50:50 wt.%) using gold as the current collector after the 7-day performance test. The gold current collector was manually removed by SiC paper before examining the sample using XRD. The chosen 2θ range best describes the presence of the secondary phases compared to the other 2θ regions where peak overlapping is significant.

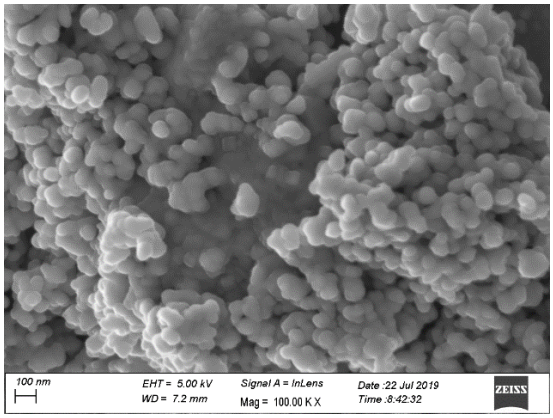


Figure 6.25: The cross-section electrode microstructure of the sample (50:50 wt.%) using gold as the current collector after the 7-day performance test.

6.9 Discussions of artifacts in the experiments

To better understand the interference between the current collector, especially platinum, and the composite electrode, the following experiments were conducted and the results are summarized in **Table 6.3**. In summary, the decomposition of $Pr_4Ni_3O_{10-\delta}$ occurs after sintering/heating the deposited platinum paste. The extent of the $Pr_4Ni_3O_{10-\delta}$ decomposition is also proportional to the subsequent temperature at which the platinum was treated. Other factors such as positive and negative bias, the presence of CGPO, humidity and high oxygen partial pressure have an insignificant impact on the $Pr_4Ni_3O_{10-\delta}$ decomposition. It is important to note that without the presence of platinum, $Pr_4Ni_3O_{10-\delta}$ demonstrates its thermodynamic stability under both sintering conditions (e.g. 900°C for 4 hours in air) and operating conditions (e.g. 700°C for 7 days in air). Sample preparation before phase identification by XRD such as dry/wet grinding to remove the platinum current collector were also found to have no impact on the $Pr_4Ni_3O_{10-\delta}$ decomposition.

Table 6.3: The summary results of the $Pr_4Ni_3O_{10-\delta}$ decomposition investigation. Both as-sintered $Pr_4Ni_3O_{10-\delta}$:CGPO (50:50 wt.%) composite electrode and as-sintered $Pr_4Ni_3O_{10-\delta}$ electrode were prepared and treated at various conditions to identify the factor resulting to the $Pr_4Ni_3O_{10-\delta}$ decomposition. Each column represents a new sample treated at different conditions/procedures before final phase identification by XRD. The columns in blue (sample 1, 3, and 6) are treated as a reference.

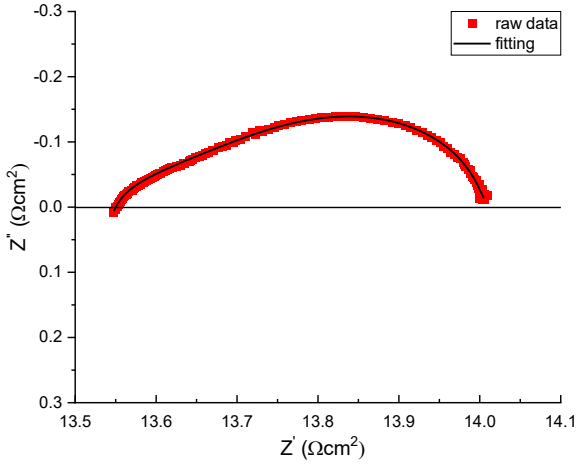
		As-sintered 50:50 wt.% composite electrode at 900°C for 2 hours in air						As-sintered $Pr_4Ni_3O_{10-\delta}$ electrode at 900°C for 2 hours in air				
Sample number		1	2	3	4	5a	5b	6	7	8	9	10
Further sample preparation/treatment condition of the as-sintered electrode	Brush-painted Pt paste	No	Yes	No	Yes	No	No	No	No	Yes	Yes	Yes
	Sintered at 900°C for 2 hours in air or other atmosph-eres	Yes air	Yes air	No	No	No	No	Yes Air	Yes Air	Yes Air	Yes O_2	Yes dry O_2
	Further heat treated at 700°C for 7 days in air	No	No	Yes	Yes	Yes	Yes	No	Yes	No	No	No
	Applying DC bias (100 mV)	No	No	No	No	Yes cath-ode side	Yes anode side	No	No	No	No	No
Final phase identification	Evidence of $Pr_4Ni_3O_{10-\delta}$ decompo-sition	No	Yes	No	Yes small	No	No	No	No	Yes	Yes	Yes

In addition, the other two unanswered questions are how the $Pr_4Ni_3O_{10-\delta}$ decomposition influences the measured electrode performance, especially for the 50:50 wt.% composition, and its electrode performance stability in a 7-day performance test. To answer the first question, the finite length Gerischer element (**Equation 6.1**) was applied to replace the previous Gerischer element in the 50:50 wt.% composite equivalent circuit model [32]. Compared with the Gerischer equation introduced in **Section 3.4.5.1**, the only difference is the presence of the hyperbolic

term in the finite length Gerischer element. L and λ_0 represent the electrode thickness and the thickness of the active area. If the ratio of L and λ_0 is high, then the hyperbolic term in **Equation 6.1** will be equal to 1 and there will be no difference from the typical Gerischer element. **Table 6.4** summarizes the L/λ_0 values at different temperatures after refitting the previous 50:50 wt.% composite AC impedance data with the finite length Gerischer element in the equivalent circuit. The quality of the new fitting for the data at 686°C can be found in **Figure 6.26**. From **Table 6.4**, it is interesting to observe that all the L/λ_0 values are greater than one. This indicates that the electrode thickness (29 µm) is always greater than the thickness of the active area. Indeed, it was observed that the active area thickness decreased with increasing temperature. As the value of λ_0 is proportional to the as-mentioned characteristic thickness (L_c), the increase of λ_0 at lower temperature is due to the fact that the activation energy of the effective k is greater than that of the effective D* [20, 22].

$$Z = \frac{\coth\left(\left(\frac{L}{\lambda_0}\right)\sqrt{1+\frac{i\omega}{GE-P}}\right)}{GE-T\sqrt{GE-P+i\omega}} \qquad \textbf{Equation 6.1}$$

where the definitions of GE-P and GE-T are the same as the typical Gerischer element discussed in **Equation 3.13**.



Temperature (°C)	L/λ_0
612	1.9
637	2.2
661	2.7
686	3.6
711	3.9
735	4.2
760	4.5
784	4.8

Figure 6.26: (left): The new AC impedance fitting of previous 50:50 wt.% electrode performance data (the one using platinum as the current collector) at 686°C in air using finite length Gerischer element in the equivalent circuit model. **Table 6.4** (right): The change of L/λ_0 at various temperatures. Refit the previous 50:50 wt.% electrode performance data (the one using platinum as the current collector) using finite length Gerischer element in the equivalent circuit model.

Moreover, to examine the penetration of the $Pr_4Ni_3O_{10-\delta}$ decomposition from the platinum current collector/50:50 wt.% composite electrode interface, the electrode was removed using SiC paper until no secondary phases such as PrO_x were detected in the composite electrode under XRD. The rest of the electrode thickness (the cross-section of the sample) was then examined by the SEM. For the 50:50 wt.% sample from which the electrode performance was measured, the electrode was removed until the electrode thickness was less than or equal to ~18 µm. It is important to consider the penetration depth of the X-ray (Cu K_α source) in the sample and this can estimated by the Beer-Lambert law (**Equation 6.2**), where I_0, I, µ, ρ and x are the X-ray intensity at the sample surface, the X-ray intensity in the sample, the mass absorption coefficient, the density of the sample and the length of light path. x is defined as an attenuation length when the intensity of X-ray (I) has dropped by 1/e (where e is a mathematical constant with value equal to around 2.718) of the initial intensity (I_0), which is about 37%. Based on the absorption data from Henke et al. [33] and assuming that the porosity volume fraction in the composite electrode is about one third, the penetration depth of the X-ray/the attenuation length is about 10 µm. Overall, the results suggest that the previous 50:50 wt.% electrode performance measurement is reliable and the $Pr_4Ni_3O_{10-\delta}$ decomposition close to the platinum current collector/composite electrode interface has a limited impact on it.

$$\ln\left(\frac{I_0}{I}\right) = \mu\rho x \qquad \textbf{Equation 6.2}$$

The same approach of grinding the sample surface and then examining the sample under XRD and SEM was also conducted for both the 7-day performance test samples using either platinum or gold as the current collector. For the 7-day performance test samples with platinum, even though the electrode thickness was removed to less than or equal to ~11 µm, both Pr_9O_{16} and $Pr_{10}O_{18}$ were still observed from the XRD data. In contrast, no secondary phases were detected in the 7-day performance test sample with a gold current collector when the remaining electrode thickness was less than or equal to ~25 µm. It is apparent that there was a propagation of $Pr_4Ni_3O_{10-\delta}$ decomposition from the platinum current collector/composite electrode interface towards the electrode bulk and then the active region whereas the decomposition propagation was much less when gold was used as the current collector. This

phenomena explains the reason for the continuous long term electrode performance degradation for the samples with a platinum current collector. Indeed, it seems that both platinum and gold will facilitate praseodymium oxidation in $Pr_4Ni_3O_{10-\delta}$ although the detailed mechanism is unclear. This is similar to the reported observation from $La_2NiO_{4+\delta}$ which was oxidised to the higher order Ruddlesden-Popper phases at a certain temperature in the presence of platinum catalyst [34]. The previous bond valence sum calculation has demonstrated that the praseodymium valence in $Pr_4Ni_3O_{10-\delta}$ was found to be +3 (**Section 5.4**). Based on the decomposition products which were Pr_9O_{16} and $Pr_{10}O_{18}$ for the samples with a platinum current collector (**Figures 6.14** and **6.18**) and Pr_7O_{12} for those with gold current collectors (**Figure 6.24**), the higher average oxidation state of praseodymium in $Pr_{10}O_{18}$ (+3.60) and Pr_9O_{16} (+3.56) than Pr_7O_{12} (+3.43) might facilitate the propagation of $Pr_4Ni_3O_{10-\delta}$ decomposition along the electrode thickness [35]. It is believed that +4 valence of praseodymium ion in coordination of 12 and 9 are too small to be stable in $Pr_4Ni_3O_{10-\delta}$ crystal structure [14]. Although more investigation is required to confirm this hypothesis, the proposed theory also explains the reason that sintering platinum paste at high oxygen partial pressure environment (**Table 6.3**) has no effect on mitigating $Pr_4Ni_3O_{10-\delta}$ decomposition.

Finally, it can be concluded that both platinum and gold should not be used as the current collector as they will promote the decomposition of $Pr_4Ni_3O_{10-\delta}$. Although the propagation of $Pr_4Ni_3O_{10-\delta}$ decomposition is more severe for platinum than gold, a gold current collector tends to from a dense thin layer at ~685°C in air which limits the gas access to the electrode active area. It is important to note that without introducing a current collector to the composite electrode (50:50 wt.%), a severe current collection issue was observed. Based on the previous measured high electrical conductivity of $Pr_4Ni_3O_{10-\delta}$ in the cell operating temperature range under air (**Section 5.6**), $Pr_4Ni_3O_{10-\delta}$ is an ideal candidate for the current collector of the composite electrode. Indeed, $Pr_4Ni_3O_{10-\delta}$ should be more chemically stable/compatible to the composite electrode active layer under air electrode operating conditions compared to the reported platinum and gold. Hence, the promising electrode performance of the composite electrode, together with its long term performance stability, can be achieved.

6.10 Summary

The composite electrode of $Pr_4Ni_3O_{10-\delta}$ and CGPO (50:50 wt.%) shows the best electrode performance of all the $Pr_4Ni_3O_{10-\delta}$ and CGPO composites investigated including pure $Pr_4Ni_3O_{10-\delta}$ electrode (100:0 wt.%) and pure CGPO electrode (0:100 wt.%). This is because of the synergistic effect of the percolated $Pr_4Ni_3O_{10-\delta}$ and CGPO networks which act as the dominant electronic and oxygen ionic conductors, respectively in the composite electrode. The electrode reaction also changes from oxygen diffusion (D*) limitation in $Pr_4Ni_3O_{10-\delta}$ and oxygen surface exchange limitation (k) in CGPO to both D* and k co-limitation in the 50:50 wt.% composite electrode. Indeed, as the overall electrode ASR of 50:50 wt.% was less than 0.15 Ωcm^2, the target electrode performance, at temperature greater than 711°C in air, it is a promising air electrode candidate for intermediate temperature solid oxide cells. It is believed that the composite electrode performance can be further enhanced if the electrode microstructure is optimized.

In terms of the composite electrode (50:50 wt.%) long term (7 days) stability at ~685°C in air, a significant electrode performance degradation was observed for the samples using platinum as the current collector. However, no electrode performance degradation was found when replacing the platinum current collector with gold. The post-mortem test for both samples shows that platinum and gold promoted decomposition of $Pr_4Ni_3O_{10-\delta}$ to PrO_x and NiO but the propagation of $Pr_4Ni_3O_{10-\delta}$ decomposition along the thickness of the electrode was much more severe for the sample with the platinum current collector. This variation between platinum and gold samples might be because of the difference in the decomposed products which include both $Pr_{10}O_{18}$ and Pr_9O_{16} and Pr_7O_{12}, respectively. Since $Pr_{10}O_{18}$ and Pr_9O_{16} have a higher average oxidation state of praseodymium, it might destabilize $Pr_4Ni_3O_{10-\delta}$ in the composite electrode. On the other hand, although the composite electrode is more stable with gold current collector, the gold current collector tends to densify and blocks air entry to the active sites of the composite electrode. Overall, the composite electrode (50:50 wt.%) performance was stable at the intermediate temperature operating range so long as a proper current collecting material can be chosen.

References

[1] P. P. Dholabhai, J. B. Adams, P. A. Crozier, R. Sharma, *Journal of Materials Chemistry,* 21, 18991-18997, 2011.

[2] D. L. Maricle, T. E. Swarr, S. Karavolis , *Solid State Ionics,* 52, 173-182, 1992.

[3] S. Cheng, C. Chatzichristodoulou, M. Søgaard, A. Kaiser, P. V. Hendriksen, *Journal of The Electrochemical Society,* 164, F1354-F1367, 2017.

[4] S. Ramesh, K. C. James Raju, *International Journal of Hydrogen Energy,* 37, 10311-10317, 2012.

[5] V. V. Kharton, A. P. Viskup, F. M. Figueiredo, E. N. Naumovich, A. A. Yaremchenko, F. M. B. Marques, *Electrochimica Acta,* 46, 2879-2889, 2001.

[6] R. Chockalingam, A. K. Ganguli, S. Basu, *Journal of Power Sources,* 250, 80-89, 2014.

[7] D. P. Fagg, I. P. Marozau, A. L. Shaula, V. V. Kharton, J. R. Frade, *Journal of Solid State Chemistry,* 179, 3347-3356, 2006.

[8] S. Lubke, H.-D. Wiemhofer, *Solid State Ionics,* 117, 229-243, 1999.

[9] S. R. Bishop, D. Chen, Y. Kuru, J. -J. Kim, T. S. Stefanik, H. L. Tuller, *ECS Transactions,* 40, 51-57, 2011.

[10] S. R. Bishop, *Journal of Materials Research,* 27, 2009-2016, 2012.

[11] W. J. Bowman, J. Zhu, R. Sharma, P. A. Crozier, *Solid State Ionics,* 272, 9-17, 2015.

[12] R. Chiba, H. Taguchi, T. Komatsu, H. Orui, K. Nozawa, H. Arai, *Solid State Ionics ,* 197, 42-48, 2011.

[13] M. Heidenreich, Ch. Kaps, A. Simon, F. Schulze-Küppers, S. Baumann, *Solid State Ionics,* 283, 56-67, 2015.

[14] V. Vibhu, A. Rougier, C. Nicollet, A. Flura, S. Fourcade, N. Penin, J. -C. Grenier, J. -M. Bassat, *Journal of Power Sources,* 317, 184-193, 2016.

[15] V. Dusastre, J. A. Kilner, *Solid State Ionics,* 126, 163-174, 1999.

[16] J. Rodriguez-Carvajal, *Physica B. ,* 192, 55-69, 1993.

[17] G. Brauer, H. Gradinger, *Journal of Inorganic and General Chemistry,* 276, 209-226, 1954.

[18] A. Montenegro-Herna´ndez, J. Vega-Castillo, L. Mogni, A. Caneiro, *International Journal of Hydrogen Energy,* 36, 15704-15714, 2011.

[19] B. A. Boukamp, M. Verbraeken, D. H. A. Blank, P. Holtappels, *Solid State Ionics,* 177, 2539-2541, 2006.

[20] S. B. Adler, J. A. Lane, B. C. H. Steele, *Journal of Electrochemical Society,* 143, 3554-3564, 1996.

[21] R. U. Atangulov, I. V. Murygin, *Solid State Ionics,* 67, 9-15, 1993.

[22] D. Chen, S. R. Bishop, H. L. Tuller, *Journal of Electroceramics,* 28, 62-69, 2012.

[23] V. Vibhu, "PhD thesis: Stability and aging studies of praseodymium-based nickelates as cathodes for solid oxide fuel cells", Universite de Bordeaux, 2016.

[24] S. Saher, J. Song, V. Vibhu, C. Nicollet, A. Flura, J. -M. Bassat, H. J. M. Bouwmeester, *Journal of Materials Chemistry A,* 6, 8331-8339, 2018.

[25] E. Fischer, J. L. Hertz, *Solid State Ionics,* 218, 18-24, 2012.

[26] A. A. Jais, S. A. Muhammed Ali, M. Anwar, M. Rao Somalu, A. Muchtar, W. N. R. Wan Isahak, C. Yong Tan, R. Singh, N. P. Brandon, *Ceramics International,* 43, 8119-8125, 2017.

[27] L. Navarro, F. Marques, J. Frade, *Journal of the Electrochemical Society,* 144, 267-273, 1997.

[28] B. Völker, R. M. McMeeking, *Journal of Power Sources,* 215, 199-215, 2012.

[29] Z. Wu, M. Liu, *Solid State Ionics,* 93, 65-84, 1996.

[30] K. Ouchetto, F. Archaimbault, J. Choisnet, M. Et-Tabirou, *Materials Chemistry and Physics,* 51, 117-124, 1997.

[31] B. A. Boukamp, A. Rolle, *Solid State Ionics,* 314, 103-111, 2018.

[32] C. Nicollet, A. Flura, V. Vibhu, A. Rougier, J. -M. Bassat, J. -C. Grenier, *International Journal of Hydrogen Energy,* 41, 15538-15544, 2016.

[33] B. L. Henke, E. M. Gullikson, J. C. Davis, *Atomic Data and Nuclear Data Tables,* 54, 181-342, 1993.

[34] S. J. Skinner, S. Cook, J. A. Kilner, "Materials for Next Generation SOFCs," in *Solid Oxide Fuel Cells: Facts and Figures (Past, Present and Future Perspectives for SOFC Technologies)*, Editors: J. T. S. Irvine, P. Connor, London, UK, Springer, 181-202, 2013.

[35] S. Ferro, *International Journal of Electrochemistry,* 2011, 561204*,* 2011.

Chapter 7 Conclusions and future work

The major advantage of using Ruddlesden-Popper phases over conventional perovskite materials as a solid oxide cell air electrode is its promising physical and electrochemical properties towards oxygen reduction reaction and oxygen evolution reaction (**sections 2.5.1-2.5.4**). As Ruddlesden-Popper phases possess a heterostructure type crystal structure, they are usually strontium free [1]. Therefore, they do not experience strontium segregation which is regarded as the major issue contributing towards long term performance degradation for perovskite type air electrode materials [2]. However, n=1 Ruddlesden-Popper phases are not thermodynamically stable at solid oxide cell operating temperatures (**section 2.5.5**). Therefore, the investigation on an air electrode including high order Ruddlesden-Popper phase was conducted.

Overall, the research has found a more stable candidate ($Pr_4Ni_3O_{10-\delta}$ and $Ce_{0.75}Gd_{0.1}Pr_{0.15}O_{2-\delta}$ (CGPO)) to replace $Pr_2NiO_{4+\delta}$ as an air electrode for intermediate temperature (500-800°C) solid oxide cells. This was achieved by firstly understanding the $Pr_2NiO_{4+\delta}$ decomposition and its chemical reaction with $Ce_{0.9}Gd_{0.1}O_{2-\delta}$ under different solid oxide cell sintering and operating temperatures in air (**Chapter 4**). Knowing that the derived products might be electrochemically active to oxygen reduction/evolution reaction in an air electrode, $Pr_4Ni_3O_{10-\delta}$ and CGPO were selected based on their promising properties previously reported in literature compared to PrO_x and NiO (**Sections 2.7**). The synthesis of $Pr_4Ni_3O_{10-\delta}$ and CGPO was then conducted but more emphasis was placed on understanding the synthesis kinetics of $Pr_4Ni_3O_{10-\delta}$, its crystal structure, the oxygen content and the electrical conductivity at intermediate temperature range (**Chapter 5**). Finally, composite electrodes of $Pr_4Ni_3O_{10-\delta}$ and CGPO with various ratios were made to test the performance, to identify the best composite ratio and to examine the long term (7 days) performance stability (**Chapter 6**).

50:50 wt.% of $Pr_4Ni_3O_{10-\delta}$ and CGPO composite showed the best electrode performance when comparing to the other ratios and it is believed that the performance can be further enhanced by optimizing the electrode microstructure. This can be simply achieved by decreasing the particle size of each phase to enhance

the active sites for oxygen reduction/evolution reaction or introducing several functionally graded electrode layers with various chemical compositions and porosity [3, 4].

The long term (7 days) performance stability of $Pr_4Ni_3O_{10-\delta}$ and CGPO composite electrode (50:50 wt.%) mainly depended on the current collector used. If the current collector causes a limited decomposition of $Pr_4Ni_3O_{10-\delta}$, then the composite electrode performance can be very stable with almost no degradation observed in the 7-day performance test. Otherwise, a significant degradation will result. It is proposed to use $Pr_4Ni_3O_{10-\delta}$ as the current collector of the composite electrode due to its better chemical compatibility and high electrical conductivity at the intermediate temperature range. $LaNi_{1-x}Fe_xO_{3-\delta}$ is the other current collecting material that can be used but its chemical compatibility with the composite electrode requires to be examined [5]. In addition, the issue of the chemical reaction between CGPO and 10Sc1CeSZ should be considered, despite its minor impact on the composite electrode long term performance. Considering the intermediate temperature operating conditions and the chemical compatibility with the composite electrode, gadolinium substituted ceria is a promising candidate to replace the zirconia based electrolyte.

Finally, in this research, all the electrode performances were measured under open circuit condition. Although this is the common procedure to examine the viability of a new air electrode material, the real operating condition in solid oxide cells such as under cathodic bias in solid oxide fuel cell mode or under anodic bias in solid oxide electrolysis cell mode can deviate from the open circuit measuring condition even at the same operating temperature (**Figure 1.6**) [6]. Therefore, it will be very interesting to understand the performance and the electrode reaction of $Pr_4Ni_3O_{10-\delta}$ and CGPO composites when a polarization is introduced. Electrode degradation under polarization is also of interest. These tests must be conducted before considering if this composite air electrode material can be commercialized, given that the aim of the research is to find a novel air electrode material which has promising and stable performance at reducing temperatures in solid oxide cells (**Section 1.3.1**).

References

[1] S. Y. Gómez, D. Hotza, *Renewable and Sustainable Energy Reviews*, 61, 155-174, 2016.

[2] C. Berger, E. Bucher, A. Egger, N. Schrödl, J. Lammer, C. Gspan, R. Merkle, W. Grogger, J. Maier, W. Sitte, *Solid State Ionics,* 348, 115282, 2020.

[3] M. Ni, M. K. H. Leung, D. Y. C. Leung, *Electrochimica Acta*, 52, 6707-6718, 2007.

[4] R. Woolley, "PhD thesis: Ruddlesden-Popper Phases as Solid Oxide Fuel Cell Cathodes: Electrochemical Performance and In Situ Characterisation," Imperial College London, London, 2014.

[5] V. Vibhu, A. Rougier, C. Nicollet, A. Flura, S. Fourcade, N. Penin, J.-C. Grenier, J.-M. Bassat, *Journal of Power Sources*, 317, 184-193, 2016.

[6] D. Pérez-Coll, A. Aguadero, M. J. Escudero, L. Daza, *Journal of Power Sources*, 192, 2-13, 2009.

Publications and presentations

- C.-Y. Tsai, C. M. McGilvery, A. Aguadero, S. J. Skinner, "Phase evolution and reactivity of $Pr_2NiO_{4+\delta}$ and $Ce_{0.9}Gd_{0.1}O_{2-\delta}$ composites under solid oxide cell sintering and operating temperatures", *International Journal of Hydrogen Energy*, 44, 31458-31465, 2019.
- C-Y. Tsai, A. Aguadero, S. J. Skinner, "High electrical conductivity and crystal structure of the solid oxide cell electrode $Pr_4Ni_3O_{10-\delta}$", *Journal of Solid State Chemistry*, 289, 121533, 2020.
- H2FC Research Conference 2017 (11^{th}-13^{th} December 2017) at University of St Andrews, poster presentation, 'Evaluation of the Resulting Ceria Composition from the Compatibility Test between $Pr_2NiO_{4+\delta}$ and Gadolinium Doped Ceria.'
- 13^{th} European SOFC and SOEC Forum (3^{th}-6^{th} July 2018) at Lucerne, Switzerland, poster presentation, 'Evaluation of the chemical composition and the physical properties of $Ce_{1-x-y}Gd_xPr_yO_{2-\delta}$ (CGPO) as a potential electrolyser anode.'
- Solid State Chemistry Group Christmas Meeting (Dec 2018) at UCL, London, poster presentation, 'Understanding the chemical reaction between $Pr_2NiO_{4+\delta}$ and gadolinium doped ceria.'
- International Workshop on Current Trends in SOFC Research- Bridging the Gap Between Fundamentals and Application (11^{th}-12^{th} February 2019) at Technische Universitat Wien, poster presentation, 'Evaluation of the performance of $Pr_4Ni_3O_{10+\delta}$/co-doped (Gd and Pr) ceria composite SOC electrodes.'
- The 22^{nd} International Conference on Solid State Ionics (SSI-22) (16^{th}-21^{st} June 2019) at PeyongCheng, Korea, poster presentation, 'Evaluation of the performance of $Pr_4Ni_3O_{10-\delta}$/co-doped (Gd and Pr) ceria composite SOC air electrodes.'

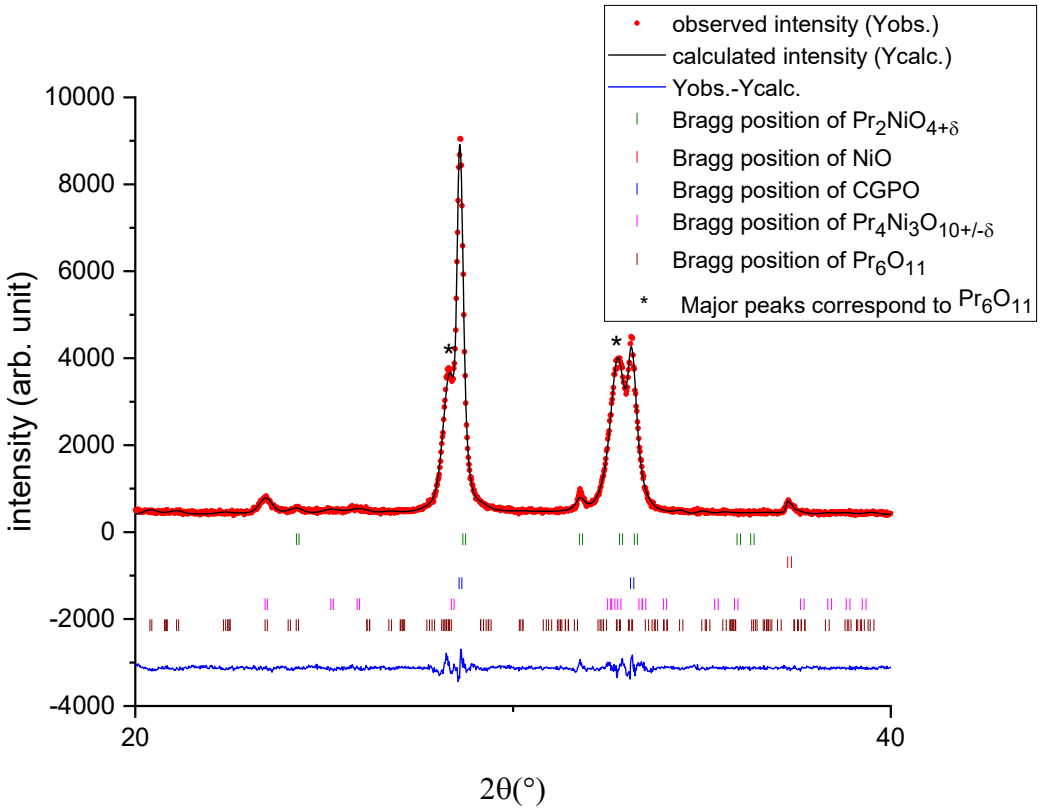


Figure A1: The magnification of **Figure 4.15** to illustrate the presence of each phase after further heating the pre-sintered (1100°C, 12 hours, air) $Pr_2NiO_{4+\delta}$:CGO10 pressed pellet sample at 800°C for 24 hours in air.

Table A1: The resulting interatomic distances in (Å) between Pr/Ni and O and Ni-O-Ni bond angles (°) from the $Pr_4Ni_3O_{10-\delta}$ Rietveld refinement results shown in **Figure 5.7** and **Table 5.1**. Reproduced from Tsai et al. [18].

Pr1-O6 x2	2.47(3), 2.41(3)
Pr1-O7	2.27(2)
Pr1-O8 x4	3.21(2), 2.31(2), 2.71(2), 2.75(2)
Pr1-O10 x2	2.82(3), 2.70(3)
Pr2-O5 x2	2.39(3), 2.40(3)
Pr2-O7 x4	2.97(2), 2.58(2), 2.86(2), 2.59(3)
Pr2-O8	2.36(2)
Pr2-O9 x2	2.65(3), 2.67(3)
Pr3-O1 x4	2.70(2), 2.48(2), 3.11(2), 2.41(3)
Pr3-O4 x4	2.29(2), 3.18(2), 2.83(2), 2.57(2)
Pr3-O6 x2	3.01(2), 2.85(2)
Pr3-O10 x2	2.58(3), 2.59(3)
Pr4-O2 x4	2.44(2), 3.07(2), 2.89(2), 2.79(2)
Pr4-O3 x4	2.42(2), 3.04(2), 2.70(2), 2.74(2)
Pr4-O5 x2	2.79(2), 2.96(2)
Pr4-O9 x2	2.59(2), 2.42(3)
Ni1-O1 x4	1.90(2) x2, 2.01(2) x2
Ni1-O4 x2	1.82(1) x2
Ni2-O2 x4	1.92(2) x2, 1.96(2) x2
Ni2-O3 x2	2.10(1) x2
Ni3-O3	1.77(2)
Ni3-O5 x2	1.98(2), 1.93(2)
Ni3-O7	2.21(2)
Ni3-O9 x2	1.91(2), 1.92(2)
Ni4-O4	2.10(2)
Ni4-O6 x2	1.97(2), 1.82(2)
Ni4-O8	2.11(2)
Ni4-O10 x2	2.03(2), 1.95(2)
Ni1-O1-Ni1	157(1)
Ni1-O4-Ni4	160(1)
Ni2-O2-Ni2	163(1)
Ni2-O3-Ni3	157(1)
Ni3-O5-Ni3	160(1)
Ni3-O9-Ni3	173(1)
Ni4-O6-Ni4	165(1)
Ni4-O10-Ni4	159(1)

Below is the electronic copy of all permission documents for the figures reused from their original sources.

Permission letter from the publisher to reuse **Figure 1.2**.

JOHN WILEY AND SONS LICENSE
TERMS AND CONDITIONS

Jul 05, 2020

This Agreement between Chen-Yu Tsai ("You") and John Wiley and Sons ("John Wiley and Sons") consists of your license details and the terms and conditions provided by John Wiley and Sons and Copyright Clearance Center.

License Number	4862670415069
License date	Jul 05, 2020
Licensed Content Publisher	John Wiley and Sons
Licensed Content Publication	Asia-Pacific Journal of Chemical Engineering
Licensed Content Title	Challenges in the development of reversible solid oxide cell technologies: a mini review
Licensed Content Author	San Ping Jiang
Licensed Content Date	Mar 29, 2016
Licensed Content Volume	11
Licensed Content Issue	3
Licensed Content Pages	6

Type of use	Dissertation/Thesis
Requestor type	University/Academic
Format	Print and electronic
Portion	Figure/table
Number of figures/tables	1
Will you be translating?	No
Title	PhD thesis: Phase evolution and reactivity of Pr2NiO4 d and Ce0.9Gd0.1O2-d solid oxide cell electrodes
Institution name	Imperial College London
Expected presentation date	Jul 2020
Portions	Figure 1
Requestor Location	Chen-Yu Tsai Flat 6 Little Chelsea House Edith Grove London, SW10 0LA United Kingdom Attn: Chen-Yu Tsai
Publisher Tax ID	EU826007151
Total	0.00 USD

Terms and Conditions

TERMS AND CONDITIONS

This copyrighted material is owned by or exclusively licensed to John Wiley & Sons, Inc. or one of its group companies (each a"Wiley Company") or handled on behalf of a society with which a Wiley Company has exclusive publishing rights in relation to a particular work (collectively "WILEY"). By clicking "accept" in connection with completing this licensing transaction, you agree that the following terms and conditions apply to this transaction (along with the billing and payment terms and conditions established by the Copyright Clearance Center Inc., ("CCC's Billing and Payment terms and conditions"), at the time that you opened your RightsLink account (these are available at any time at http://myaccount.copyright.com).

Terms and Conditions

- The materials you have requested permission to reproduce or reuse (the "Wiley Materials") are protected by copyright.

- You are hereby granted a personal, non-exclusive, non-sub licensable (on a stand-alone basis), non-transferable, worldwide, limited license to reproduce the Wiley Materials for the purpose specified in the licensing process. This license, **and any CONTENT (PDF or image file) purchased as part of your order,** is for a one-time use only and limited to any maximum distribution number specified in the license. The first instance of republication or reuse granted by this license must be completed within two years of the date of the grant of this license (although copies prepared before the end date may be distributed thereafter). The Wiley Materials shall not be used in any other manner or for any other purpose, beyond what is granted in the license. Permission is granted subject to an appropriate acknowledgement given to the author, title of the material/book/journal and the publisher. You shall also duplicate the copyright notice that appears in the Wiley publication in your use of the Wiley Material. Permission is also granted on the understanding that nowhere in the text is a previously published source acknowledged for all or part of this Wiley Material. Any third party content is expressly excluded from this permission.

- With respect to the Wiley Materials, all rights are reserved. Except as expressly granted by the terms of the license, no part of the Wiley Materials may be copied, modified, adapted (except for minor reformatting required by the new Publication), translated, reproduced, transferred or distributed, in any form or by any means, and no derivative works may be made based on the Wiley Materials without the prior permission of the respective copyright owner.**For STM Signatory Publishers clearing permission under the terms of the STM Permissions Guidelines only, the terms of the license are extended to include subsequent editions and for editions in other languages, provided such editions are for the work as a whole in situ and does not involve the separate exploitation of the permitted figures or extracts,** You may not alter, remove or suppress in any manner any copyright, trademark or other notices displayed by the Wiley Materials. You may not license, rent, sell, loan, lease, pledge, offer as security, transfer or assign the Wiley Materials on a stand-alone basis, or any of the rights granted to you hereunder to any other person.

- The Wiley Materials and all of the intellectual property rights therein shall at all times remain the exclusive property of John Wiley & Sons Inc, the Wiley Companies, or their respective licensors, and your interest therein is only that of having possession of and the right to reproduce the Wiley Materials pursuant to Section 2 herein during the continuance of this Agreement. You agree that you own no right, title or interest in or to the Wiley Materials or any of the intellectual property rights therein. You shall have no rights hereunder other than the license as provided for above in Section 2. No right,

license or interest to any trademark, trade name, service mark or other branding ("Marks") of WILEY or its licensors is granted hereunder, and you agree that you shall not assert any such right, license or interest with respect thereto

- NEITHER WILEY NOR ITS LICENSORS MAKES ANY WARRANTY OR REPRESENTATION OF ANY KIND TO YOU OR ANY THIRD PARTY, EXPRESS, IMPLIED OR STATUTORY, WITH RESPECT TO THE MATERIALS OR THE ACCURACY OF ANY INFORMATION CONTAINED IN THE MATERIALS, INCLUDING, WITHOUT LIMITATION, ANY IMPLIED WARRANTY OF MERCHANTABILITY, ACCURACY, SATISFACTORY QUALITY, FITNESS FOR A PARTICULAR PURPOSE, USABILITY, INTEGRATION OR NON-INFRINGEMENT AND ALL SUCH WARRANTIES ARE HEREBY EXCLUDED BY WILEY AND ITS LICENSORS AND WAIVED BY YOU.

- WILEY shall have the right to terminate this Agreement immediately upon breach of this Agreement by you.

- You shall indemnify, defend and hold harmless WILEY, its Licensors and their respective directors, officers, agents and employees, from and against any actual or threatened claims, demands, causes of action or proceedings arising from any breach of this Agreement by you.

- IN NO EVENT SHALL WILEY OR ITS LICENSORS BE LIABLE TO YOU OR ANY OTHER PARTY OR ANY OTHER PERSON OR ENTITY FOR ANY SPECIAL, CONSEQUENTIAL, INCIDENTAL, INDIRECT, EXEMPLARY OR PUNITIVE DAMAGES, HOWEVER CAUSED, ARISING OUT OF OR IN CONNECTION WITH THE DOWNLOADING, PROVISIONING, VIEWING OR USE OF THE MATERIALS REGARDLESS OF THE FORM OF ACTION, WHETHER FOR BREACH OF CONTRACT, BREACH OF WARRANTY, TORT, NEGLIGENCE, INFRINGEMENT OR OTHERWISE (INCLUDING, WITHOUT LIMITATION, DAMAGES BASED ON LOSS OF PROFITS, DATA, FILES, USE, BUSINESS OPPORTUNITY OR CLAIMS OF THIRD PARTIES), AND WHETHER OR NOT THE PARTY HAS BEEN ADVISED OF THE POSSIBILITY OF SUCH DAMAGES. THIS LIMITATION SHALL APPLY NOTWITHSTANDING ANY FAILURE OF ESSENTIAL PURPOSE OF ANY LIMITED REMEDY PROVIDED HEREIN.

- Should any provision of this Agreement be held by a court of competent jurisdiction to be illegal, invalid, or unenforceable, that provision shall be deemed amended to achieve as nearly as possible the same economic effect as the original provision, and the legality, validity and enforceability of the remaining provisions of this Agreement shall not be affected or impaired thereby.

- The failure of either party to enforce any term or condition of this Agreement shall not constitute a waiver of either party's right to enforce each and every term and condition of this Agreement. No breach under this agreement shall be deemed waived or excused by either party unless such waiver or consent is in writing signed by the party granting such waiver or consent. The waiver by or consent of a party to a breach of any provision of this Agreement shall not operate or be construed as a waiver of or consent to any other or subsequent breach by such other party.

- This Agreement may not be assigned (including by operation of law or otherwise) by you without WILEY's prior written consent.

- Any fee required for this permission shall be non-refundable after thirty (30) days from receipt by the CCC.
- These terms and conditions together with CCC's Billing and Payment terms and conditions (which are incorporated herein) form the entire agreement between you and WILEY concerning this licensing transaction and (in the absence of fraud) supersedes all prior agreements and representations of the parties, oral or written. This Agreement may not be amended except in writing signed by both parties. This Agreement shall be binding upon and inure to the benefit of the parties' successors, legal representatives, and authorized assigns.
- In the event of any conflict between your obligations established by these terms and conditions and those established by CCC's Billing and Payment terms and conditions, these terms and conditions shall prevail.
- WILEY expressly reserves all rights not specifically granted in the combination of (i) the license details provided by you and accepted in the course of this licensing transaction, (ii) these terms and conditions and (iii) CCC's Billing and Payment terms and conditions.
- This Agreement will be void if the Type of Use, Format, Circulation, or Requestor Type was misrepresented during the licensing process.
- This Agreement shall be governed by and construed in accordance with the laws of the State of New York, USA, without regards to such state's conflict of law rules. Any legal action, suit or proceeding arising out of or relating to these Terms and Conditions or the breach thereof shall be instituted in a court of competent jurisdiction in New York County in the State of New York in the United States of America and each party hereby consents and submits to the personal jurisdiction of such court, waives any objection to venue in such court and consents to service of process by registered or certified mail, return receipt requested, at the last known address of such party.

WILEY OPEN ACCESS TERMS AND CONDITIONS

Wiley Publishes Open Access Articles in fully Open Access Journals and in Subscription journals offering Online Open. Although most of the fully Open Access journals publish open access articles under the terms of the Creative Commons Attribution (CC BY) License only, the subscription journals and a few of the Open Access Journals offer a choice of Creative Commons Licenses. The license type is clearly identified on the article.

The Creative Commons Attribution License

The Creative Commons Attribution License (CC-BY) allows users to copy, distribute and transmit an article, adapt the article and make commercial use of the article. The CC-BY license permits commercial and non-

Creative Commons Attribution Non-Commercial License

The Creative Commons Attribution Non-Commercial (CC-BY-NC)License permits use, distribution and reproduction in any medium, provided the original work is properly cited and is not used for commercial purposes.(see below)

Creative Commons Attribution-Non-Commercial-NoDerivs License

The Creative Commons Attribution Non-Commercial-NoDerivs License (CC-BY-NC-ND) permits use, distribution and reproduction in any medium, provided the original work is properly cited, is not used for commercial purposes and no modifications or adaptations are made. (see below)

Use by commercial "for-profit" organizations

Use of Wiley Open Access articles for commercial, promotional, or marketing purposes requires further explicit permission from Wiley and will be subject to a fee.

Further details can be found on Wiley Online Library
http://olabout.wiley.com/WileyCDA/Section/id-410895.html

Other Terms and Conditions:

v1.10 Last updated September 2015

Questions? customercare@copyright.com or +1-855-239-3415 (toll free in the US) or +1-978-646-2777.

Permission letter from the publisher to reuse **Figure 1.3**.

ELSEVIER LICENSE
TERMS AND CONDITIONS

Jul 08, 2020

This Agreement between Chen-Yu Tsai ("You") and Elsevier ("Elsevier") consists of your license details and the terms and conditions provided by Elsevier and Copyright Clearance Center.

License Number	4864460830175
License date	Jul 08, 2020
Licensed Content Publisher	Elsevier
Licensed Content Publication	Elsevier Books
Licensed Content Title	Carbon Dioxide Utilisation
Licensed Content Author	Rachael Elder,Denis Cumming,Mogens Bjerg Mogensen
Licensed Content Date	Jan 1, 2015
Licensed Content Pages	27
Start Page	183
End Page	209
Type of Use	reuse in a thesis/dissertation
Portion	figures/tables/illustrations

Number of figures/tables/illustrations	1
Format	both print and electronic
Are you the author of this Elsevier chapter?	No
Will you be translating?	No
Title	PhD thesis: Phase evolution and reactivity of Pr2NiO4 d and Ce0.9Gd0.1O2-d solid oxide cell electrodes
Institution name	Imperial College London
Expected presentation date	Jul 2020
Portions	Figure 11.3
Requestor Location	Chen-Yu Tsai Flat 6 Little Chelsea House Edith Grove London, SW10 0LA United Kingdom Attn: Chen-Yu Tsai
Publisher Tax ID	GB 494 6272 12
Total	0.00 USD

Terms and Conditions

INTRODUCTION

1. The publisher for this copyrighted material is Elsevier. By clicking "accept" in connection with completing this licensing transaction, you agree that the following terms and conditions apply to this transaction (along with the Billing and Payment terms and conditions established by Copyright Clearance Center, Inc. ("CCC"), at the time that you opened your Rightslink account and that are available at any time at http://myaccount.copyright.com).

GENERAL TERMS

2. Elsevier hereby grants you permission to reproduce the aforementioned material subject to the terms and conditions indicated.

3. Acknowledgement: If any part of the material to be used (for example, figures) has appeared in our publication with credit or acknowledgement to another source, permission must also be sought from that source. If such permission is not obtained then that material may not be included in your publication/copies. Suitable acknowledgement to the source must be made, either as a footnote or in a reference list at the end of your publication, as follows:

"Reprinted from Publication title, Vol /edition number, Author(s), Title of article / title of chapter, Pages No., Copyright (Year), with permission from Elsevier [OR APPLICABLE SOCIETY COPYRIGHT OWNER]." Also Lancet special credit - "Reprinted from The Lancet, Vol. number, Author(s), Title of article, Pages No., Copyright (Year), with permission from Elsevier."

4. Reproduction of this material is confined to the purpose and/or media for which permission is hereby given.

5. Altering/Modifying Material: Not Permitted. However figures and illustrations may be altered/adapted minimally to serve your work. Any other abbreviations, additions, deletions and/or any other alterations shall be made only with prior written authorization of Elsevier Ltd. (Please contact Elsevier at permissions@elsevier.com). No modifications can be made to any Lancet figures/tables and they must be reproduced in full.

6. If the permission fee for the requested use of our material is waived in this instance, please be advised that your future requests for Elsevier materials may attract a fee.

7. Reservation of Rights: Publisher reserves all rights not specifically granted in the combination of (i) the license details provided by you and accepted in the course of this licensing transaction, (ii) these terms and conditions and (iii) CCC's Billing and Payment terms and conditions.

8. License Contingent Upon Payment: While you may exercise the rights licensed immediately upon issuance of the license at the end of the licensing process for the transaction, provided that you have disclosed complete and accurate details of your proposed use, no license is finally effective unless and until full payment is received from you (either by publisher or by CCC) as provided in CCC's Billing and Payment terms and conditions. If full payment is not received on a timely basis, then any license preliminarily granted shall be deemed automatically revoked and shall be void as if never granted. Further, in the event that you breach any of these terms and conditions or any of CCC's Billing and Payment terms and conditions, the license is automatically revoked and shall be void as if never granted. Use of materials as described in a revoked license, as well as any use of the materials beyond the scope of an unrevoked license, may constitute copyright infringement and publisher reserves the right to take any and all action to protect its copyright in the materials.

9. Warranties: Publisher makes no representations or warranties with respect to the licensed material.

10. Indemnity: You hereby indemnify and agree to hold harmless publisher and CCC, and their respective officers, directors, employees and agents, from and against any and all claims arising out of your use of the licensed material other than as specifically authorized pursuant to this license.

11. No Transfer of License: This license is personal to you and may not be sublicensed, assigned, or transferred by you to any other person without publisher's written permission.

12. No Amendment Except in Writing: This license may not be amended except in a writing signed by both parties (or, in the case of publisher, by CCC on publisher's behalf).

13. Objection to Contrary Terms: Publisher hereby objects to any terms contained in any purchase order, acknowledgment, check endorsement or other writing prepared by you, which terms are inconsistent with these terms and conditions or CCC's Billing and Payment terms and conditions. These terms and conditions, together with CCC's Billing and Payment terms and conditions (which are incorporated herein), comprise the entire agreement between you and publisher (and CCC) concerning this licensing transaction. In the event of any conflict between your obligations established by these terms and conditions and those established by CCC's Billing and Payment terms and conditions, these terms and conditions shall control.

14. Revocation: Elsevier or Copyright Clearance Center may deny the permissions described in this License at their sole discretion, for any reason or no reason, with a full refund payable to you. Notice of such denial will be made using the contact information provided by you. Failure to receive such notice will not alter or invalidate the denial. In no event will Elsevier or Copyright Clearance Center be responsible or liable for any costs, expenses or damage incurred by you as a result of a denial of your permission request, other than a refund of the amount(s) paid by you to Elsevier and/or Copyright Clearance Center for denied permissions.

LIMITED LICENSE

The following terms and conditions apply only to specific license types:

15. **Translation**: This permission is granted for non-exclusive world **English** rights only unless your license was granted for translation rights. If you licensed translation rights you may only translate this content into the languages you requested. A professional translator must perform all translations and reproduce the content word for word preserving the integrity of the article.

16. **Posting licensed content on any Website**: The following terms and conditions apply as follows: Licensing material from an Elsevier journal: All content posted to the web site must maintain the copyright information line on the bottom of each image; A hyper-text must be included to the Homepage of the journal from which you are licensing at http://www.sciencedirect.com/science/journal/xxxxx or the Elsevier homepage for books at http://www.elsevier.com; Central Storage: This license does not include permission for a scanned version of the material to be stored in a central repository such as that provided by Heron/XanEdu.

Licensing material from an Elsevier book: A hyper-text link must be included to the Elsevier homepage at http://www.elsevier.com . All content posted to the web site must maintain the copyright information line on the bottom of each image.

Posting licensed content on Electronic reserve: In addition to the above the following clauses are applicable: The web site must be password-protected and made available only to bona fide students registered on a relevant course. This permission is granted for 1 year only. You may obtain a new license for future website posting.

17. **For journal authors:** the following clauses are applicable in addition to the above:

Preprints:

A preprint is an author's own write-up of research results and analysis, it has not been peer-reviewed, nor has it had any other value added to it by a publisher (such as formatting, copyright, technical enhancement etc.).

Authors can share their preprints anywhere at any time. Preprints should not be added to or enhanced in any way in order to appear more like, or to substitute for, the final versions of articles however authors can update their preprints on arXiv or RePEc with their Accepted Author Manuscript (see below).

If accepted for publication, we encourage authors to link from the preprint to their formal publication via its DOI. Millions of researchers have access to the formal publications on ScienceDirect, and so links will help users to find, access, cite and use the best available version. Please note that Cell Press, The Lancet and some society-owned have different preprint policies. Information on these policies is available on the journal homepage.

Accepted Author Manuscripts: An accepted author manuscript is the manuscript of an article that has been accepted for publication and which typically includes author-incorporated changes suggested during submission, peer review and editor-author communications.

Authors can share their accepted author manuscript:

- immediately
  - via their non-commercial person homepage or blog
  - by updating a preprint in arXiv or RePEc with the accepted manuscript
  - via their research institute or institutional repository for internal institutional uses or as part of an invitation-only research collaboration work-group
  - directly by providing copies to their students or to research collaborators for their personal use
  - for private scholarly sharing as part of an invitation-only work group on commercial sites with which Elsevier has an agreement
- After the embargo period
  - via non-commercial hosting platforms such as their institutional repository
  - via commercial sites with which Elsevier has an agreement

In all cases accepted manuscripts should:

- link to the formal publication via its DOI
- bear a CC-BY-NC-ND license - this is easy to do
- if aggregated with other manuscripts, for example in a repository or other site, be shared in alignment with our hosting policy not be added to or enhanced in any way to appear more like, or to substitute for, the published journal article.

Published journal article (JPA): A published journal article (PJA) is the definitive final record of published research that appears or will appear in the journal and embodies all value-adding publishing activities including peer review co-ordination, copy-editing, formatting, (if relevant) pagination and online enrichment.

Policies for sharing publishing journal articles differ for subscription and gold open access articles:

Subscription Articles: If you are an author, please share a link to your article rather than the full-text. Millions of researchers have access to the formal publications on ScienceDirect,

and so links will help your users to find, access, cite, and use the best available version.

Theses and dissertations which contain embedded PJAs as part of the formal submission can be posted publicly by the awarding institution with DOI links back to the formal publications on ScienceDirect.

If you are affiliated with a library that subscribes to ScienceDirect you have additional private sharing rights for others' research accessed under that agreement. This includes use for classroom teaching and internal training at the institution (including use in course packs and courseware programs), and inclusion of the article for grant funding purposes.

Gold Open Access Articles: May be shared according to the author-selected end-user license and should contain a CrossMark logo, the end user license, and a DOI link to the formal publication on ScienceDirect.

Please refer to Elsevier's posting policy for further information.

18. **For book authors** the following clauses are applicable in addition to the above: Authors are permitted to place a brief summary of their work online only. You are not allowed to download and post the published electronic version of your chapter, nor may you scan the printed edition to create an electronic version. **Posting to a repository:** Authors are permitted to post a summary of their chapter only in their institution's repository.

19. **Thesis/Dissertation**: If your license is for use in a thesis/dissertation your thesis may be submitted to your institution in either print or electronic form. Should your thesis be published commercially, please reapply for permission. These requirements include permission for the Library and Archives of Canada to supply single copies, on demand, of the complete thesis and include permission for Proquest/UMI to supply single copies, on demand, of the complete thesis. Should your thesis be published commercially, please reapply for permission. Theses and dissertations which contain embedded PJAs as part of the formal submission can be posted publicly by the awarding institution with DOI links back to the formal publications on ScienceDirect.

Elsevier Open Access Terms and Conditions

You can publish open access with Elsevier in hundreds of open access journals or in nearly 2000 established subscription journals that support open access publishing. Permitted third party re-use of these open access articles is defined by the author's choice of Creative Commons user license. See our open access license policy for more information.

Terms & Conditions applicable to all Open Access articles published with Elsevier:

Any reuse of the article must not represent the author as endorsing the adaptation of the article nor should the article be modified in such a way as to damage the author's honour or reputation. If any changes have been made, such changes must be clearly indicated.

The author(s) must be appropriately credited and we ask that you include the end user license and a DOI link to the formal publication on ScienceDirect.

If any part of the material to be used (for example, figures) has appeared in our publication with credit or acknowledgement to another source it is the responsibility of the user to ensure their reuse complies with the terms and conditions determined by the rights holder.

Additional Terms & Conditions applicable to each Creative Commons user license:

CC BY: The CC-BY license allows users to copy, to create extracts, abstracts and new works from the Article, to alter and revise the Article and to make commercial use of the Article (including reuse and/or resale of the Article by commercial entities), provided the user gives appropriate credit (with a link to the formal publication through the relevant DOI), provides a link to the license, indicates if changes were made and the licensor is not represented as endorsing the use made of the work. The full details of the license are available at http://creativecommons.org/licenses/by/4.0.

CC BY NC SA: The CC BY-NC-SA license allows users to copy, to create extracts, abstracts and new works from the Article, to alter and revise the Article, provided this is not done for commercial purposes, and that the user gives appropriate credit (with a link to the formal publication through the relevant DOI), provides a link to the license, indicates if changes were made and the licensor is not represented as endorsing the use made of the work. Further, any new works must be made available on the same conditions. The full details of the license are available at http://creativecommons.org/licenses/by-nc-sa/4.0.

CC BY NC ND: The CC BY-NC-ND license allows users to copy and distribute the Article, provided this is not done for commercial purposes and further does not permit distribution of the Article if it is changed or edited in any way, and provided the user gives appropriate credit (with a link to the formal publication through the relevant DOI), provides a link to the license, and that the licensor is not represented as endorsing the use made of the work. The full details of the license are available at http://creativecommons.org/licenses/by-nc-nd/4.0. Any commercial reuse of Open Access articles published with a CC BY NC SA or CC BY NC ND license requires permission from Elsevier and will be subject to a fee.

Commercial reuse includes:

- Associating advertising with the full text of the Article
- Charging fees for document delivery or access
- Article aggregation
- Systematic distribution via e-mail lists or share buttons

Posting or linking by commercial companies for use by customers of those companies.

20. **Other Conditions**:

v1.9

Questions? customercare@copyright.com or +1-855-239-3415 (toll free in the US) or +1-978-646-2777.

Permission letter from the publisher to reuse **Figure 1.4**.

ELSEVIER LICENSE
TERMS AND CONDITIONS

Jul 06, 2020

This Agreement between Chen-Yu Tsai ("You") and Elsevier ("Elsevier") consists of your license details and the terms and conditions provided by Elsevier and Copyright Clearance Center.

License Number	4863070027171
License date	Jul 06, 2020
Licensed Content Publisher	Elsevier
Licensed Content Publication	Elsevier Books
Licensed Content Title	Advances in Catalysis
Licensed Content Author	Seval Gunduz,Dhruba J. Deka,Umit S. Ozkan
Licensed Content Date	Jan 1, 2018
Licensed Content Pages	53
Start Page	113
End Page	165
Type of Use	reuse in a thesis/dissertation
Portion	figures/tables/illustrations

Number of figures/tables/illustrations	1
Format	both print and electronic
Are you the author of this Elsevier chapter?	No
Will you be translating?	No
Title	PhD thesis: Phase evolution and reactivity of Pr2NiO4 d and Ce0.9Gd0.1O2-d solid oxide cell electrodes
Institution name	Imperial College London
Expected presentation date	Jul 2020
Portions	Fig. 4
Requestor Location	Chen-Yu Tsai Flat 6 Little Chelsea House Edith Grove London, SW10 0LA United Kingdom Attn: Chen-Yu Tsai
Publisher Tax ID	GB 494 6272 12
Total	0.00 USD

Terms and Conditions

INTRODUCTION

1. The publisher for this copyrighted material is Elsevier. By clicking "accept" in connection with completing this licensing transaction, you agree that the following terms and conditions apply to this transaction (along with the Billing and Payment terms and conditions established by Copyright Clearance Center, Inc. ("CCC"), at the time that you opened your Rightslink account and that are available at any time at http://myaccount.copyright.com).

GENERAL TERMS

2. Elsevier hereby grants you permission to reproduce the aforementioned material subject to the terms and conditions indicated.

3. Acknowledgement: If any part of the material to be used (for example, figures) has appeared in our publication with credit or acknowledgement to another source, permission must also be sought from that source. If such permission is not obtained then that material may not be included in your publication/copies. Suitable acknowledgement to the source must be made, either as a footnote or in a reference list at the end of your publication, as follows:

"Reprinted from Publication title, Vol /edition number, Author(s), Title of article / title of chapter, Pages No., Copyright (Year), with permission from Elsevier [OR APPLICABLE SOCIETY COPYRIGHT OWNER]." Also Lancet special credit - "Reprinted from The Lancet, Vol. number, Author(s), Title of article, Pages No., Copyright (Year), with permission from Elsevier."

4. Reproduction of this material is confined to the purpose and/or media for which permission is hereby given.

5. Altering/Modifying Material: Not Permitted. However figures and illustrations may be altered/adapted minimally to serve your work. Any other abbreviations, additions, deletions and/or any other alterations shall be made only with prior written authorization of Elsevier Ltd. (Please contact Elsevier at permissions@elsevier.com). No modifications can be made to any Lancet figures/tables and they must be reproduced in full.

6. If the permission fee for the requested use of our material is waived in this instance, please be advised that your future requests for Elsevier materials may attract a fee.

7. Reservation of Rights: Publisher reserves all rights not specifically granted in the combination of (i) the license details provided by you and accepted in the course of this licensing transaction, (ii) these terms and conditions and (iii) CCC's Billing and Payment terms and conditions.

8. License Contingent Upon Payment: While you may exercise the rights licensed immediately upon issuance of the license at the end of the licensing process for the transaction, provided that you have disclosed complete and accurate details of your proposed use, no license is finally effective unless and until full payment is received from you (either by publisher or by CCC) as provided in CCC's Billing and Payment terms and conditions. If full payment is not received on a timely basis, then any license preliminarily granted shall be deemed automatically revoked and shall be void as if never granted. Further, in the event that you breach any of these terms and conditions or any of CCC's Billing and Payment terms and conditions, the license is automatically revoked and shall be void as if never granted. Use of materials as described in a revoked license, as well as any use of the materials beyond the scope of an unrevoked license, may constitute copyright infringement and publisher reserves the right to take any and all action to protect its copyright in the materials.

9. Warranties: Publisher makes no representations or warranties with respect to the licensed material.

10. Indemnity: You hereby indemnify and agree to hold harmless publisher and CCC, and their respective officers, directors, employees and agents, from and against any and all claims arising out of your use of the licensed material other than as specifically authorized pursuant to this license.

11. No Transfer of License: This license is personal to you and may not be sublicensed, assigned, or transferred by you to any other person without publisher's written permission.

12. No Amendment Except in Writing: This license may not be amended except in a writing signed by both parties (or, in the case of publisher, by CCC on publisher's behalf).

13. Objection to Contrary Terms: Publisher hereby objects to any terms contained in any purchase order, acknowledgment, check endorsement or other writing prepared by you, which terms are inconsistent with these terms and conditions or CCC's Billing and Payment terms and conditions. These terms and conditions, together with CCC's Billing and Payment terms and conditions (which are incorporated herein), comprise the entire agreement between you and publisher (and CCC) concerning this licensing transaction. In the event of any conflict between your obligations established by these terms and conditions and those established by CCC's Billing and Payment terms and conditions, these terms and conditions shall control.

14. Revocation: Elsevier or Copyright Clearance Center may deny the permissions described in this License at their sole discretion, for any reason or no reason, with a full refund payable to you. Notice of such denial will be made using the contact information provided by you. Failure to receive such notice will not alter or invalidate the denial. In no event will Elsevier or Copyright Clearance Center be responsible or liable for any costs, expenses or damage incurred by you as a result of a denial of your permission request, other than a refund of the amount(s) paid by you to Elsevier and/or Copyright Clearance Center for denied permissions.

LIMITED LICENSE

The following terms and conditions apply only to specific license types:

15. **Translation**: This permission is granted for non-exclusive world **English** rights only unless your license was granted for translation rights. If you licensed translation rights you may only translate this content into the languages you requested. A professional translator must perform all translations and reproduce the content word for word preserving the integrity of the article.

16. **Posting licensed content on any Website**: The following terms and conditions apply as follows: Licensing material from an Elsevier journal: All content posted to the web site must maintain the copyright information line on the bottom of each image; A hyper-text must be included to the Homepage of the journal from which you are licensing at http://www.sciencedirect.com/science/journal/xxxxx or the Elsevier homepage for books at http://www.elsevier.com; Central Storage: This license does not include permission for a scanned version of the material to be stored in a central repository such as that provided by Heron/XanEdu.

Licensing material from an Elsevier book: A hyper-text link must be included to the Elsevier homepage at http://www.elsevier.com . All content posted to the web site must maintain the copyright information line on the bottom of each image.

Posting licensed content on Electronic reserve: In addition to the above the following clauses are applicable: The web site must be password-protected and made available only to bona fide students registered on a relevant course. This permission is granted for 1 year only. You may obtain a new license for future website posting.

17. **For journal authors:** the following clauses are applicable in addition to the above:

Preprints:

A preprint is an author's own write-up of research results and analysis, it has not been peer-reviewed, nor has it had any other value added to it by a publisher (such as formatting, copyright, technical enhancement etc.).

Authors can share their preprints anywhere at any time. Preprints should not be added to or enhanced in any way in order to appear more like, or to substitute for, the final versions of articles however authors can update their preprints on arXiv or RePEc with their Accepted Author Manuscript (see below).

If accepted for publication, we encourage authors to link from the preprint to their formal publication via its DOI. Millions of researchers have access to the formal publications on ScienceDirect, and so links will help users to find, access, cite and use the best available version. Please note that Cell Press, The Lancet and some society-owned have different preprint policies. Information on these policies is available on the journal homepage.

Accepted Author Manuscripts: An accepted author manuscript is the manuscript of an article that has been accepted for publication and which typically includes author-incorporated changes suggested during submission, peer review and editor-author communications.

Authors can share their accepted author manuscript:

- immediately
  - via their non-commercial person homepage or blog
  - by updating a preprint in arXiv or RePEc with the accepted manuscript
  - via their research institute or institutional repository for internal institutional uses or as part of an invitation-only research collaboration work-group
  - directly by providing copies to their students or to research collaborators for their personal use
  - for private scholarly sharing as part of an invitation-only work group on commercial sites with which Elsevier has an agreement
- After the embargo period
  - via non-commercial hosting platforms such as their institutional repository
  - via commercial sites with which Elsevier has an agreement

In all cases accepted manuscripts should:

- link to the formal publication via its DOI
- bear a CC-BY-NC-ND license - this is easy to do
- if aggregated with other manuscripts, for example in a repository or other site, be shared in alignment with our hosting policy not be added to or enhanced in any way to appear more like, or to substitute for, the published journal article.

Published journal article (JPA): A published journal article (PJA) is the definitive final record of published research that appears or will appear in the journal and embodies all value-adding publishing activities including peer review co-ordination, copy-editing, formatting, (if relevant) pagination and online enrichment.

Policies for sharing publishing journal articles differ for subscription and gold open access articles:

Subscription Articles: If you are an author, please share a link to your article rather than the full-text. Millions of researchers have access to the formal publications on ScienceDirect,

and so links will help your users to find, access, cite, and use the best available version.

Theses and dissertations which contain embedded PJAs as part of the formal submission can be posted publicly by the awarding institution with DOI links back to the formal publications on ScienceDirect.

If you are affiliated with a library that subscribes to ScienceDirect you have additional private sharing rights for others' research accessed under that agreement. This includes use for classroom teaching and internal training at the institution (including use in course packs and courseware programs), and inclusion of the article for grant funding purposes.

Gold Open Access Articles: May be shared according to the author-selected end-user license and should contain a CrossMark logo, the end user license, and a DOI link to the formal publication on ScienceDirect.

Please refer to Elsevier's posting policy for further information.

18. **For book authors** the following clauses are applicable in addition to the above: Authors are permitted to place a brief summary of their work online only. You are not allowed to download and post the published electronic version of your chapter, nor may you scan the printed edition to create an electronic version. **Posting to a repository:** Authors are permitted to post a summary of their chapter only in their institution's repository.

19. **Thesis/Dissertation**: If your license is for use in a thesis/dissertation your thesis may be submitted to your institution in either print or electronic form. Should your thesis be published commercially, please reapply for permission. These requirements include permission for the Library and Archives of Canada to supply single copies, on demand, of the complete thesis and include permission for Proquest/UMI to supply single copies, on demand, of the complete thesis. Should your thesis be published commercially, please reapply for permission. Theses and dissertations which contain embedded PJAs as part of the formal submission can be posted publicly by the awarding institution with DOI links back to the formal publications on ScienceDirect.

Elsevier Open Access Terms and Conditions

You can publish open access with Elsevier in hundreds of open access journals or in nearly 2000 established subscription journals that support open access publishing. Permitted third party re-use of these open access articles is defined by the author's choice of Creative Commons user license. See our open access license policy for more information.

Terms & Conditions applicable to all Open Access articles published with Elsevier:

Any reuse of the article must not represent the author as endorsing the adaptation of the article nor should the article be modified in such a way as to damage the author's honour or reputation. If any changes have been made, such changes must be clearly indicated.

The author(s) must be appropriately credited and we ask that you include the end user license and a DOI link to the formal publication on ScienceDirect.

If any part of the material to be used (for example, figures) has appeared in our publication with credit or acknowledgement to another source it is the responsibility of the user to ensure their reuse complies with the terms and conditions determined by the rights holder.

Additional Terms & Conditions applicable to each Creative Commons user license:

CC BY: The CC-BY license allows users to copy, to create extracts, abstracts and new works from the Article, to alter and revise the Article and to make commercial use of the Article (including reuse and/or resale of the Article by commercial entities), provided the user gives appropriate credit (with a link to the formal publication through the relevant DOI), provides a link to the license, indicates if changes were made and the licensor is not represented as endorsing the use made of the work. The full details of the license are available at http://creativecommons.org/licenses/by/4.0.

CC BY NC SA: The CC BY-NC-SA license allows users to copy, to create extracts, abstracts and new works from the Article, to alter and revise the Article, provided this is not done for commercial purposes, and that the user gives appropriate credit (with a link to the formal publication through the relevant DOI), provides a link to the license, indicates if changes were made and the licensor is not represented as endorsing the use made of the work. Further, any new works must be made available on the same conditions. The full details of the license are available at http://creativecommons.org/licenses/by-nc-sa/4.0.

CC BY NC ND: The CC BY-NC-ND license allows users to copy and distribute the Article, provided this is not done for commercial purposes and further does not permit distribution of the Article if it is changed or edited in any way, and provided the user gives appropriate credit (with a link to the formal publication through the relevant DOI), provides a link to the license, and that the licensor is not represented as endorsing the use made of the work. The full details of the license are available at http://creativecommons.org/licenses/by-nc-nd/4.0. Any commercial reuse of Open Access articles published with a CC BY NC SA or CC BY NC ND license requires permission from Elsevier and will be subject to a fee.

Commercial reuse includes:

- Associating advertising with the full text of the Article
- Charging fees for document delivery or access
- Article aggregation
- Systematic distribution via e-mail lists or share buttons

Posting or linking by commercial companies for use by customers of those companies.

20. **Other Conditions**:

v1.9

Questions? customercare@copyright.com or +1-855-239-3415 (toll free in the US) or +1-978-646-2777.

Permission letter from the publisher to reuse **Figure 1.7**, **1.8**, **2.3**, **2.5** and **2.6**.

ELSEVIER LICENSE
TERMS AND CONDITIONS

Jul 08, 2020

This Agreement between Chen-Yu Tsai ("You") and Elsevier ("Elsevier") consists of your license details and the terms and conditions provided by Elsevier and Copyright Clearance Center.

License Number	4864451142208
License date	Jul 08, 2020
Licensed Content Publisher	Elsevier
Licensed Content Publication	Elsevier Books
Licensed Content Title	Functional Materials for Sustainable Energy Applications
Licensed Content Author	J.-C. Grenier,J.-M. Bassat,F. Mauvy
Licensed Content Date	Jan 1, 2012
Licensed Content Pages	43
Start Page	402
End Page	444
Type of Use	reuse in a thesis/dissertation
Portion	figures/tables/illustrations

Number of figures/tables/illustrations	6
Format	both print and electronic
Are you the author of this Elsevier chapter?	No
Will you be translating?	No
Title	PhD thesis: Phase evolution and reactivity of Pr2NiO4 d and Ce0.9Gd0.1O2-d solid oxide cell electrodes
Institution name	Imperial College London
Expected presentation date	Jul 2020
Portions	Figure 13.2, 13.3, 13.5, 13.13, 13.14 and 13.15
Requestor Location	Chen-Yu Tsai Flat 6 Little Chelsea House Edith Grove London, SW10 0LA United Kingdom Attn: Chen-Yu Tsai
Publisher Tax ID	GB 494 6272 12
Total	0.00 USD
Terms and Conditions	

INTRODUCTION

1. The publisher for this copyrighted material is Elsevier. By clicking "accept" in connection with completing this licensing transaction, you agree that the following terms and conditions apply to this transaction (along with the Billing and Payment terms and conditions established by Copyright Clearance Center, Inc. ("CCC"), at the time that you opened your Rightslink account and that are available at any time at http://myaccount.copyright.com).

GENERAL TERMS

2. Elsevier hereby grants you permission to reproduce the aforementioned material subject to the terms and conditions indicated.

3. Acknowledgement: If any part of the material to be used (for example, figures) has appeared in our publication with credit or acknowledgement to another source, permission must also be sought from that source. If such permission is not obtained then that material may not be included in your publication/copies. Suitable acknowledgement to the source must be made, either as a footnote or in a reference list at the end of your publication, as follows:

"Reprinted from Publication title, Vol /edition number, Author(s), Title of article / title of chapter, Pages No., Copyright (Year), with permission from Elsevier [OR APPLICABLE SOCIETY COPYRIGHT OWNER]." Also Lancet special credit - "Reprinted from The Lancet, Vol. number, Author(s), Title of article, Pages No., Copyright (Year), with permission from Elsevier."

4. Reproduction of this material is confined to the purpose and/or media for which permission is hereby given.

5. Altering/Modifying Material: Not Permitted. However figures and illustrations may be altered/adapted minimally to serve your work. Any other abbreviations, additions, deletions and/or any other alterations shall be made only with prior written authorization of Elsevier Ltd. (Please contact Elsevier at permissions@elsevier.com). No modifications can be made to any Lancet figures/tables and they must be reproduced in full.

6. If the permission fee for the requested use of our material is waived in this instance, please be advised that your future requests for Elsevier materials may attract a fee.

7. Reservation of Rights: Publisher reserves all rights not specifically granted in the combination of (i) the license details provided by you and accepted in the course of this licensing transaction, (ii) these terms and conditions and (iii) CCC's Billing and Payment terms and conditions.

8. License Contingent Upon Payment: While you may exercise the rights licensed immediately upon issuance of the license at the end of the licensing process for the transaction, provided that you have disclosed complete and accurate details of your proposed use, no license is finally effective unless and until full payment is received from you (either by publisher or by CCC) as provided in CCC's Billing and Payment terms and conditions. If full payment is not received on a timely basis, then any license preliminarily granted shall be deemed automatically revoked and shall be void as if never granted. Further, in the event that you breach any of these terms and conditions or any of CCC's Billing and Payment terms and conditions, the license is automatically revoked and shall be void as if never granted. Use of materials as described in a revoked license, as well as any use of the materials beyond the scope of an unrevoked license, may constitute copyright infringement and publisher reserves the right to take any and all action to protect its copyright in the materials.

9. Warranties: Publisher makes no representations or warranties with respect to the licensed material.

10. Indemnity: You hereby indemnify and agree to hold harmless publisher and CCC, and their respective officers, directors, employees and agents, from and against any and all claims arising out of your use of the licensed material other than as specifically authorized pursuant to this license.

11. No Transfer of License: This license is personal to you and may not be sublicensed, assigned, or transferred by you to any other person without publisher's written permission.

12. No Amendment Except in Writing: This license may not be amended except in a writing signed by both parties (or, in the case of publisher, by CCC on publisher's behalf).

13. Objection to Contrary Terms: Publisher hereby objects to any terms contained in any purchase order, acknowledgment, check endorsement or other writing prepared by you, which terms are inconsistent with these terms and conditions or CCC's Billing and Payment terms and conditions. These terms and conditions, together with CCC's Billing and Payment terms and conditions (which are incorporated herein), comprise the entire agreement between you and publisher (and CCC) concerning this licensing transaction. In the event of any conflict between your obligations established by these terms and conditions and those established by CCC's Billing and Payment terms and conditions, these terms and conditions shall control.

14. Revocation: Elsevier or Copyright Clearance Center may deny the permissions described in this License at their sole discretion, for any reason or no reason, with a full refund payable to you. Notice of such denial will be made using the contact information provided by you. Failure to receive such notice will not alter or invalidate the denial. In no event will Elsevier or Copyright Clearance Center be responsible or liable for any costs, expenses or damage incurred by you as a result of a denial of your permission request, other than a refund of the amount(s) paid by you to Elsevier and/or Copyright Clearance Center for denied permissions.

LIMITED LICENSE

The following terms and conditions apply only to specific license types:

15. **Translation**: This permission is granted for non-exclusive world **English** rights only unless your license was granted for translation rights. If you licensed translation rights you may only translate this content into the languages you requested. A professional translator must perform all translations and reproduce the content word for word preserving the integrity of the article.

16. **Posting licensed content on any Website**: The following terms and conditions apply as follows: Licensing material from an Elsevier journal: All content posted to the web site must maintain the copyright information line on the bottom of each image; A hyper-text must be included to the Homepage of the journal from which you are licensing at http://www.sciencedirect.com/science/journal/xxxxx or the Elsevier homepage for books at http://www.elsevier.com; Central Storage: This license does not include permission for a scanned version of the material to be stored in a central repository such as that provided by Heron/XanEdu.

Licensing material from an Elsevier book: A hyper-text link must be included to the Elsevier homepage at http://www.elsevier.com . All content posted to the web site must maintain the copyright information line on the bottom of each image.

Posting licensed content on Electronic reserve: In addition to the above the following clauses are applicable: The web site must be password-protected and made available only to bona fide students registered on a relevant course. This permission is granted for 1 year only. You may obtain a new license for future website posting.

17. **For journal authors:** the following clauses are applicable in addition to the above:

Preprints:

A preprint is an author's own write-up of research results and analysis, it has not been peer-reviewed, nor has it had any other value added to it by a publisher (such as formatting, copyright, technical enhancement etc.).

Authors can share their preprints anywhere at any time. Preprints should not be added to or enhanced in any way in order to appear more like, or to substitute for, the final versions of articles however authors can update their preprints on arXiv or RePEc with their Accepted Author Manuscript (see below).

If accepted for publication, we encourage authors to link from the preprint to their formal publication via its DOI. Millions of researchers have access to the formal publications on ScienceDirect, and so links will help users to find, access, cite and use the best available version. Please note that Cell Press, The Lancet and some society-owned have different preprint policies. Information on these policies is available on the journal homepage.

Accepted Author Manuscripts: An accepted author manuscript is the manuscript of an article that has been accepted for publication and which typically includes author-incorporated changes suggested during submission, peer review and editor-author communications.

Authors can share their accepted author manuscript:

- immediately
  - via their non-commercial person homepage or blog
  - by updating a preprint in arXiv or RePEc with the accepted manuscript
  - via their research institute or institutional repository for internal institutional uses or as part of an invitation-only research collaboration work-group
  - directly by providing copies to their students or to research collaborators for their personal use
  - for private scholarly sharing as part of an invitation-only work group on commercial sites with which Elsevier has an agreement
- After the embargo period
  - via non-commercial hosting platforms such as their institutional repository
  - via commercial sites with which Elsevier has an agreement

In all cases accepted manuscripts should:

- link to the formal publication via its DOI
- bear a CC-BY-NC-ND license - this is easy to do
- if aggregated with other manuscripts, for example in a repository or other site, be shared in alignment with our hosting policy not be added to or enhanced in any way to appear more like, or to substitute for, the published journal article.

Published journal article (JPA): A published journal article (PJA) is the definitive final record of published research that appears or will appear in the journal and embodies all value-adding publishing activities including peer review co-ordination, copy-editing, formatting, (if relevant) pagination and online enrichment.

Policies for sharing publishing journal articles differ for subscription and gold open access articles:

Subscription Articles: If you are an author, please share a link to your article rather than the full-text. Millions of researchers have access to the formal publications on ScienceDirect,

and so links will help your users to find, access, cite, and use the best available version.

Theses and dissertations which contain embedded PJAs as part of the formal submission can be posted publicly by the awarding institution with DOI links back to the formal publications on ScienceDirect.

If you are affiliated with a library that subscribes to ScienceDirect you have additional private sharing rights for others' research accessed under that agreement. This includes use for classroom teaching and internal training at the institution (including use in course packs and courseware programs), and inclusion of the article for grant funding purposes.

Gold Open Access Articles: May be shared according to the author-selected end-user license and should contain a CrossMark logo, the end user license, and a DOI link to the formal publication on ScienceDirect.

Please refer to Elsevier's posting policy for further information.

18. **For book authors** the following clauses are applicable in addition to the above: Authors are permitted to place a brief summary of their work online only. You are not allowed to download and post the published electronic version of your chapter, nor may you scan the printed edition to create an electronic version. **Posting to a repository:** Authors are permitted to post a summary of their chapter only in their institution's repository.

19. **Thesis/Dissertation**: If your license is for use in a thesis/dissertation your thesis may be submitted to your institution in either print or electronic form. Should your thesis be published commercially, please reapply for permission. These requirements include permission for the Library and Archives of Canada to supply single copies, on demand, of the complete thesis and include permission for Proquest/UMI to supply single copies, on demand, of the complete thesis. Should your thesis be published commercially, please reapply for permission. Theses and dissertations which contain embedded PJAs as part of the formal submission can be posted publicly by the awarding institution with DOI links back to the formal publications on ScienceDirect.

Elsevier Open Access Terms and Conditions

You can publish open access with Elsevier in hundreds of open access journals or in nearly 2000 established subscription journals that support open access publishing. Permitted third party re-use of these open access articles is defined by the author's choice of Creative Commons user license. See our open access license policy for more information.

Terms & Conditions applicable to all Open Access articles published with Elsevier:

Any reuse of the article must not represent the author as endorsing the adaptation of the article nor should the article be modified in such a way as to damage the author's honour or reputation. If any changes have been made, such changes must be clearly indicated.

The author(s) must be appropriately credited and we ask that you include the end user license and a DOI link to the formal publication on ScienceDirect.

If any part of the material to be used (for example, figures) has appeared in our publication with credit or acknowledgement to another source it is the responsibility of the user to ensure their reuse complies with the terms and conditions determined by the rights holder.

Additional Terms & Conditions applicable to each Creative Commons user license:

CC BY: The CC-BY license allows users to copy, to create extracts, abstracts and new works from the Article, to alter and revise the Article and to make commercial use of the Article (including reuse and/or resale of the Article by commercial entities), provided the user gives appropriate credit (with a link to the formal publication through the relevant DOI), provides a link to the license, indicates if changes were made and the licensor is not represented as endorsing the use made of the work. The full details of the license are available at http://creativecommons.org/licenses/by/4.0.

CC BY NC SA: The CC BY-NC-SA license allows users to copy, to create extracts, abstracts and new works from the Article, to alter and revise the Article, provided this is not done for commercial purposes, and that the user gives appropriate credit (with a link to the formal publication through the relevant DOI), provides a link to the license, indicates if changes were made and the licensor is not represented as endorsing the use made of the work. Further, any new works must be made available on the same conditions. The full details of the license are available at http://creativecommons.org/licenses/by-nc-sa/4.0.

CC BY NC ND: The CC BY-NC-ND license allows users to copy and distribute the Article, provided this is not done for commercial purposes and further does not permit distribution of the Article if it is changed or edited in any way, and provided the user gives appropriate credit (with a link to the formal publication through the relevant DOI), provides a link to the license, and that the licensor is not represented as endorsing the use made of the work. The full details of the license are available at http://creativecommons.org/licenses/by-nc-nd/4.0. Any commercial reuse of Open Access articles published with a CC BY NC SA or CC BY NC ND license requires permission from Elsevier and will be subject to a fee.

Commercial reuse includes:

- Associating advertising with the full text of the Article
- Charging fees for document delivery or access
- Article aggregation
- Systematic distribution via e-mail lists or share buttons

Posting or linking by commercial companies for use by customers of those companies.

20. **Other Conditions**:

v1.9

Questions? customercare@copyright.com or +1-855-239-3415 (toll free in the US) or +1-978-646-2777.

Permission letter from the publisher to reuse **Figure 2.1**.

ELSEVIER LICENSE
TERMS AND CONDITIONS

Jul 05, 2020

This Agreement between Chen-Yu Tsai ("You") and Elsevier ("Elsevier") consists of your license details and the terms and conditions provided by Elsevier and Copyright Clearance Center.

License Number	4862721068486
License date	Jul 05, 2020
Licensed Content Publisher	Elsevier
Licensed Content Publication	Journal of Power Sources
Licensed Content Title	Electrolytes for solid oxide fuel cells
Licensed Content Author	Jeffrey W. Fergus
Licensed Content Date	Nov 8, 2006
Licensed Content Volume	162
Licensed Content Issue	1
Licensed Content Pages	11
Start Page	30
End Page	40

Type of Use	reuse in a thesis/dissertation
Portion	figures/tables/illustrations
Number of figures/tables/illustrations	1
Format	both print and electronic
Are you the author of this Elsevier article?	No
Will you be translating?	No
Title	PhD thesis: Phase evolution and reactivity of Pr2NiO4 d and Ce0.9Gd0.1O2-d solid oxide cell electrodes
Institution name	Imperial College London
Expected presentation date	Jul 2020
Portions	Fig. 1
Requestor Location	Chen-Yu Tsai Flat 6 Little Chelsea House Edith Grove London, SW10 0LA United Kingdom Attn: Chen-Yu Tsai
Publisher Tax ID	GB 494 6272 12
Total	0.00 USD
Terms and Conditions	

INTRODUCTION

1. The publisher for this copyrighted material is Elsevier. By clicking "accept" in connection with completing this licensing transaction, you agree that the following terms and conditions apply to this transaction (along with the Billing and Payment terms and conditions established by Copyright Clearance Center, Inc. ("CCC"), at the time that you opened your Rightslink account and that are available at any time at http://myaccount.copyright.com).

GENERAL TERMS

2. Elsevier hereby grants you permission to reproduce the aforementioned material subject to the terms and conditions indicated.

3. Acknowledgement: If any part of the material to be used (for example, figures) has appeared in our publication with credit or acknowledgement to another source, permission must also be sought from that source. If such permission is not obtained then that material may not be included in your publication/copies. Suitable acknowledgement to the source must be made, either as a footnote or in a reference list at the end of your publication, as follows:

"Reprinted from Publication title, Vol /edition number, Author(s), Title of article / title of chapter, Pages No., Copyright (Year), with permission from Elsevier [OR APPLICABLE SOCIETY COPYRIGHT OWNER]." Also Lancet special credit - "Reprinted from The Lancet, Vol. number, Author(s), Title of article, Pages No., Copyright (Year), with permission from Elsevier."

4. Reproduction of this material is confined to the purpose and/or media for which permission is hereby given.

5. Altering/Modifying Material: Not Permitted. However figures and illustrations may be altered/adapted minimally to serve your work. Any other abbreviations, additions, deletions and/or any other alterations shall be made only with prior written authorization of Elsevier Ltd. (Please contact Elsevier at permissions@elsevier.com). No modifications can be made to any Lancet figures/tables and they must be reproduced in full.

6. If the permission fee for the requested use of our material is waived in this instance, please be advised that your future requests for Elsevier materials may attract a fee.

7. Reservation of Rights: Publisher reserves all rights not specifically granted in the combination of (i) the license details provided by you and accepted in the course of this licensing transaction, (ii) these terms and conditions and (iii) CCC's Billing and Payment terms and conditions.

8. License Contingent Upon Payment: While you may exercise the rights licensed immediately upon issuance of the license at the end of the licensing process for the transaction, provided that you have disclosed complete and accurate details of your proposed use, no license is finally effective unless and until full payment is received from you (either by publisher or by CCC) as provided in CCC's Billing and Payment terms and conditions. If full payment is not received on a timely basis, then any license preliminarily granted shall be deemed automatically revoked and shall be void as if never granted. Further, in the event that you breach any of these terms and conditions or any of CCC's Billing and Payment terms and conditions, the license is automatically revoked and shall be void as if never granted. Use of materials as described in a revoked license, as well as any use of the materials beyond the scope of an unrevoked license, may constitute copyright infringement and publisher reserves the right to take any and all action to protect its copyright in the materials.

9. Warranties: Publisher makes no representations or warranties with respect to the licensed material.

10. Indemnity: You hereby indemnify and agree to hold harmless publisher and CCC, and their respective officers, directors, employees and agents, from and against any and all claims arising out of your use of the licensed material other than as specifically authorized pursuant to this license.

11. No Transfer of License: This license is personal to you and may not be sublicensed, assigned, or transferred by you to any other person without publisher's written permission.

12. No Amendment Except in Writing: This license may not be amended except in a writing signed by both parties (or, in the case of publisher, by CCC on publisher's behalf).

13. Objection to Contrary Terms: Publisher hereby objects to any terms contained in any purchase order, acknowledgment, check endorsement or other writing prepared by you, which terms are inconsistent with these terms and conditions or CCC's Billing and Payment terms and conditions. These terms and conditions, together with CCC's Billing and Payment terms and conditions (which are incorporated herein), comprise the entire agreement between you and publisher (and CCC) concerning this licensing transaction. In the event of any conflict between your obligations established by these terms and conditions and those established by CCC's Billing and Payment terms and conditions, these terms and conditions shall control.

14. Revocation: Elsevier or Copyright Clearance Center may deny the permissions described in this License at their sole discretion, for any reason or no reason, with a full refund payable to you. Notice of such denial will be made using the contact information provided by you. Failure to receive such notice will not alter or invalidate the denial. In no event will Elsevier or Copyright Clearance Center be responsible or liable for any costs, expenses or damage incurred by you as a result of a denial of your permission request, other than a refund of the amount(s) paid by you to Elsevier and/or Copyright Clearance Center for denied permissions.

LIMITED LICENSE

The following terms and conditions apply only to specific license types:

15. **Translation**: This permission is granted for non-exclusive world **English** rights only unless your license was granted for translation rights. If you licensed translation rights you may only translate this content into the languages you requested. A professional translator must perform all translations and reproduce the content word for word preserving the integrity of the article.

16. **Posting licensed content on any Website**: The following terms and conditions apply as follows: Licensing material from an Elsevier journal: All content posted to the web site must maintain the copyright information line on the bottom of each image; A hyper-text must be included to the Homepage of the journal from which you are licensing at http://www.sciencedirect.com/science/journal/xxxxx or the Elsevier homepage for books at http://www.elsevier.com; Central Storage: This license does not include permission for a scanned version of the material to be stored in a central repository such as that provided by Heron/XanEdu.

Licensing material from an Elsevier book: A hyper-text link must be included to the Elsevier homepage at http://www.elsevier.com . All content posted to the web site must maintain the copyright information line on the bottom of each image.

Posting licensed content on Electronic reserve: In addition to the above the following clauses are applicable: The web site must be password-protected and made available only to bona fide students registered on a relevant course. This permission is granted for 1 year only. You may obtain a new license for future website posting.

17. **For journal authors:** the following clauses are applicable in addition to the above:

Preprints:

A preprint is an author's own write-up of research results and analysis, it has not been peer-reviewed, nor has it had any other value added to it by a publisher (such as formatting, copyright, technical enhancement etc.).

Authors can share their preprints anywhere at any time. Preprints should not be added to or enhanced in any way in order to appear more like, or to substitute for, the final versions of articles however authors can update their preprints on arXiv or RePEc with their Accepted Author Manuscript (see below).

If accepted for publication, we encourage authors to link from the preprint to their formal publication via its DOI. Millions of researchers have access to the formal publications on ScienceDirect, and so links will help users to find, access, cite and use the best available version. Please note that Cell Press, The Lancet and some society-owned have different preprint policies. Information on these policies is available on the journal homepage.

Accepted Author Manuscripts: An accepted author manuscript is the manuscript of an article that has been accepted for publication and which typically includes author-incorporated changes suggested during submission, peer review and editor-author communications.

Authors can share their accepted author manuscript:

- immediately
  - via their non-commercial person homepage or blog
  - by updating a preprint in arXiv or RePEc with the accepted manuscript
  - via their research institute or institutional repository for internal institutional uses or as part of an invitation-only research collaboration work-group
  - directly by providing copies to their students or to research collaborators for their personal use
  - for private scholarly sharing as part of an invitation-only work group on commercial sites with which Elsevier has an agreement
- After the embargo period
  - via non-commercial hosting platforms such as their institutional repository
  - via commercial sites with which Elsevier has an agreement

In all cases accepted manuscripts should:

- link to the formal publication via its DOI
- bear a CC-BY-NC-ND license - this is easy to do
- if aggregated with other manuscripts, for example in a repository or other site, be shared in alignment with our hosting policy not be added to or enhanced in any way to appear more like, or to substitute for, the published journal article.

Published journal article (JPA): A published journal article (PJA) is the definitive final record of published research that appears or will appear in the journal and embodies all

value-adding publishing activities including peer review co-ordination, copy-editing, formatting, (if relevant) pagination and online enrichment.

Policies for sharing publishing journal articles differ for subscription and gold open access articles:

Subscription Articles: If you are an author, please share a link to your article rather than the full-text. Millions of researchers have access to the formal publications on ScienceDirect, and so links will help your users to find, access, cite, and use the best available version.

Theses and dissertations which contain embedded PJAs as part of the formal submission can be posted publicly by the awarding institution with DOI links back to the formal publications on ScienceDirect.

If you are affiliated with a library that subscribes to ScienceDirect you have additional private sharing rights for others' research accessed under that agreement. This includes use for classroom teaching and internal training at the institution (including use in course packs and courseware programs), and inclusion of the article for grant funding purposes.

Gold Open Access Articles: May be shared according to the author-selected end-user license and should contain a CrossMark logo, the end user license, and a DOI link to the formal publication on ScienceDirect.

Please refer to Elsevier's posting policy for further information.

18. **For book authors** the following clauses are applicable in addition to the above: Authors are permitted to place a brief summary of their work online only. You are not allowed to download and post the published electronic version of your chapter, nor may you scan the printed edition to create an electronic version. **Posting to a repository:** Authors are permitted to post a summary of their chapter only in their institution's repository.

19. **Thesis/Dissertation**: If your license is for use in a thesis/dissertation your thesis may be submitted to your institution in either print or electronic form. Should your thesis be published commercially, please reapply for permission. These requirements include permission for the Library and Archives of Canada to supply single copies, on demand, of the complete thesis and include permission for Proquest/UMI to supply single copies, on demand, of the complete thesis. Should your thesis be published commercially, please reapply for permission. Theses and dissertations which contain embedded PJAs as part of the formal submission can be posted publicly by the awarding institution with DOI links back to the formal publications on ScienceDirect.

Elsevier Open Access Terms and Conditions

You can publish open access with Elsevier in hundreds of open access journals or in nearly 2000 established subscription journals that support open access publishing. Permitted third party re-use of these open access articles is defined by the author's choice of Creative Commons user license. See our open access license policy for more information.

Terms & Conditions applicable to all Open Access articles published with Elsevier:

Any reuse of the article must not represent the author as endorsing the adaptation of the article nor should the article be modified in such a way as to damage the author's honour or reputation. If any changes have been made, such changes must be clearly indicated.

The author(s) must be appropriately credited and we ask that you include the end user license and a DOI link to the formal publication on ScienceDirect.

If any part of the material to be used (for example, figures) has appeared in our publication with credit or acknowledgement to another source it is the responsibility of the user to ensure their reuse complies with the terms and conditions determined by the rights holder.

Additional Terms & Conditions applicable to each Creative Commons user license:

CC BY: The CC-BY license allows users to copy, to create extracts, abstracts and new works from the Article, to alter and revise the Article and to make commercial use of the Article (including reuse and/or resale of the Article by commercial entities), provided the user gives appropriate credit (with a link to the formal publication through the relevant DOI), provides a link to the license, indicates if changes were made and the licensor is not represented as endorsing the use made of the work. The full details of the license are available at http://creativecommons.org/licenses/by/4.0.

CC BY NC SA: The CC BY-NC-SA license allows users to copy, to create extracts, abstracts and new works from the Article, to alter and revise the Article, provided this is not done for commercial purposes, and that the user gives appropriate credit (with a link to the formal publication through the relevant DOI), provides a link to the license, indicates if changes were made and the licensor is not represented as endorsing the use made of the work. Further, any new works must be made available on the same conditions. The full details of the license are available at http://creativecommons.org/licenses/by-nc-sa/4.0.

CC BY NC ND: The CC BY-NC-ND license allows users to copy and distribute the Article, provided this is not done for commercial purposes and further does not permit distribution of the Article if it is changed or edited in any way, and provided the user gives appropriate credit (with a link to the formal publication through the relevant DOI), provides a link to the license, and that the licensor is not represented as endorsing the use made of the work. The full details of the license are available at http://creativecommons.org/licenses/by-nc-nd/4.0. Any commercial reuse of Open Access articles published with a CC BY NC SA or CC BY NC ND license requires permission from Elsevier and will be subject to a fee.

Commercial reuse includes:

- Associating advertising with the full text of the Article
- Charging fees for document delivery or access
- Article aggregation
- Systematic distribution via e-mail lists or share buttons

Posting or linking by commercial companies for use by customers of those companies.

20. **Other Conditions**:

v1.9

Questions? customercare@copyright.com or +1-855-239-3415 (toll free in the US) or +1-978-646-2777.

Permission letter from the publisher to reuse **Figure 2.4**.

ELSEVIER LICENSE
TERMS AND CONDITIONS

Jul 05, 2020

This Agreement between Chen-Yu Tsai ("You") and Elsevier ("Elsevier") consists of your license details and the terms and conditions provided by Elsevier and Copyright Clearance Center.

License Number	4862721375390
License date	Jul 05, 2020
Licensed Content Publisher	Elsevier
Licensed Content Publication	Solid State Ionics
Licensed Content Title	A comparative study of the Ruddlesden-Popper series, La n+1Ni n O3n+1 (n =1, 2 and 3), for solid-oxide fuel-cell cathode applications
Licensed Content Author	G. Amow,I.J. Davidson,S.J. Skinner
Licensed Content Date	May 1, 2006
Licensed Content Volume	177
Licensed Content Issue	13-14
Licensed Content Pages	6
Start Page	1205
End Page	1210

Type of Use	reuse in a thesis/dissertation
Portion	figures/tables/illustrations
Number of figures/tables/illustrations	1
Format	both print and electronic
Are you the author of this Elsevier article?	No
Will you be translating?	No
Title	PhD thesis: Phase evolution and reactivity of Pr2NiO4 d and Ce0.9Gd0.1O2-d solid oxide cell electrodes
Institution name	Imperial College London
Expected presentation date	Jul 2020
Portions	Fig. 1
Requestor Location	Chen-Yu Tsai Flat 6 Little Chelsea House Edith Grove London, SW10 0LA United Kingdom Attn: Chen-Yu Tsai
Publisher Tax ID	GB 494 6272 12
Total	0.00 USD
Terms and Conditions	

INTRODUCTION

1. The publisher for this copyrighted material is Elsevier. By clicking "accept" in connection with completing this licensing transaction, you agree that the following terms and conditions apply to this transaction (along with the Billing and Payment terms and conditions established by Copyright Clearance Center, Inc. ("CCC"), at the time that you opened your Rightslink account and that are available at any time at http://myaccount.copyright.com).

GENERAL TERMS

2. Elsevier hereby grants you permission to reproduce the aforementioned material subject to the terms and conditions indicated.

3. Acknowledgement: If any part of the material to be used (for example, figures) has appeared in our publication with credit or acknowledgement to another source, permission must also be sought from that source. If such permission is not obtained then that material may not be included in your publication/copies. Suitable acknowledgement to the source must be made, either as a footnote or in a reference list at the end of your publication, as follows:

"Reprinted from Publication title, Vol /edition number, Author(s), Title of article / title of chapter, Pages No., Copyright (Year), with permission from Elsevier [OR APPLICABLE SOCIETY COPYRIGHT OWNER]." Also Lancet special credit - "Reprinted from The Lancet, Vol. number, Author(s), Title of article, Pages No., Copyright (Year), with permission from Elsevier."

4. Reproduction of this material is confined to the purpose and/or media for which permission is hereby given.

5. Altering/Modifying Material: Not Permitted. However figures and illustrations may be altered/adapted minimally to serve your work. Any other abbreviations, additions, deletions and/or any other alterations shall be made only with prior written authorization of Elsevier Ltd. (Please contact Elsevier at permissions@elsevier.com). No modifications can be made to any Lancet figures/tables and they must be reproduced in full.

6. If the permission fee for the requested use of our material is waived in this instance, please be advised that your future requests for Elsevier materials may attract a fee.

7. Reservation of Rights: Publisher reserves all rights not specifically granted in the combination of (i) the license details provided by you and accepted in the course of this licensing transaction, (ii) these terms and conditions and (iii) CCC's Billing and Payment terms and conditions.

8. License Contingent Upon Payment: While you may exercise the rights licensed immediately upon issuance of the license at the end of the licensing process for the transaction, provided that you have disclosed complete and accurate details of your proposed use, no license is finally effective unless and until full payment is received from you (either by publisher or by CCC) as provided in CCC's Billing and Payment terms and conditions. If full payment is not received on a timely basis, then any license preliminarily granted shall be deemed automatically revoked and shall be void as if never granted. Further, in the event that you breach any of these terms and conditions or any of CCC's Billing and Payment terms and conditions, the license is automatically revoked and shall be void as if never granted. Use of materials as described in a revoked license, as well as any use of the materials beyond the scope of an unrevoked license, may constitute copyright infringement and publisher reserves the right to take any and all action to protect its copyright in the materials.

9. Warranties: Publisher makes no representations or warranties with respect to the licensed material.

10. Indemnity: You hereby indemnify and agree to hold harmless publisher and CCC, and their respective officers, directors, employees and agents, from and against any and all claims arising out of your use of the licensed material other than as specifically authorized pursuant to this license.

11. No Transfer of License: This license is personal to you and may not be sublicensed, assigned, or transferred by you to any other person without publisher's written permission.

12. No Amendment Except in Writing: This license may not be amended except in a writing signed by both parties (or, in the case of publisher, by CCC on publisher's behalf).

13. Objection to Contrary Terms: Publisher hereby objects to any terms contained in any purchase order, acknowledgment, check endorsement or other writing prepared by you, which terms are inconsistent with these terms and conditions or CCC's Billing and Payment terms and conditions. These terms and conditions, together with CCC's Billing and Payment terms and conditions (which are incorporated herein), comprise the entire agreement between you and publisher (and CCC) concerning this licensing transaction. In the event of any conflict between your obligations established by these terms and conditions and those established by CCC's Billing and Payment terms and conditions, these terms and conditions shall control.

14. Revocation: Elsevier or Copyright Clearance Center may deny the permissions described in this License at their sole discretion, for any reason or no reason, with a full refund payable to you. Notice of such denial will be made using the contact information provided by you. Failure to receive such notice will not alter or invalidate the denial. In no event will Elsevier or Copyright Clearance Center be responsible or liable for any costs, expenses or damage incurred by you as a result of a denial of your permission request, other than a refund of the amount(s) paid by you to Elsevier and/or Copyright Clearance Center for denied permissions.

LIMITED LICENSE

The following terms and conditions apply only to specific license types:

15. **Translation**: This permission is granted for non-exclusive world **English** rights only unless your license was granted for translation rights. If you licensed translation rights you may only translate this content into the languages you requested. A professional translator must perform all translations and reproduce the content word for word preserving the integrity of the article.

16. **Posting licensed content on any Website**: The following terms and conditions apply as follows: Licensing material from an Elsevier journal: All content posted to the web site must maintain the copyright information line on the bottom of each image; A hyper-text must be included to the Homepage of the journal from which you are licensing at http://www.sciencedirect.com/science/journal/xxxxx or the Elsevier homepage for books at http://www.elsevier.com; Central Storage: This license does not include permission for a scanned version of the material to be stored in a central repository such as that provided by Heron/XanEdu.

Licensing material from an Elsevier book: A hyper-text link must be included to the Elsevier homepage at http://www.elsevier.com . All content posted to the web site must maintain the copyright information line on the bottom of each image.

Posting licensed content on Electronic reserve: In addition to the above the following clauses are applicable: The web site must be password-protected and made available only to bona fide students registered on a relevant course. This permission is granted for 1 year only. You may obtain a new license for future website posting.

17. **For journal authors:** the following clauses are applicable in addition to the above:

Preprints:

A preprint is an author's own write-up of research results and analysis, it has not been peer-reviewed, nor has it had any other value added to it by a publisher (such as formatting, copyright, technical enhancement etc.).

Authors can share their preprints anywhere at any time. Preprints should not be added to or enhanced in any way in order to appear more like, or to substitute for, the final versions of articles however authors can update their preprints on arXiv or RePEc with their Accepted Author Manuscript (see below).

If accepted for publication, we encourage authors to link from the preprint to their formal publication via its DOI. Millions of researchers have access to the formal publications on ScienceDirect, and so links will help users to find, access, cite and use the best available version. Please note that Cell Press, The Lancet and some society-owned have different preprint policies. Information on these policies is available on the journal homepage.

Accepted Author Manuscripts: An accepted author manuscript is the manuscript of an article that has been accepted for publication and which typically includes author-incorporated changes suggested during submission, peer review and editor-author communications.

Authors can share their accepted author manuscript:

- immediately
  - via their non-commercial person homepage or blog
  - by updating a preprint in arXiv or RePEc with the accepted manuscript
  - via their research institute or institutional repository for internal institutional uses or as part of an invitation-only research collaboration work-group
  - directly by providing copies to their students or to research collaborators for their personal use
  - for private scholarly sharing as part of an invitation-only work group on commercial sites with which Elsevier has an agreement
- After the embargo period
  - via non-commercial hosting platforms such as their institutional repository
  - via commercial sites with which Elsevier has an agreement

In all cases accepted manuscripts should:

- link to the formal publication via its DOI
- bear a CC-BY-NC-ND license - this is easy to do
- if aggregated with other manuscripts, for example in a repository or other site, be shared in alignment with our hosting policy not be added to or enhanced in any way to appear more like, or to substitute for, the published journal article.

Published journal article (JPA): A published journal article (PJA) is the definitive final record of published research that appears or will appear in the journal and embodies all

value-adding publishing activities including peer review co-ordination, copy-editing, formatting, (if relevant) pagination and online enrichment.

Policies for sharing publishing journal articles differ for subscription and gold open access articles:

Subscription Articles: If you are an author, please share a link to your article rather than the full-text. Millions of researchers have access to the formal publications on ScienceDirect, and so links will help your users to find, access, cite, and use the best available version.

Theses and dissertations which contain embedded PJAs as part of the formal submission can be posted publicly by the awarding institution with DOI links back to the formal publications on ScienceDirect.

If you are affiliated with a library that subscribes to ScienceDirect you have additional private sharing rights for others' research accessed under that agreement. This includes use for classroom teaching and internal training at the institution (including use in course packs and courseware programs), and inclusion of the article for grant funding purposes.

Gold Open Access Articles: May be shared according to the author-selected end-user license and should contain a CrossMark logo, the end user license, and a DOI link to the formal publication on ScienceDirect.

Please refer to Elsevier's posting policy for further information.

18. **For book authors** the following clauses are applicable in addition to the above: Authors are permitted to place a brief summary of their work online only. You are not allowed to download and post the published electronic version of your chapter, nor may you scan the printed edition to create an electronic version. **Posting to a repository:** Authors are permitted to post a summary of their chapter only in their institution's repository.

19. **Thesis/Dissertation**: If your license is for use in a thesis/dissertation your thesis may be submitted to your institution in either print or electronic form. Should your thesis be published commercially, please reapply for permission. These requirements include permission for the Library and Archives of Canada to supply single copies, on demand, of the complete thesis and include permission for Proquest/UMI to supply single copies, on demand, of the complete thesis. Should your thesis be published commercially, please reapply for permission. Theses and dissertations which contain embedded PJAs as part of the formal submission can be posted publicly by the awarding institution with DOI links back to the formal publications on ScienceDirect.

Elsevier Open Access Terms and Conditions

You can publish open access with Elsevier in hundreds of open access journals or in nearly 2000 established subscription journals that support open access publishing. Permitted third party re-use of these open access articles is defined by the author's choice of Creative Commons user license. See our open access license policy for more information.

Terms & Conditions applicable to all Open Access articles published with Elsevier:

Any reuse of the article must not represent the author as endorsing the adaptation of the article nor should the article be modified in such a way as to damage the author's honour or reputation. If any changes have been made, such changes must be clearly indicated.

The author(s) must be appropriately credited and we ask that you include the end user license and a DOI link to the formal publication on ScienceDirect.

If any part of the material to be used (for example, figures) has appeared in our publication with credit or acknowledgement to another source it is the responsibility of the user to ensure their reuse complies with the terms and conditions determined by the rights holder.

Additional Terms & Conditions applicable to each Creative Commons user license:

CC BY: The CC-BY license allows users to copy, to create extracts, abstracts and new works from the Article, to alter and revise the Article and to make commercial use of the Article (including reuse and/or resale of the Article by commercial entities), provided the user gives appropriate credit (with a link to the formal publication through the relevant DOI), provides a link to the license, indicates if changes were made and the licensor is not represented as endorsing the use made of the work. The full details of the license are available at http://creativecommons.org/licenses/by/4.0.

CC BY NC SA: The CC BY-NC-SA license allows users to copy, to create extracts, abstracts and new works from the Article, to alter and revise the Article, provided this is not done for commercial purposes, and that the user gives appropriate credit (with a link to the formal publication through the relevant DOI), provides a link to the license, indicates if changes were made and the licensor is not represented as endorsing the use made of the work. Further, any new works must be made available on the same conditions. The full details of the license are available at http://creativecommons.org/licenses/by-nc-sa/4.0.

CC BY NC ND: The CC BY-NC-ND license allows users to copy and distribute the Article, provided this is not done for commercial purposes and further does not permit distribution of the Article if it is changed or edited in any way, and provided the user gives appropriate credit (with a link to the formal publication through the relevant DOI), provides a link to the license, and that the licensor is not represented as endorsing the use made of the work. The full details of the license are available at http://creativecommons.org/licenses/by-nc-nd/4.0. Any commercial reuse of Open Access articles published with a CC BY NC SA or CC BY NC ND license requires permission from Elsevier and will be subject to a fee.

Commercial reuse includes:

- Associating advertising with the full text of the Article
- Charging fees for document delivery or access
- Article aggregation
- Systematic distribution via e-mail lists or share buttons

Posting or linking by commercial companies for use by customers of those companies.

20. **Other Conditions**:

v1.9

Questions? customercare@copyright.com or +1-855-239-3415 (toll free in the US) or +1-978-646-2777.

Permission letter from the publisher to reuse **Figure 2.7**.

ELSEVIER LICENSE
TERMS AND CONDITIONS

Jul 05, 2020

This Agreement between Chen-Yu Tsai ("You") and Elsevier ("Elsevier") consists of your license details and the terms and conditions provided by Elsevier and Copyright Clearance Center.

License Number	4862730740494
License date	Jul 05, 2020
Licensed Content Publisher	Elsevier
Licensed Content Publication	International Journal of Hydrogen Energy
Licensed Content Title	Overstoichiometric oxides Ln2NiO4+δ (Ln = La, Pr or Nd) as oxygen anodic electrodes for solid oxide electrolysis application
Licensed Content Author	Tiphaine Ogier,Fabrice Mauvy,Jean-Marc Bassat,Jérôme Laurencin,Julie Mougin,Jean-Claude Grenier
Licensed Content Date	Dec 14, 2015
Licensed Content Volume	40
Licensed Content Issue	46
Licensed Content Pages	8
Start Page	15885
End Page	15892

Type of Use	reuse in a thesis/dissertation
Portion	figures/tables/illustrations
Number of figures/tables/illustrations	2
Format	both print and electronic
Are you the author of this Elsevier article?	No
Will you be translating?	No
Title	PhD thesis: Phase evolution and reactivity of Pr2NiO4 d and Ce0.9Gd0.1O2-d solid oxide cell electrodes
Institution name	Imperial College London
Expected presentation date	Jul 2020
Portions	Fig. 2(b) and Fig. 5
Requestor Location	Chen-Yu Tsai Flat 6 Little Chelsea House Edith Grove London, SW10 0LA United Kingdom Attn: Chen-Yu Tsai
Publisher Tax ID	GB 494 6272 12
Total	0.00 USD
Terms and Conditions	

INTRODUCTION

1. The publisher for this copyrighted material is Elsevier. By clicking "accept" in connection with completing this licensing transaction, you agree that the following terms and conditions apply to this transaction (along with the Billing and Payment terms and conditions established by Copyright Clearance Center, Inc. ("CCC"), at the time that you opened your Rightslink account and that are available at any time at http://myaccount.copyright.com).

GENERAL TERMS

2. Elsevier hereby grants you permission to reproduce the aforementioned material subject to the terms and conditions indicated.

3. Acknowledgement: If any part of the material to be used (for example, figures) has appeared in our publication with credit or acknowledgement to another source, permission must also be sought from that source. If such permission is not obtained then that material may not be included in your publication/copies. Suitable acknowledgement to the source must be made, either as a footnote or in a reference list at the end of your publication, as follows:

"Reprinted from Publication title, Vol /edition number, Author(s), Title of article / title of chapter, Pages No., Copyright (Year), with permission from Elsevier [OR APPLICABLE SOCIETY COPYRIGHT OWNER]." Also Lancet special credit - "Reprinted from The Lancet, Vol. number, Author(s), Title of article, Pages No., Copyright (Year), with permission from Elsevier."

4. Reproduction of this material is confined to the purpose and/or media for which permission is hereby given.

5. Altering/Modifying Material: Not Permitted. However figures and illustrations may be altered/adapted minimally to serve your work. Any other abbreviations, additions, deletions and/or any other alterations shall be made only with prior written authorization of Elsevier Ltd. (Please contact Elsevier at permissions@elsevier.com). No modifications can be made to any Lancet figures/tables and they must be reproduced in full.

6. If the permission fee for the requested use of our material is waived in this instance, please be advised that your future requests for Elsevier materials may attract a fee.

7. Reservation of Rights: Publisher reserves all rights not specifically granted in the combination of (i) the license details provided by you and accepted in the course of this licensing transaction, (ii) these terms and conditions and (iii) CCC's Billing and Payment terms and conditions.

8. License Contingent Upon Payment: While you may exercise the rights licensed immediately upon issuance of the license at the end of the licensing process for the transaction, provided that you have disclosed complete and accurate details of your proposed use, no license is finally effective unless and until full payment is received from you (either by publisher or by CCC) as provided in CCC's Billing and Payment terms and conditions. If full payment is not received on a timely basis, then any license preliminarily granted shall be deemed automatically revoked and shall be void as if never granted. Further, in the event that you breach any of these terms and conditions or any of CCC's Billing and Payment terms and conditions, the license is automatically revoked and shall be void as if never granted. Use of materials as described in a revoked license, as well as any use of the materials beyond the scope of an unrevoked license, may constitute copyright infringement and publisher reserves the right to take any and all action to protect its copyright in the materials.

9. Warranties: Publisher makes no representations or warranties with respect to the licensed material.

10. Indemnity: You hereby indemnify and agree to hold harmless publisher and CCC, and their respective officers, directors, employees and agents, from and against any and all claims arising out of your use of the licensed material other than as specifically authorized pursuant to this license.

11. No Transfer of License: This license is personal to you and may not be sublicensed, assigned, or transferred by you to any other person without publisher's written permission.

12. No Amendment Except in Writing: This license may not be amended except in a writing signed by both parties (or, in the case of publisher, by CCC on publisher's behalf).

13. Objection to Contrary Terms: Publisher hereby objects to any terms contained in any purchase order, acknowledgment, check endorsement or other writing prepared by you, which terms are inconsistent with these terms and conditions or CCC's Billing and Payment terms and conditions. These terms and conditions, together with CCC's Billing and Payment terms and conditions (which are incorporated herein), comprise the entire agreement between you and publisher (and CCC) concerning this licensing transaction. In the event of any conflict between your obligations established by these terms and conditions and those established by CCC's Billing and Payment terms and conditions, these terms and conditions shall control.

14. Revocation: Elsevier or Copyright Clearance Center may deny the permissions described in this License at their sole discretion, for any reason or no reason, with a full refund payable to you. Notice of such denial will be made using the contact information provided by you. Failure to receive such notice will not alter or invalidate the denial. In no event will Elsevier or Copyright Clearance Center be responsible or liable for any costs, expenses or damage incurred by you as a result of a denial of your permission request, other than a refund of the amount(s) paid by you to Elsevier and/or Copyright Clearance Center for denied permissions.

LIMITED LICENSE

The following terms and conditions apply only to specific license types:

15. **Translation**: This permission is granted for non-exclusive world **English** rights only unless your license was granted for translation rights. If you licensed translation rights you may only translate this content into the languages you requested. A professional translator must perform all translations and reproduce the content word for word preserving the integrity of the article.

16. **Posting licensed content on any Website**: The following terms and conditions apply as follows: Licensing material from an Elsevier journal: All content posted to the web site must maintain the copyright information line on the bottom of each image; A hyper-text must be included to the Homepage of the journal from which you are licensing at http://www.sciencedirect.com/science/journal/xxxxx or the Elsevier homepage for books at http://www.elsevier.com; Central Storage: This license does not include permission for a scanned version of the material to be stored in a central repository such as that provided by Heron/XanEdu.

Licensing material from an Elsevier book: A hyper-text link must be included to the Elsevier homepage at http://www.elsevier.com . All content posted to the web site must maintain the copyright information line on the bottom of each image.

Posting licensed content on Electronic reserve: In addition to the above the following clauses are applicable: The web site must be password-protected and made available only to bona fide students registered on a relevant course. This permission is granted for 1 year only. You may obtain a new license for future website posting.

17. **For journal authors:** the following clauses are applicable in addition to the above:

Preprints:

A preprint is an author's own write-up of research results and analysis, it has not been peer-reviewed, nor has it had any other value added to it by a publisher (such as formatting, copyright, technical enhancement etc.).

Authors can share their preprints anywhere at any time. Preprints should not be added to or enhanced in any way in order to appear more like, or to substitute for, the final versions of articles however authors can update their preprints on arXiv or RePEc with their Accepted Author Manuscript (see below).

If accepted for publication, we encourage authors to link from the preprint to their formal publication via its DOI. Millions of researchers have access to the formal publications on ScienceDirect, and so links will help users to find, access, cite and use the best available version. Please note that Cell Press, The Lancet and some society-owned have different preprint policies. Information on these policies is available on the journal homepage.

Accepted Author Manuscripts: An accepted author manuscript is the manuscript of an article that has been accepted for publication and which typically includes author-incorporated changes suggested during submission, peer review and editor-author communications.

Authors can share their accepted author manuscript:

- immediately
  - via their non-commercial person homepage or blog
  - by updating a preprint in arXiv or RePEc with the accepted manuscript
  - via their research institute or institutional repository for internal institutional uses or as part of an invitation-only research collaboration work-group
  - directly by providing copies to their students or to research collaborators for their personal use
  - for private scholarly sharing as part of an invitation-only work group on commercial sites with which Elsevier has an agreement
- After the embargo period
  - via non-commercial hosting platforms such as their institutional repository
  - via commercial sites with which Elsevier has an agreement

In all cases accepted manuscripts should:

- link to the formal publication via its DOI
- bear a CC-BY-NC-ND license - this is easy to do
- if aggregated with other manuscripts, for example in a repository or other site, be shared in alignment with our hosting policy not be added to or enhanced in any way to appear more like, or to substitute for, the published journal article.

Published journal article (JPA): A published journal article (PJA) is the definitive final record of published research that appears or will appear in the journal and embodies all

value-adding publishing activities including peer review co-ordination, copy-editing, formatting, (if relevant) pagination and online enrichment.

Policies for sharing publishing journal articles differ for subscription and gold open access articles:

Subscription Articles: If you are an author, please share a link to your article rather than the full-text. Millions of researchers have access to the formal publications on ScienceDirect, and so links will help your users to find, access, cite, and use the best available version.

Theses and dissertations which contain embedded PJAs as part of the formal submission can be posted publicly by the awarding institution with DOI links back to the formal publications on ScienceDirect.

If you are affiliated with a library that subscribes to ScienceDirect you have additional private sharing rights for others' research accessed under that agreement. This includes use for classroom teaching and internal training at the institution (including use in course packs and courseware programs), and inclusion of the article for grant funding purposes.

Gold Open Access Articles: May be shared according to the author-selected end-user license and should contain a CrossMark logo, the end user license, and a DOI link to the formal publication on ScienceDirect.

Please refer to Elsevier's posting policy for further information.

18. **For book authors** the following clauses are applicable in addition to the above: Authors are permitted to place a brief summary of their work online only. You are not allowed to download and post the published electronic version of your chapter, nor may you scan the printed edition to create an electronic version. **Posting to a repository:** Authors are permitted to post a summary of their chapter only in their institution's repository.

19. **Thesis/Dissertation**: If your license is for use in a thesis/dissertation your thesis may be submitted to your institution in either print or electronic form. Should your thesis be published commercially, please reapply for permission. These requirements include permission for the Library and Archives of Canada to supply single copies, on demand, of the complete thesis and include permission for Proquest/UMI to supply single copies, on demand, of the complete thesis. Should your thesis be published commercially, please reapply for permission. Theses and dissertations which contain embedded PJAs as part of the formal submission can be posted publicly by the awarding institution with DOI links back to the formal publications on ScienceDirect.

Elsevier Open Access Terms and Conditions

You can publish open access with Elsevier in hundreds of open access journals or in nearly 2000 established subscription journals that support open access publishing. Permitted third party re-use of these open access articles is defined by the author's choice of Creative Commons user license. See our open access license policy for more information.

Terms & Conditions applicable to all Open Access articles published with Elsevier:

Any reuse of the article must not represent the author as endorsing the adaptation of the article nor should the article be modified in such a way as to damage the author's honour or reputation. If any changes have been made, such changes must be clearly indicated.

The author(s) must be appropriately credited and we ask that you include the end user license and a DOI link to the formal publication on ScienceDirect.

If any part of the material to be used (for example, figures) has appeared in our publication with credit or acknowledgement to another source it is the responsibility of the user to ensure their reuse complies with the terms and conditions determined by the rights holder.

Additional Terms & Conditions applicable to each Creative Commons user license:

CC BY: The CC-BY license allows users to copy, to create extracts, abstracts and new works from the Article, to alter and revise the Article and to make commercial use of the Article (including reuse and/or resale of the Article by commercial entities), provided the user gives appropriate credit (with a link to the formal publication through the relevant DOI), provides a link to the license, indicates if changes were made and the licensor is not represented as endorsing the use made of the work. The full details of the license are available at http://creativecommons.org/licenses/by/4.0.

CC BY NC SA: The CC BY-NC-SA license allows users to copy, to create extracts, abstracts and new works from the Article, to alter and revise the Article, provided this is not done for commercial purposes, and that the user gives appropriate credit (with a link to the formal publication through the relevant DOI), provides a link to the license, indicates if changes were made and the licensor is not represented as endorsing the use made of the work. Further, any new works must be made available on the same conditions. The full details of the license are available at http://creativecommons.org/licenses/by-nc-sa/4.0.

CC BY NC ND: The CC BY-NC-ND license allows users to copy and distribute the Article, provided this is not done for commercial purposes and further does not permit distribution of the Article if it is changed or edited in any way, and provided the user gives appropriate credit (with a link to the formal publication through the relevant DOI), provides a link to the license, and that the licensor is not represented as endorsing the use made of the work. The full details of the license are available at http://creativecommons.org/licenses/by-nc-nd/4.0. Any commercial reuse of Open Access articles published with a CC BY NC SA or CC BY NC ND license requires permission from Elsevier and will be subject to a fee.

Commercial reuse includes:

- Associating advertising with the full text of the Article
- Charging fees for document delivery or access
- Article aggregation
- Systematic distribution via e-mail lists or share buttons

Posting or linking by commercial companies for use by customers of those companies.

20. **Other Conditions**:

v1.9

Questions? customercare@copyright.com or +1-855-239-3415 (toll free in the US) or +1-978-646-2777.

Permission letter from the publisher and the consent letter from the author to reuse **Figure 2.9**.

Copyright Clearance Center Marketplace™

IOP Publishing, Ltd - License Terms and Conditions

This is a License Agreement between Chen-Yu Tsai ("You") and IOP Publishing, Ltd ("Publisher") provided by Copyright Clearance Center ("CCC"). The license consists of your order details, the terms and conditions provided by IOP Publishing, Ltd, and the CCC terms and conditions.

All payments must be made in full to CCC.

Order Date	06-Jul-2020	**Type of Use**	Republish in a thesis/dissertation
Order license ID	1046340-1		
ISSN	1938-6737	**Publisher**	IOP Publishing
		Portion	Chart/graph/table/figure

LICENSED CONTENT

Publication Title	ECS transactions	**Publication Type**	e-Journal
Article Title	Influence of La/Pr Ratio on the Ageing Properties of La2-XPrxNiO4+ as Cathodes in IT-SOFCs	**Start Page**	825
		End Page	835
		Issue	1
Author/Editor	Electrochemical Society.	**Volume**	68
Date	01/01/2005	**URL**	http://rzblx1.uni-regensburg.de/ezeit/warpto.phtml?colors=7&jour_id=81944
Language	English		
Country	United States of America		
Rightsholder	IOP Publishing, Ltd		

REQUEST DETAILS

Portion Type	Chart/graph/table/figure	**Distribution**	Worldwide
Number of charts / graphs / tables / figures requested	2	**Translation**	Original language of publication
		Copies for the disabled?	No
Format (select all that apply)	Print, Electronic	**Minor editing privileges?**	Yes
Who will republish the content?	Academic institution	**Incidental promotional use?**	No
Duration of Use	Life of current edition	**Currency**	GBP
Lifetime Unit Quantity	Up to 499		
Rights Requested	Main product		

NEW WORK DETAILS

Title	PhD thesis: Phase evolution and reactivity of Pr2NiO4+d and Ce0.9Gd0.1O2-d solid oxide cell electrodes	**Institution name**	Imperial College London
		Expected presentation date	2020-07-20

Instructor name	Chen-Yu Tsai

ADDITIONAL DETAILS

Order reference number	N/A	**The requesting person / organization to appear on the license**	Chen-Yu Tsai

REUSE CONTENT DETAILS

Title, description or numeric reference of the portion(s)	Figure 4(b) and Figure 5	**Title of the article/chapter the portion is from**	Influence of La/Pr Ratio on the Ageing Properties of La2-XPrxNiO4+ as Cathodes in IT-SOFCs
Editor of portion(s)	Vibhu, V.; Bassat, J.-M.; Flura, A.; Nicollet, C.; Grenier, J.-C.; Rougier, A.	**Author of portion(s)**	Vibhu, V.; Bassat, J.-M.; Flura, A.; Nicollet, C.; Grenier, J.-C.; Rougier, A.
Volume of serial or monograph	68	**Issue, if republishing an article from a serial**	1
Page or page range of portion	825-835	**Publication date of portion**	2015-07-17

PUBLISHER TERMS AND CONDITIONS

These special terms and conditions are in addition to the standard terms and conditions for CCC's Republication Service and, together with those standard terms and conditions, govern the use of the Works. As the User you will make all reasonable efforts to contact the author(s) of the article which the Work is to be reused from, to seek consent for your intended use. Contacting one author who is acting expressly as authorised agent for their co-author(s) is acceptable. User will reproduce the following wording prominently alongside the Work: the source of the Work, including author, article title, title of journal, volume number, issue number (if relevant), page range (or first page if this is the only information available) and date of first publication. This information can be contained in a footnote or reference note; and a link back to the article (via DOI); and if practicable, and IN ALL CASES for new works published under any of the Creative Commons licences, the words "© IOP Publishing. Reproduced with permission. All rights reserved" Without the express permission of the author(s) and the Rightsholder of the article from which the Work is to be reused, User shall not use it in any way which, in the opinion of the Rightsholder, could: (i) distort or alter the author(s)' original intention(s) and meaning; (ii) be prejudicial to the honour or reputation of the author(s); and/or (iii) imply endorsement by the author(s) and/or the Rightsholder. This licence does not apply to any article which is credited to another source and which does not have the copyright line '© IOP Publishing Ltd'. User must check the copyright line of the article from which the Work is to be reused to check that IOP Publishing Ltd has all the necessary rights to be able to grant permission. User is solely responsible for identifying and obtaining separate licences and permissions from the copyright owner for reuse of any such third party material/figures which the Rightsholder is not the copyright owner of. The Rightsholder shall not reimburse any fees which User pays for a republication license for such third party content. This licence does not apply to any material/figure which is credited to another source in the Rightsholder's publication or has been obtained from a third party. User must check the Version of Record of the article from which the Work is to be reused, to check whether any of the material in the Work is third party material. Third party citations and/or copyright notices and/or permissions statements may not be included in any other version of the article from which the Work is to be reused and so cannot be relied upon by the User. User is solely responsible for identifying and obtaining separate licences and permissions from the copyright owner for reuse of any such third party material/figures where the Rightsholder is not the copyright owner. The Rightsholder shall not reimburse any fees which User pays for a republication license for such third party content. User and CCC acknowledge that the Rightsholder may, from time to time, make changes or additions to these special terms and conditions without express notification, provided that these shall not apply to permissions already secured and paid for by User prior to such change or addition. User acknowledges that the Rightsholder (which includes companies within its group and third parties for whom it publishes its titles) may make use of personal data collected through the service in the course of their business. If User is the author of the Work, User may automatically have the right to reuse it under the rights granted back when User transferred the copyright in the article to the Rightsholder. User should check the copyright form and the relevant author rights policy to check whether permission is required. If User is the author of the

Work and does require permission for proposed reuse of the Work, User should select 'Author of requested content' as the Requestor Type. The Rightsholder shall not reimburse any fees which User pays for a republication license. If User is the author of the article which User wishes to reuse in User's thesis or dissertation, the republication licence covers the right to include the Accepted Manuscript version (not the Version of Record) of the article. User must include citation details and, for online use, a link to the Version of Record of the article on the Rightsholder's website. User may need to obtain separate permission for any third party content included within the article. User must check this with the copyright owner of such third party content. User may not include the article in a thesis or dissertation which is published by ProQuest. Any other commercial use of User's thesis or dissertation containing the article would also need to be expressly notified in writing to the Rightsholder at the time of request and would require separate written permission from the Rightsholder. User does not need to request permission for Work which has been published under a CC BY licence. User must check the Version of Record of the CC BY article from which the Work is to be reused, to check whether any of the material in the Work is third party material and so not published under the CC BY licence. User is solely responsible for identifying and obtaining separate licences and permissions from the copyright owner for reuse of any such third party material/figures. The Rightsholder shall not reimburse any fees which User pays for such licences and permissions. As well as CCC, the Rightsholder shall have the right to bring any legal action that it deems necessary to enforce its rights should it consider that the Work infringes those rights in any way. For STM Signatories ONLY (as agreed as part of the STM Guidelines) Any licence granted for a particular edition of a Work will apply also to subsequent editions of it and for editions in other languages, provided such editions are for the Work as a whole in situ and do not involve the separate exploitation of the permitted illustrations or excerpts.

CCC Republication Terms and Conditions

1. Description of Service; Defined Terms. This Republication License enables the User to obtain licenses for republication of one or more copyrighted works as described in detail on the relevant Order Confirmation (the "Work(s)"). Copyright Clearance Center, Inc. ("CCC") grants licenses through the Service on behalf of the rightsholder identified on the Order Confirmation (the "Rightsholder"). "Republication", as used herein, generally means the inclusion of a Work, in whole or in part, in a new work or works, also as described on the Order Confirmation. "User", as used herein, means the person or entity making such republication.

2. The terms set forth in the relevant Order Confirmation, and any terms set by the Rightsholder with respect to a particular Work, govern the terms of use of Works in connection with the Service. By using the Service, the person transacting for a republication license on behalf of the User represents and warrants that he/she/it (a) has been duly authorized by the User to accept, and hereby does accept, all such terms and conditions on behalf of User, and (b) shall inform User of all such terms and conditions. In the event such person is a "freelancer" or other third party independent of User and CCC, such party shall be deemed jointly a "User" for purposes of these terms and conditions. In any event, User shall be deemed to have accepted and agreed to all such terms and conditions if User republishes the Work in any fashion.

3. Scope of License; Limitations and Obligations.

    3.1. All Works and all rights therein, including copyright rights, remain the sole and exclusive property of the Rightsholder. The license created by the exchange of an Order Confirmation (and/or any invoice) and payment by User of the full amount set forth on that document includes only those rights expressly set forth in the Order Confirmation and in these terms and conditions, and conveys no other rights in the Work(s) to User. All rights not expressly granted are hereby reserved.

    3.2. General Payment Terms: You may pay by credit card or through an account with us payable at the end of the month. If you and we agree that you may establish a standing account with CCC, then the following terms apply: Remit Payment to: Copyright Clearance Center, 29118 Network Place, Chicago, IL 60673-1291. Payments Due: Invoices are payable upon their delivery to you (or upon our notice to you that they are available to you for downloading). After 30 days, outstanding amounts will be subject to a service charge of 1-1/2% per month or, if less, the maximum rate allowed by applicable law. Unless otherwise specifically set forth in the Order Confirmation or in a separate written agreement signed by CCC, invoices are due and payable on "net 30" terms. While User may exercise the rights licensed immediately upon issuance of the Order Confirmation, the license is automatically revoked and is null and void, as if it had never been issued, if complete payment for the license is not received on a timely basis either from User directly or through a payment agent, such as a credit card company.

3.3. Unless otherwise provided in the Order Confirmation, any grant of rights to User (i) is "one-time" (including the editions and product family specified in the license), (ii) is non-exclusive and non-transferable and (iii) is subject to any and all limitations and restrictions (such as, but not limited to, limitations on duration of use or circulation) included in the Order Confirmation or invoice and/or in these terms and conditions. Upon completion of the licensed use, User shall either secure a new permission for further use of the Work(s) or immediately cease any new use of the Work(s) and shall render inaccessible (such as by deleting or by removing or severing links or other locators) any further copies of the Work (except for copies printed on paper in accordance with this license and still in User's stock at the end of such period).

3.4. In the event that the material for which a republication license is sought includes third party materials (such as photographs, illustrations, graphs, inserts and similar materials) which are identified in such material as having been used by permission, User is responsible for identifying, and seeking separate licenses (under this Service or otherwise) for, any of such third party materials; without a separate license, such third party materials may not be used.

3.5. Use of proper copyright notice for a Work is required as a condition of any license granted under the Service. Unless otherwise provided in the Order Confirmation, a proper copyright notice will read substantially as follows: "Republished with permission of [Rightsholder's name], from [Work's title, author, volume, edition number and year of copyright]; permission conveyed through Copyright Clearance Center, Inc. " Such notice must be provided in a reasonably legible font size and must be placed either immediately adjacent to the Work as used (for example, as part of a by-line or footnote but not as a separate electronic link) or in the place where substantially all other credits or notices for the new work containing the republished Work are located. Failure to include the required notice results in loss to the Rightsholder and CCC, and the User shall be liable to pay liquidated damages for each such failure equal to twice the use fee specified in the Order Confirmation, in addition to the use fee itself and any other fees and charges specified.

3.6. User may only make alterations to the Work if and as expressly set forth in the Order Confirmation. No Work may be used in any way that is defamatory, violates the rights of third parties (including such third parties' rights of copyright, privacy, publicity, or other tangible or intangible property), or is otherwise illegal, sexually explicit or obscene. In addition, User may not conjoin a Work with any other material that may result in damage to the reputation of the Rightsholder. User agrees to inform CCC if it becomes aware of any infringement of any rights in a Work and to cooperate with any reasonable request of CCC or the Rightsholder in connection therewith.

4. Indemnity. User hereby indemnifies and agrees to defend the Rightsholder and CCC, and their respective employees and directors, against all claims, liability, damages, costs and expenses, including legal fees and expenses, arising out of any use of a Work beyond the scope of the rights granted herein, or any use of a Work which has been altered in any unauthorized way by User, including claims of defamation or infringement of rights of copyright, publicity, privacy or other tangible or intangible property.

5. Limitation of Liability. UNDER NO CIRCUMSTANCES WILL CCC OR THE RIGHTSHOLDER BE LIABLE FOR ANY DIRECT, INDIRECT, CONSEQUENTIAL OR INCIDENTAL DAMAGES (INCLUDING WITHOUT LIMITATION DAMAGES FOR LOSS OF BUSINESS PROFITS OR INFORMATION, OR FOR BUSINESS INTERRUPTION) ARISING OUT OF THE USE OR INABILITY TO USE A WORK, EVEN IF ONE OF THEM HAS BEEN ADVISED OF THE POSSIBILITY OF SUCH DAMAGES. In any event, the total liability of the Rightsholder and CCC (including their respective employees and directors) shall not exceed the total amount actually paid by User for this license. User assumes full liability for the actions and omissions of its principals, employees, agents, affiliates, successors and assigns.

6. Limited Warranties. THE WORK(S) AND RIGHT(S) ARE PROVIDED "AS IS". CCC HAS THE RIGHT TO GRANT TO USER THE RIGHTS GRANTED IN THE ORDER CONFIRMATION DOCUMENT. CCC AND THE RIGHTSHOLDER DISCLAIM ALL OTHER WARRANTIES RELATING TO THE WORK(S) AND RIGHT(S), EITHER EXPRESS OR IMPLIED, INCLUDING WITHOUT LIMITATION IMPLIED WARRANTIES OF MERCHANTABILITY OR FITNESS FOR A PARTICULAR PURPOSE. ADDITIONAL RIGHTS MAY BE REQUIRED TO USE ILLUSTRATIONS, GRAPHS, PHOTOGRAPHS, ABSTRACTS, INSERTS OR OTHER PORTIONS OF THE WORK (AS OPPOSED TO THE ENTIRE WORK) IN A MANNER CONTEMPLATED BY USER;

USER UNDERSTANDS AND AGREES THAT NEITHER CCC NOR THE RIGHTSHOLDER MAY HAVE SUCH ADDITIONAL RIGHTS TO GRANT.

7. Effect of Breach. Any failure by User to pay any amount when due, or any use by User of a Work beyond the scope of the license set forth in the Order Confirmation and/or these terms and conditions, shall be a material breach of the license created by the Order Confirmation and these terms and conditions. Any breach not cured within 30 days of written notice thereof shall result in immediate termination of such license without further notice. Any unauthorized (but licensable) use of a Work that is terminated immediately upon notice thereof may be liquidated by payment of the Rightsholder's ordinary license price therefor; any unauthorized (and unlicensable) use that is not terminated immediately for any reason (including, for example, because materials containing the Work cannot reasonably be recalled) will be subject to all remedies available at law or in equity, but in no event to a payment of less than three times the Rightsholder's ordinary license price for the most closely analogous licensable use plus Rightsholder's and/or CCC's costs and expenses incurred in collecting such payment.

8. Miscellaneous.

    8.1. User acknowledges that CCC may, from time to time, make changes or additions to the Service or to these terms and conditions, and CCC reserves the right to send notice to the User by electronic mail or otherwise for the purposes of notifying User of such changes or additions; provided that any such changes or additions shall not apply to permissions already secured and paid for.

    8.2. Use of User-related information collected through the Service is governed by CCC's privacy policy, available online here:https://marketplace.copyright.com/rs-ui-web/mp/privacy-policy

    8.3. The licensing transaction described in the Order Confirmation is personal to User. Therefore, User may not assign or transfer to any other person (whether a natural person or an organization of any kind) the license created by the Order Confirmation and these terms and conditions or any rights granted hereunder; provided, however, that User may assign such license in its entirety on written notice to CCC in the event of a transfer of all or substantially all of User's rights in the new material which includes the Work(s) licensed under this Service.

    8.4. No amendment or waiver of any terms is binding unless set forth in writing and signed by the parties. The Rightsholder and CCC hereby object to any terms contained in any writing prepared by the User or its principals, employees, agents or affiliates and purporting to govern or otherwise relate to the licensing transaction described in the Order Confirmation, which terms are in any way inconsistent with any terms set forth in the Order Confirmation and/or in these terms and conditions or CCC's standard operating procedures, whether such writing is prepared prior to, simultaneously with or subsequent to the Order Confirmation, and whether such writing appears on a copy of the Order Confirmation or in a separate instrument.

    8.5. The licensing transaction described in the Order Confirmation document shall be governed by and construed under the law of the State of New York, USA, without regard to the principles thereof of conflicts of law. Any case, controversy, suit, action, or proceeding arising out of, in connection with, or related to such licensing transaction shall be brought, at CCC's sole discretion, in any federal or state court located in the County of New York, State of New York, USA, or in any federal or state court whose geographical jurisdiction covers the location of the Rightsholder set forth in the Order Confirmation. The parties expressly submit to the personal jurisdiction and venue of each such federal or state court.If you have any comments or questions about the Service or Copyright Clearance Center, please contact us at 978-750-8400 or send an e-mail to support@copyright.com.

v 1.1

RE: Request for permission to use the figures on your published paper on ECS Transactions

Vibhu, Vaibhav <v.vibhu@fz-juelich.de>
Wed 08/07/2020 11:52
To: Tsai, Chen-Yu <chen-yu.tsai14@imperial.ac.uk>

Dear Mr. Tsai,

Thank you for your email and sorry for my late answer.

For my side it's completely fine.
You can use in your thesis.

Best wishes.
Vaibhav.

--
Dr. Vaibhav Vibhu
Institute of Energy and Climate Research (IEK-9)
Forschungszentrum Jülich GmbH
Tel.: +49-2461-61-6553 (O)
+49-1525-56-77928 (M)
Fax.: +49-2461-61-9550



From: Tsai, Chen-Yu [mailto:chen-yu.tsai14@imperial.ac.uk]
Sent: Tuesday, July 7, 2020 12:37 PM
To: Vibhu, Vaibhav <v.vibhu@fz-juelich.de>
Subject: Request for permission to use the figures on your published paper on ECS Transactions

Dear Dr. Vibhu,

I am writing you to ask for your permission to reuse Figure 4(b) and Figure 5 of the 'Influence of La/Pr Ratio on the Ageing Properties of La2-xPrxNiO4+d as Cathodes in IT-SOFCs', published in 2015 on ECS Transactions, vol. 68, no. 1, p.825-835,(10.1149/06801.0825ecst) in my PhD thesis.

I have made the request to the publisher (IOP publishing) and they have issued me a licence agreement but with a conditon to recieve permission from at least one of the authors of the paper. I will be very grateful if you can do me a favor.

Best regards,
Chen-Yu Tsai
PhD candiate at Materials Department, Imperial College London

Permission letter from the publisher to reuse **Figure 2.10**.

ELSEVIER LICENSE
TERMS AND CONDITIONS

Jul 05, 2020

This Agreement between Chen-Yu Tsai ("You") and Elsevier ("Elsevier") consists of your license details and the terms and conditions provided by Elsevier and Copyright Clearance Center.

License Number	4862741024874
License date	Jul 05, 2020
Licensed Content Publisher	Elsevier
Licensed Content Publication	International Journal of Hydrogen Energy
Licensed Content Title	An innovative efficient oxygen electrode for SOFC: Pr6O11 infiltrated into Gd-doped ceria backbone
Licensed Content Author	Clément Nicollet,Aurélien Flura,Vaibhav Vibhu,Aline Rougier,Jean-Marc Bassat,Jean-Claude Grenier
Licensed Content Date	Sep 14, 2016
Licensed Content Volume	41
Licensed Content Issue	34
Licensed Content Pages	7
Start Page	15538
End Page	15544

Type of Use	reuse in a thesis/dissertation
Portion	figures/tables/illustrations
Number of figures/tables/illustrations	1
Format	both print and electronic
Are you the author of this Elsevier article?	No
Will you be translating?	No
Title	PhD thesis: Phase evolution and reactivity of Pr2NiO4 d and Ce0.9Gd0.1O2-d solid oxide cell electrodes
Institution name	Imperial College London
Expected presentation date	Jul 2020
Portions	Fig. 4
Requestor Location	Chen-Yu Tsai Flat 6 Little Chelsea House Edith Grove London, SW10 0LA United Kingdom Attn: Chen-Yu Tsai
Publisher Tax ID	GB 494 6272 12
Total	0.00 USD
Terms and Conditions	

INTRODUCTION

1. The publisher for this copyrighted material is Elsevier. By clicking "accept" in connection with completing this licensing transaction, you agree that the following terms and conditions apply to this transaction (along with the Billing and Payment terms and conditions established by Copyright Clearance Center, Inc. ("CCC"), at the time that you opened your Rightslink account and that are available at any time at http://myaccount.copyright.com).

GENERAL TERMS

2. Elsevier hereby grants you permission to reproduce the aforementioned material subject to the terms and conditions indicated.

3. Acknowledgement: If any part of the material to be used (for example, figures) has appeared in our publication with credit or acknowledgement to another source, permission must also be sought from that source. If such permission is not obtained then that material may not be included in your publication/copies. Suitable acknowledgement to the source must be made, either as a footnote or in a reference list at the end of your publication, as follows:

"Reprinted from Publication title, Vol /edition number, Author(s), Title of article / title of chapter, Pages No., Copyright (Year), with permission from Elsevier [OR APPLICABLE SOCIETY COPYRIGHT OWNER]." Also Lancet special credit - "Reprinted from The Lancet, Vol. number, Author(s), Title of article, Pages No., Copyright (Year), with permission from Elsevier."

4. Reproduction of this material is confined to the purpose and/or media for which permission is hereby given.

5. Altering/Modifying Material: Not Permitted. However figures and illustrations may be altered/adapted minimally to serve your work. Any other abbreviations, additions, deletions and/or any other alterations shall be made only with prior written authorization of Elsevier Ltd. (Please contact Elsevier at permissions@elsevier.com). No modifications can be made to any Lancet figures/tables and they must be reproduced in full.

6. If the permission fee for the requested use of our material is waived in this instance, please be advised that your future requests for Elsevier materials may attract a fee.

7. Reservation of Rights: Publisher reserves all rights not specifically granted in the combination of (i) the license details provided by you and accepted in the course of this licensing transaction, (ii) these terms and conditions and (iii) CCC's Billing and Payment terms and conditions.

8. License Contingent Upon Payment: While you may exercise the rights licensed immediately upon issuance of the license at the end of the licensing process for the transaction, provided that you have disclosed complete and accurate details of your proposed use, no license is finally effective unless and until full payment is received from you (either by publisher or by CCC) as provided in CCC's Billing and Payment terms and conditions. If full payment is not received on a timely basis, then any license preliminarily granted shall be deemed automatically revoked and shall be void as if never granted. Further, in the event that you breach any of these terms and conditions or any of CCC's Billing and Payment terms and conditions, the license is automatically revoked and shall be void as if never granted. Use of materials as described in a revoked license, as well as any use of the materials beyond the scope of an unrevoked license, may constitute copyright infringement and publisher reserves the right to take any and all action to protect its copyright in the materials.

9. Warranties: Publisher makes no representations or warranties with respect to the licensed material.

10. Indemnity: You hereby indemnify and agree to hold harmless publisher and CCC, and their respective officers, directors, employees and agents, from and against any and all claims arising out of your use of the licensed material other than as specifically authorized pursuant to this license.

11. No Transfer of License: This license is personal to you and may not be sublicensed, assigned, or transferred by you to any other person without publisher's written permission.

12. No Amendment Except in Writing: This license may not be amended except in a writing signed by both parties (or, in the case of publisher, by CCC on publisher's behalf).

13. Objection to Contrary Terms: Publisher hereby objects to any terms contained in any purchase order, acknowledgment, check endorsement or other writing prepared by you, which terms are inconsistent with these terms and conditions or CCC's Billing and Payment terms and conditions. These terms and conditions, together with CCC's Billing and Payment terms and conditions (which are incorporated herein), comprise the entire agreement between you and publisher (and CCC) concerning this licensing transaction. In the event of any conflict between your obligations established by these terms and conditions and those established by CCC's Billing and Payment terms and conditions, these terms and conditions shall control.

14. Revocation: Elsevier or Copyright Clearance Center may deny the permissions described in this License at their sole discretion, for any reason or no reason, with a full refund payable to you. Notice of such denial will be made using the contact information provided by you. Failure to receive such notice will not alter or invalidate the denial. In no event will Elsevier or Copyright Clearance Center be responsible or liable for any costs, expenses or damage incurred by you as a result of a denial of your permission request, other than a refund of the amount(s) paid by you to Elsevier and/or Copyright Clearance Center for denied permissions.

LIMITED LICENSE

The following terms and conditions apply only to specific license types:

15. **Translation**: This permission is granted for non-exclusive world **English** rights only unless your license was granted for translation rights. If you licensed translation rights you may only translate this content into the languages you requested. A professional translator must perform all translations and reproduce the content word for word preserving the integrity of the article.

16. **Posting licensed content on any Website**: The following terms and conditions apply as follows: Licensing material from an Elsevier journal: All content posted to the web site must maintain the copyright information line on the bottom of each image; A hyper-text must be included to the Homepage of the journal from which you are licensing at http://www.sciencedirect.com/science/journal/xxxxx or the Elsevier homepage for books at http://www.elsevier.com; Central Storage: This license does not include permission for a scanned version of the material to be stored in a central repository such as that provided by Heron/XanEdu.

Licensing material from an Elsevier book: A hyper-text link must be included to the Elsevier homepage at http://www.elsevier.com . All content posted to the web site must maintain the copyright information line on the bottom of each image.

Posting licensed content on Electronic reserve: In addition to the above the following clauses are applicable: The web site must be password-protected and made available only to bona fide students registered on a relevant course. This permission is granted for 1 year only. You may obtain a new license for future website posting.

17. **For journal authors:** the following clauses are applicable in addition to the above:

Preprints:

A preprint is an author's own write-up of research results and analysis, it has not been peer-reviewed, nor has it had any other value added to it by a publisher (such as formatting, copyright, technical enhancement etc.).

Authors can share their preprints anywhere at any time. Preprints should not be added to or enhanced in any way in order to appear more like, or to substitute for, the final versions of articles however authors can update their preprints on arXiv or RePEc with their Accepted Author Manuscript (see below).

If accepted for publication, we encourage authors to link from the preprint to their formal publication via its DOI. Millions of researchers have access to the formal publications on ScienceDirect, and so links will help users to find, access, cite and use the best available version. Please note that Cell Press, The Lancet and some society-owned have different preprint policies. Information on these policies is available on the journal homepage.

Accepted Author Manuscripts: An accepted author manuscript is the manuscript of an article that has been accepted for publication and which typically includes author-incorporated changes suggested during submission, peer review and editor-author communications.

Authors can share their accepted author manuscript:

- immediately
  - via their non-commercial person homepage or blog
  - by updating a preprint in arXiv or RePEc with the accepted manuscript
  - via their research institute or institutional repository for internal institutional uses or as part of an invitation-only research collaboration work-group
  - directly by providing copies to their students or to research collaborators for their personal use
  - for private scholarly sharing as part of an invitation-only work group on commercial sites with which Elsevier has an agreement
- After the embargo period
  - via non-commercial hosting platforms such as their institutional repository
  - via commercial sites with which Elsevier has an agreement

In all cases accepted manuscripts should:

- link to the formal publication via its DOI
- bear a CC-BY-NC-ND license - this is easy to do
- if aggregated with other manuscripts, for example in a repository or other site, be shared in alignment with our hosting policy not be added to or enhanced in any way to appear more like, or to substitute for, the published journal article.

Published journal article (JPA): A published journal article (PJA) is the definitive final record of published research that appears or will appear in the journal and embodies all

value-adding publishing activities including peer review co-ordination, copy-editing, formatting, (if relevant) pagination and online enrichment.

Policies for sharing publishing journal articles differ for subscription and gold open access articles:

Subscription Articles: If you are an author, please share a link to your article rather than the full-text. Millions of researchers have access to the formal publications on ScienceDirect, and so links will help your users to find, access, cite, and use the best available version.

Theses and dissertations which contain embedded PJAs as part of the formal submission can be posted publicly by the awarding institution with DOI links back to the formal publications on ScienceDirect.

If you are affiliated with a library that subscribes to ScienceDirect you have additional private sharing rights for others' research accessed under that agreement. This includes use for classroom teaching and internal training at the institution (including use in course packs and courseware programs), and inclusion of the article for grant funding purposes.

Gold Open Access Articles: May be shared according to the author-selected end-user license and should contain a CrossMark logo, the end user license, and a DOI link to the formal publication on ScienceDirect.

Please refer to Elsevier's posting policy for further information.

18. **For book authors** the following clauses are applicable in addition to the above: Authors are permitted to place a brief summary of their work online only. You are not allowed to download and post the published electronic version of your chapter, nor may you scan the printed edition to create an electronic version. **Posting to a repository:** Authors are permitted to post a summary of their chapter only in their institution's repository.

19. **Thesis/Dissertation**: If your license is for use in a thesis/dissertation your thesis may be submitted to your institution in either print or electronic form. Should your thesis be published commercially, please reapply for permission. These requirements include permission for the Library and Archives of Canada to supply single copies, on demand, of the complete thesis and include permission for Proquest/UMI to supply single copies, on demand, of the complete thesis. Should your thesis be published commercially, please reapply for permission. Theses and dissertations which contain embedded PJAs as part of the formal submission can be posted publicly by the awarding institution with DOI links back to the formal publications on ScienceDirect.

Elsevier Open Access Terms and Conditions

You can publish open access with Elsevier in hundreds of open access journals or in nearly 2000 established subscription journals that support open access publishing. Permitted third party re-use of these open access articles is defined by the author's choice of Creative Commons user license. See our open access license policy for more information.

Terms & Conditions applicable to all Open Access articles published with Elsevier:

Any reuse of the article must not represent the author as endorsing the adaptation of the article nor should the article be modified in such a way as to damage the author's honour or reputation. If any changes have been made, such changes must be clearly indicated.

The author(s) must be appropriately credited and we ask that you include the end user license and a DOI link to the formal publication on ScienceDirect.

If any part of the material to be used (for example, figures) has appeared in our publication with credit or acknowledgement to another source it is the responsibility of the user to ensure their reuse complies with the terms and conditions determined by the rights holder.

Additional Terms & Conditions applicable to each Creative Commons user license:

CC BY: The CC-BY license allows users to copy, to create extracts, abstracts and new works from the Article, to alter and revise the Article and to make commercial use of the Article (including reuse and/or resale of the Article by commercial entities), provided the user gives appropriate credit (with a link to the formal publication through the relevant DOI), provides a link to the license, indicates if changes were made and the licensor is not represented as endorsing the use made of the work. The full details of the license are available at http://creativecommons.org/licenses/by/4.0.

CC BY NC SA: The CC BY-NC-SA license allows users to copy, to create extracts, abstracts and new works from the Article, to alter and revise the Article, provided this is not done for commercial purposes, and that the user gives appropriate credit (with a link to the formal publication through the relevant DOI), provides a link to the license, indicates if changes were made and the licensor is not represented as endorsing the use made of the work. Further, any new works must be made available on the same conditions. The full details of the license are available at http://creativecommons.org/licenses/by-nc-sa/4.0.

CC BY NC ND: The CC BY-NC-ND license allows users to copy and distribute the Article, provided this is not done for commercial purposes and further does not permit distribution of the Article if it is changed or edited in any way, and provided the user gives appropriate credit (with a link to the formal publication through the relevant DOI), provides a link to the license, and that the licensor is not represented as endorsing the use made of the work. The full details of the license are available at http://creativecommons.org/licenses/by-nc-nd/4.0. Any commercial reuse of Open Access articles published with a CC BY NC SA or CC BY NC ND license requires permission from Elsevier and will be subject to a fee.

Commercial reuse includes:

- Associating advertising with the full text of the Article
- Charging fees for document delivery or access
- Article aggregation
- Systematic distribution via e-mail lists or share buttons

Posting or linking by commercial companies for use by customers of those companies.

20. **Other Conditions**:

v1.9

Questions? customercare@copyright.com or +1-855-239-3415 (toll free in the US) or +1-978-646-2777.

Permission letter from the publisher to reuse **Figure 2.11**.

Copyright Clearance Center Marketplace™

Royal Society of Chemistry - License Terms and Conditions

This is a License Agreement between Chen-Yu Tsai ("You") and Royal Society of Chemistry ("Publisher") provided by Copyright Clearance Center ("CCC"). The license consists of your order details, the terms and conditions provided by Royal Society of Chemistry, and the CCC terms and conditions.

All payments must be made in full to CCC.

Order Date	07-Jul-2020	**Type of Use**	Republish in a thesis/dissertation
Order license ID	1046726-1		
ISSN	2050-7496	**Publisher**	Royal Society of Chemistry
		Portion	Chart/graph/table/figure

LICENSED CONTENT

Publication Title	Journal of materials chemistry. A, Materials for energy and sustainability	**Country**	United Kingdom of Great Britain and Northern Ireland
Author/Editor	Royal Society of Chemistry (Great Britain)	**Rightsholder**	Royal Society of Chemistry
		Publication Type	e-Journal
Date	01/01/2013	**URL**	http://pubs.rsc.org/en/journals/journalissues/ta
Language	English		

REQUEST DETAILS

Portion Type	Chart/graph/table/figure	**Distribution**	Worldwide
Number of charts / graphs / tables / figures requested	1	**Translation**	Original language of publication
		Copies for the disabled?	No
Format (select all that apply)	Print, Electronic	**Minor editing privileges?**	Yes
		Incidental promotional use?	No
Who will republish the content?	Academic institution		
		Currency	GBP
Duration of Use	Life of current edition		
Lifetime Unit Quantity	Up to 499		
Rights Requested	Main product		

NEW WORK DETAILS

Title	PhD thesis: Phase evolution and reactivity of Pr2NiO4+d and Ce0.9Gd0.1O2-d solid oxide cell electrodes	**Institution name**	Imperial College London
		Expected presentation date	2020-07-20
Instructor name	Chen-Yu Tsai		

ADDITIONAL DETAILS

Order reference number	N/A	**The requesting person / organization to appear on the license**	Chen-Yu Tsai

REUSE CONTENT DETAILS

Title, description or numeric reference of the portion(s)	Fig. 7	**Title of the article/chapter the portion is from**	Influence of annealing at intermediate temperature on oxygen transport kinetics of Pr2NiO4+δ
Editor of portion(s)	Saim Saher, Jia Song, Vaibhav Vibhu, Clément Nicollet, Aurélien Flura, Jean-Marc Bassat, Henny J. M. Bouwmeester	**Author of portion(s)**	Saim Saher, Jia Song, Vaibhav Vibhu, Clément Nicollet, Aurélien Flura, Jean-Marc Bassat, Henny J. M. Bouwmeester
Volume of serial or monograph	6	**Issue, if republishing an article from a serial**	N/A
Page or page range of portion	8331-8339	**Publication date of portion**	2018-03-27

CCC Republication Terms and Conditions

1. Description of Service; Defined Terms. This Republication License enables the User to obtain licenses for republication of one or more copyrighted works as described in detail on the relevant Order Confirmation (the "Work(s)"). Copyright Clearance Center, Inc. ("CCC") grants licenses through the Service on behalf of the rightsholder identified on the Order Confirmation (the "Rightsholder"). "Republication", as used herein, generally means the inclusion of a Work, in whole or in part, in a new work or works, also as described on the Order Confirmation. "User", as used herein, means the person or entity making such republication.

2. The terms set forth in the relevant Order Confirmation, and any terms set by the Rightsholder with respect to a particular Work, govern the terms of use of Works in connection with the Service. By using the Service, the person transacting for a republication license on behalf of the User represents and warrants that he/she/it (a) has been duly authorized by the User to accept, and hereby does accept, all such terms and conditions on behalf of User, and (b) shall inform User of all such terms and conditions. In the event such person is a "freelancer" or other third party independent of User and CCC, such party shall be deemed jointly a "User" for purposes of these terms and conditions. In any event, User shall be deemed to have accepted and agreed to all such terms and conditions if User republishes the Work in any fashion.

3. Scope of License; Limitations and Obligations.

   3.1. All Works and all rights therein, including copyright rights, remain the sole and exclusive property of the Rightsholder. The license created by the exchange of an Order Confirmation (and/or any invoice) and payment by User of the full amount set forth on that document includes only those rights expressly set forth in the Order Confirmation and in these terms and conditions, and conveys no other rights in the Work(s) to User. All rights not expressly granted are hereby reserved.

   3.2. General Payment Terms: You may pay by credit card or through an account with us payable at the end of the month. If you and we agree that you may establish a standing account with CCC, then the following terms apply: Remit Payment to: Copyright Clearance Center, 29118 Network Place, Chicago, IL 60673-1291. Payments Due: Invoices are payable upon their delivery to you (or upon our notice to you that they are available to you for downloading). After 30 days, outstanding amounts will be subject to a service charge of 1-1/2% per month or, if less, the maximum rate allowed by applicable law. Unless otherwise specifically set forth in the Order Confirmation or in a separate written agreement signed by CCC, invoices are due and payable on "net 30" terms. While User may exercise the rights licensed immediately upon issuance of the Order Confirmation, the license is automatically revoked and is null and void, as if it had never been

issued, if complete payment for the license is not received on a timely basis either from User directly or through a payment agent, such as a credit card company.

3.3. Unless otherwise provided in the Order Confirmation, any grant of rights to User (i) is "one-time" (including the editions and product family specified in the license), (ii) is non-exclusive and non-transferable and (iii) is subject to any and all limitations and restrictions (such as, but not limited to, limitations on duration of use or circulation) included in the Order Confirmation or invoice and/or in these terms and conditions. Upon completion of the licensed use, User shall either secure a new permission for further use of the Work(s) or immediately cease any new use of the Work(s) and shall render inaccessible (such as by deleting or by removing or severing links or other locators) any further copies of the Work (except for copies printed on paper in accordance with this license and still in User's stock at the end of such period).

3.4. In the event that the material for which a republication license is sought includes third party materials (such as photographs, illustrations, graphs, inserts and similar materials) which are identified in such material as having been used by permission, User is responsible for identifying, and seeking separate licenses (under this Service or otherwise) for, any of such third party materials; without a separate license, such third party materials may not be used.

3.5. Use of proper copyright notice for a Work is required as a condition of any license granted under the Service. Unless otherwise provided in the Order Confirmation, a proper copyright notice will read substantially as follows: "Republished with permission of [Rightsholder's name], from [Work's title, author, volume, edition number and year of copyright]; permission conveyed through Copyright Clearance Center, Inc. " Such notice must be provided in a reasonably legible font size and must be placed either immediately adjacent to the Work as used (for example, as part of a by-line or footnote but not as a separate electronic link) or in the place where substantially all other credits or notices for the new work containing the republished Work are located. Failure to include the required notice results in loss to the Rightsholder and CCC, and the User shall be liable to pay liquidated damages for each such failure equal to twice the use fee specified in the Order Confirmation, in addition to the use fee itself and any other fees and charges specified.

3.6. User may only make alterations to the Work if and as expressly set forth in the Order Confirmation. No Work may be used in any way that is defamatory, violates the rights of third parties (including such third parties' rights of copyright, privacy, publicity, or other tangible or intangible property), or is otherwise illegal, sexually explicit or obscene. In addition, User may not conjoin a Work with any other material that may result in damage to the reputation of the Rightsholder. User agrees to inform CCC if it becomes aware of any infringement of any rights in a Work and to cooperate with any reasonable request of CCC or the Rightsholder in connection therewith.

4. Indemnity. User hereby indemnifies and agrees to defend the Rightsholder and CCC, and their respective employees and directors, against all claims, liability, damages, costs and expenses, including legal fees and expenses, arising out of any use of a Work beyond the scope of the rights granted herein, or any use of a Work which has been altered in any unauthorized way by User, including claims of defamation or infringement of rights of copyright, publicity, privacy or other tangible or intangible property.

5. Limitation of Liability. UNDER NO CIRCUMSTANCES WILL CCC OR THE RIGHTSHOLDER BE LIABLE FOR ANY DIRECT, INDIRECT, CONSEQUENTIAL OR INCIDENTAL DAMAGES (INCLUDING WITHOUT LIMITATION DAMAGES FOR LOSS OF BUSINESS PROFITS OR INFORMATION, OR FOR BUSINESS INTERRUPTION) ARISING OUT OF THE USE OR INABILITY TO USE A WORK, EVEN IF ONE OF THEM HAS BEEN ADVISED OF THE POSSIBILITY OF SUCH DAMAGES. In any event, the total liability of the Rightsholder and CCC (including their respective employees and directors) shall not exceed the total amount actually paid by User for this license. User assumes full liability for the actions and omissions of its principals, employees, agents, affiliates, successors and assigns.

6. Limited Warranties. THE WORK(S) AND RIGHT(S) ARE PROVIDED "AS IS". CCC HAS THE RIGHT TO GRANT TO USER THE RIGHTS GRANTED IN THE ORDER CONFIRMATION DOCUMENT. CCC AND THE RIGHTSHOLDER DISCLAIM ALL OTHER WARRANTIES RELATING TO THE WORK(S) AND RIGHT(S), EITHER EXPRESS OR IMPLIED, INCLUDING

WITHOUT LIMITATION IMPLIED WARRANTIES OF MERCHANTABILITY OR FITNESS FOR A PARTICULAR PURPOSE. ADDITIONAL RIGHTS MAY BE REQUIRED TO USE ILLUSTRATIONS, GRAPHS, PHOTOGRAPHS, ABSTRACTS, INSERTS OR OTHER PORTIONS OF THE WORK (AS OPPOSED TO THE ENTIRE WORK) IN A MANNER CONTEMPLATED BY USER; USER UNDERSTANDS AND AGREES THAT NEITHER CCC NOR THE RIGHTSHOLDER MAY HAVE SUCH ADDITIONAL RIGHTS TO GRANT.

7. Effect of Breach. Any failure by User to pay any amount when due, or any use by User of a Work beyond the scope of the license set forth in the Order Confirmation and/or these terms and conditions, shall be a material breach of the license created by the Order Confirmation and these terms and conditions. Any breach not cured within 30 days of written notice thereof shall result in immediate termination of such license without further notice. Any unauthorized (but licensable) use of a Work that is terminated immediately upon notice thereof may be liquidated by payment of the Rightsholder's ordinary license price therefor; any unauthorized (and unlicensable) use that is not terminated immediately for any reason (including, for example, because materials containing the Work cannot reasonably be recalled) will be subject to all remedies available at law or in equity, but in no event to a payment of less than three times the Rightsholder's ordinary license price for the most closely analogous licensable use plus Rightsholder's and/or CCC's costs and expenses incurred in collecting such payment.

8. Miscellaneous.

   8.1. User acknowledges that CCC may, from time to time, make changes or additions to the Service or to these terms and conditions, and CCC reserves the right to send notice to the User by electronic mail or otherwise for the purposes of notifying User of such changes or additions; provided that any such changes or additions shall not apply to permissions already secured and paid for.

   8.2. Use of User-related information collected through the Service is governed by CCC's privacy policy, available online here:https://marketplace.copyright.com/rs-ui-web/mp/privacy-policy

   8.3. The licensing transaction described in the Order Confirmation is personal to User. Therefore, User may not assign or transfer to any other person (whether a natural person or an organization of any kind) the license created by the Order Confirmation and these terms and conditions or any rights granted hereunder; provided, however, that User may assign such license in its entirety on written notice to CCC in the event of a transfer of all or substantially all of User's rights in the new material which includes the Work(s) licensed under this Service.

   8.4. No amendment or waiver of any terms is binding unless set forth in writing and signed by the parties. The Rightsholder and CCC hereby object to any terms contained in any writing prepared by the User or its principals, employees, agents or affiliates and purporting to govern or otherwise relate to the licensing transaction described in the Order Confirmation, which terms are in any way inconsistent with any terms set forth in the Order Confirmation and/or in these terms and conditions or CCC's standard operating procedures, whether such writing is prepared prior to, simultaneously with or subsequent to the Order Confirmation, and whether such writing appears on a copy of the Order Confirmation or in a separate instrument.

   8.5. The licensing transaction described in the Order Confirmation document shall be governed by and construed under the law of the State of New York, USA, without regard to the principles thereof of conflicts of law. Any case, controversy, suit, action, or proceeding arising out of, in connection with, or related to such licensing transaction shall be brought, at CCC's sole discretion, in any federal or state court located in the County of New York, State of New York, USA, or in any federal or state court whose geographical jurisdiction covers the location of the Rightsholder set forth in the Order Confirmation. The parties expressly submit to the personal jurisdiction and venue of each such federal or state court.If you have any comments or questions about the Service or Copyright Clearance Center, please contact us at 978-750-8400 or send an e-mail to support@copyright.com.

v 1.1

Permission letter from the publisher to reuse **Figure 2.12**.

ELSEVIER LICENSE
TERMS AND CONDITIONS

Jul 05, 2020

This Agreement between Chen-Yu Tsai ("You") and Elsevier ("Elsevier") consists of your license details and the terms and conditions provided by Elsevier and Copyright Clearance Center.

License Number	4862751005412
License date	Jul 05, 2020
Licensed Content Publisher	Elsevier
Licensed Content Publication	Solid State Ionics
Licensed Content Title	Modelling of ambipolar transport properties of composite mixed ionic-electronic conductors
Licensed Content Author	Zhonglin Wu,Meilin Liu
Licensed Content Date	Dec 1, 1996
Licensed Content Volume	93
Licensed Content Issue	1-2
Licensed Content Pages	20
Start Page	65
End Page	84

Type of Use	reuse in a thesis/dissertation
Portion	figures/tables/illustrations
Number of figures/tables/illustrations	2
Format	both print and electronic
Are you the author of this Elsevier article?	No
Will you be translating?	No
Title	PhD thesis: Phase evolution and reactivity of Pr2NiO4 d and Ce0.9Gd0.1O2-d solid oxide cell electrodes
Institution name	Imperial College London
Expected presentation date	Jul 2020
Portions	Fig. 13 and Fig. 14
Requestor Location	Chen-Yu Tsai Flat 6 Little Chelsea House Edith Grove London, SW10 0LA United Kingdom Attn: Chen-Yu Tsai
Publisher Tax ID	GB 494 6272 12
Total	0.00 USD
Terms and Conditions	

INTRODUCTION

1. The publisher for this copyrighted material is Elsevier. By clicking "accept" in connection with completing this licensing transaction, you agree that the following terms and conditions apply to this transaction (along with the Billing and Payment terms and conditions established by Copyright Clearance Center, Inc. ("CCC"), at the time that you opened your Rightslink account and that are available at any time at http://myaccount.copyright.com).

GENERAL TERMS

2. Elsevier hereby grants you permission to reproduce the aforementioned material subject to the terms and conditions indicated.

3. Acknowledgement: If any part of the material to be used (for example, figures) has appeared in our publication with credit or acknowledgement to another source, permission must also be sought from that source. If such permission is not obtained then that material may not be included in your publication/copies. Suitable acknowledgement to the source must be made, either as a footnote or in a reference list at the end of your publication, as follows:

"Reprinted from Publication title, Vol /edition number, Author(s), Title of article / title of chapter, Pages No., Copyright (Year), with permission from Elsevier [OR APPLICABLE SOCIETY COPYRIGHT OWNER]." Also Lancet special credit - "Reprinted from The Lancet, Vol. number, Author(s), Title of article, Pages No., Copyright (Year), with permission from Elsevier."

4. Reproduction of this material is confined to the purpose and/or media for which permission is hereby given.

5. Altering/Modifying Material: Not Permitted. However figures and illustrations may be altered/adapted minimally to serve your work. Any other abbreviations, additions, deletions and/or any other alterations shall be made only with prior written authorization of Elsevier Ltd. (Please contact Elsevier at permissions@elsevier.com). No modifications can be made to any Lancet figures/tables and they must be reproduced in full.

6. If the permission fee for the requested use of our material is waived in this instance, please be advised that your future requests for Elsevier materials may attract a fee.

7. Reservation of Rights: Publisher reserves all rights not specifically granted in the combination of (i) the license details provided by you and accepted in the course of this licensing transaction, (ii) these terms and conditions and (iii) CCC's Billing and Payment terms and conditions.

8. License Contingent Upon Payment: While you may exercise the rights licensed immediately upon issuance of the license at the end of the licensing process for the transaction, provided that you have disclosed complete and accurate details of your proposed use, no license is finally effective unless and until full payment is received from you (either by publisher or by CCC) as provided in CCC's Billing and Payment terms and conditions. If full payment is not received on a timely basis, then any license preliminarily granted shall be deemed automatically revoked and shall be void as if never granted. Further, in the event that you breach any of these terms and conditions or any of CCC's Billing and Payment terms and conditions, the license is automatically revoked and shall be void as if never granted. Use of materials as described in a revoked license, as well as any use of the materials beyond the scope of an unrevoked license, may constitute copyright infringement and publisher reserves the right to take any and all action to protect its copyright in the materials.

9. Warranties: Publisher makes no representations or warranties with respect to the licensed material.

10. Indemnity: You hereby indemnify and agree to hold harmless publisher and CCC, and their respective officers, directors, employees and agents, from and against any and all claims arising out of your use of the licensed material other than as specifically authorized pursuant to this license.

11. No Transfer of License: This license is personal to you and may not be sublicensed, assigned, or transferred by you to any other person without publisher's written permission.

12. No Amendment Except in Writing: This license may not be amended except in a writing signed by both parties (or, in the case of publisher, by CCC on publisher's behalf).

13. Objection to Contrary Terms: Publisher hereby objects to any terms contained in any purchase order, acknowledgment, check endorsement or other writing prepared by you, which terms are inconsistent with these terms and conditions or CCC's Billing and Payment terms and conditions. These terms and conditions, together with CCC's Billing and Payment terms and conditions (which are incorporated herein), comprise the entire agreement between you and publisher (and CCC) concerning this licensing transaction. In the event of any conflict between your obligations established by these terms and conditions and those established by CCC's Billing and Payment terms and conditions, these terms and conditions shall control.

14. Revocation: Elsevier or Copyright Clearance Center may deny the permissions described in this License at their sole discretion, for any reason or no reason, with a full refund payable to you. Notice of such denial will be made using the contact information provided by you. Failure to receive such notice will not alter or invalidate the denial. In no event will Elsevier or Copyright Clearance Center be responsible or liable for any costs, expenses or damage incurred by you as a result of a denial of your permission request, other than a refund of the amount(s) paid by you to Elsevier and/or Copyright Clearance Center for denied permissions.

LIMITED LICENSE

The following terms and conditions apply only to specific license types:

15. **Translation**: This permission is granted for non-exclusive world **English** rights only unless your license was granted for translation rights. If you licensed translation rights you may only translate this content into the languages you requested. A professional translator must perform all translations and reproduce the content word for word preserving the integrity of the article.

16. **Posting licensed content on any Website**: The following terms and conditions apply as follows: Licensing material from an Elsevier journal: All content posted to the web site must maintain the copyright information line on the bottom of each image; A hyper-text must be included to the Homepage of the journal from which you are licensing at http://www.sciencedirect.com/science/journal/xxxxx or the Elsevier homepage for books at http://www.elsevier.com; Central Storage: This license does not include permission for a scanned version of the material to be stored in a central repository such as that provided by Heron/XanEdu.

Licensing material from an Elsevier book: A hyper-text link must be included to the Elsevier homepage at http://www.elsevier.com . All content posted to the web site must maintain the copyright information line on the bottom of each image.

Posting licensed content on Electronic reserve: In addition to the above the following clauses are applicable: The web site must be password-protected and made available only to bona fide students registered on a relevant course. This permission is granted for 1 year only. You may obtain a new license for future website posting.

17. **For journal authors:** the following clauses are applicable in addition to the above:

Preprints:

A preprint is an author's own write-up of research results and analysis, it has not been peer-reviewed, nor has it had any other value added to it by a publisher (such as formatting, copyright, technical enhancement etc.).

Authors can share their preprints anywhere at any time. Preprints should not be added to or enhanced in any way in order to appear more like, or to substitute for, the final versions of articles however authors can update their preprints on arXiv or RePEc with their Accepted Author Manuscript (see below).

If accepted for publication, we encourage authors to link from the preprint to their formal publication via its DOI. Millions of researchers have access to the formal publications on ScienceDirect, and so links will help users to find, access, cite and use the best available version. Please note that Cell Press, The Lancet and some society-owned have different preprint policies. Information on these policies is available on the journal homepage.

Accepted Author Manuscripts: An accepted author manuscript is the manuscript of an article that has been accepted for publication and which typically includes author-incorporated changes suggested during submission, peer review and editor-author communications.

Authors can share their accepted author manuscript:

- immediately
  - via their non-commercial person homepage or blog
  - by updating a preprint in arXiv or RePEc with the accepted manuscript
  - via their research institute or institutional repository for internal institutional uses or as part of an invitation-only research collaboration work-group
  - directly by providing copies to their students or to research collaborators for their personal use
  - for private scholarly sharing as part of an invitation-only work group on commercial sites with which Elsevier has an agreement
- After the embargo period
  - via non-commercial hosting platforms such as their institutional repository
  - via commercial sites with which Elsevier has an agreement

In all cases accepted manuscripts should:

- link to the formal publication via its DOI
- bear a CC-BY-NC-ND license - this is easy to do
- if aggregated with other manuscripts, for example in a repository or other site, be shared in alignment with our hosting policy not be added to or enhanced in any way to appear more like, or to substitute for, the published journal article.

Published journal article (JPA): A published journal article (PJA) is the definitive final record of published research that appears or will appear in the journal and embodies all

value-adding publishing activities including peer review co-ordination, copy-editing, formatting, (if relevant) pagination and online enrichment.

Policies for sharing publishing journal articles differ for subscription and gold open access articles:

Subscription Articles: If you are an author, please share a link to your article rather than the full-text. Millions of researchers have access to the formal publications on ScienceDirect, and so links will help your users to find, access, cite, and use the best available version.

Theses and dissertations which contain embedded PJAs as part of the formal submission can be posted publicly by the awarding institution with DOI links back to the formal publications on ScienceDirect.

If you are affiliated with a library that subscribes to ScienceDirect you have additional private sharing rights for others' research accessed under that agreement. This includes use for classroom teaching and internal training at the institution (including use in course packs and courseware programs), and inclusion of the article for grant funding purposes.

Gold Open Access Articles: May be shared according to the author-selected end-user license and should contain a CrossMark logo, the end user license, and a DOI link to the formal publication on ScienceDirect.

Please refer to Elsevier's posting policy for further information.

18. **For book authors** the following clauses are applicable in addition to the above: Authors are permitted to place a brief summary of their work online only. You are not allowed to download and post the published electronic version of your chapter, nor may you scan the printed edition to create an electronic version. **Posting to a repository:** Authors are permitted to post a summary of their chapter only in their institution's repository.

19. **Thesis/Dissertation**: If your license is for use in a thesis/dissertation your thesis may be submitted to your institution in either print or electronic form. Should your thesis be published commercially, please reapply for permission. These requirements include permission for the Library and Archives of Canada to supply single copies, on demand, of the complete thesis and include permission for Proquest/UMI to supply single copies, on demand, of the complete thesis. Should your thesis be published commercially, please reapply for permission. Theses and dissertations which contain embedded PJAs as part of the formal submission can be posted publicly by the awarding institution with DOI links back to the formal publications on ScienceDirect.

Elsevier Open Access Terms and Conditions

You can publish open access with Elsevier in hundreds of open access journals or in nearly 2000 established subscription journals that support open access publishing. Permitted third party re-use of these open access articles is defined by the author's choice of Creative Commons user license. See our open access license policy for more information.

Terms & Conditions applicable to all Open Access articles published with Elsevier:

Any reuse of the article must not represent the author as endorsing the adaptation of the article nor should the article be modified in such a way as to damage the author's honour or reputation. If any changes have been made, such changes must be clearly indicated.

The author(s) must be appropriately credited and we ask that you include the end user license and a DOI link to the formal publication on ScienceDirect.

If any part of the material to be used (for example, figures) has appeared in our publication with credit or acknowledgement to another source it is the responsibility of the user to ensure their reuse complies with the terms and conditions determined by the rights holder.

Additional Terms & Conditions applicable to each Creative Commons user license:

CC BY: The CC-BY license allows users to copy, to create extracts, abstracts and new works from the Article, to alter and revise the Article and to make commercial use of the Article (including reuse and/or resale of the Article by commercial entities), provided the user gives appropriate credit (with a link to the formal publication through the relevant DOI), provides a link to the license, indicates if changes were made and the licensor is not represented as endorsing the use made of the work. The full details of the license are available at http://creativecommons.org/licenses/by/4.0.

CC BY NC SA: The CC BY-NC-SA license allows users to copy, to create extracts, abstracts and new works from the Article, to alter and revise the Article, provided this is not done for commercial purposes, and that the user gives appropriate credit (with a link to the formal publication through the relevant DOI), provides a link to the license, indicates if changes were made and the licensor is not represented as endorsing the use made of the work. Further, any new works must be made available on the same conditions. The full details of the license are available at http://creativecommons.org/licenses/by-nc-sa/4.0.

CC BY NC ND: The CC BY-NC-ND license allows users to copy and distribute the Article, provided this is not done for commercial purposes and further does not permit distribution of the Article if it is changed or edited in any way, and provided the user gives appropriate credit (with a link to the formal publication through the relevant DOI), provides a link to the license, and that the licensor is not represented as endorsing the use made of the work. The full details of the license are available at http://creativecommons.org/licenses/by-nc-nd/4.0. Any commercial reuse of Open Access articles published with a CC BY NC SA or CC BY NC ND license requires permission from Elsevier and will be subject to a fee.

Commercial reuse includes:

- Associating advertising with the full text of the Article
- Charging fees for document delivery or access
- Article aggregation
- Systematic distribution via e-mail lists or share buttons

Posting or linking by commercial companies for use by customers of those companies.

20. **Other Conditions**:

v1.9

Questions? customercare@copyright.com or +1-855-239-3415 (toll free in the US) or +1-978-646-2777.